PHOTOPHYSICAL INVESTIGATION AND PHARMACEUTICAL APPLICATIONS OF CHLORIN e6 IN BIODEGRADABLE CARRIERS

SHUBHAJIT PAUL

NATIONAL UNIVERSITY OF SINGAPORE

2013

PHOTOPHYSICAL INVESTIGATION AND PHARMACEUTICAL APPLICATIONS OF CHLORIN e6 IN BIODEGRADABLE CARRIERS

SHUBHAJIT PAUL

M.Pharm (Hons.), Jadavpur University

A THESIS SUBMITTED

FOR THE DEGREE OF DOCTOR OF PHILOSOPHY

DEPARTMENT OF PHARMACY

NATIONAL UNIVERSITY OF SINGAPORE

2013

DECLARATION

I hereby declare that the thesis is my original work and it has been written by me in its entirety. I have duly acknowledged all the sources of information which have been used in the thesis.

This thesis has also not been submitted for any degree in any university previously.

Shubhajit Paul

23 January, 2013

ACKNOWLEDGEMENT

I would like to express my heartfelt thanks to my supervisors, A/P Chan Lai Wah and A/P Paul Heng Wan Sia for their patience, guidance, encouragements and opportunities in mentoring me throughout my candidature. I am grateful to both of them for their critical and valuable suggestions and ideas in framing this thesis. I would also like to thank Asst. Prof. Celine Liew and Prof. Kurup for their suggestions to improve my work and for being so cordial.

I would like to acknowledge the kindness of Asst. Prof. Gigi Chew, Asst. Prof. Eng Hui and A/P Victor Yu to let me use the zetasizer, epifluorescence and confocal microscope.

I'm highly indebted to National University of Singapore for providing the research scholarship as well as the research opportunity to pursue Doctor of Philosophy. I would also like to thank Teresa and Mei Yin for their kind support and being so approachable.

I would also like to extend my heartfelt thanks to all other faculty members, lab technicians, office staffs, and department friends for their cooperation and contribution towards the completion of my project. My sincere appreciation goes to each of my present friends and past colleagues in GEANUS, who always extended their hands when I asked for help.

A very special thanks to all of my flatmates and friends in Singapore, who stood beside me in every tortuous experience of my life and made these four years enjoyable and memorable.

Finally, I want to express my deepest respect to my Late grandmother and Late mother for their heartiest inspirations in the path to achieve a higher degree. I'm also highly indebted to my cousin brother and my close friends for their unconditional support to my family during my absence. I'm thankful to Susmita for her inspirations for successful completion of my candidature. Above all, I thank The Supreme Being for giving me the strength to endure the loss of my dearest grandmother and mother and the determination to look forward in life.

I believe, the virtues and qualities I earned in this journey, will hone my strength and determination for future endeavour.

Shubhajit

Jan, 2013

DEDICATION

Mom,

There is no feeling so comforting and solacing than knowing you are right next to me for every endeavour I step in. They say you are no more, but your lessons, inspirations and commitments to make me a good human being will always be remembered.

TABLE OF CONTENTS

SUMMARY

Photodynamic therapy is an emerging treatment modality for cancer as it is a non-invasive, inexpensive and able to produce targeted effect. It is based on the dynamic interaction of light, oxygen and a fluorescence molecule (photosensitizer) to induce oxidative damage in cancerous cells. Chlorin e6 (Ce6), introduced in the early 90's has widely been used as photosensitizer of interest. However, the photodynamic efficacy of Ce6 is largely limited by its tendency to form aggregates. In addition, strong hydrophobicity of Ce6 adversely affects its bioavailability.

In this study, it was hypothesized that aggregation of Ce6 could be prevented by using suitable pharmaceutical adjuvants, which would render Ce6 aggregates into its monomeric form. Furthermore, it was anticipated that these adjuvants could also be used as drug carrier for Ce6 if appropriately formulated. Their dual characteristics would therefore satisfy the necessity of a disaggregating agent and a drug carrier together.

The study was divided into two parts, comprising photophysical investigation and pharmaceutical applications. In the first part, the influence of physicochemical factors such as pH and Ce6 concentration on the aggregate formation were extensively studied. The findings suggested that Ce6 preferentially exist as aggregates in the acidic to near neutral pH conditions as exhibited by broadened absorption spectra, reduced fluorescence intensity and lower quantum yield in the afore-mentioned pH conditions. In these pH conditions, Ce6 had a higher octanol/water partition coefficient value with lower aqueous solubility, suggesting aggregation was promoted by hydrophobic force. Novel chemometric quantification was applied employing Parallel Factor (PARAFAC)

algorithm to determine the fraction of different species of Ce6 (aggregate or monomer) at varying pH conditions. The results obtained were in good agreement with the spectroscopic findings, confirming significant influence of pH on Ce6 aggregation and photophysical properties.

The disaggregation potential of polyvinylpyrrolidone (PVP) and sucrose esters (SE) was investigated. Disaggregation efficiency of PVP and SE gradually increased on decreasing the PVP molecular weight and increasing the alkyl chain of SE respectively. Using thermodynamic studies, the disaggregation effect was found to be mediated by hydrophobic interactions. Simulations at molecular level showed that Ce6 monomers could be entangled at different locations of the PVP macromolecules or incorporated into the hydrophobic core of SE.

In the second part, selected formulations were evaluated. A modified hot-melt emulsification method was used to prepare Ce6-SE nanosuspension, where Ce6 was encapsulated as amorphous form in the SE matrix resulting in enhanced *in vitro* dissolution. Encapsulating Ce6-PVP complex in alginate nanoparticles further enhanced the mucoadhesivity of the formulation. These formulations were optimized using appropriate statistical designs. The photodynamic efficacy of these formulations was evaluated using extent of singlet oxygen generation, cellular uptake and phototoxicity to oral squamous carcinoma cells as determining parameters. The optimized formulations were found to exhibit superior photodynamic activity against oral squamous carcinoma cells in comparison with aggregate-rich solution form of Ce6.

LIST OF TABLES

LIST OF FIGURES

LIST OF SYMBOLS AND ABBREVIATIONS

$< h^2 >^{1/2}$	End-to-end distance
AC	Acetone
ALA	Amino levulinic acid
Alg	Sodium alginate
AMD	Age-related macular degeneration
CAM	Chorio allantoic membrane
CCD	Central composite design
C_{cd}	Concentration for complete disaggregation
Ce6	Chlorin e6
Cp6	Chlorin p6
Ce6-PVP-Alg	Optimized formulation of Ce6-PVP encapsulated in alginate
CMC	Critical micellar concentration
D	Diffusion coefficient
DCM	Dichloromethane
d_i	Desirability function
DMEM	Dulbecco's modified eagle's medium
DMSO	Dimethyl sulfoxide
DPc	Dendrimer pthalocyanine
DPD	Dissipative particle dynamics
DPPC	Dipalmitoyldiphophatidylcholine
DSC	Differential scanning calorimetry
EE	Encapsulation efficiency
EEM	Excitation emission matrix
EPR	Enhanced permeability and retention effect

$\mathbf{F}_{ij}^{C}$	Conservative force between beads, *i* and *j*
$\mathbf{F}_{ij}^{D}$	Dissipative force between beads, *i* and *j*
$\mathbf{F}_{ij}^{R}$	Random force between beads, *i* and *j*
FBS	Fetal bovine serum
FRET	Förster resonance energy transfer
FT-IR	Fourier transformed infrared
HIV	Human immuno deficiency
Hp	Hematoporphyrin
HPPH	2-[1-Hexyloxyethyl]-2-devinyl pyropheophorbide
K_a	Ce6-PVP binding constant
K_b	Ce6-sucrose ester binding constant
k_B	Boltzmann constant
K_i	Dissolution constant
LED	Light emitting diode
M	Ratio of sucrose ester micelle to Ce6 monomer
MACE	Mono-aspertyl chlorin e6
N	Number of species
n	Number of binding sites per PVP monomer
N_0	Number of Ce6 binding sites per PVP molecule
NIR	Near infrared
OSC	Oral Squamous carcinoma
P	Number of PVP monomers per binding site
PAA	Polyacrylamide
PARAFAC	Parallel factor algorithm
PBS	Phosphate buffer solution

Pc	Pthalocyanine
PDI	Polydispersity index
PDT	Photodynamic therapy
PE	Phosphatidyl ethanolamine
PEO-PCL	Polyethylene oxide-polycaprolactone
PLA-PEG	Polylactic acid-polyethyelene glycol
PPI	Polypropyleneimine
PpIX	Protoporphyrin IX
PVP	Polyvinylpyrrolidone
QD	Quantum dot
r	Moles of Ce6 per mole of PVP monomer
R	Universal gas constant
R^2	Determination coefficient in ANNOVA
r^a	Correlation coefficient
RB	Rhodamine B
r_c	Radius of diffusing molecule
RES	Reticuloendothelial system
RMS	Root mean square
RNO	p-nitroso aniline
SE	Sucrose esters
SEL	Sucrose ester monolaurate
SEM	Sucrose ester monomyristate
SEP	Sucrose ester monopalmitate
SEP/SEL-Ce6	Optimized formulation of Ce6 and sucrose esters
t_{90}	Time required for 90 % drug release

T	Temperature
t	Time
TEM	Transmission electron microscopy
THPC	Tetra-hydroxy phenyl chlorin
THPP	Tetra-hydroxy phenyl porphyrin
uv-vis	Ultraviolet-visible
X_1	SEP:SEL ratio (for CCD design)
X_2	Amount of Ce6 (for CCD design)
X_3	DCM:AC ratio (for CCD design)
x_1	Amount of Ce6 (for 3^2 factorial design)
x_2	Amount of PVP (for 3^2 factorial design)
x	Fraction of PVP-bound Ce6
XRD	X ray diffraction
Y_1	Particle size of SEP/SEL-Ce6 NS
Y_2	Zeta potential of SEP/SEL-Ce6 NS
Y_3	Encapsulation efficiency of SEP/SEL-Ce6 NS
Y_4	Time required for 90 % drug release SEP/SEL-Ce6 NS
y_1	Particle size of Ce6-PVP-ALG NP
y_2	Encapsulation efficiency of Ce6-PVP-ALG NP
y_3	Percent mucoadhesivity of Ce6-PVP-ALG NP
y_4	In *vitro* drug release of Ce6-PVP-ALG NP
ZP	Zeta potential
α	Area under the curve
γ	Parameter in central composite design
δ	Viscosity of fluid

ΔH	Variation in enthalpy
ΔS	Variation in entropy
η	Refractive index
λ_{em}	Wavelength of maximum emission
λ_{ex}	Wavelength of maximum excitation
μ	Fluorescence anisotropy
ρ	Compressibility of fluid
ϕ	Quantum yield
χ_{ij}	Repulsion parameter between beads, *i* and *j*

PART 1: INTRODUCTION

1. INTRODUCTION

1.1. Background

Cancer is one of the potentially fatal diseases responsible for the rising death toll in many countries nowadays. Apart from surgical intervention, photodynamic therapy (PDT) is one of the emerging treatments of interest for premalignant and malignant conditions. This mode of treatment is based on dynamic interaction of light, oxygen and a photoactive drug to induce oxidative damage in target tissues [1-3]. In the last decade, this treatment modality had gained increased attention as it is mostly non-invasive and potentially devoid of the toxic adverse effects associated with chemotherapy [4]. The molecular and pharmacological basis for photodynamic therapy was established in the early 1990's [5]. For PDT, the patient is usually administered the photoactive drug either intravenously or topically (for superficial tumours) and exposed to light of higher wavelengths (usually red light) for a period of time. The photons from light activate the drug molecules and subsequently produce highly reactive oxygen radicals, which are thought to be the main mediator of cellular death induced by PDT [6]. PDT is now well-established as an acceptable option in lung, esophagus, bladder, skin or head and neck cancers [7,8]. In addition, employing such photoactive compounds (known as photosensitizers) as probes greatly enhance the detection of small or poorly differentiated neoplastic tissues based on fluorescence light emission after accumulation of the photoactive compounds in the affected tissues. Interestingly, one of the prominent advantages of using this treatment modality is the selective destruction of tumour cells with minimal involvement of surrounding healthy tissues. This is achieved by a

combination of specific photosensitizer properties affecting cellular accumulation and control of the light geometry and illumination parameters of the photodynamic source [9].

1.2. Photosensitizers in the treatment of cancer

Many photosensitizers have been extracted from natural sources or synthesized and evaluated for their biological activities. Over time, several new generations of photosensitizers have been introduced and evaluated [10]. The earliest application of PDT in the treatment of a cancerous disease can be traced back to 4000 years ago when the ancient Egyptians used a combination of plant extracts (containing photoactive psoralens) and sunlight to treat vitiligo [11]. Contemporary research in PDT began around the late 19th century with the discovery by Finsen that the skin disease, *Lupus vulgaris* could be treated using ultraviolet (uv) light [12.]. In 1903, Trappeiner used eosin and light to treat skin disease [13]. PDT research underwent a new phase by the venturous experiments of Meyer-Betz in 1913 when he injected himself with 200 mg of hematoporphyrin (Hp) and found no ill effects until he was exposed to sunlight, whereupon he suffered extreme swelling and photosensitivity over several months [14]. In the early 1950's, Schwartz discovered that it was not the monomeric hematoporphyrin but an oligomeric mixture that actuated long term phototoxic effect in the Meyer-Betz's experiment [15]. Schwartz synthesized a new Hp derivative (HpD) containing enriched oligomer fractions by treating Hp with sulfuric acid in acetic acid and then followed by treatment with alkali. By 1960, the combination of HpD and selective light irradiation marked the start of the usage of PDT in the treatment of cancerous diseases [16-18].

1.2.1. Different classes of photosensitizers

Photosensitizers can be characterized by their chemical structures and origins. They are generally divided into three categories, namely first generation photosensitizers, second generation photosensitizers and dyes, according to their history of synthesis and use (Figure 1). Hematoporphyrin derivative (HpD), a first generation photosensitizer, was introduced by Schwartz and it was marketed as Photofrin® after purification for the treatment of lung cancer [19-20]. Porphyrins are heteroaromatic compounds characterized by a tetrapyrrolic structure that consists of four pentagonal pyrroles linked by four methylene bridges [Figure 1]. Porphyrins are considered to be stable although they can be oxidized or reduced. They are characterized by an absorption spectrum with a specific band around 400 nm (Soret band) and four further specific bands in the region 500-650 nm [21]. Photofrin® was marketed as the first generation photosensitizer by Axcan Pharma, USA in 1982 and subsequently approved for clinical use by the regulatory agencies of other countries [22]. However, Photofrin® posed several deficiencies, including poor tumour selectivity, weak absorption in the near infrared region and induction of long-lasting retinal and skin photosensitizing effects [23-25].

The second generation photosensitizers were developed by further modification of HpD or the porphyrin macrocycle for better photodynamic efficacy. Further emphasis was put forth in modification of porphyrin nucleus to induce specificity, such as to remain preferentially inactivated in absence of light. Low cytotoxicity in absence of laser irradiation (dark toxicity) was observed in these photosensitizers. Examples include 5-amino levulinic acid (ALA) and chlorin/purpurin derivatives. ALA is a prodrug, enzymatically transformed into protoporphyrin IX *in situ* (Fig. 1). It is a hydrophilic

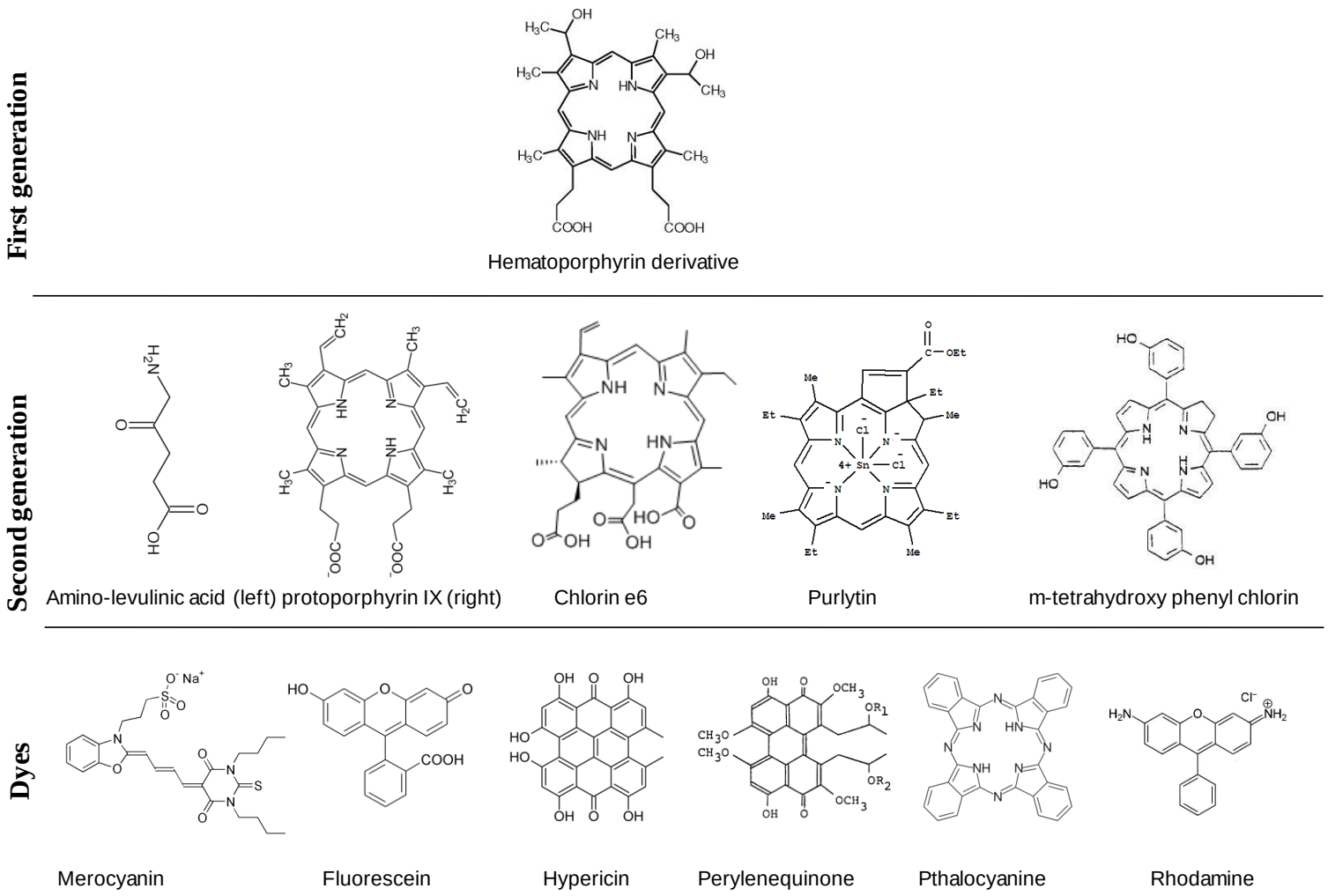

Figure 1: Different categories of photosensitizers.

molecule and does not penetrate intact skin, cell membrane or biological barriers easily. Although lacking in the ability to produce high fluorescence intensity at 630 nm, ALA has been efficiently used in dermatology for the treatment of neoplastic skin carcinoma [26-27].

Another group of promising second generation photosensitizers is the chlorin derivatives which are produced from chlorophyll by chemical synthesis. Unlike porphyrins, chlorins strongly absorb in the red region (between 640 and 700 nm), possess high fluorescence half-life and are devoid of the afore-mentioned disadvantages of first generation photosensitizers [28-29]. Chlorin derivatives are localized in the cellular lysozomes and exert cytotoxic effects after light irradiation.

Purpurins are benzoporphyrin-based derivatives, either free-base or complexed with a metal (silver, nickel, tin, zinc, etc.). They show a strong light absorption in the red region but only the metallic purpurins of tin or zinc are useful for PDT [30]. One of the highly effective purpurins representative of this class is purlytin (Fig. 1), which is a tin ethyl etiopurpurin dichloride ($SnET_2$), used for several ophthalmological, oncological and urological indications [31]. An effective benzoporphyrin derivative, Verteporphin or Visudyne®, has been approved by the Food and Drug Administration of the United States (US FDA) particularly for ophthalmologic applications, and age-related macular degeneration (AMD). The intracellular localization of this photosensitizer at the tumour site was reported to be rapid immediately after injection, which showed potent cytotoxicity following light irradiation at 690 nm [32].

Other notable second generation photosensitizers include tetrahydroxyphenylchlorin (THPC), pthalocyanines and texaphyrins derivatives, which are characterized by strong absorption in the red region and approved for photodiagnosis and treatment of proliferative diseases and infections [33, 34].

Some dyes are useful photosensitizers. They include anthraquinones and perylenequinones, hypericin, xanthenes, fluorescein, rhodamines and cyanines. Some of these compounds have been approved by US FDA and other drug regulatory agencies for the treatment of malignant carcinomas [35].

1.2.2. Mechanism of photosensitization

The mechanism of light absorption and energy transfer in the event of photodynamic therapy is illustrated by a modified Jabolonski diagram in Figure 2 [36]. The photosensitizer absorbs energy from light and is excited from its ground state (S_0) into an excited singlet state (S_1). The excited molecule can return to S_0 by non-radiative decay or fluorescence. Alternatively, the excited molecule can undergo inter-system crossing to an excited triplet state (T_1). The photosensitizer in the excited triplet state can undergo two types of reactions (Figure 2). In the Type 1 reaction, it can react directly with a substrate, such as the cell membrane or a molecule, and transfer a proton or an electron to form a radical anion or radical cation, respectively. These radicals may further react with oxygen to produce reactive oxygen species. In the Type 2 reaction, the photosensitizer in the triplet state can transfer its energy directly to molecular oxygen ($^3O_2$) to form excited state singlet oxygen ($^1O_2$). Both Type 1 and Type 2 reactions usually occur spontaneously and the ratio between these two reactions depends on the kind of photosensitizer used as

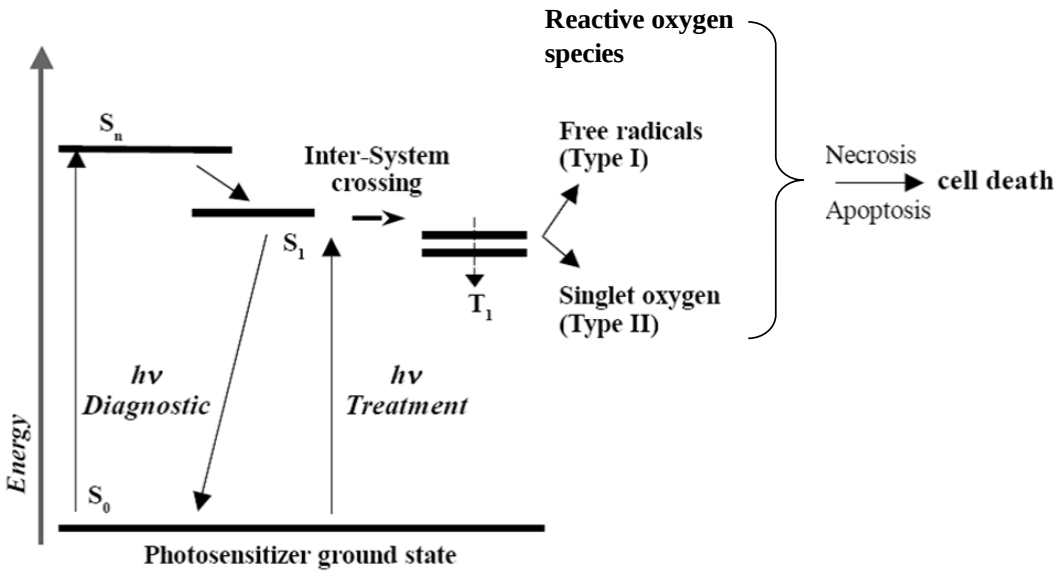

Figure 2: Graphical illustration of photophysical and photochemical pathways of PDT.

well as the concentrations of substrate and oxygen available. The free radicals or singlet oxygen generated are highly active oxidizing agents, which cause damage to DNA base-pair, or modification of various functional proteins in the cell organelles through oxidation. The free radicals could also result in cell death by direct oxidative attack on protein biomolecules, leading to inhibition of protein synthesis. The lifetime of singlet oxygen in cellular systems ranges from 100 ns to 250 ns and its diffusion range is limited to approximately 45 nm. Therefore, only molecules and structures that are proximal to the area of its generation (areas of photosensitizer localization) are directly affected by PDT [37-40].

1.2.3. Chemical and photophysical properties of photosensitizers

Considering the afore-mentioned principles of photoexcitation for PDT, a photosensitizer should ideally have the following characteristics [41-43]:

- Strong absorption in the higher wavelength of visible light spectral region (> 650 nm)
- High quantum yield of the triplet formation with a triplet energy greater than 94 KJ/mol, which is the energy required for conversion of $^3O_2$ to $^1O_2$
- High singlet oxygen quantum yield
- Low dark toxicity and selective cytotoxic effect in the presence of light
- High absorption band or molar extinction coefficient (> 20,000-30,000M^{-1} cm^{-1}) to minimize the dose of photosensitizer needed to achieve the desired effect
- Rapid clearance from the body to ensure low systemic toxicity
- Selective accumulation in the tumour tissues compared to healthy tissues
- Adequate lipophilicity to efficiently permeate into the affected cell
- Facile synthesis from readily available starting compounds that are inexpensive

1.2.4. Factors affecting photosensitization

The therapeutic efficacy of PDT depends on several factors, which when collectively triggered, produce the optimal outcome. The sensitizing efficiency has often been reported to be affected by physico-chemical factors, resulting in deviation from the desired behaviour of an ideal photosensitizer. The various factors that affect the sensitizing efficiency are discussed below.

1.2.4.1. Aggregation of photosensitizers

The self-association of hydrophobic or amphiphilic photosensitizers in solution is frequently encountered owing to the strong intermolecular van der Waals-like attractive forces between the relatively large molecules. Aggregation is characterized by the reduction in fluorescence emission along with compromised photophysical properties for

porphyrins, chlorins, cyanines and various other dyes [44]. The aggregates in solution exhibit distinct changes in the absorption band as compared to the monomeric species. From the spectral shifts, various aggregation patterns of the compounds in different media have been proposed. Bathochromically-shifted J-bands and hypsochromically-shifted H-bands of the aggregates have been explained in terms of molecular exciton coupling theory. For bathochromatic shifts, spectral bands migrate to lower frequencies (longer wavelengths) and are informally referred to as red shifts. In contrast, hypsochromic shift refers to the migration of a spectral band to a higher frequency (shorter wavelength) and is commonly known as a blue shift [45]. Extensive studies on J- and H-aggregates have revealed that these aggregates exist as one-dimensional assemblies in solution. Based on these proposals, various arrangements such as brickwork, ladder or staircase type of association are possible (Figure 3) [46]. These aggregates are typically composed of parallel photosensitizer molecules stacked plane-to-plane or end-to-end and form two-dimensional crystals. The presence of aggregates can be identified by bi-exponential or tri-exponential fluorescence decays, exhibiting very short decay component, usually smaller than 50 ps. In addition, the fluorescence intensity and the singlet oxygen quantum yield of an aggregated species are significantly lower than those of the corresponding monomer. This observation is attributed to the association of photosensitizer molecules, where the relaxation energy is released by non-radiative way without attaining the triplet state, thereby resulting in reduced singlet oxygen generation [47-50]. Consequently, the fluorescence life-time of aggregated species is shorter and thereby reduces the transition from singlet (S_1) to triplet (T_1) state, which is an essential step in the photochemical pathway of PDT modality. Therefore, the

aggregated species is not advantageous for PDT action and the understanding of how to avoid aggregation of photosensitizer molecules is important.

(a) Ladder-type (b) Staircase-type (c) Brickwork-type

Figure 3: Schematic representation of different arrangements of fluorophores during aggregation.

1.2.4.2. Interaction with solvents

The surrounding solvent molecules can affect fluorescence emission and self-association of dye molecules. In fact, a high degree of sensitivity in fluorescence is primarily due to interactions occurring in the local environment during the excited state lifetime, when the fluorophore is considered as an entirely different entity due to some of its unique properties. In solution, solvent molecules surrounding the ground state fluorophore have dipole moments that can interact with the dipole moment of the fluorophore to build an ordered distribution of solvent molecules around the fluorophore [51]. Due to energy level difference between the ground and excited states, the dipole moment of the fluorophore changes, which subsequently induces a rearrangement in dipole moment of surrounding solvent molecules to maintain the ordered distribution (Figure 4). Upon excitation of a fluorophore, the molecule achieves a higher electronic energy level in a far shorter timeframe. This is a couple of folds shorter than the time required for the fluorophore and solvent molecules to re-orient themselves within the ideal solute-solvent

interactive environment. Once the fluorophore is excited to higher vibrational levels of the first excited singlet state (S_1), excess vibrational energy is rapidly lost to surrounding solvent molecules as the fluorophore slowly relaxes to the lowest vibrational energy level. Solvent molecules assist in stabilizing and further lowering the energy level of the excited state by re-orienting around the excited fluorophore. This induces reduction in the energy separation between the ground and excited states and results in a red shift of the fluorescence emission. Increasing the solvent polarity produces a correspondingly larger

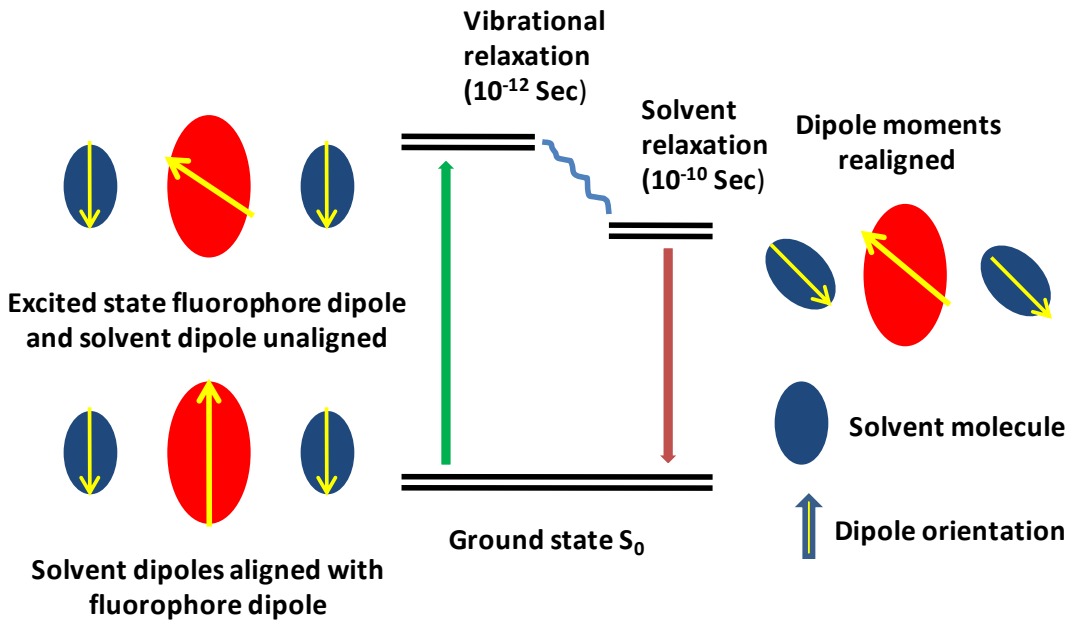

Figure 4: Schematic representation of solvent-induced photophysical transformations of fluorophores.

reduction in the energy level of the excited state while decreasing the solvent polarity reduces the solvent effect on the excited state energy level. In addition, specific solvent-solute interactions, such as H-bonding between a polar solvent and polar fluorophore in the excited state, produce strong absorption bands and high fluorescence intensities. This is usually followed by a large red shift, implying a π-π^* transition of the fluorophore and

enhanced fluorescence activity in the excited state. However, weak non-covalent interactions persist between non-polar solvents and fluorophore, resulting in weak fluorescence emission, indicating increased propensity for the formation of aggregates [52-55].

1.2.4.3. Quenching Phenomenon

Quenching refers to the reduction in fluorescence intensity of a photosensitizer due to the presence of an external agent. This results in concomitant decrease in fluorescence quantum yield and attenuates the sensitizing efficacy during PDT. There are two quenching conditions characterized by the mechanisms of interaction between quencher and fluorophore: static and dynamic quenching. Static quenching refers to the formation of a non-fluorescence photosensitizer-quencher complex. In dynamic or collisional quenching, the quencher in the excited state diffuses towards the fluorophore and upon contact with the fluorophore, returns to the ground state without emission of a photon, thereby diminishing the fluorescence intensity [56]. Fluorescence quenching has been utilized mainly for the determination of protein folding sequence, conformational changes of amino acid residues or oxygen diffusion through membranes [57]. It has been reported that effective use of biodegradable quenchers for photosensitizer delivery results in enhanced sensitizing efficacy. The biodegradable quencher selectively delivers the drug at the site of action and it is then gradually eliminated from the target site. Thus, if the quencher is used as a photoactive drug carrier, a profound increase in fluorescence activity could be observed through gradual degradation of the carrier at the target site. Whereas, fluorescence intensity is attenuated at the non-target site due to the quenching action resulting in preserving the PDT activity [58-60].

1.2.4.4. Light dosimetry

Light is either scattered or absorbed when it enters the tissue and the extent of both processes depends on tissue type and light wavelength. In PDT, it is important to be able to predict the spatial distribution of light in the target tissue because the biological tissue is inhomogeneous and the presence of microscopic inhomogenities, such as macromolecules, cell organelles and interstitial layers, makes it turbid. Multiple scattering within a turbid medium leads to spreading or attenuation of a light beam and loss of directionality [61]. Scattering is generally the most important factor in limiting light penetration into most tissues and is measured by μ_s (which for soft tissues is in the range 100-1000 cm^{-1}). Absorption is usually of less importance and measured by μ_a (values in the range of 0.1-5 cm^{-1} for most tissues at green and longer wavelengths). The average penetration depth is about 1-3 mm at 630 nm, the wavelength used for clinical applications of photosensitizers. The penetration depth is approximately twice that at 700-850 nm. This observation led to the development of novel naphthylocyanines and bacteriochlorins, which possess excellent penetration power in the near infra-red (NIR) region [62-64]. Reduction of unwanted tissue damage and minimization of the absorption by endogenous chromophores are important considerations in the design of lasers to possess narrow bandwidth with well-controlled and focused light output. Table 1 lists the various types of light sources for PDT. In particular, xenon and tungsten lamps are often used when a broader spectrum of light is required for the photosensitizer. These are relatively inexpensive and easier to handle as compared to lasers, which require adjustments using optical filters for the desirable emission [65]. The amount of light dose emitted from the laser is an essential factor in modulating photodynamic efficiency.

Table 1: List of various irradiation sources used in PDT

Light source		Wavelength (nm)/adjustable	Irradiance (mW m^{-2})
Laser	Ar^+ laser	488, 514.5/No	500-1000
	Metal vapor laser	UV or visible/Yes	Up to several thousand
	Dye laser	Depending on dye/Yes	10-500
	Diode laser	600-950/Yes	Up to 700
	Titanium-sapphire	670-1100/Yes	Up to several thousand
Non-laser	Halogen bulb	> 400/ Yes	Up to 250
	Xenon lamp	UV-IR full spectrum/Yes	Up to 250
	LEDs	Visible and infrared/Yes	Up to 250

The effective light dose becomes further complicated depending on the tumour size and shape. Generally, a threshold photodynamic response is considered to be the function of the following parameters [66]:

$$R = E\, k_s\, T\, \varepsilon\, D\, \phi\, f \qquad \textbf{\textit{Equation}}\ (\mathbf{1})$$

where

R is the threshold concentration of the oxidizing radicals to elicit the PDT effect,

E is the irradiance on the tissue surface (w/cm^2),

k_s is the backscatter factor due to reflected light from the underlying tissue,

T is the exposure time of light,

ε is the extinction coefficient of photosensitive drug,

D is the concentration of the photosensitive drug,

Φ is the quantum yield of the singlet oxygen radical and

f is the fraction of the generated oxidizing radicals which attack the sensitive cellular sites.

In principle, the light dosimetry quantity is determined by the amount of light delivered (E) and the exposure time (T). Therefore, the amount of light dose (L) given is:

$$L = \frac{R}{k_S \, \varepsilon \, D \, \phi \, f} \qquad \textbf{\textit{Equation}} \ (2)$$

Considering that k_s, ε, and D are constant for a particular photosensitizer, L is proportional to R / ϕ f, which is also known as the threshold dose for that particular photosensitizer. For PDT studies *in vitro*, the commonly used light dose (L) is in the range of 0.1–10 J cm^{-2}, whereas, it could be as high as 1–600 J cm^{-2} for *in vivo* studies [67].

1.2.5. Advantages and disadvantages of PDT

The prominent advantages of PDT can be summarized as follows:

- PDT is recommended when surgery is contraindicated because of the tumour spread and other complications due to associated diseases.
- PDT produces a targeted effect. The red light selectively damages the tumour whereas surrounding tissues are less affected.

- As PDT is used for localized treatment of malignant carcinomas, the patient will not be subjected to an unwanted systemic effect. Therefore, the typical side effects of conventional chemotherapy such as nausea, vomiting, stomatitis, loss of hair and inhibition of hematopoiesis could be avoided.
- PDT is cost-effective. It is also a tolerable, localized and inexpensive technique, which can be used to treat a variety of malignant tumours (primary, relapsing and metastatic).
- Besides cancerous tissues, many skin conditions such as acne, Bowen's disease and sebaceous hyperplasia can be treated by PDT. It was recently reported that the photosensitizer, Photofrin®, is active against HIV as is it able to significantly reduce the intracellular and extracellular concentrations of HIV virus *in vitro* [68].

Apart from the non-invasive and cost-effective advantages, PDT also poses some limitations and these include the following.

- PDT is ideally recommended for the treatment of superficial tumours. As the depth of penetrating laser light is few millimeters, PDT has little effect on deep-seated tissue tumours.
- Another disadvantage is that following PDT treatment, the patient remains photosensitive and may suffer from severe swelling, skin rashes and dark pigmentation if exposed to light. For example, the light sensitivity of Photofrin® can last as long as two months [69].

- Another minor side effect is the inconvenience experienced by the patient as the time gap between photosensitizer administration and light irradiation, which could be extended to as long as 12-14 hr for ALA [70].

1.2.6. Challenges in PDT

Despite the various advantages of PDT, it is still regarded as a second line treatment in cancer therapy. Over the years, researchers have reported various limitations of PDT with regard to its *in vivo* efficacy. Most of the organic photosensitizers are hydrophobic and penetrate the cell membrane readily. However, the poor water solubility of the photosensitizers makes them unsuitable for systemic administration. In addition, the efficacy of a photosensitizer is largely attributed to its monomeric form, while the self-association of the monomers results in drastic reduction of photodynamic efficacy. Furthermore, during the transport of photosensitizers, physiological barriers and nonspecific uptake can affect their access to the target sites. Moreover, PDT outcome becomes clinically questionable by non-selective biodistribution of a photosensitizer, which necessitates the administration of higher doses of the photosensitizer with the consequence of increased incidence of side effects [71-74]. These limitations can be mitigated by synthesizing new photosensitizers or exploring a carrier to selectively target at the site of action. However, synthesis involves complicated steps as well as regulatory approval of the new drug substance. Therefore, fabrication of a delivery device with multi-functional capabilities will be an optimum choice to selectively target the photosensitizer and increase its therapeutic efficacy.

1.2.7. Nanoparticles as delivery platform for PDT

Nanoparticles are specially engineered materials, generally in the 1-100 nm dimension range. They have unique physicochemical properties, such as small size, large surface area to mass ratio and high reactivity, which are used to overcome various limitations of conventional therapeutic agents [75]. Moreover, nanoparticles-based delivery systems have been extensively utilized to improve the solubility of poorly water-soluble drugs, prolong the circulation half-life of the drug in the blood, minimize degradation of the drug after administration, decrease its side effects and increase its bioavailability [76]. Nanoparticles have been reported to preferentially accumulate at the tumour sites rather than healthy tissues due to enhanced permeability and retention (EPR) effect. This is based on the fact that the vasculature in pathological areas is ‘‘leaky’’, unlike in normal healthy tissues. The pore sizes in normal tumours usually vary from 100 to 780 nm, which allows the spontaneous accumulation of size-specific nanoparticles in the interstitial tumour tissues [77-78]. A large number of drug-loaded therapeutic nanoassemblies are now available. These include polymeric nanoparticles, liposomes, niosomes, solid lipid nanoparticles, nanocrystals, micelles, dendrimers, superparamagnetic iron oxide nanoparticles and carbon nanoplatforms. The use of PDT-based nanotherapeutics has also been explored [79-90]. Apart from the external factors such as hydrophobic properties of the photosensitizer, variations in light dosimetry and aggregation-related issues, effective delivery to the target site is equally crucial for improving therapeutic outcomes in PDT. In this context, nanoparticles with adjuvants can increase the solubility of hydrophobic photosensitizers and offer the benefits of hydrophilicity and proper size to accumulate in the tumour tissue via the EPR effect. In

addition, increase in hydrophilicity could also reduce the likelihood of aggregation by the photosensitizer in the physiological media. A summarized overview of various nanotherapeutic delivery systems for efficient delivery of photosensitizers (Table 2) will be discussed with emphasis on the salient features of each of the delivery systems.

1.2.7.1. Polymeric nanoparticles

Both biodegradable and non-biodegradable polymers have been used for drug delivery applications in PDT. A large variety of polymers are available for product design to meet the requirements for high drug loading capacity, controlled release, and targeted delivery. Nanospheres (polymeric matrix systems) or nanocapsules (aqueous or oily cores surrounded by a polymeric membrane) are the two distinctive polymeric nanoparticle structures that can be prepared by different methods for the delivery of photosensitizers [91]. The photosensitizer can be either adsorbed on the surface or entrapped in polymeric nanoparticles. Verteporfin and benzoporphyrin-loaded poly-lactic-coglycolide-based biodegradable nanoparticles showed excellent photocytotoxity against EMT-6 mammary tumour cells in comparison with the free drug [92]. Bourdon et al. (2000) investigated the photosensitizing efficiency of m-HTPC in surface-modified PLA-PEG nanocapsules with the aim to achieve long *in vivo* circulation time. These nanocapsules showed significantly lower accumulation in macrophage-like J774 cells, indicating potential to be long circulating carriers with limited uptake by reticulo-endothelial cells (RES) [93]. Konan et al. (2003) studied sub-200 nm PLGA nanoparticles of hydrophobic photosensitizer meso-tetra(p-hydroxyphenyl) porphyrin (m- THPP) by emulsion-solvent diffusion technique and the uniform-sized nanoparticles had average drug loading and high phototoxicity against EMT-6 mammary tumour cells [94].

Table 2: Types of nanoparticle-based PDT system

Delivery system	Size	Shape	Photosensitizers used
Polymer-based nanoparticles	< 1000 nm	Nanocapsules, nanospheres	*m*THPC, *m*THPP, verteporphin, PpIX
Polymeric micelles	10-100 nm	Spherical	PpIX, *m*THPP, $Si(sol)_2Pc$
Liposomes	25 nm to several microns	Spherical multilamellar or unilamellar	Photofrin®, *m*THPC,
Dendrimers	1 nm to over 10 nm	Spherical structure	ALA, PpIX, RB
Ceramic nanoparticles	~30 nm	Mesoporous nanosphere	HPPH, *m*THPC, PpIX
Gold nanoparticles	1-150 nm	Nanosphere, nanorod, nanoshell	Pc, ALA
Quantum dots	< 10 nm	Nanosphere, nanorod	CdSe QD-Pc4
Magnetic nanoparticles	< 200 nm	Nanosphere	HPPH, Photofrin®
Others	Variable	Nanosphere	Merocyanine 540. TiO_2, fullerenes

Hydrophilic polyacrylamide (PAA)-based non-biodegradable polymers have also been employed to encapsulate photosensitizers and they offer unique advantages like minimal protein adsorption, low aggregation and good biocompatibility. Tang et al. (2008)

demonstrated the photo-induced cytotoxicity of methylene blue (MB)-loaded PAA nanoparticles to tumour cells, where the drug carrier prevented diaphorase enzyme-mediated reduction of MB, thus preserving the active form of MB [95].

Polymeric nanoparticles such as chitosan nanocarriers have shown numerous advantages, such as high drug-loading efficiency and rapid cellular uptake of protoporphyrin IX [96]. Pullulan-based nanogels have been successfully employed in the treatment of articular joints using chlorin photosensitizers. Selective delivery to macrophages was evident in arheumatoid arthritis mouse model [97].

Polymer-photosensitizer conjugates of hydrophilic polymers provide an alternative pathway for PDT applications. Improved efficacy of poly-L-lysine-chlorin e6 conjugates was demonstrated with the addition of PEG, where higher phototoxicity to ovarian cancer cells and less damage to macrophage cells were observed [98]. Water-soluble PEG-zinc protoporphyrin conjugates have been studied *in vitro* and showed potential phototoxic effects after laser irradiation [99].

1.2.7.2. Polymeric micelles

Polymeric micelles are composed of amphiphilic block copolymers with hydrophobic interior cores suitable to house a wide variety of poorly water-soluble photosensitizers [81, 82, 100]. These micelles have the potential for targeted PDT drug delivery and were shown to be useful in recent studies with various hydrophobic photosensitizers. Roby et al. (2006) reported the efficiency of PEG-phosphatidyl ethanolamine (PE)-based micellar carrier for the delivery of meso-tetraphenylporphine (mTPP) [101]. The TPP-containing PEG-PE micelles showed significant improvement of photocytotoxicity *in*

vivo compared to free TPP against cancer cells. Rijcken et al. (2007) showed the improved sensitizing ability of hydrophobic solketal-substituted phthalocyanine when it was encapsulated in thermosensitive poly(ethyleneglycol)-block-poly(N-(2-hydroxypropyl) methacrylamide-dilactate) micelles [102]. These micelles with an average size of 75 nm were able to deliver monomeric form of the photosensitizer, when the substituted-pthalocyanine was used at low concentrations (≤ 0.05 μM). Other diblock copolymer-based micelles such as poly-(ethyleneoxide-b-ω-caprolactone) (PEO–PCL) were reported to possess great potential to deliver hydrophobic photosensitizers. Li et al. (2007) demonstrated high loading efficiency of PpIX (82.4%) with narrow size distribution (52.2 nm) when incorporated in PEO-PCL micelles [103]. Compared to the free PpIX, the PpIX in micelles showed a higher cellular uptake as well as higher PDT effect upon irradiation in RIF-1 cells. Nishiyama et al. (2009) reported the efficacy of ionic dendritic photosensitizer-incorporated polyion complex micelles. By means of electrostatic interaction, the charged block copolymer PEG-poly(L-lysine) block copolymers (PEG-b-PLL) and anionic dendrimer phthalocyanine (DPc) formed micelles [104]. The PDT effect of the DPcZn was double compared to the free DPc for the same irradiation time. The DPc-loaded micelles showed a higher anti-proliferative activity than free DPc and Photofrin®.

1.2.7.3. Liposomes

Liposomes are self-assembled spherical structures composed of one or more lipid bilayers with aqueous cores [84,85]. The main components are biocompatible phospholipids and cholesterol. Liposomal structures can accommodate both hydrophobic and hydrophilic photosensitizers [85]. Several studies have reported successful

application of liposomes for PDT drug delivery. One of the earliest reported liposome applications was to improve the solubility of verteporfin, and the liposomal formulation was approved for use in clinical trials for choroidal neovascularization associated with AMD [105-106]. Dipalmitoyldiphosphatidylcholine (DPPC) liposome encapsulating Photofrin® demonstrated enhanced drug uptake and tumour destruction compared to Photofrin® in dextrose solution [107]. Intravenous injection of m-THPC encapsulated in DPPC liposomes exhibited highest m-THPC tumour-to-muscle accumulation at 6 hr post-injection. Several factors, such as half-life, stability in the presence of plasma lipoproteins, opsonization followed by clearance from the blood stream by mono-nuclear phagocyte system, affect the therapeutic effects of liposomes *in vitro*. More recently, a number of liposomal formulations have been developed to improve the plasma stability and circulation lifetime of bioactives. Incorporation of PEG and glycolipids showed stealth characteristics by avoiding fast detection by the immune system, thereby prolonging the circulation time of the photosensitizer [108]. Improved skin penetration for ALA was obtained when ALA was entrapped in liposomes comprising PE/cholesterol/sodium stearate in the molecular ratio 2:1:2.5 [109]. Incorporation of ALA hexyl esters in the afore-mentioned liposomes also showed similar effects with increased stability [110].

1.2.7.4. Quantum dots

Quantum dots (QD) are single crystals of semiconductor with size range of a few nanometers to less than 10 nm [89]. The light absorption ability of the QDs can be varied from ultraviolet (UV) to the IR region by changing their size and composition [111]. These nanomaterials of constant composition possess high photoluminescence quantum

yield, photostability and molar extinction coefficient. They are relatively simple and inexpensive to synthesize and are non-cytotoxic in the absence of light but have the potential to induce cytotoxicity under UV irradiation. Another useful advantage is their ability to resist metabolic degradation [112]. Currently, surface coating of QDs makes them water-soluble, biocompatible and target specific for efficient delivery of various therapeutic and diagnostic agents [113-114]. Samia et al. (2003) first demonstrated the possibility of using QDs as a photosensitizer for PDT during the study of a QD system composed of cadmium, selenium and pthalocyanine (Cd-Se-Pc) [115]. Phthalocyanine molecules attached on QDs can be indirectly excited via QDs at 488 nm and emit at 680 nm with 77% fourier resonance energy transfer (FRET) efficiency, implying potential application of QDs for NIR sensitization. More recently, Tsay et al. (2007) produced stable and multifunctional peptide-coated QD-photosensitizer conjugates with singlet oxygen generation yield as high as 31 % [116]. They also conjugated RB and chlorin e6 in peptide-coated CdSe/CdS/Zn QDs with high singlet oxygen generation efficiency. The results showed that singlet oxygen could be produced via energy transfer from nanocrystal donors to the photosensitizer acceptor by FRET mechanism.

1.2.7.5. Dendrimers

Dendrimers are monodispersed spherical or globular macromolecular structures with repeated branches [87]. Their highly branched symmetric architecture, consisting of a multivalent functional surface, interior shell and a core, offers three unique approaches for PDT drug delivery. Kojima et al. (2007) studied the PEG-attached poly(amidoamine) dendrimers and the PEG-attached poly(propylene imine) (PPI) dendrimers for hydrophilic rose bengal and hydrophobic PpIX photosensitizers for PDT drug delivery

[117]. Stabilization of the photosensitizer inside the dendrimer core was achieved through interaction of the acidic moieties of both molecules with the inner tertiary amino group in the dendrimers. Based on confocal fluorescence imaging, the complex of PpIX with PEG–PPI dendrimers could be delivered to mitochondria more efficiently compared to the free PpIX. More recently, Ideta et al. (2009) reported the feasibility of using dendrimer porphyrins (DPs) with different charges on the periphery [118]. The study showed the occurrence of charge dependent interaction with the cells, where positively charged DPs showed better PDT effect.

1.2.7.6. Gold nanoparticles

Gold nanoparticles have emerged as a useful therapeutic carrier for the transport of peptides, proteins as well as nucleic acids for gene therapy [119-120]. This system has been recently explored for PDT drug delivery through covalent and non-covalent approaches. Hone et al. (2002) had produced phthalocyanine-stabilized gold nanoparticles through strong covalent attachment by Au-S bond [121]. Although the formulation showed high singlet oxygen generation, it was insoluble in water and exhibited dark toxicity in HeLa cells to some extent. Therefore, a non-covalent approach through electrostatic or hydrophobic interactions with gold nanoparticles provides a promising delivery strategy as it maintains the active form of the drug. Recently, Oo et al. (2008) demonstrated PDT efficacy of electrostatically-conjugated ALA to positively charged Au nanoparticles by selective destruction and inhibition of the proliferation of fibrosarcoma cells through high singlet oxygen generation [122]. Using Au nanoparticles for hydrophobic photosensitizers, Oo et al. developed a non-covalent approach to entrap the hydrophobic pthalocyanine (Pc) in Au nanoparticles. Pthalocyanine was found

attached to the Au nanoparticle surface through a nitrogen-gold bond via the terminal amine group of the drug. *In vitro* studies indicated an excellent biocompatibility and good PDT effect of the Au-Pc conjugates in HeLa cells.

1.2.7.7. Other nanoassemblies

Apart from the afore-mentioned nanotherapeutic drug carriers, photosensitizer-loaded ceramic nanoparticles, magnetic nanoparticles and fullerene-based nanoparticles have also been explored as drug delivery systems for PDT.

Silica-based mesoporous nanoparticles were prepared in order to achieve high drug loading and stability against degradation. Photosensitizers can be either encapsulated in the mesoporous matrix or directly linked to the nanoparticle surface through covalent bonds [123]. In 1993, Prasad et al. first reported the efficiency of mesoporous nanoparticles of the hydrophobic drug pyrophorbide. These nanoparticles had average size of 30 nm and showed high singlet generation, increased stability and phototoxicity against tumour cells [124, 125].

Magnetic nanoparticles offer a myriad of applications in the field of magnetic resonance imaging, hyperthermia therapy, drug delivery and disease diagnosis [126-128]. Superparamagnetic iron oxides (> 50 nm) and ultrasmall supermagnetic iron oxides (< 50 nm) have been reported to possess biocompatibility and usefulness for drug delivery. Gu et al. demonstrated the efficacy of iron oxide nanoparticles by anchoring porphyrin covalently on the nanoparticle surface for PDT and hyperthermia therapy [129]. *In vitro* studies demonstrated that the conjugates could be taken up by HeLa cells and showed

considerable PDT effect. Combination of magnetic carriers and polymeric micelles or chitosan-based hydrophilic conjugates showed marked increase in PDT efficacy.

Fullerenes (C_{60} and C_{70}) have high triplet yield and thus can efficiently transfer energy to surrounding molecules such as oxygen and form reactive oxygen species [130]. Andrievsky et al. (2009) reported the photo-activity of water-soluble fullerene carboxylic acid, which showed strong activity against HeLa cells with selective DNA cleaving ability under irradiation [131].

1.2.7.8. Marketed formulations and current developments

Many drug delivery systems have been investigated with the aim of achieving high PDT efficacy, increased drug stability and least toxicity. A few of these delivery systems have been approved by the drug regulatory agencies for clinical use. ALA was formulated for oral, topical and intravenous administration, which proved to be highly efficacious against skin malignancies and squamous cell tumours. This prodrug is enzymatically converted to protoporphyrin IX, thus eliciting its photodynamic effect [132]. Verteporfin (Photofrin®), which was approved by FDA in 2000, is a liposome-based system recommended for AMD complications. Verteporfin, which was recently used to treat choroidal neovascularization, showed beneficial effects [133]. Foscan® was approved in EU in 2001 for the treatment of head and neck cancers. The product contains 1-4 mg/mL of temporfin in an injectable dosage form [134]. In 2002, a 1:1 chlorin e6-polyvinylpyrrolidone injectable formulation (known as Photolon®) was registered in Belarus. It was proven to be highly effective against basal cell skin cancer, breast cancer, Caposi's sarcoma, cervix and rectum cancer [135]. Tin ethyl etiopurpurin ($SnET_2$) is a hydrophilic purpurin derivative, which is a degradation product of chlorophyll. It is often

formulated in an egg-based carrier and has shown promising PDT efficacy against cutaneous basal cell cancer, breast metastasis and Kaposi's sarcoma [136]. An aluminum pthalocyanine tetrasulfate has also offered excellent clinical response in naturally occurring veterinary tumors. Photosens® (Sulfonated Aluminum Phtalocyanine) was approved in Russia in 2003. It showed enhanced PDT efficacy in the form of intravenous and aerosol formulation, particularly in the treatment of primary lung, recurrent lung, pharyngeal, laryngeal, and esophageal tumours [137]. Texaphyrin (Motexafin Lutetium or Lu-Tex) is a hydrophilic porphyrin and has been formulated for intravenous administration. It is an excellent singlet oxygen producer and was particularly effective against cutaneous metastasis for breast cancer and prostate cancer [138]. A formulation containing mTHPC loaded into DPPC liposomes (Foslip®) is currently undergoing phase III clinical trial and has shown promising efficiency, enhanced selectivity and reduced side effects [139]. HPPH, which showed improved efficacy against endobronchial lung cancer with minimal photosensitivity reactions, is also currently undergoing phase III clinical trial [140].

1.2.8. Chlorins as promising photosensitizer

Chlorins, which are the reduced form of porphyrins, provide better photophysical properties than porphyrin-based photosensitizers. The porphyrin core absorbs light of wavelengths that are too short for penetration to be effective in PDT modality. The reduction of a pyrrole double bond at the porphyrin periphery gives the chlorin core a high band I absorption at longer wavelengths of 650-670 nm than those of porphyrin band I [48]. In addition, chlorins maintain the proper photophysics needed for the production of singlet oxygen, namely high quantum yield, lifetime and energy

($\geq$ 94 kJ mol^{-1}) of the triplet state. These three parameters are collectively known as quantum yield (Φ_{Δ}) of singlet oxygen, which was experimentally found to be adequately high for chlorins. In the last decade, chlorins were actively investigated for their photodynamic efficacy in cancer treatment. [141]. Among the chlorins evaluated, the naturally occurring Ce6 is of particular interest [142]. Ce6 has shown improved efficacy, decreased side effects and faster clearance from the skin tissues. It also facilitates deeper light penetration leading to PDT-induced necrosis of the carcinoma cells. The widely-used Ce6 derivatives are meso-tetrahydroxyphenyl chlorin (mTHPC) and monoaspartyl-Ce6 (MACE), which were preclinically found to have optimum hydrophilic-lipophilic balance, thereby actuating efficient transport and permeation to the affected cells.

1.2.9. Research gaps in photophysical aspects and formulation strategies for Ce6

Various approaches were undertaken to improve tumour targeting and selectivity of chlorin-based photosensitizers, either by chemically altering the chlorin moiety or by incorporating a physical carrier to efficiently deliver the photosensitizer to the site of action. The common disadvantages of Ce6 include its poor solubility in neutral to acidic pH conditions, which accentuates the self-association of Ce6 molecules. These aggregates drastically reduce the sensitizing efficiency and therefore, Ce6 products susceptible to form aggregates are not considered ideal for PDT modality. In fact, the aggregation factor is given much importance because of the characteristic physiology of the tumour microenvironment. In tumour tissue and its adjacent surroundings, the pH is generally reduced due to low oxygen content (hypoxia) of the affected cells [83, 121]. It has been reported that in most instances, the pH of the tumour cells lies between 5 to 6 with high carbon dioxide content. Such neutral to acidic pH reduces Ce6 solubility and

enhances its propensity for self-association. Isakau et al. (2008) demonstrated the significant reduction of sensitizing ability of aggregated Ce6 molecules in relation to reduced quantum yield of singlet oxygen, which resulted in poor therapeutic efficacy after laser irradiation [135]. Chin et al. (2010) illustrated the poor activity of Ce6 aggregates in human bladder carcionoma cell lines and chick chorio-allantoic membrane (CAM) model [143-145]. In the presence of the water-soluble polymer, polyvinylpyrrolidone (PVP), Ce6:PVP complex was formed and it exhibited manifold increase in sensitizing efficacy with respect to the corresponding aggregates. These findings necessitate the incorporation of a suitable adjuvant or modification of the chlorin nucleus to reduce the extent of aggregate formation. More recently, Xiao et al. (2012) devised chitosan-coated single-walled carbon nanotubes with conjugated Ce6, which exhibited high uptake by HeLa cells and low dark toxicity [146]. Lee et al. (2012) demonstrated the efficiency of multifunctional nanoparticles comprising poly(lactide-coglycolide) (PLGA) coupled with Ce6, prepared by Steglitch esterification method. Incorporation of Fe_3O_4 in the nanoparticles enabled simultaneous imaging and phototherapy at the tumour site [147]. Park et al. (2011) reported the photodynamic efficacy of a water-soluble conjugate that comprised polyethyleneglycol (PEG), polyethyleneimine (PEI) and Ce6. Rapid internalization of these 100 nm particles with selective accumulation at the tumour site was observed [148]. High phototoxicity and enhanced uptake of Ce6 incorporated in chitosan nanogels was demonstrated in rheumatoid arthritis-induced mouse xenograft model by Schmitt et al. (2010) [149]. Taima et al. (2005) reported the synthesis of water-soluble esters of Ce6 through esterification with aminoalcohols. Absorption and circular dichroism spectra revealed

that the synthesized products were readily soluble as monomers [150]. Hydrophilic conjugates based on the glycosylation of chlorin nuclei were designed by Statio et al. (2005) and they showed a 3-fold increase in cellular uptake due to reduced aggregate formation [151]. Clearly, decreasing hydrophobicity of porphyrin nucleus by chemical conjugation or synthesis is one of more efficient ways to increase the therapeutic activity of Ce6 in PDT modality. However, these synthesis-based approaches are less preferred as they involve complicated steps with lack of reproducibility and the need for stringent new regulatory approvals. Similarly, physical carriers employed to deliver Ce6 such as polymeric nanoparticles, iron-oxide based magnetic nanoparticles, chitosan and PEI-based hydrophilic conjugates possess their own limitations. Prolonged release from biodegradable polymer PLGA and chitosan could fluctuate the therapeutic efficacy *in vivo*. Furthermore, in actual PDT modality, the time gap between the dosage administration and laser irradiation should be accurately adjusted so as to avoid the inconvenience experienced by patients or human volunteers. Biodegradable synthetic polymers and other prolonged release polymers grossly fail these criteria. Polyethyleneimines are toxic to the cells and therefore, the anti-proliferative activity elicited by Ce6-PEI conjugates does not necessarily reflect the high therapeutic efficacy of the photosensitizer itself [148]. In addition, toxicities arising from inorganic-based nanoparticles (iron oxide, Cd-Se QDs, carbon nanotubes) are still a major concern and the more practical approach devoid of toxic side effects needs to be revisited. Moreover, due to the very small size of these nano-carriers ($\leq$ 25 nm), they are often prone to be detected by RES and are subsequently eliminated from the blood stream, resulting in compromised photodynamic efficacy.

As mentioned earlier, understanding the evolution of aggregate formation and the various photophysical properties of the photosensitizer, which are affected by aggregation is important. Traditionally, the aggregation phenomenon is elucidated by differences in characteristic absorption and fluorescence spectral features along with parameters like quantum yield, fluorescence half-life and singlet oxygen generation efficiency. Disaggregation of Ce6 aggregates with the use of PVP was partially described by Isakau et al. in terms of fluorescence half-life and triplet-triplet absorption spectra [135]. Besides, surfactant-induced disaggregation of a chlorin analog, chlorin p6 (Cp6), has been reported by Dutta et al. (2006) [152]. No other studies on the disaggregation potential of pharmaceutical adjuvants for improved PDT efficacy of Ce6 have been reported. Apart from exploring suitable carriers for the delivery of Ce6 to the target site, investigation of agents with disaggregation ability is highly recommended because it could also improve drug delivery. The limited quantitative determination of aggregate to monomer conversion is in part due to the lack of proper computational tools. In fact, aggregate to monomer conversion of various photosensitizers has been illustrated only on the basis of qualitative estimation of spectral shifts. Likewise, disaggregation of porphyrin-based photosensitizers was demonstrated by red shifts in the fluorescence emission spectra. However, accurate quantitative determination of aggregate to monomer conversion is imperative as it reveals the relative disaggregation efficiencies of different disaggregating agents when they are incorporated in the formulations. This facilitates the selection of desired concentration of a disaggregating agent to be therapeutically optimal. Thus, a suitable computational tool to determine the underlying species of a fluorophore mixture (aggregate and monomer) is highly warranted.

The application of molecular simulation as a theoretical basis for explanation of drug-polymer binding has gained tremendous interest in recent years. Molecular modeling methods are now routinely used to investigate the structure, dynamics, surface properties and thermodynamics of inorganic, biological and polymeric systems. The application of coarse grain simulations has also gained considerable interest with the availability of a larger time frame and a larger number of molecules to incorporate into the system [153-155]. In many complex systems, such as dispersions of colloids and submicron drug carriers, the afore-mentioned simulation method has been found to be useful in such studies [156, 157]. Elucidation of aggregation-disaggregation of Ce6 by molecular simulation has yet been established. Therefore, such simulations as a visualization tool could greatly reinforce the understanding of the interactive system, comprising Ce6 and disaggregating agent, at the molecular level.

Taking into consideration the significance of the afore-mentioned research gaps, a substantial research work on the selection of an effective disaggregating agents, which could be further used as drug carrier for Ce6 is still lacking. Since water is the most widely used vehicle in the preparation of pharmaceutical dosage forms, a good understanding of the aggregation phenomenon in aqueous medium is also necessary. An exploratory study on aggregation as a function of pH and concentration of Ce6 may elucidate the optimized conditions for delivery of monomer-rich Ce6 for better PDT efficacy. The photophysical changes accompanying aggregate to monomer conversion need to be generalized for identification of other disaggregating agents having similar potential. Such disaggregating agents could be used as effective drug carrier alone or in combination with suitable pharmaceutical adjuvants.

PART 2: HYPOTHESES AND OBJECTIVES

2. HYPOTHESES AND OBJECTIVES

Aggregation of chlorin e6 is a topic of interest. A good understanding of the factors that affect aggregate formation and use of disaggregating agents are pertinent for improved therapeutic efficacy of the anti-cancer drug. Conversion of aggregate to monomer and vice versa may be induced by variation in pH, solvent type and other accompanying adjuvants. A substantial reduction of therapeutic activity due to aggregate formation in a formulation could be precluded by suitable absorption and fluorescence-based characterization techniques. The exploration of commonly used pharmaceutical excipients as potential disaggregating agents could thus also be helpful as their non-toxic and compatible properties will not complicate the usability and application of the formulation. As mentioned previously, the interactive mechanism and changes in photophysical characteristics of Ce6-PVP marketed formulation have not been widely investigated in terms of simple spectroscopic parameters. The utilization of simple absorption and fluorescence spectroscopic techniques could efficiently detect the aggregation-disaggregation behaviour of Ce6 and facilitate the exploration of other potential disaggregating agents showing similar effects as polyvinylpyrrolidone. These technique will also enable a good understanding of the different predisposing factors and selection of suitable conditions to reduce the occurrence of aggregate formation. In recent years, sucrose-based esters have been extensively used in food industries for their low toxicity and biodegradability as solubilizers [158-160]. Studies had shown that nanosuspension preparation for enhancing drug dissolution through increasing specific surface area of particulates is one of the simplest approaches to overcome bioavailability related problems. It was thus anticipated that Ce6 could be formulated as monomers in

nanocarriers of sucrose ester matrix for rapid release as well as enhanced photodynamic activity.

PDT is a direct and promising approach for cancer treatment with particular relevance to non-deeply seated tumours. Studies have shown high *in vivo* efficacy of chlorin- and porphyrin- based photosensitizers in the treatment of skin, neck and bladder cancers. These photosensitizers are more effective in the superficial surface layers where laser light can penetrate easily. As mentioned in the introduction part, the different formulation approaches considered for improved PDT efficacy of Ce6 possess limitations to different extents. Ce6 incorporated in polysaccharide-based chitosan nanogels showed improved phototoxicity in rheumatoid arthritis-induced mouse xenograft model [149]. However, the delayed release of Ce6 from chitosan-based carriers increased the time interruption between dosage administration and laser light irradiation, which could lead to patient non-compliance. Recently, anti-cancer drug-loaded alginate-based micro/nanospheres and hydrogel beads were shown to be promising in various forms of mucosal cancers [161-164]. These polysaccharide-based drug delivery systems have gained much attention because of their flexibility in achieving the desired drug release profile, cost effectiveness, broad range of physicochemical properties and high regulatory acceptance. Therefore, the mucoadhesive sodium alginate could be employed to encapsulate Ce6 for targeted delivery to the oral mucosal tumour cells. Unlike chitosan, sodium alginate is soluble above pH 4.0. Thus, the oral mucosal pH (pH ~ 6.4) would favour the fast release of Ce6 from the formulation to attain a high drug concentration for absorption. The incorporation of PVP with Ce6 in alginate may further enhance mucoadhesivity and Ce6 dissolution in addition to its potential disaggregation effect.

Therefore, the main hypotheses of this project are:

1. Aggregation of Ce6 can be prevented by utilization of pharmaceutical adjuvants such as PVP and sucrose esters.
2. The PDT efficacy of Ce6 could be improved by incorporating the pharmaceutical adjuvants as disaggregating agents alone or in combination with alginate.
3. Improved *in vitro* dissolution of Ce6 could be achieved by formulating Ce6 as nanoparticles with sucrose esters.
4. Enhanced mucoadhesivity of Ce6 formulation could be achieved with alginate nanoparticles consisting of Ce6-PVP complex.

To test the afore-mentioned hypotheses, studies were carried out to accomplish the following objectives:

- Elucidation of various factors associated with aggregate formation of Ce6 and their effects on the characteristic features of aggregate-to-monomer conversion by spectroscopic techniques.
- Study of photophysical characteristics of aggregate-to-monomer conversion of Ce6 in the presence of PVP and sucrose esters respectively by absorption and fluorescence-based techniques.
- Determination of PDT response parameters of Ce6, such as singlet oxygen generation, cellular uptake and photo-toxicity to tumour cells, in the presence of PVP and sucrose esters respectively.

- Quantification of relative disaggregation efficiency of PVP and sucrose esters by employing suitable computational tool and optimization of their concentrations for *in vitro* studies.
- Illustration of interactive mechanism between Ce6 and the disaggregating agents at the molecular level using molecular modeling and coarse grain simulation method.
- Formulation preparation of Ce6-sucrose ester nanoparticles and alginate nanoparticles consisting of Ce6-PVP complex with the aim to increase *in vitro* dissolution and mucoadhesivity of Ce6.
- Evaluation of the improved photodynamic efficacy of the formulations using oral mucosal carcinoma cells as tumour xenograft model.

For ease of understanding the multi-disciplinary objectives of this research project, a schematic diagram of the different studies in relation to the thesis objectives is shown below:

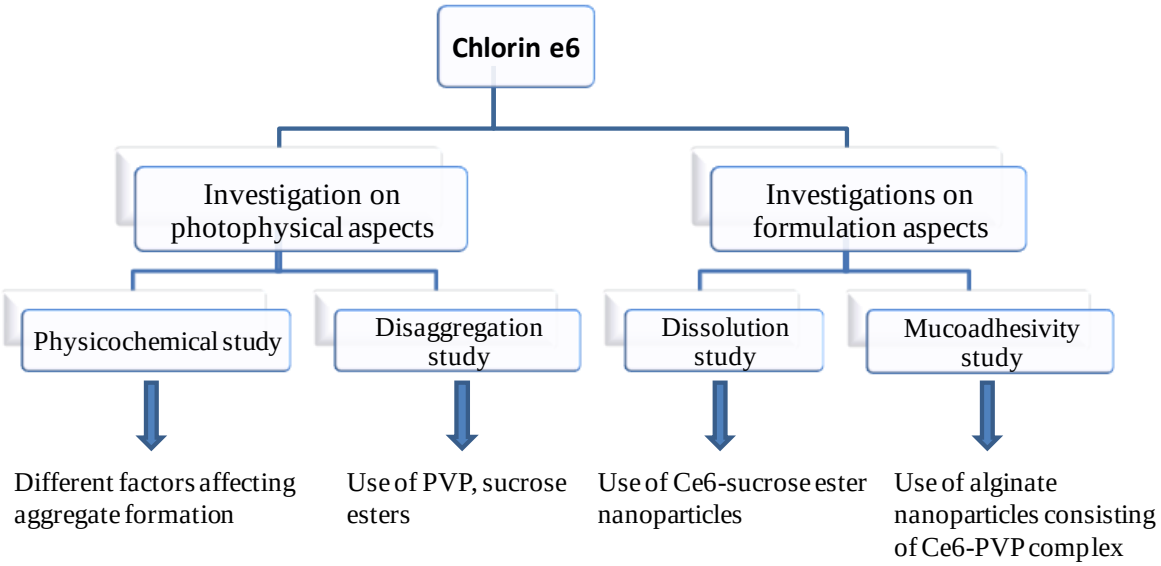

Figure 5: Schematic diagram of the multidisciplinary studies conducted in the project.

PART 3: EXPERIMENTAL

3. EXPERIMENTAL

3.A. Materials

Chlorin e6 (~ 98% purity, SPE Chemical Co. Ltd., Shanghai, China) was employed as the model drug. n-Octanol (AR grade, Sigma Aldrich, Singapore) was used in the partition coefficient experiments. The pharmaceutical adjuvants for disaggregation study consisted of polyvinylpyrrolidone of different molecular weights (PVP: K17, K25, K30; ISP Pharmaceuticals, NJ, USA) and sucrose esters of different alkyl chain lengths (laurate/myristate/palmitate; Compass Foods Pvt. Ltd., Singapore). Organic solvents (AR grade, Merck, Singapore) such as dichloromethane (DCM) and acetone (AC) were used in the preparations of the nanosuspensions. Sodium alginate (Sigma Aldrich, Singapore) and calcium chloride (Merck, Singapore) were employed in the production of alginate nanoparticles. Mucin type IS (Sigma Aldritch, Singapore) and periodic acid (MP Biomedicals Inc., Singapore) were used in the determination of *in vitro* mucoadhesivity of the alginate nanoparticles. Hydrochloric acid, potassium dihydrogen phosphate and sodium hydroxide (AR grade, Merck, Singapore) were used for the preparation of buffers.

Human oral squamous carcinoma (OSC) cell line used to represent the *in vitro* tumour model was obtained from the American Type Culture Collection (Rockville, MD, USA). Dulbecco's modified eagle's media (DMEM) and fetal bovine serum albumin (FBS) with supplemented nutrients (HyClone Laboratories, Logan, UT, USA) were used as cultivation media for OSC cells. A trypsin-EDTA (PAA Laboratories GmbH, Somerset, UK) mixture was used to dislodge the OSC cells. While Penicillin-Streptomycin (PAN Biotech GmbH, Aidenbach, Germany) was used to prevent contamination of the cultured

cells. N-N'-dimethyl-p-nitrosoaniline (RNO) (MP Biomedicals Inc., Singapore) and histidine (Merck, Singapore) were used for the determination of singlet oxygen generation, while the anti-proliferative activity of different formulations were tested using MTT reagent (3-(4,5-dimethylthiazolyl-2)-2,5-diphenyltetrazolium bromide) (MP Biomedicals Inc., Singapore). Intracellular distribution of Ce6 was evaluated with the use of the nucleus staining dye, DAPI (MP Biomedicals Inc., Singapore).

3.B. Photophysical studies of Ce6

3.B.1. Aggregation study of Ce6 in aqueous media

3.B.1.1. Determination of Ce6 solubility at different pH

Solubility of Ce6 was determined from acidic to alkaline pH conditions ranging from pH 2 to pH 10 at pH interval of 2. Buffers of different pH were prepared according to the USP procedure, using sodium hydroxide, potassium dihydrogen phosphate and phosphoric acid. Buffers of different pH and excess amounts of Ce6 were agitated in a shaker water-bath at 37°C for 24 hr. Ce6 concentration of the supernatant was determined by high performance liquid chromatography (HPLC) using C18 column (Thermo Electron corporation, NJ, USA) under the following conditions: mobile phase – 90 % methanol and 10 % PBS (phosphate buffer solution; acetic acid and potassium-di-hydrogen phosphate, pH 4.0), detection wavelength – 405 nm, flow rate – 1 mL/min. Each determination was carried out in triplicate and the average Ce6 solubility at each pH reported.

3.B.1.2. Determination of Ce6 partition coefficient at different pH

The octanol/buffer partition coefficients of Ce6 were determined by the equilibration technique at 37°C at the pH conditions stated in section 3.B.1.1. Two mg of Ce6 was

added to 5 mL of 1:1 binary mixture of n-octanol and buffer prepared at different pH, and agitated with a vortex mixer for 5 min. The mixture was then centrifuged for 2 min at 4000 rpm to separate the n-octanol from the buffer. Ce6 concentration in the buffer was determined by HPLC according to the set of parameters stated in section 3.B.1.1. Ce6 concentration in the n-octanol was determined by subtracting the amount present in the buffer from the original amount of Ce6 used in the experiment. The partition coefficient was calculated as:

$$P_{octanol/buffer} = \frac{C_{octanol}}{C_{buffer}} \qquad \textbf{\textit{Equation}}\ (\mathbf{3})$$

Mean values of partition coefficients at different pH conditions were reported from triplicate studies.

3.B.1.3. Determination of spectroscopic characteristics of Ce6 at different pH

A fixed concentration of Ce6 (50 μM) was selected for absorption and fluorescence studies at different pH conditions. A series of buffers with pH ranging from 1.2 to 10 was prepared according to the USP method as previously described. Ce6 was dissolved in 0.1 % (w/v) NaOH solution to prepare a stock from which 30 μL was withdrawn and added to each of the buffers (pH 1.2 to 10) to produce a final Ce6 concentration of 50 μM in 5 mL. The absorption and fluorescence spectra of Ce6 in the buffers were then recorded using ultraviolet-visible spectrophotometer (Shimadzu, UVPC 2010, Kyoto, Japan) and spectrofluorimeter (Fluoromax-P, Jovin Yvon, Edison, NJ, USA) respectively. The absorption and fluorescence measurements were also conducted with increasing concentration of Ce6, ranging from 5 μM to 100 μM, at physiological pH 7.4 to investigate the effect of Ce6 concentration on aggregate formation.

3.B.1.4. Quantification of Ce6 species at different pH

The quantification of different underlying species of Ce6 at various pH conditions was accomplished by excitation-emission matrix (EEM) spectroscopy. This method allows the accurate detection of various fluorophores present in a mixture on the basis of selective excitation and emission characteristics of the underlying constituents. EEM spectra of Ce6 (50 μM) at various pH conditions, from pH 1.2 to 10, were obtained using a spectrofluorometer (Fluoromax-P, Jovin Yvon, Edison, NJ, USA) from 600 nm to 750 nm, in 2 nm increments, at increasing excitation wavelengths from 390 nm to 690 nm, in 5 nm increments with an excitation and emission slit width of 2 nm. The obtained spectra were analyzed using PARAFAC algorithm in the Matlab computational software, (version 7.10; Mathworks, MA, USA). The number of underlying Ce6 species (*N*) and their concentrations at different pH conditions were determined from the PARAFAC analysis.

3.B.1.5. Determination of relative quantum yield of Ce6 at different pH

Lipert's equation was used to calculate the fluorescence quantum yield of Ce6 at various pH conditions. The quantum yield (Φ_1) at pH 10 was set at 1.0 and the relative quantum yields at other pH conditions (Φ_2) were determined from the following equation [165]:

$$\frac{\Phi_1}{\Phi_2} = \frac{(1 - 10^{A_2})}{(1 - 10^{A_1})} \frac{\eta_1^2}{\eta_2^2} \frac{\alpha_1}{\alpha_2} \qquad \textbf{\textit{Equation}} \ (\mathbf{4})$$

where A is the absorbance, η is the refractive index and α is the area under the fluorescence emission spectra for standard (sample 1) and test (sample 2) respectively. All the measurements were carried out at room temperature (298 K), keeping Ce6

concentration very low in order to avoid self-absorption. For quantum yield determination, Ce6 concentration in each of the buffers was adjusted such that absorbance value was around 0.2 to ensure that roughly equal numbers of photons were absorbed. It was assumed that Ce6 existed primarily as monomers at pH 10 and exhibited the highest quantum yield.

3.B.2. Disaggregation study using PVP and sucrose esters

3.B.2.1. Preparation of test solutions for disaggregation study

A fixed concentration of Ce6 (50 μM) was used for the disaggregation study with the afore-mentioned pharmaceutical adjuvants. For PVP-induced disaggregation study, different amounts of PVP were added to 50 μM Ce6 solution to give Ce6 to PVP ratios of 1:10 to 1:1000. Similarly, sucrose ester concentrations ranging from well below to above critical micelle concentration (CMC) were employed to investigate the disaggregation effect of sucrose esters of different alkyl chain lengths. Briefly, the required amounts of sucrose esters were each added to 5 mL of 50 μM Ce6 solution to produce the varying concentrations of the sucrose ester below and above its CMC. In both set of studies, solutions were prepared at pH 5 to simulate the *in vivo* tumour physiological pH condition. The respective solutions were then placed in a bath sonicator for 5 min and absorption and fluorescence measurements were conducted immediately thereafter.

3.B.2.2. Measurement of absorption and fluorescence

The absorption and fluorescence spectra of the solutions consisting of Ce6 and varying concentrations of PVP and sucrose esters were recorded spectrophotometrically as described in section 3.B.1.3.

3.B.2.3. Determination of disaggregation efficiency of PVP and sucrose esters

In order to determine the disaggregation efficiency of different grades of PVP and sucrose esters, EEM spectroscopic principles were further employed. It was speculated that the proportion of monomeric Ce6 species generated from its corresponding aggregate fraction by the action of the PVP or sucrose ester could be quantified on the basis of EEM spectral differences. EEM spectra of Ce6 in the presence of increasing concentration of each PVP and sucrose ester grade were obtained and analyzed according to the procedure described in section 3.B.1.4.

3.B.2.4. Measurement of fluorescence anisotropy

The steady-state fluorescence anisotropy (μ) measures the resistance to the rotational motion of a fluorescence molecule during its photochemical transformation from ground state to excited state. Therefore, changes in the fluorescence anisotropy value of Ce6 were recorded for varying concentrations of each of the PVP and sucrose ester grades. The fluorescence anisotropy of Ce6 in varying concentrations of each PVP and sucrose ester grade was obtained using a fluorescence spectrophotometer (Fluoromax-P, Jovin Yvon, Edison, NJ, USA). It is calculated based on the following equation [166]:

$$\mu = \frac{I_{VV} - GI_{VH}}{I_{VV} + 2GI_{VH}} \qquad \textbf{\textit{Equation}}\ (5)$$

where I_{VV} and I_{VH} are the fluorescence intensities and the subscripts indicate the vertical (V) and horizontal (H) orientations of the excitation and emission polarizers and G is the instrumental correction factor. Fluorescence anisotropy was measured in triplicates and the average was reported.

3.B.2.5. Determination of Ce6-disaggregating agent binding constant

3.B.2.5.1. Ce6-PVP system

The binding of Ce6 with PVP was evaluated at physiological pH 7.4 with Ce6 concentrations not exceeding 10 μM, where Ce6 molecules mostly existed in monomeric forms. Binding constants and the number of binding sites for different PVP grades were determined using a simple model based on drug-polymer binding [167]. The assumptions of this model are based on the fact that the drug molecule has similar affinity towards each of the monomer units comprising the polymeric macromolecule. Depending on the physicochemical factors like drug molecule size, molecular weight of polymer and length of monomer units, each drug molecule has binding ability with one or several monomer units. In the present study, Ce6 and PVP were designated as drug and polymer respectively. The fraction of Ce6 bound with PVP, i.e., *x* was determined from a set of Ce6 absorbances in a system with various concentrations of PVP, where on addition of PVP, free Ce6 molecules began to bind with PVP (partially) and virtually all the Ce6 molecules were bound at a certain maximum PVP concentration employed. Linear superposition was applied by assuming that the Ce6 absorbance, D at a given PVP concentration, is a linear superposition of the absorbance of fully free and fully bound Ce6 molecules, D_1 and D_2, respectively:

$$D = x.D_2 + (1 - x).D_1, 0 < x < 1 \qquad \textbf{\textit{Equation}}\ (6)$$

Therefore, the concentration of PVP-bound Ce6 (C_B) is given by:

$$C_B = x \times C_T = \frac{D - D_1}{D_2 - D_1} \times C_T \qquad \textbf{\textit{Equation}}\ (7)$$

Hence, free or unbound Ce6 (C_F) is calculated as, $C_F = C_T - C_B$, where C_T is the total Ce6

concentration, which is a known quantity. Therefore, number of moles of Ce6 bound per mole of PVP monomer unit, r is given by:

$$r = \frac{C_B}{[PVP]} \qquad \textbf{Equation (8)}$$

The binding constants and number of binding sites for different PVP grades were calculated using the slope and intercept of the Klotz double reciprocal plot given by [167]:

$$\frac{1}{r} = \frac{1}{n} + \frac{1}{nK_a C_F} \qquad \textbf{Equation (9)}$$

where n (>1) is the number of binding sites per mole of monomer unit and K_a is the binding constant. When the ligand molecule is larger and the molecular weight of monomer unit is less, n is much smaller than 1, which introduces a new term P (1/n) that represents the number of monomer units required to constitute one binding site. The mean number of binding sites per PVP molecule is given by:

$$N_0 = \frac{W}{W_{mono}} \times n \qquad \textbf{Equation (10)}$$

where W and W_{mono} are the molecular weight of the PVP polymer and each monomer unit respectively.

3.B.2.5.2. Ce6-sucrose ester system

The association of Ce6 with each of the sucrose esters of different alkyl chain lengths was determined using the following equation [152]:

$$A = A_f + \frac{(A_b - A_f)}{\frac{1}{K_b([S]_0 - CMC)^M} + 1} \qquad \textbf{Equation (11)}$$

where A_f, A and A_b are absorbances of Ce6 in the absence of sucrose ester, at a certain sucrose ester concentration ($[S]_0$) and at the maximum concentration of sucrose ester

employed. *M* is the number of micelles per Ce6 molecule, which was set at unity for simplicity, considering each micelle was ascribed for incorporation of single Ce6 monomer into its core [152]. Absorbance was measured using a ultraviolet-visible spectrophotomer (UV 2010 PC, Shimadzu, Japan) at a constant slit width of 5 nm.

3.B.2.6. Determination of Ce6-disaggregating agent binding mode

3.A.2.6.1. Fourier Transformed-Infrared (FT-IR) Spectroscopy

The FT-IR spectra of pure Ce6, PVP, sucrose ester and the freeze-dried Ce6-PVP/sucrose ester complex were recorded for solid state characterization using a FT-IR spectrophotometer (IR Solutions, Shimadzu, Japan) over the range of 400-4000 cm^{-1}. The spectra thus obtained were analyzed using the IR Solutions software. The above test samples were prepared as follows. Dry KBR (50 mg) was finely ground in a morter, and the respective test sample (5 mg) added and gently mixed. A manual press capable of delivering 8-10 MPa pressure was used to compress the mixture into thin pellets for spectroscopic measurements.

3.A.2.6.2. Temperature-dependent thermodynamic study

The mode of binding between Ce6 and different grades of PVP and sucrose ester were further affirmed by a thermodynamic study. Briefly, the binding constant for each Ce6-PVP/sucrose ester system was calculated at three specified temperature, 288 K, 297 K and 310 K. The thermodynamic parameters were calculated from Van't Hoff's equation:

$$\ln K_a = -\frac{\Delta H}{RT} + \frac{\Delta S}{R} \qquad \textbf{\textit{Equation}}\ (\mathbf{12})$$

where K_a is the binding constant at a particular temperature while ΔH and ΔS are the changes in enthalpy and entropy of the system and R is the gas constant. Binding

constant values obtained (employing Eq. 9 or Eq. 11) at different temperature points were plotted against 1/T and the thermodynamic parameters were calculated from the slope and intercept of the plot [168]. The free energy change (ΔG) was estimated from the following relationship:

$$\Delta G = -RT\ln K_a = \Delta H - T\Delta S \qquad \textbf{\textit{Equation}}\ (\mathbf{13})$$

The mode of binding between Ce6 and PVP/sucrose ester was determined with the obtained values of ΔG, ΔH and ΔS in reference to thermodynamic standpoint.

3.B.2.7. Theoretical simulation of Ce6-disaggregating agent system

3.B.2.7.1. Molecular dynamics simulation of Ce6-PVP system

Molecular dynamics simulation was performed using Hyperchem 8.0 (Hypercube Inc., Gainesville, FL, USA) to visualize the Ce6-PVP interaction at the molecular level. Repeating monomer unit of PVP was built using Polymer builder toolbox of Materials Studio (version 5.0; Accelrys Inc., San Diego, CA, USA) and a model PVP polymer with 20 repeating units was generated. The Ce6 structure was constructed using Chemdraw software (Version 7.0, Perkin Elmer Informatics, Cambridge, MA, USA). Ce6 and PVP structures were then optimized using PM3 (modified Austin model) parameterization using Hyperchem software. The individual molecules were subjected to complete energy minimization in periodic boundary of dimensions 20-15-40 Å (*x*-*y*-*z*) containing 483 water molecules. An AMBER force field and Polak-Ribiere conjugate gradient optimizer was used for the molecular dynamics simulation. In the present study, a run time of 0.6 ps was selected with an initial heat time of 0.1 ps to increase the temperature of the system

from 100 K to 300 K in 30 K steps. The free energy was calculated after the simulation run and molecular orientation of Ce6-PVP complex was demonstrated.

3.B.2.7.2. Coarse grain modeling of Ce6 – sucrose ester system by dissipative particle dynamics (DPD)

3.B.2.7.2.1. DPD theory

DPD is a coarse-grain simulation technique often used to simulate complex fluid dynamical behaviour. A DPD bead represents a group of atoms or a volume of fluid that is large on the atomistic scale but still macroscopically small. In DPD simulations, a set of beads move according to Newton's equation of motion [156]:

$$\frac{\mathrm{d}\mathbf{r}_i}{\mathrm{dt}} = \mathbf{V}_i, \qquad \mathrm{m}_i \frac{d\mathbf{V}_i}{\mathrm{dt}} = \mathbf{f}_i, \qquad \textbf{\textit{Equation}}\ (\mathbf{14})$$

where $\mathbf{r}_i$, $\mathbf{v}_i$, m_i, $\mathbf{f}_i$ are the position, velocity, mass and force of bead i, respectively. All bead masses are assumed to be the same and set to unity for simplicity. The force acting on each bead is the sum of conservative force ($\mathbf{F}_{ij}^{\mathrm{C}}$), dissipative force ($\mathbf{F}_{ij}^{\mathrm{D}}$), and random force ($\mathbf{F}_{ij}^{\mathrm{R}}$).

$$\mathbf{f}_i = \sum_{j \neq i} \left(\mathbf{F}_{ij}^{\mathrm{C}} + \mathbf{F}_{ij}^{\mathrm{D}} + \mathbf{F}_{ij}^{\mathrm{R}} \right), \qquad \textbf{\textit{Equation}}\ (\mathbf{15})$$

The conservative force for non-bonded particles is defined by soft repulsion acting along the line of centers and given by:

$$\mathbf{F}_{ij}^{C} = \begin{cases} a_{ij}\left(1 - r_{ij}\right)\hat{\mathbf{r}}_{ij}, & (r_{ij} < 1) \\ 0, & (r_{ij} \geq 1) \end{cases} \qquad \textbf{\textit{Equation}}\ (\mathbf{16})$$

where a_{ij} is the maximum repulsion between bead *i* and bead *j* with the following relation:

$$\mathbf{r}_{ij} = \mathbf{r}_i - \mathbf{r}_j, \mathbf{r}_{ij} = |\mathbf{r}_{ij}|, \hat{\mathbf{r}}_{ij} = \mathbf{r}_{ij} / |\mathbf{r}_{ij}| \qquad \textbf{Equation (17)}$$

The dissipative force is regarded as a frictional force, which depends on the position and relative velocities of the beads, and given by:

$$\mathbf{F}_{ij}^{D} = -\frac{\sigma^2 \left(\omega(r_{ij})\right)^2}{2k_B T} (\mathbf{V}_{ij} . \hat{\mathbf{r}}_{ij}) \hat{\mathbf{r}}_{ij}, \qquad \textbf{Equation (18)}$$

The random force is the random interaction between two adjacent beads *i* and *j* and given by:

$$\mathbf{F}_{ij}^{R} = \frac{\sigma \omega(r_{ij}) \hat{\mathbf{r}}_{ij} \zeta}{\sqrt{\delta_t}}, \qquad \textbf{Equation (19)}$$

where $\mathbf{v}_{ij} = \mathbf{v}_i - \mathbf{v}_j$, ζ is a random variable with zero mean and variance 1, δ_t is the time step used, the r-dependent weight function $w(r) = 1 - r$ for $r < 1$ and $w(r) = 0$ for $r > 1$.

3.B.2.7.2.2. Spring force

In the DPD model, atoms of each molecule are grouped together into beads. According to Groot and Warren, the harmonic spring force acting among the different beads in a molecule is designated by the following relation [157]:

$$\mathbf{F}_i^{S} = \sum_j C r_{ij} , \qquad \textbf{Equation (20)}$$

where C is the spring constant, and the mean distance between two consecutive chain beads is governed by the spring force and repulsive interaction. In the present study, the default value C = 4 was used, resulting in a slightly smaller distance for bonded beads than non-bonded beads.

3.B.2.7.2.3. Simulation parameters used in DPD

In order to calculate the conservative force, the repulsion parameter a_{ij} between any two beads should be calculated. The repulsion parameter between beads of same type, a_{ii}, is given by [157]:

$$a_{ii} = \frac{75k_BT}{\rho}, \qquad \rho = 3 \qquad \textbf{Equation (21)}$$

The compressibility of the pure fluid, ρ, is equal to 3 which is close to that of water [163]. k_B is the Boltzmann constant and T is the temperature of the system. In this study, conservative interactive potential with $k_B = 1$ was used. The repulsion parameter between different types of beads is given by [157]:

$$a_{ij} = a_{ii} + 3.27\chi_{ij}, \qquad \rho = 3 \qquad \textbf{Equation (22)}$$

where χ_{ij} is the Flory-Huggins parameter, which could be calculated from the solubility parameters as follows:

$$\chi_{ij} = \frac{V_{bead}}{kT}(\delta_i - \delta_j)^2, \qquad \textbf{Equation (23)}$$

where V is the arithmetic average of molar volumes of beads *i* and *j*. δ_i and δ_j are the solubility parameters of beads *i* and *j*, which depend on the chemical nature of the species and can be obtained from molecular dynamics simulations.

3.B.2.7.2.4. Assignment of DPD simulation parameters for disaggregation study

In the DPD simulation, single beads were used to represent Ce6 and water respectively, while the surfactant molecules were designated as two (connected) beads, one representing the hydrophilic head and the other the hydrophobic tail end. All the structures were drawn and energy minimized in Chemdraw software (Perkin Elmer, NJ,

USA). The repulsion parameters were determined using Materials Studio 5.0 software (Accelrys Inc., CA, USA). Each Ce6 aggregate comprised an average of 5 beads, which were connected by non-rigid bonded interactions, so as make them labile in order to be disrupted by sucrose esters. All the structures and sub-structures were energy minimized using COMPASS force field of Forcite energy minimizer. The Flory-Huggins interaction parameters (χ_{ij}) between a pair of similar and dissimilar beads were then calculated using Blend toolbox of the software. DPD simulations were performed in a cubic box of dimension 20 x 20 x 20 (DPD units), implementing periodic boundary conditions in all three directions. The fraction of each of the components per system was determined from the molar concentrations of the beads present in the system. Dimensionless time step 0.05 was employed with 20000 steps to obtain a steady phase at a constant temperature of 298 K.

3.C. Preparation of Ce6 formulation

3.C.1. Dissolution enhancement of Ce6 by formulating into sucrose ester-based nanosuspension

3.C.1.1. Experimental design for the study of Ce6-sucrose ester nanosuspension production

A 3 factor central composite design (CCD) was employed as it requires fewer runs to show the effects of the variables investigated. Using this statistical design, the effects of the process variables, such as the ratio of sucrose palmitate to sucrose laurate (X_1), amount of Ce6 (X_2) and ratio of dichloromethane to acetone in the solvent mixture (X_3) were investigated over five levels. The circumscribed CCD model consisted of a total of 17 runs with 3 center points and constructed using Design expert® statistical software (version 7.1.3; Statease Inc., MN, USA). Table 3 shows the different independent

variables and their levels in the construction of the CCD model. Four different response variables, such as formulation particle size, zeta potential, encapsulation efficiency and time required for 90 % drug release, were designated as dependent variables. A statistical second-order model incorporating interactive and polynomial terms was used to fit the data (coded values):

$$Y = b_0 b_1 X_1 + b_2 X_2 + b_3 X_3 + b_{11} X_1^2 + b_{22} X_2^2 + b_{33} X_3^2 + b_{12} X_1 X_2 + b_{13} X_1 X_2$$

$$\boldsymbol{Equation}\ (\mathbf{24})$$

where Y is the observed response for each of the dependent variables, b_0, constant coefficient, b_i and b_{ij} are the coefficients of effects of variables X_i and X_iX_j respectively. The interaction term X_iX_j represents the interaction between X_i and X_j and shows how the response changes when the two variables are simultaneously changed. The polynomial terms X_i^2 is used to evaluate the non-linearity effects of variable X_i.

Table 3: Composition of central composite design model

Factor	**Levels used**				
Independent variables	-γ	-1	0	1	+ γ
X_1 = SEP:SEL ratio	0.11	1.91	4.55	7.2	9
X_2 = Ce6 (mg)	5	12.9	22.5	32.9	40
X_3 = DCM/AC ratio	4	1.01	2.13	3.24	0.25

γ = Parameter which determines the location of points in CCD design

3.C.1.2. Preparation of Ce6-sucrose ester nanosuspension

The nanosuspension was prepared according to a modified hot-melt emulsification process [169]. Required quantities of sucrose ester and Ce6 were first dissolved in 5 mL of solvent mixture consisting of a specified proportion of dichloromethane to acetone with the aid of heating at 60°C for 15 min. 15 mL of MilliQ water was also heated at the same temperature and slowly poured into the solvent mixture under controlled magnetic stirring at 60°C. The O/W emulsion formed was quickly added into a beaker containing 40 mL of ice-cold water at 2-4°C to allow rapid solvent diffusion, hardening of the sucrose ester micelles and stabilization of the nano-droplets. The resultant nanosuspension was magnetically stirred overnight to allow complete evaporation of the organic solvents.

3.C.2. Enhanced mucoadhesivity of nanoparticles by formulating Ce6-PVP complex in alginate-based carriers

3.C.2.1. Experimental design for the study of alginate nanoparticles containing Ce6-PVP complex

The production of alginate nanoparticles consisting of Ce6-PVP complex was investigated by employing a 2 factor 3 level statistical design layout (Design Expert®, version 7.1.3; Statease Inc., MN, USA). Amounts of PVP (x_1) and Ce6 (x_2) were designated as the independent variables and were varied in 3 levels. The levels for these two factors were determined based on the results of preliminary trials. All the experiments were carried out in duplicates. Nanoparticle size, encapsulation efficiency, *in vitro* mucoadhesivity and *in vitro* drug release were designated as dependent or response variables. The effects of the afore-mentioned factors on the formulation characteristics

were illustrated on the basis of statistically significant p-values and R^2 values. The regression equation for this 3^2 factorial design is given below:

$$y = b_0 + b_1x_1 + b_2x_2 + b_{12}x_1x_2 + b_{11}x_1^2 + b_{22}x_2^2 \qquad \textbf{\textit{Equation}} (25)$$

where y is the dependent variable, b_0 is constant and b_i is the estimated coefficient for the factor x_i. The main effects (x_1 and x_2) represent the average result of changing one variable at a time from its low to high values. The interaction term (x_1 x_2) shows how the response changes when the two factors were changed simultaneously. Table 4 summarizes the independent variables with their levels.

Table 4: Composition of 3^2 full factorial design model

Factor	**Levels used**		
Independent variables	-1	0	1
x_1 = Ce6 (mg)	5	12.5	20
x_2 = PVP (mg)	10	55	100

3.C.2.2. Method for preparing Ce6-PVP complex in alginate nanoparticles

Alginate nanoparticles containing Ce6-PVP complex was prepared by a modified solvent diffusion-polymer gelation technique. Briefly, 50 mL of dilute sodium alginate solution (0.075 %, w/v) was prepared in MilliQ water and heated in a water bath at 70°C for 30 min. The required amounts of Ce6 and PVP according to the factorial design lay out, were added in 2 mL of 1:1 ethanol-acetone mixture and heated to 70°C for 30 min and added into the alginate solution with brief sonication. 2 mL (0.3 %, w/v) $CaCl_2$ was then immediately poured drop wise in the alginate solution containing Ce6-PVP mixture using a 19-gauge needle under controlled magnetic stirring. The nanoparticle suspension was

stirred for 8 hr for complete evaporation of solvent and the fresh nanoparticle suspension was transferred into a refrigerator at 4°C until use.

3.D. Determination of various dependent variables of different Ce6 formulations

3.D.1. Particle size and zeta potential

The mean particle size and particle size distribution of the nanoparticles of the two different Ce6 formulations were determined using a dynamic light scattering particle size analyzer (Horiba LB-500, Japan). The nanoparticle suspension was appropriately diluted and a suitable volume was placed in a quartz cuvette for measurements. The results obtained were derived from 100 laser scans of the nanoparticles in the sample. The mean particle size was then determined from the average of three replicates with the aid of a particle size analysis software attached to the equipment.

The zeta potential of the corresponding Ce6 nanoparticles was measured using a zetasizer (Malvern Nano-ZS90, UK). The nanosuspension was appropriately diluted and a suitable volume was placed in a cuvette for measurement at 25°C. The zeta potential was derived from 6 scans of the sample and the average value obtained from three replicates was reported.

3.D.2. Encapsulation efficiency

Different procedures were employed to calculate the amount of Ce6 encapsulated in sucrose ester and calcium alginate nanoparticles respectively. Freshly prepared Ce6-sucrose ester nanosuspension was centrifuged at 5000 rpm for 5 min (Beckman, CA, USA) to isolate undissolved materials. The supernatant consisting of encapsulated Ce6 was collected for analysis. 0.1 mL of the supernatant was diluted to 2 mL using methanol

to ensure that the sucrose ester with Ce6 was fully dissolved. The Ce6 content was then determined by HPLC under the following conditions: column – C18 (Thermo Electron corporation, NJ, USA), mobile phase – 20 % PBS (acetic acid and potassium-di-hydrogen phosphate, pH 4.0) with 80 % methanol for 15 min; 10 % PBS with 90 % methanol for 15-23 min; 50 % MilliQ water with 50 % methanol for 23-30 min, flow rate – 1 mL/min, detection wavelength – 405 nm. The encapsulation efficiency of Ce6 was calculated from the average of five replicates according to the following equation:

$$\text{EE\%} = \frac{Ce6_{NS}}{Ce6_{T}} \times 100 \qquad \textbf{\textit{Equation}}\ (\mathbf{26})$$

where $Ce6_{NS}$ and $Ce6_{T}$ are the amount of encapsulated Ce6 present in the total volume of nanosuspension and total amount of Ce6 used in the preparation respectively.

Freshly prepared suspension of alginate nanoparticles (containing Ce6-PVP complex) was centrifuged at 20000 rpm for 30 min. The clear supernatant was separated from the pellet composed of alginate nanoparticles. The Ce6 concentration of the supernatant was determined by HPLC according to the experimental conditions stated in section 3.B.1.1. The encapsulation efficiency was calculated as follows:

$$\text{EE\%} = \frac{\text{Amount of Ce6 loaded} - \text{Amount of Ce6 in supernatant}}{\text{Amount of Ce6 loaded}} \times 100$$

$$\textbf{\textit{Equation}}\ (\mathbf{27})$$

The encapsulation efficiency was determined in triplicate and the average was reported.

3.D.3. *In vitro* release of Ce6

In vitro release study of Ce6 from the sucrose ester nanosuspension and alginate nanoparticles was carried out in a USP paddle type II dissolution apparatus (Distek 2100C, USA) at 37°C. Sucrose ester nanosuspension consisting of 5 mg of Ce6 was placed in a dialysis bag (M.W. cut off 14000, Spectrum Medical Industries Inc., Singapore), which was then immersed in 500 mL of dissolution medium agitated at 100 rpm. The dissolution medium was composed of acidic buffer (pH 1.2) in the first 2 hr, and its pH adjusted to 6.8 thereafter using 3 M trisodium phosphate. Samples of 5 mL were withdrawn at regular time intervals and replaced with an equal volume of fresh dissolution medium. The amount of Ce6 released in the dissolution medium was determined by HPLC as described in section 3.D.2. For alginate nanoparticles, the suspension was first centrifuged at 20000 rpm for 30 min to collect the pellet composed of the nanoparticles. The pellet, equivalent to 5 mg of Ce6, was diluted with 5 mL of MiliiQ water and introduced into a dialysis bag (M.W. cut off 14000 Da), which was then immersed in 400 mL of dissolution medium maintained at pH 6.2 to simulate the *in vitro* oral mucosal pH. Samples of 5 mL were withdrawn at regular time intervals and replaced with an equal volume of fresh dissolution medium. The amount of Ce6 released into the dissolution medium was assayed by HPLC equipped with the C18 column under the following conditions: mobile phase – 90 % methanol and 10 % PBS buffer (acetic acid and potassium-di-hydrogen phosphate, pH 4.0), detection wavelength – 405 nm, flow rate – 1 mL/min. The dissolution test was carried out in triplicate.

Ce6 release from the polymeric alginate nanoparticles was appropriately modeled employing conventional dissolution modeling approaches and the theoretical basis of

drug release was discussed.

3.D.4. *In vitro* mucoadhesivity of alginate nanoparticles consisting Ce6-PVP complex

The method reported by Lee et al. for the determination of *in vitro* mucoadhesivity of a formulation was employed with little modification [170]. In the experiment, the t_{50} values of the various test formulations were first calculated from their *in vitro* release data. The bulk pellet obtained after centrifugation of alginate nanoparticle suspension was dried at room temperature, and from this approximately 10 mg of alginate nanoparticles was mixed with type I-S mucin solution (4 mg/mL) at pH 6.2. The mixture was then incubated for the corresponding t_{50} time period at 37˚C. This established the assumption that the mucoadhesivity of the formulation was attributed to the alginate polymer and the Ce6-PVP complex on equal weightage. The undissolved 50 % of the nanoparticles and the 50 % Ce6-PVP complex released would bind to the mucin in the mixture. The mucin bound by the alginate nanoparticles and Ce6-PVP complex were isolated by centrifuging the mixture at 20000 rpm for 10 min and the free mucin present in the supernatant was assayed by a colorimetric method using periodic acid and Schiff's reagent. The latter was prepared by diluting p-nitrosoaniline solution (40 gm/L in 2 M HCl) with water to give a final concentration of 1.0 %. Sodium bisulfate (80 mg) was added to 5 mL of Schiff's reagent and the resultant solution was incubated at 37°C until it became pale yellow. Periodic acid solution was freshly prepared by adding 10 µL of 50 % periodic acid to 7 mL of 7 % acetic acid. 100 µL of periodic acid solution was added to the supernatant, which was incubated for 2 hr at 37°C. 100 µL of the pre-treated Schiff's reagent was then added and absorbance of the mixture was measured at 560 nm after 30 min. The

percentage of mucin adsorbed by alginate nanoparticles ($Mucin_{ad}$) was calculated according to the following equation:

$$Mucin_{ad} = \frac{Mucin_T - Mucin_S}{Mucin_T} \times 100 \qquad \textbf{Equation (28)}$$

where $Mucin_S$ and $Mucin_T$ are the amount of mucin present in the supernatant and total amount of mucin used in experiment, respectively. The experiment was carried out in triplicate.

3.E. Response surface optimization and statistical analysis

The Ce6 formulations were optimized with the aid of three dimensional response surface plots constructed from the experimental data obtained. The effect of independent variables on the responses was calculated by ANOVA through Fisher's test. The p-value less than 0.05 was considered to be statistically significant. To evaluate the fitness of second-order polynomial equation, determination coefficient (R^2) and adjusted R^2 were employed as quality indicators. All responses observed were fitted to linear, second-order and quadratic models, and were evaluated in terms of statistically significant coefficients, p-value and R^2 values. The three dimensional surface plots were used to demonstrate the relationship and interaction between the coded variables and the responses. Response surface optimization was carried out based on the assigned values of the dependent variables, which were selected according to the desired characteristics of the optimized formulation. A few theoretical solutions along with the resultant experimental values of dependent variables were generated to achieve the desired optimized formulation. Experimental responses were then compared with that of the theoretical responses assigned for RSM optimization. Predicted error which is the difference between the

experimental value and the predicted value per predicted value was calculated for validation of the experimental design. Predicted error less than 5 % has generally been recommended for full statistical validation.

3.F. Characterization of optimized Ce6 nanoparticles of different formulations

3.F.1. Transmission electron microscopy

The morphology of Ce6 nanoparticles was visualized by transmission electron microscopy (TEM). The diluted nanoparticle suspension was applied onto carbon coated copper grids for TEM observation. Excess liquid was blotted out and the samples on the grids were allowed to dry at room temperatures for 24 hr. Photomicrographs were obtained using a transmission electronic microscope (JEOL JEM 2010, NJ, USA) operated at 200 kV.

The various solid state characteristics of the optimized Ce6 nanoparticle formulations were demonstrated by the following studies.

3.F.2. FT-IR spectroscopy

FT-IR spectra of pure Ce6, formulation components (sucrose esters/PVP and alginate) and the freeze-dried nanoparticle suspension of different optimized formulations were recorded using a FT-IR spectrophotometer (IR Solutions, Shimadzu, Japan) according to the method described in section 3.B.2.6. Efficient encapsulation of Ce6 and calcium alginate complex formation was inferred from the obtained spectra.

3.F.3. Differential Scanning Calorimetry

DSC thermograms of pure Ce6, formulation components (sucrose esters/PVP and alginate) and the freeze-dried nanoparticle suspension of different optimized formulations were obtained using a DSC instrument (TA60, Waters LLC, USA). Aluminium pan was used as reference cell. The temperature was varied from 25-300°C with a heating rate of 8°C per min under nitrogen atmosphere. Improved formulation characteristics such as efficient encapsulation or crystalline to amorphous transformation of Ce6 were deduced from the obtained thermograms.

3.F.4. X-ray diffraction

Powder x-ray diffractograms of pure Ce6, mixture of Ce6 and formulation components (sucrose esters) and the freeze-dried nanoparticle suspension of different optimized formulations were obtained using an x-ray diffractometer (X'Pert PRO MPD, Singapore) under the following measurement conditions: source – nickel filter Cu anode tube, wavelength – 1.54 Å, voltage – 30 kV, current – 15 mA, scan speed – 2° per min. Improved formulation characteristics such as efficient encapsulation or crystalline to amorphous transformation of Ce6 were extrapolated from the obtained diffractograms.

3.G. Evaluation of *in vitro* PDT efficacy of Ce6 formulations

In vitro PDT efficacy of optimized Ce6-sucrose ester nanosuspension and alginate nanoparticles consisting of Ce6-PVP complex, as well as the Ce6-disaggregating agent mixtures, was evaluated. The different response parameters for PDT efficacy were extent of singlet oxygen generation, intracellular uptake and cell cytotoxicity.

3.G.1. Singlet oxygen generation efficiency

The singlet oxygen generation was determined using RNO as singlet oxygen sensor and histidine as imidazole sensing group to trap singlet oxygen. Briefly, 100 µL of 250 µM RNO in distilled water and 300 µL of 30 µM histidine in distilled water were mixed together (Mixture A) in a quartz cuvette [171]. Free Ce6 and different Ce6-disaggregating agent solutions containing 1 µg of Ce6 were each mixed with 700 µL of distilled water containing 1 % DMSO. The resultant solution was combined with Mixture A in the quartz cuvette and bubbled with oxygen for 10 min. It was then irradiated with laser light (655 nm, 30 mW/cm^2) for 30 min. In the presence of oxygen, the labile nitroso group of RNO is converted to the stable nitro group, which is detected by decrease in RNO absorbance at a wavelength of 440 nm. Therefore, the extent of singlet oxygen generation was determined by monitoring the decrease in RNO absorbance every 2 min as a function of time up to 30 min. The singlet oxygen generation efficiency for different concentrations of PVP/sucrose ester was expressed in terms of proportional decrease in RNO absorbance over 30 min. For determination of extent of singlet oxygen production from the nanoparticle formulations, similar procedure was employed with little modification. Briefly, the nanoparticle formulations equivalent to 0.1 mg of Ce6 was dissolved in 10 mL of PBS (pH 6.8) and continuously stirred and then 700 µL from this solution was added to 300 µL of Mixture A in the quartz cuvette at different time intervals (30, 60, 120 min) and the afore-mentioned procedure for quantification was followed. Each determination was carried out in triplicate and the average results analyzed.

3.G.2. Uptake of Ce6 nanoparticle formulations by OSC cells

OSC cells (100,000 cells/mL) were seeded into each well of the 12-well plate (Cellstar®; Greiner Bio-one GmbH, Frickenhaussen, Germany), which was incubated in a humidified atmosphere containing 5 % CO_2 at 37°C for 24 hr. The cell culture medium was then replaced with fresh medium without fetal bovine serum, followed by the addition of nanoparticle formulation equivalent to 10 µg/mL Ce6. In order to investigate the effect of Ce6 aggregation on cellular uptake, solutions consisting of Ce6 with/without disaggregating agent (prepared at pH 5.0) were also tested. The cells were incubated with the samples for different time periods, ranging from 4 to 8, 12 and 24 hr. After the respective incubation period, the cells were washed thrice with cold PBS (4°C, pH 7.4, 10 mM) and then lysed by incubating with 0.5 mL of 0.5 % Triton-X solution for 1 hr. To determine the level of cellular uptake of Ce6 from the various samples, 1.5 mL of methanol was added to the lysate sample and vortexed for 1 min. The methanol phase was then isolated by centrifuging the mixture at 4000 rpm for 5 min at room temperature. Suitable dilutions were prepared to determine the Ce6 concentration by HPLC (LC solutions Shimadzu, Japan) under the following conditions: Column – C18, Mobile phase – 80 % methanol and 20% distilled water for 15 min; 70 % methanol, 20 % distilled water and 10 % PBS (acetic acid and potassium-di-hydrogen phosphate, pH 4.0) for 15-23 min; 50 % methanol and 50% distilled water for 23-30 min, Detection wavelength – 405 nm. The experiment was conducted in triplicate and the average values were reported.

3.G.3. *In vitro* phototoxicity

OSC cells were seeded in 96-well plates at a density of 6 x 10^3 cells per well and incubated in DMEM medium for 24 hr at 37°C in a 5 % CO_2 humidified incubator. The culture medium was then removed and replaced with 100 µL of fresh medium without fetal serum albumin followed by the addition of nanoparticle formulation or Ce6-PVP/sucrose ester mixture equivalent to 5 µg/mL of Ce6. Wells filled with only DMEM represented the blank. After another 24 hr of incubation, 10 µL of MTT solution (5 mg/mL in sterile PBS) was added to each well. The plate was further incubated for 4 hr. The mixture in each well was then removed and 100 µL of DMSO was added and shaken at 100 rpm for 30 min. Absorbance of the contents in each well was measured using a multi-plate reader (itecan M200, Mannedorf, Switzerland) at 590 nm. The percent proliferation (%) of the OSC cells was calculated as follows:

$$Percent\ Proliferation\ = \frac{sample\ reading - blank\ reading}{control\ reading - blank\ reading} \times 100$$

***Equation* (29)**

The percent cell inhibition was obtained by subtracting the percent proliferation from 100. The control represents the wells, which only consisted of incubating media (DMEM) and MTT solution. A plot of percent cell inhibition was constructed for varying PVP/sucrose ester or Ce6 concentrations and the IC_{50} (inhibitory concentration for 50 % cell population) value was derived from the plot.

3.G.4. Confocal laser scanning microscopy

Gelatin-coated cover slip was placed in each well of a 12-well plate. OSC cells were introduced on to the cover slip and allowed to grow for 24 hr under normal cell culture

conditions as mentioned previously. 0.5 mL of optimized Ce6 formulation consisting of 2 µg of Ce6 per mL was added to each well, followed by 0.5 mL of serum free DMEM medium. The cells were further incubated for predetermined time periods (1, 4, 8 hr). The medium was then removed and the cells washed thrice with ice cold PBS (pH 6.8). 500 µL of 3 % paraformaldehyde (PFA) was added in each well to fix the cells. After 20 min, PFA was removed and the cells were washed thrice with PBS buffer (pH 6.8). 200 µL of 500 nM DAPI solution was then added to stain the cells. After 20 min, the DAPI solution was washed off and the cover slip was removed from the well. It was then placed on to a slide with 1:1 glycerol-water mixture (40 µL) as the mounting medium for microscopic examination. Intracellular distribution of Ce6 was visualized using a confocal laser microscope (FV10i, Olympus, USA). Images were taken after selective excitation of DAPI and Ce6 using a DAPI (λ_x = 380 nm, λ_m = 450 nm) and Cy5.5 (λ_x = 400 nm, λ_m = 650 nm) filter set.

3.H. Statistical analysis of data

Independent sample t-test was performed for comparison of two sample means. One-way analysis of variance (ANOVA) was performed when more than two sample means were required. The correlation between two different sets of data was assessed using the square of the Pearson correlation coefficient (R^2). The statistical analysis of these data was performed using data analysis toolbox of Microsoft Excel (Microsoft office, 2007).

PART 4: RESULTS AND DISCUSSION

4. RESULTS AND DISCUSSION

4.A.1. Elucidation of photophysical properties of aggregated Ce6 in aqueous media

4.A.1.1. Overview

Investigation of aggregate formation is an important consideration. A good understanding of the influence of the aggregation mechanism on the photophysical parameters of Ce6 allows the use of these parameters in characterizing the extent of Ce6 aggregation in a system. As discussed in the introduction, extensive aggregation of Ce6 in aqueous media was observed and considering the importance of water as a vehicle in pharmaceutical preparation, the aggregation phenomenon of Ce6 in water needed to be investigated. This section discusses the investigations by spectroscopic studies of aqueous solutions of Ce6 as a function of pH and concentration.

4.A.1.2. Effect of pH on Ce6 solubility and partition coefficient

Ce6 solubility at different pH was investigated by equilibrating the respective buffers with excess Ce6 in a shaker water bath at 37°C for 24 hr. Figure 6 shows the relationship between Ce6 solubility and pH of the medium. Clearly, solubility of Ce6 was relatively low in the acidic to near-neutral pH conditions, as observed from pH 2 to pH 6. However, a more than 8-fold increase in solubility was observed in the alkaline pH region. It has been reported that the strong hydrophobic manifestations in the acidic pH conditions provide the main driving force for self-association of porphyrin photosensitizers to form aggregates [135]. Significant increment in solubility in the alkaline pH suggests possible reduction in extent of aggregate formation. NMR spectroscopic findings from earlier work showed that the ionization of peripheral carboxylic groups was initiated above

pH 8, which accounted for the increased solubility when the pH was increased [172]. Therefore, in order to examine if hydrophobicity is the major contributor to aggregation, partition coefficients of Ce6 at the different pH conditions were determined. A 4-fold decrease in partition coefficient was found when pH was increased from pH 2 to pH 10. The decrease in partition coefficient in the alkaline pH suggests that as pH increased, much higher amount of Ce6 partitioned into PBS than into the octanol phase. The reduction in affinity of Ce6 for the lipophilic octanol phase ascertains the increase in hydrophilicity of the Ce6 microenvironment, which leads to the disruption of aggregates and predominance of Ce6 monomers in the alkaline pH conditions. The ionization and hydrophilicity of Ce6 is important as it aids in the solubility and promotion of

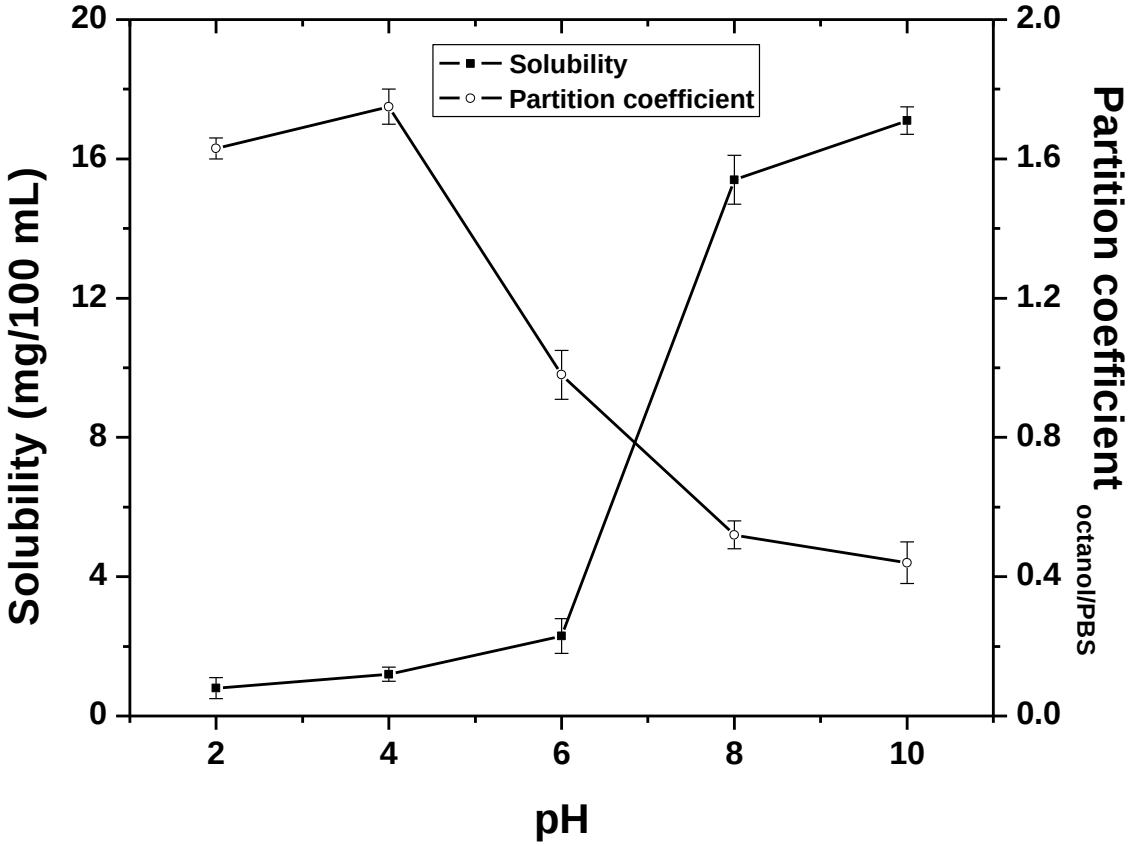

Figure 6: Effect of pH on solubility and octanol/buffer partition coefficient of Ce6 (n = 3).

aggregate-free monomerized form of Ce6. The steep reduction in partition coefficient which tends to level off from about pH 8 suggests that almost complete ionization and monomerization of Ce6 occurred at around this pH condition.

4.A.1.3. Effect of pH on absorption and fluorescence spectra of Ce6

The influence of pH on Ce6 aggregation was investigated over a pH range of 1.2 to 10 with 50 μM Ce6, which was reported to be a moderate concentration in previous studies [135, 173]. This concentration was also within the range above which self-absorption or scattering was observed in the absorption and fluorescence spectra, respectively. The absorbance spectra of Ce6 under the specified pH conditions are shown in Figure 7. Preliminary studies suggested that a strong Soret band (at about 400 nm) and less intense Q band (in the visible region of 650-700 nm) were characteristic absorption peaks of Ce6. These features are similar to those observed for analogues of porphyrins. As the ionization of three peripheral carboxylic acid groups took place in the alkaline pH conditions, it was hypothesized that the unionized carboxylic groups formed intermolecular H-bonds and facilitated aggregate formation in the acidic to near-neutral pH conditions. Figure 7 shows the spectral shifts in Soret and Q bands over the pH range of 1.2 to 10. The wavelengths of the absorption maxima (λ_{max}) for the Soret and Q bands in water (pH 6.8) were found to be 404 nm and 653 nm respectively, (Figure 7a and 7c). On increasing the pH from 6.8 to 10, the λ_{max} for both the Soret and Q bands were unaffected but their absorbance values significantly increased. Interestingly, significant spectral changes were observed for both Soret and Q bands when the pH was varied from 6.8 to about 1.2. Soret band exhibited a red shift from 404 nm to 409 nm while the Q band consisted of a sharp peak at 642 nm (peak 1) and another small hump at 673 nm

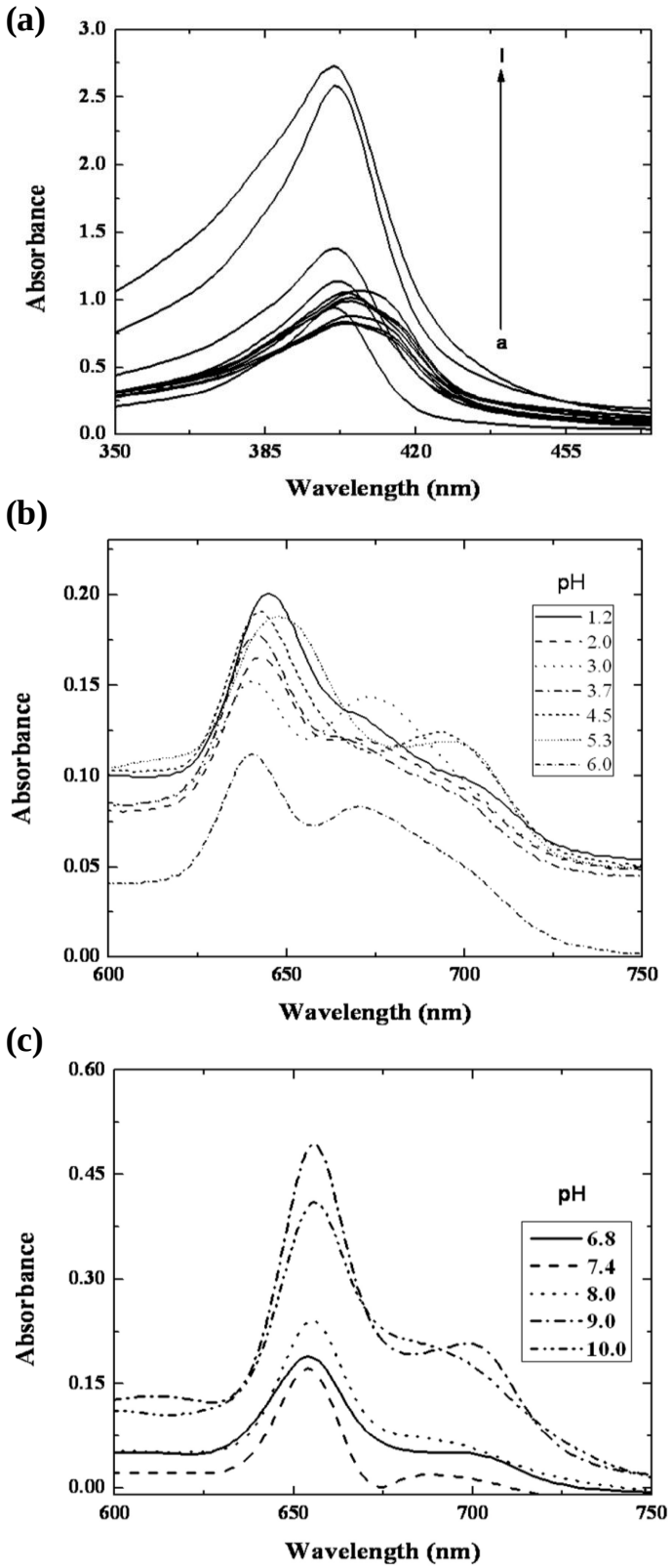

Figure 7: Absorbance of (a) Soret band (pH, a to l = 1.2 to 10) and Q band in (b) acidic and (c) neutral to alkaline pH.

(peak 2). The intensity also generally decreased on decreasing the pH of the solution (Figure 7a and 7b). Interestingly, a less broadened Q band devoid of any hump at pH 1.2 was observed, which implied reduced aggregation state of Ce6. At very low pH, the imino nitrogens in the pyrrole ring of porphyrin nucleus were protonated, which could result in repulsion of adjacent Ce6 molecule, thereby dispersing the Ce6 aggregates [174]. From the corresponding fluorescence spectrum, the wavelength of maximum emission (λ_{em}) was obtained at 656 nm with an excitation wavelength of 405 nm (Figure 8a). On increasing the pH from 6.8 to 10, λ_{em} remained the same at 656 nm but the fluorescence intensity increased significantly. The fluorescence emission peak maxima exhibited a blue shift from 656 nm to 644 nm when the pH was decreased from 6.8 to 3.0. Further decrease in pH to 1.2 shifted the λ_{em} to 651 nm. Nonetheless, fluorescence intensity gradually decreased with decreasing pH in the pH range 6 to 2. A blue shift implies a hydrophobic environment, thus concluding that the aggregates preferentially existed in the acidic pH condition.

In order to determine how the fractions of aggregate and monomers of Ce6 varied under different pH conditions, EEM spectroscopic principles were applied. This trilinear model had facilitated the accurate determination of various fluorophores present in a mixture of sample. This was achieved by collecting the emission spectra at a number of excitation wavelengths, followed by the use of advanced multivariate deconvolution technique. The PARAFAC algorithm is typically used for deconvolution purpose. The technique employed is based on the following proposition:

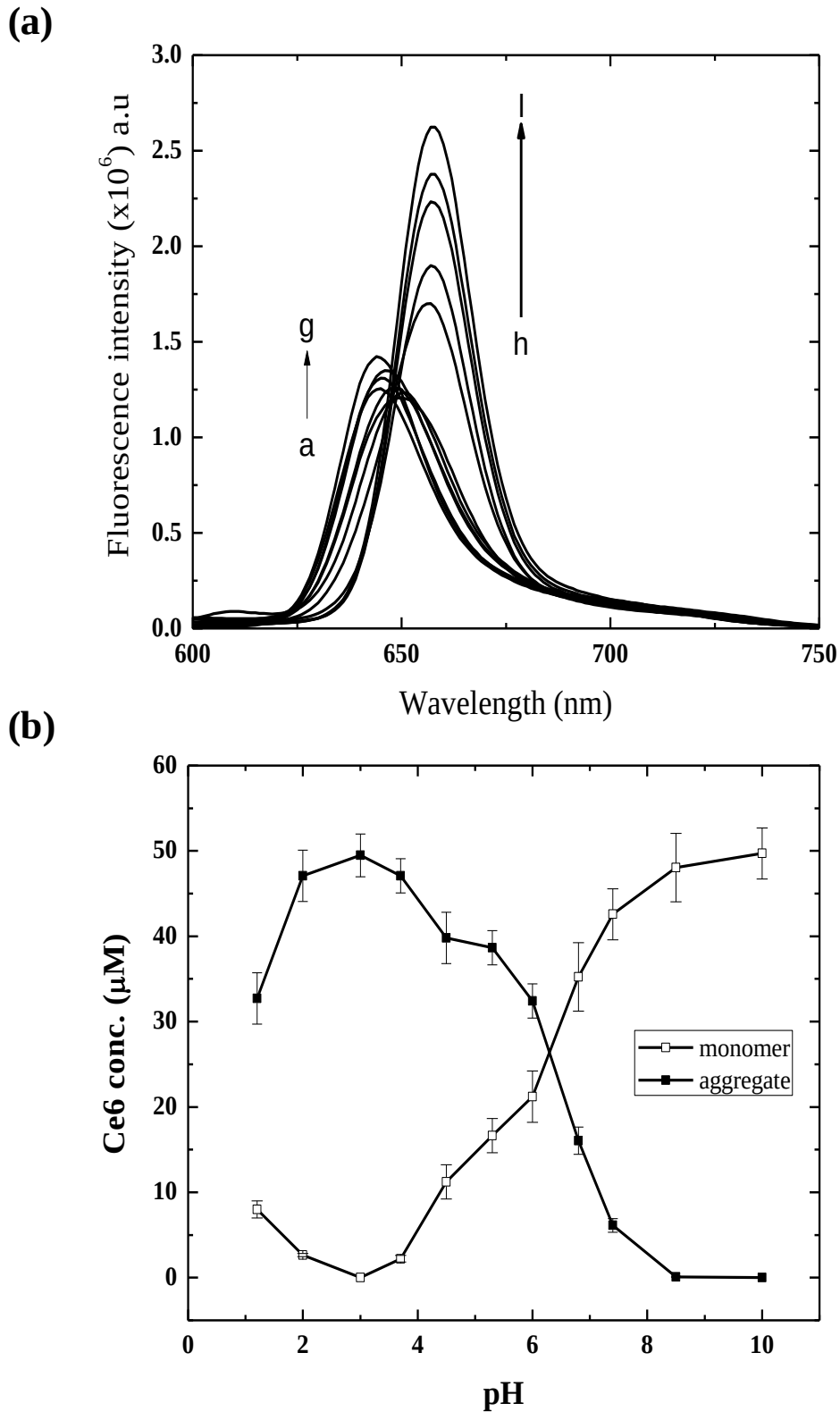

Figure 8: (a) effect of pH on fluorescence emission spectra of Ce6 (pH, a to g = 1.2 to 6.0, h to l = 6.8 to 10.0); (b) fraction of different species of Ce6 present in the pH range 1.2 to 10 (n = 3).

$$r_{i,j,k} = \sum_{n=1}^{N} x_{i,n} y_{i,n} z_{i,n} + e_{i,j,k} \qquad \textbf{\textit{Equation}}\ (30)$$

where $r_{i,j,k}$ represents the measured response of the *k*th sample at the *i*th excitation and *j*th emission wavelengths. In this study, each *k*th slice of the trilinear data cube R represents one EEM fluorescence spectrum in a series of samples and has the dimensions of I, J, where I is the number of excitation wavelengths and J is the number of emission wavelengths. The number of factors, *N*, chosen to model the system, is defined by the user [175, 176]. Generally, the predicted *N* value meets the actual number of species when the correlation coefficient is close to unity.

In the present study, when the *N* value was taken as 2 in the PARAFAC analysis, the highest correlation coefficient (98.2 %) was attained, suggesting aggregate and monomer fractions could be the only possible species present from pH 1.2 to 10. As can be seen from Figure 8(b), the corresponding aggregate and monomer fractions of Ce6 followed a reversible trend. Aggregate fraction predominated in the acidic to neutral pH range, while monomer fraction significantly increased in the alkaline pH range. Closer examination revealed that the decrease in aggregate fraction and the corresponding increase in monomer fraction from pH 6.8 to 10 was statistically significant ($p = 0.02$). This further confirmed the preferential existence of aggregates under acidic pH conditions.

Thus, from the above findings, the aggregation of Ce6 could be rationalized to occur in the pH range of 2 to 6, which showed characteristic changes in the uv-vis and fluorescence spectra. From the fluorescence emission spectra, the Ce6 species in the acidic pH (pH 2 to 6) differed from those found in the near neutral to alkaline pH. The fluorescence spectra of Ce6 aggregates in the acidic pH region showed a blue shift with

reduced fluorescence emission intensity as pH decreased. The corresponding absorption spectra of Ce6 exhibited a blue shift with broadened Q band, illustrating specific features of aggregation. The quantification of aggregate and monomer fractions using EEM spectroscopy further confirmed the evidence of aggregate formation in the afore-mentioned pH range. These observations corroborated earlier findings that Ce6 existed in two different forms, predominantly as aggregates in acidic pH and monomeric form in alkaline pH [177].

4.A.1.4. Effect of pH on Ce6 quantum yield

Studies conducted by Isakau et al. showed that Ce6-PVP complexes had higher quantum yield than Ce6 aggregates [135]. Thus, it would be interesting to investigate if pH had any influence on the quantum yield of Ce6. In present study, relative quantum yield measurements were determined as it is a simple approach that did not require any standard dye. The quantum yield of Ce6 in pH 10 was assumed to be the highest possible and therefore assigned a value of unity. The relative quantum yields of Ce6 in other pH solutions were subsequently calculated using Eq. (4). Figure 9 shows the relative quantum yields of Ce6 in media of different pH conditions. The quantum yield increased significantly from pH 2 to 6, followed by a steep increase above pH 6. It has been reported that a reduction in quantum yield could be caused by a nonspontaneous excited state transformation resulting from decrease in singlet oxygen generation [178]. Hence, it could be inferred that the aggregated Ce6 molecules drastically reduced the quantum yield values with a subsequent decrease in the sensitizing efficacy. The influence of pH on quantum yield of Ce6 was largely associated with its effect on Ce6 aggregation.

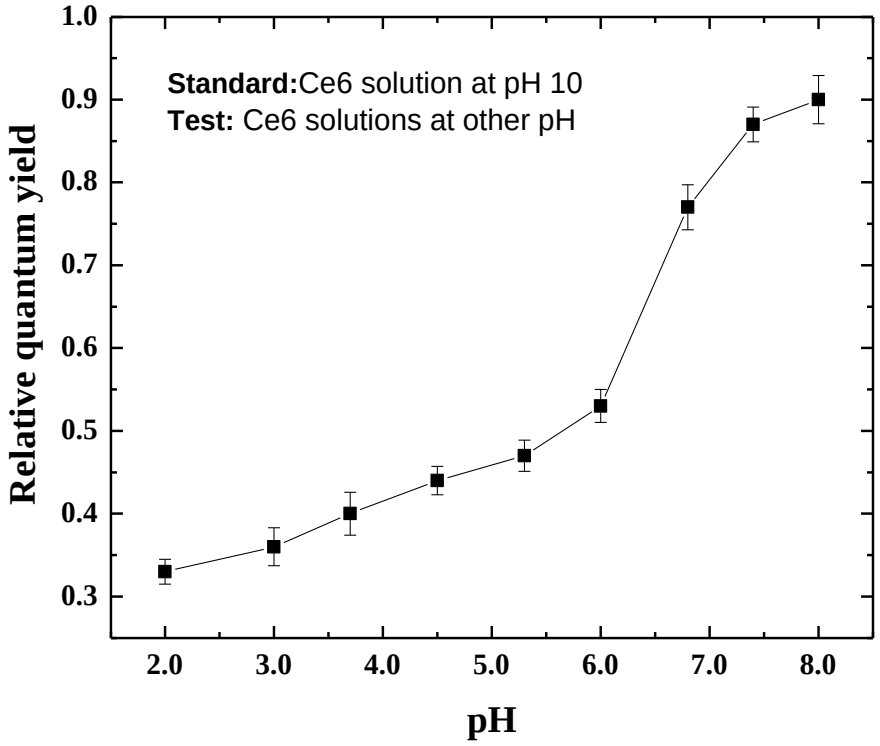

Figure 9: Effect of pH on relative quantum yield of Ce6 (n = 3).

4.A.1.5. Effect of Ce6 concentration on aggregate formation

In addition to the above, it is important to investigate whether aggregation was dependent on the concentration of Ce6. If aggregation is concentration-dependent, this concentration effect has to be considered in the estimation of Ce6 needed for generation of the desired photodynamic activity. Figure 10 shows the absorption and fluorescence spectra of Ce6 at concentrations ranging from 5 µM to 100 µM in buffer of pH 7.4. It was rationalized that pH 7.4 did not promote aggregation and a larger proportion of the Ce6 existed as monomers. Therefore, any effect of Ce6 concentration on aggregation would be more clearly seen. Besides, Ce6 will be exposed to the physiological pH of 7.4 when administered *in vivo*. The absorption spectra showed a narrow Q band at 673 nm, suggesting the existence of monomer-rich Ce6 at pH 7.4. Figure 10(b) shows the corresponding fluorescence spectra with λ_{em} at 656 nm. The emission wavelength did not

exhibit any spectral shift on gradual increase of Ce6 concentration. In order to determine whether the proportion of aggregate species increased with increase in concentration,

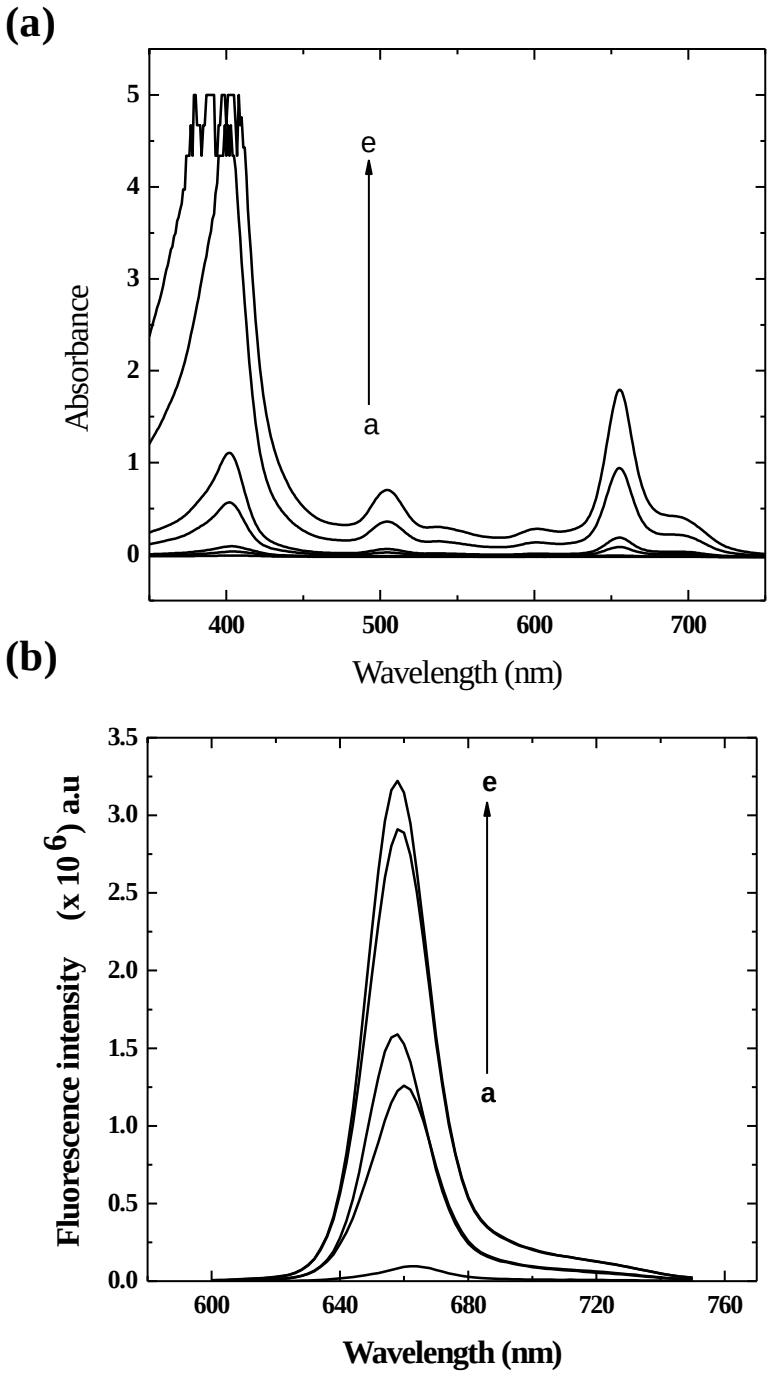

Figure 10: (a) absorption and corresponding (b) fluorescence spectra of Ce6 at pH 7.4 (a to e = 5 μM to 100 μM).

PARAFAC analysis was conducted by collecting the EEM spectra at various Ce6 concentrations from 5 µM to 100 µM. Figure 11 shows that the monomeric form predominated over the concentration range with insignificant increase in aggregate proportion (p value = 0.18). The concentration of aggregates slightly increased with increasing concentration of Ce6 used but the monomer to aggregate fraction ratio was fairly constant (ratio = 8.8-12.1). Thus, with the set of concentration range and pH, it was concluded that aggregation was independent of concentration. Instead, aggregation was largely affected by pH through its effect on the extent of ionization of the peripheral carboxylic acid groups.

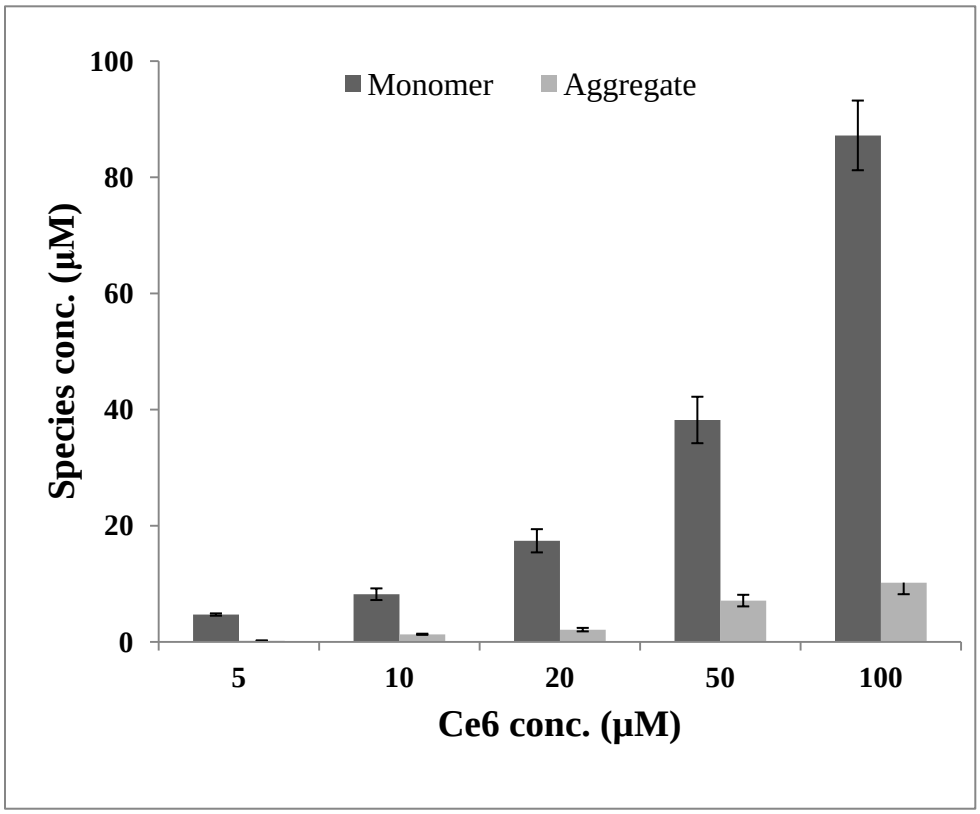

Figure 11: Fraction of different species present in varying Ce6 concentrations from 5 µM to 100 µM (n = 3).

4.A.1.6. Summary

The studies in this section showed the important aspects of aggregation of Ce6 and the effects of aggregation on the photophysical properties of Ce6. Solubility and partition coefficient measurements showed that Ce6 had remained in highly hydrophobic state in acidic pH conditions; however, its hydrophobicity decreased significantly in alkaline pH, which could be ascribed to ionization of the hydrophilic carboxylic moieties. Aggregation was not affected by Ce6 concentration in the range of 5 μM to 100 μM, studied at physiological pH. The spectroscopic findings suggested that the aggregation was a largely pH-dependent phenomenon, where ionization in the alkaline pH aided in solubility enhancement and disruption of aggregates.

4.A.2. Utilization of PVP for disaggregation of Ce6 aggregates

4.A.2.1. Overview

This section demonstrates the useful application of PVP in solubilizing the Ce6 aggregates. PVP is a common excipient used in formulations to enhance solubility [179]. PVP has been reported to induce disaggregation of Ce6 aggregates. However, the effects of PVP of different molecular weights on the photophysical properties of disaggregated Ce6 species has been lacking. In this study, different grades of PVP were used to investigate the changes in photophysical properties of Ce6 in relation to disaggregation by the use of simple spectroscopic techniques. The relative disaggregation potentials of different grades of PVP were then determined by EEM spectroscopic methods. The interactive mechanism of complex formation was demonstrated using thermodynamic studies and theoretical molecular dynamic simulation.

4.A.2.2. Effect of PVP on absorption and fluorescence spectra of Ce6

Three different PVP grades, K17, K25 and K30, were used for the disaggregation studies. From the earlier study on media pH, the extent of aggregation was mainly observed for pH below 6. Hence, the effect of PVP K25 on the Ce6 aggregates was first investigated in the acidic pH range. The changes in both fluorescence intensity and fluorescence anisotropy over pH 2 to 6 followed similar trends, suggesting that the use of any pH condition within pH 2 to 6 for comparison of disaggregation effects of different PVP grades would be acceptable. This led to the investigation of the other two grades of PVP at pH 5 only. This pH value was chosen for study based on the consideration that the pH of the tumour microenvironment generally lies between pH 5-6. Figure 12(a) shows the absorption spectra of Ce6 with increasing concentrations of PVP. The absorbance values

of both Soret and Q bands increased with the concentration of PVP, which suggested increasing hydrophilicity of the Ce6-PVP complex. Close examination of Q band

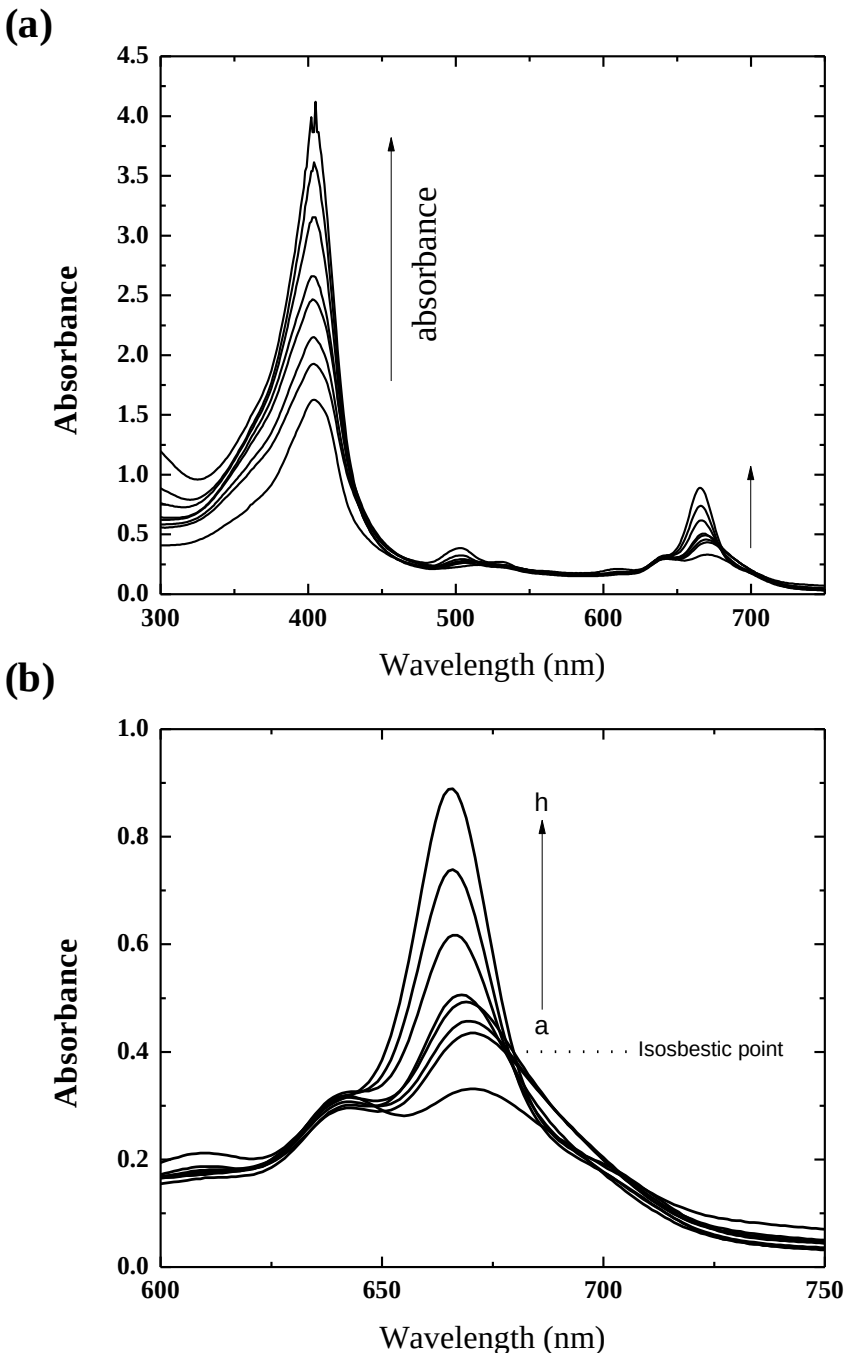

Figure 12: (a) absorption spectra of Ce6 and (b) close view of Q band with increasing PVP concentrations at pH 5.0 (a to h = PVP:Ce6 ratio, 10:1 to 1000:1).

revealed 2 peaks: peak 1 (λ_{max} at 642 nm) and peak 2 (λ_{max} at 673 nm). Interestingly, peak 2 became more prominent with the addition of PVP K25 (Figure 12b). The absorbance of peak 1 remained relatively constant, whereas the absorbance of peak 2 gradually increased as the PVP to Ce6 ratio changed from 10:1 to 1000:1. The evolution of characteristic peak 2 in the presence of PVP indicated its disaggregation effect on Ce6. Isosbestic point, the intersection point of one upward and another downward curve of two species where one species is converted to another, was also clearly observed in Ce6 spectra in presence of PVP. The isosbestic points observed in Q band on addition of PVP clearly demonstrated an aggregate-to-monomer equilibrium in the Ce6-PVP system. The concomitant increase in A_{673}/A_{642} ratio intensity with increasing PVP:Ce6 ratio from 0 to 100 is consistent throughout the pH range of 2 to 6. Figure 13(b) shows the variation of A_{673}/A_{642} with PVP:Ce6 ratio for all the PVP grades at pH 5. A sharp increase in A_{673}/A_{642} was observed when PVP:Ce6 ratio was increased from 0 to about 100. Further increase in PVP:Ce6 ratio resulted in more gradual rise in A_{673}/A_{642}. Since the absorbance of A_{642} was constant and A_{673} kept increasing with increasing PVP concentrations, the gradual rise in A_{673}/A_{642} up to PVP:Ce6 ratio of about 100 translated to the fact that significant monomerization of Ce6 aggregates was mostly achieved at that PVP concentration. Further increase in PVP concentration resulted in complete monomerization of the remaining aggregates at a PVP to Ce6 ratio of 1000 as indicated by no further increase in absorbance values. This is an important observation and it could be regarded as an index of disaggregation of Ce6 aggregates.

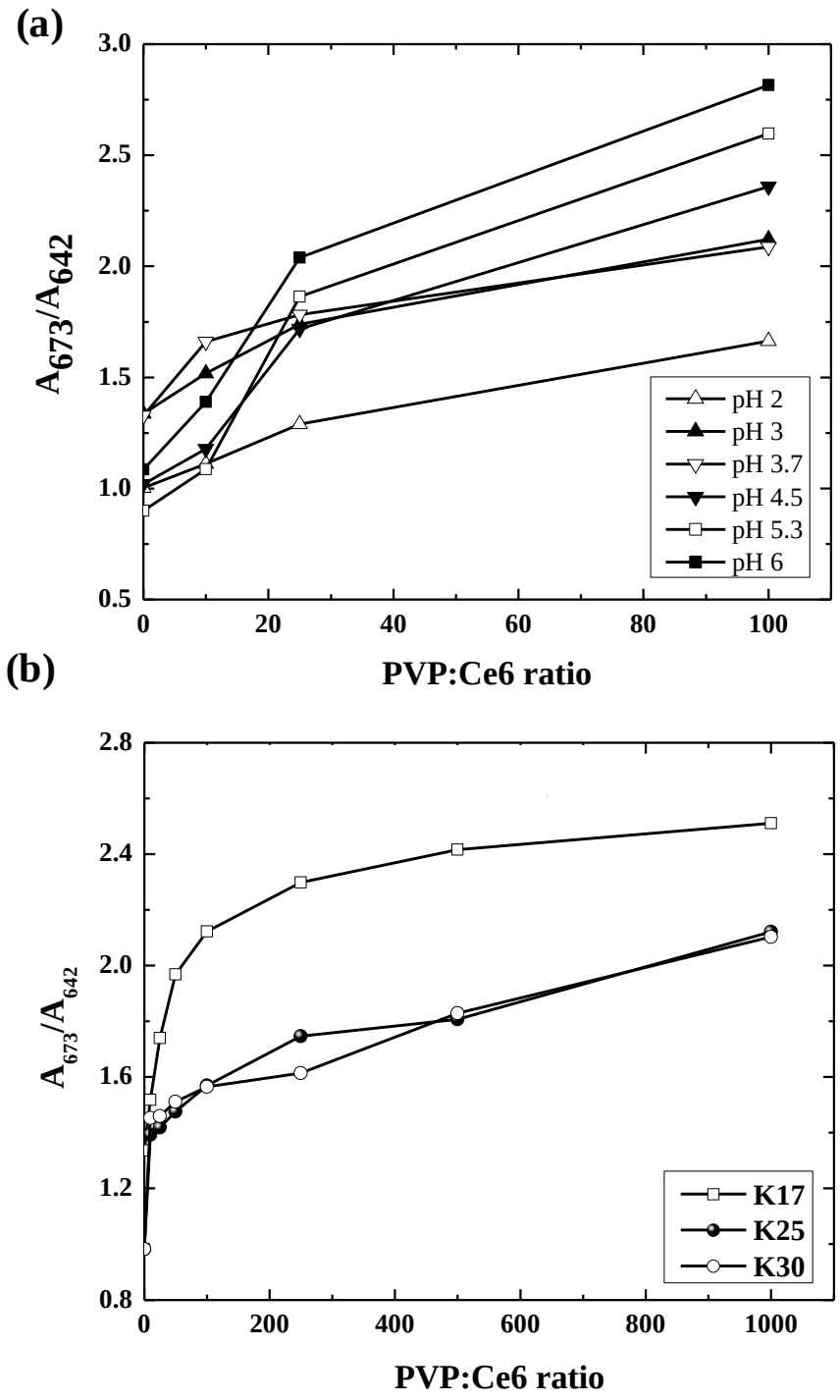

Figure 13: Effect of (a) pH and (b) PVP molecular weights on the ratio of absorbance between 673 nm and 642 nm.

The fluorescence emission spectra of Ce6 for various Ce6:PVP K25 ratios at pH 5 are shown in Figure14(a). Two interesting observations were noted here. Firstly, on addition

of PVP, fluorescence intensity decreased and the emission spectrum exhibited a bathochromic shift. At a moderate PVP:Ce6 ratio (100:1), two emission peaks were observed, with one peak at 645 nm and another at 665 nm when excitation wavelength was set at 405 nm. On further addition of PVP, the peak at 645 nm gradually diminished and at a very high PVP concentration (PVP:Ce6 ratio of 500:1), only one intense peak was observed at 672 nm. No further change in peak position occurred when PVP:Ce6

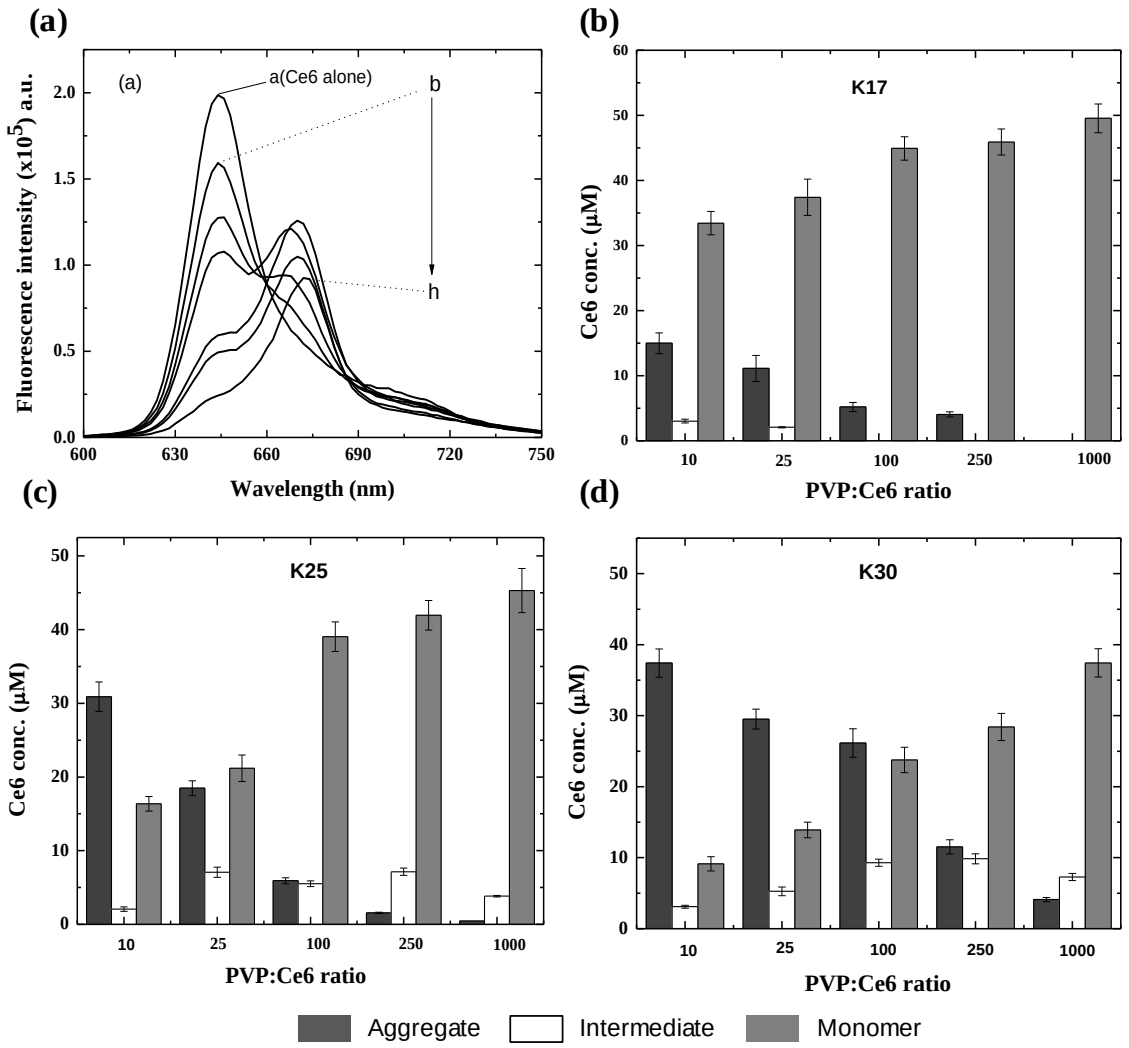

Figure 14: (a) Emission spectra of Ce6 for varying Ce6:PVP K25 ratios (b to h, = 1:10 to 1:1000), (b) to (d) amounts of different Ce6 species present at varying Ce6:PVP ratios for different PVP grades at pH 5 (n = 3).

ratio was further increased to 1000, implying all the Ce6 molecules were eventually converted to monomers. Similar spectral changes were also observed with PVP K17 and K30 (figure not shown). A quenching-like effect was observed as the fluorescence intensity of Ce6 was found to decrease in the presence of PVP. However, PVP was found to be non-fluorescent when excited in the range 250-600 nm, suggesting the triplet state attainment of Ce6 was increased in the presence of PVP, instead of returning to singlet state following high fluorescence. Collectively, the results indicate monomerization of Ce6 aggregates by complex formation between Ce6 and PVP. Ce6 would bind to certain sites of the PVP molecule, thereby overcoming Ce6 aggregation. At very high PVP concentration, all the Ce6 molecules were bound to PVP and no further shift in emission spectra was observed. The fluorescence emission spectra of Ce6 were collected for all the PVP grades and PARAFAC algorithm was applied. Figure 14(b) to (d) shows the proportions of varying species of Ce6 evolved by the action of each of the grades of PVP. The determining Factor, *N*, for calculating the number of different species present was found to vary between 2 and 3. When *N* was taken as 3, the average correlation coefficient for all the grades increased from 0.932 to 0.987. The presence of these three species could be identified as pure Ce6 aggregate, Ce6 partially bound with PVP and fully PVP-bound Ce6 monomers. Such proposition can be rationalized based on the fact that Ce6 emission spectra shifted from 644 nm to 665 nm at moderate PVP concentrations, suggesting that pure Ce6 aggregates were converted to Ce6 partially bound with PVP. Further shift from 665 nm to 672 nm indicated complete disaggregation of Ce6 at sufficiently high concentrations of PVP. Interestingly, the proportions of these species also varied significantly for different grades of PVP. As can be seen from

Figure 14(b) to 14(d), PVP K17 showed highest disaggregation efficiency than its counterparts as the fraction of PVP-bound Ce6 monomer was found to be highest for the minimum concentration of PVP employed (Ce6:PVP ratio = 1:10). Thus, the rank order of disaggregation efficiency was K17 > K25 > K30. The detailed explanation of varying disaggregation efficiency of different PVP grades is discussed in section describing Ce6-PVP binding constant study.

4.A.2.3. Effect of PVP on fluorescence anisotropy

The fluorescence anisotropy (μ) values were calculated to assess the extent of complex formation between Ce6 and PVP. Fluorescence anisotropy measurements are often used to estimate the rotational movement during the photochemical transformation of a fluorophore from singlet to excited state [165]. Figure 15 shows the plot of fluorescence

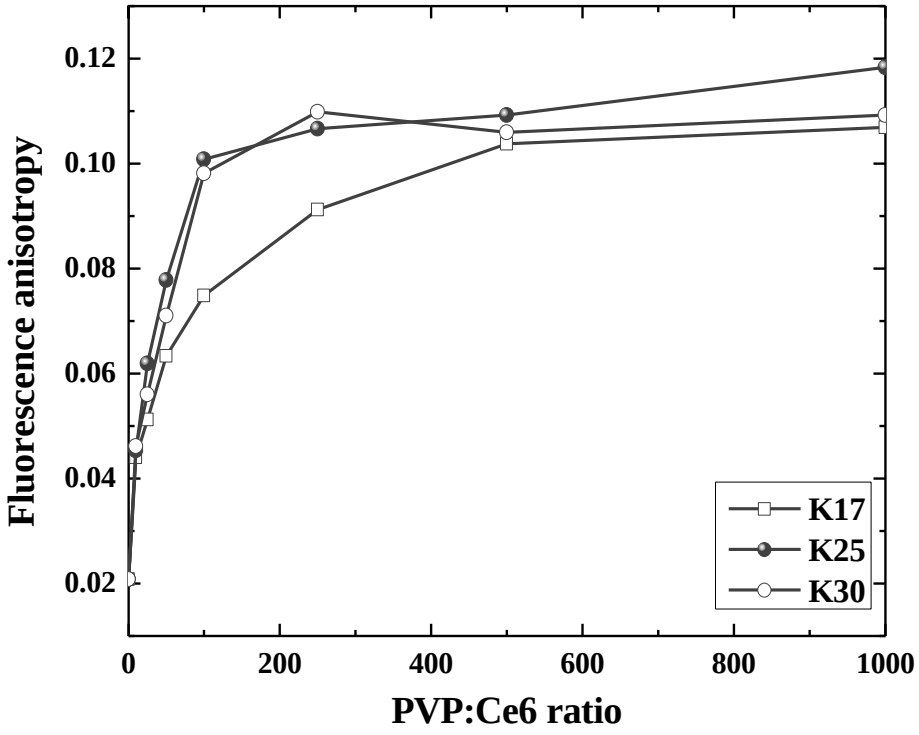

Figure 15: Effect of PVP molecular weight on fluorescence anisotropy of Ce6.

anisotropy values against PVP concentration for all the three PVP grades at pH 5. A sharp increase in fluorescence anisotropy was observed when the PVP:Ce6 ratio was increased up to 100:1, beyond which the fluorescence anisotropy gradually leveled off. Increase in anisotropy values with PVP concentration confirmed the association of Ce6 with bulky PVP molecules, which restricted their rotational movement.

4.A.2.4. Binding constant of Ce6-PVP complex

As mentioned earlier, Ce6 molecules tend to aggregate in aqueous media especially under acidic conditions. In order to avoid complications of Ce6 aggregation and to simulate physiological pH, binding of Ce6 to PVP was studied at pH 7.4. One of the efficient ways to determine the binding constant of a fluorophore involves quenching studies [180]. The fluorescence emission of Ce6 was found to decrease in the presence of PVP, suggesting a quenching-like phenomenon. However, when the decrease in fluorescence intensity was plotted against PVP concentration using the Stern-Volmer equation, it did not exhibit a linear relationship. Moreover, PVP was found to be non-fluorescent in the range of 250-600 nm. Consequently, the binding parameters were determined using the Klotz plot, a model used to study the interaction between polymers and drug molecules. From the characteristic spectral features it was found that all the Ce6 aggregates were bound to PVP at high PVP concentration (PVP:Ce6 ratio greater than 500:1). Therefore, the absorption spectrum of Ce6 at PVP:Ce6 ratio of 1000:1 was used to calculate the concentration of fully PVP-bound Ce6 (C_B) molecules (employing Eq. 6). Figure 16(a) shows the bound fraction of Ce6 (x) (calculated from Eq. 6 and 7) with increasing PVP:Ce6 ratio for different PVP grades. The fraction of bound Ce6 (x) was observed to increase with increasing PVP:Ce6 ratio in a logarithmic manner ($r^2 > 0.96$). For a given

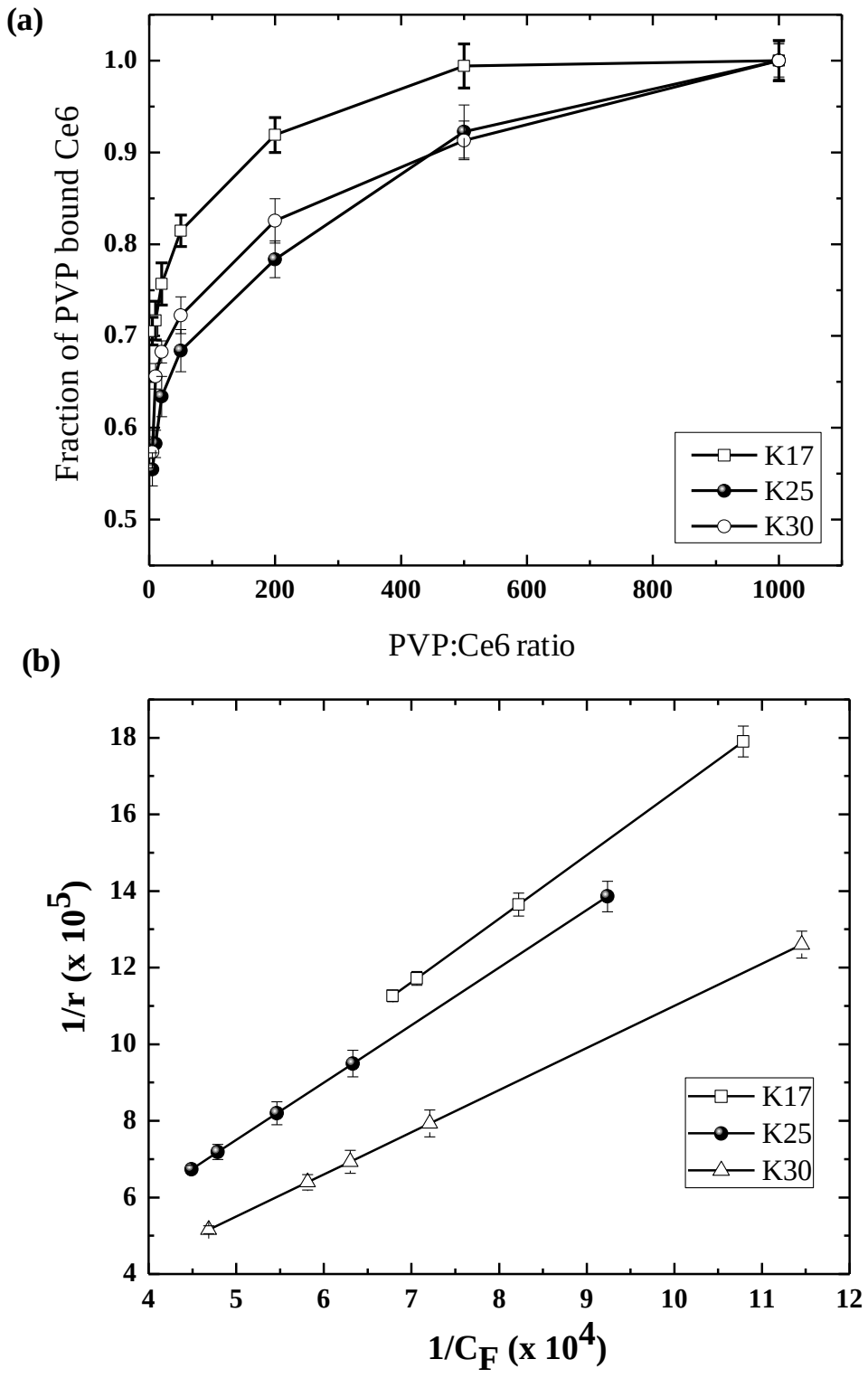

Figure 16: (a) Effect of PVP molecular weights on the fraction of PVP-bound Ce6 and (b) Fitting to Klotz reciprocal plot for different grades of PVP (n = 3).

PVP:Ce6 ratio, the fraction of PVP-bound Ce6 increased with decrease in molecular weight of PVP. All the Ce6 monomers were complexed with PVP at PVP:Ce6 ratio of 1000. As can be seen, PVP of lower molecular weight grade facilitated improved binding efficacy and followed the order: K17 > K25 > K30. Based on the fraction of PVP-bound Ce6, the number of moles of Ce6 per mole of PVP monomer unit was calculated and used in the construction of the Klotz plot. All the three PVP grades generally showed good linearity in the Klotz plot (Figure 16b). The binding parameters, K_a and *n* were then calculated from the slope and intercept of the Klotz plot for each of the PVP grades. The values of *n* was found to be smaller than 1 for the PVP macromolecule, indicating that more than one PVP monomer unit was involved in the binding with one Ce6 molecule. The P values (1/n) were calculated from the reciprocal of *n*. The number of probable binding sites in PVP molecule (N_0) was calculated using Eq. (10). The binding parameters, such as K_a, P and N_0 are shown in Table 5. PVP of lower molecular weight would produce a larger number of PVP molecules per unit weight of polymer. The results showed that the efficiency of binding to Ce6 was promoted by the availability of a larger number of PVP molecules, albeit shorter in chain length. PVP with a higher molecular weight will have a longer polymer chain and thus more binding sites. This aptly accounted for the high N_0 value for PVP of higher molecular weight. The increase in N_0 value was however inconsistent, probably due to polydispersity of the polymer. The number of PVP monomers per binding site, P consistently decreased with increasing molecular weight of PVP. Increase in the p value implies association of a greater number of PVP monomers to each Ce6 molecule, resulting in strong interaction between them. In addition to binding efficiency, PVP K17 also exhibited the highest binding strength,

leading to the formation of the most stable Ce6-PVP complex. According to the literature, the molecular weight of PVP for systemic use should be less than $5x10^4$ - $8x10^4$. Based on the results obtained, K17 grade will make a favorable choice for Ce6-PVP formulation.

Table 5: Binding parameters of Ce6 with PVP of different molecular weights

PVP Grade	M_w[a]	K_a ($x10^4$ mol^{-1})	P	N_0
K17	10,000	3.66 ± 0.8	61 ± 4	1.62 ± 0.2
K25	24,000	3.51 ± 0.6	53 ± 4	4.23 ± 0.3
K30	41,000	3.34 ± 0.6	37 ± 7	8.07 ± 0.8

[a] average molecular weight of the PVP grade

4.A.2.5. Binding mode of Ce6-PVP complex

The interactive forces behind the Ce6-PVP complex formation was investigated by FT-IR spectroscopy and thermodynamic studies. The interaction between a drug and a macromolecule may involve hydrogen bonds, van der Waals forces, electrostatic forces and hydrophobic interactions [168]. Thermodynamic parameters, such as enthalpy changes (ΔH) and entropy changes (ΔS), are the main evidence to confirm binding modes. From the thermodynamic standpoint, $\Delta H > 0$ and $\Delta S > 0$ imply a hydrophobic interaction; $\Delta H < 0$ and $\Delta S < 0$ reflect interaction via van der Waals forces or hydrogen bonds; and $\Delta H \approx 0$ and $\Delta S > 0$ suggest an electrostatic force of attraction [181]. From the spectroscopic standpoint, FT-IR has been widely used over the years in the analysis of drug-polymer interactions [182]. Figure 17 shows the FT-IR spectra of Ce6, PVP K25

and freeze-dried Ce6-PVP complex (at PVP:Ce6 ratio of 10:1). It was observed that the FTIR spectrum of Ce6-PVP complex was merely the superposition of Ce6 and PVP spectrum without any noticeable shifts. This was reflected by the individual stretching vibrations of Ce6 near 1700 cm^{-1}, 2300 cm^{-1}, 2900 cm^{-1}; and PVP near 1330 cm^{-1}, 1420 cm^{-1}, 1700 cm^{-1}, 2800 cm^{-1}, 3200 cm^{-1}), which were also present in the spectrum of Ce6-PVP complex. The finding suggested that Ce6 was probably shielded by the macromolecular PVP structure indicating the absence of any electrostatic or covalent interaction. This accentuated the possibility of hydrophobic interaction between Ce6 and PVP.

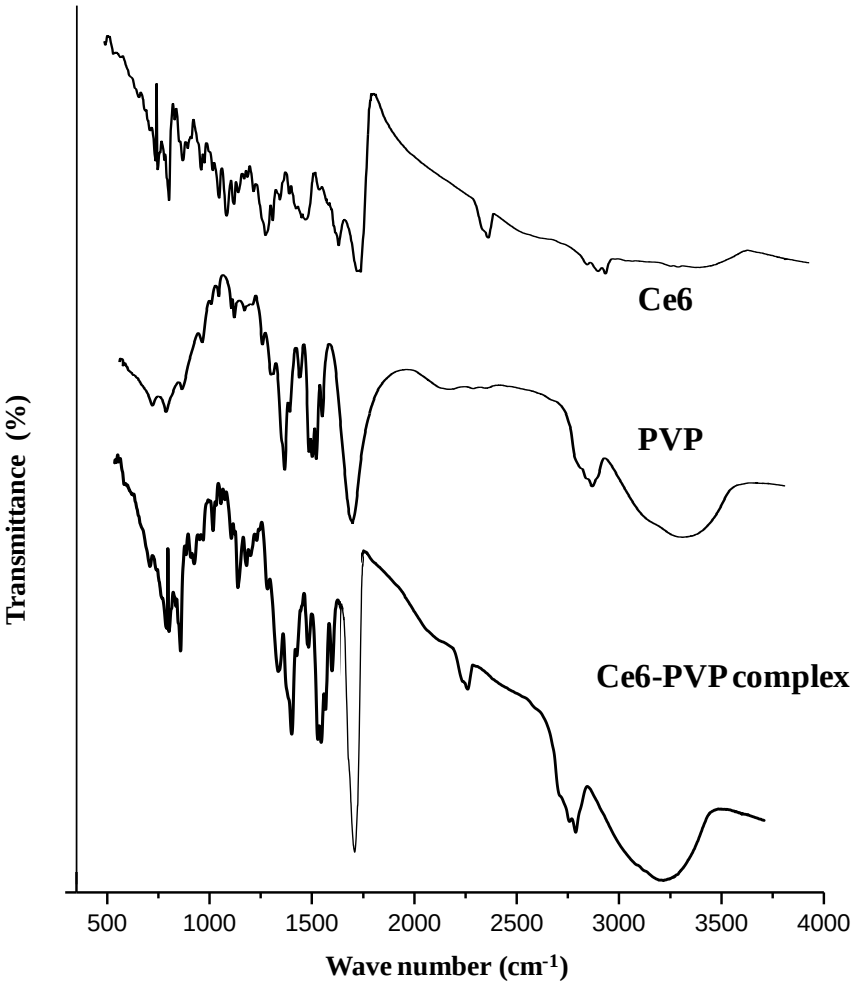

Figure 17: FT-IR spectra of Ce6, PVP K25 and their resultant complex at PVP:Ce6 ratio of 10:1.

The binding mode was further investigated by thermodynamic studies at 288 K, 297 K and 310 K. Two temperature points, one above (310 K) and the other below (288 K) the room temperature (297 K) were selected to study the effect of temperature difference on the binding mechanism. The binding constant at each temperature point was calculated using Eq. (9) and the values were then fitted into Van't Hoff's equation. The changes in entropy and enthalpy were obtained from the slope and intercept of the plot. The various thermodynamic parameters, such as changes in free energy (ΔG), enthalpy (ΔH) and entropy (ΔS), were calculated using Eq. (12) and (13) and presented in Table 6. The negative values of ΔG indicate that the binding processes were spontaneous for all three grades of PVP. The positive values of ΔH and ΔS suggest hydrophobic interaction between PVP and Ce6. This suggests that the Ce6 molecules were possibly entangled with the long polymeric chains of PVP where hydrophobic forces predominated, resulting in the formation of Ce6-PVP complex.

Table 6: Thermodynamic parameters for binding of Ce6 with different PVP grades

PVP Grade	ΔG, 288 K (kJ mol^{-1})	ΔG, 297 K (kJ mol^{-1})	ΔG, 310 K (kJ mol^{-1})	ΔH (kJ mol^{-1})	ΔS (kJ $mol^{-1}T^{-1}$)
K17	-8543	-8822	-9225	385.5	31.9
K25	-8352	-8626	-9311	290.2	30.5
K30	-8368	-8638	-9024	272.1	30.1

4.A.2.6. Molecular dynamics simulation of Ce6-PVP complex

The interaction between Ce6 and PVP was further investigated by geometry optimization of Ce6-PVP system using Hyperchem software with in-built molecular dynamics simulation [183]. The energy-minimized structures of Ce6 and PVP were used for simulation within a periodic box including water molecules to simulate the experimental condition. The optimized structure of the Ce6-PVP complex at the end of the simulation is shown in Figure 18(a). In the solvated condition, the porphyrin ring of Ce6 was found

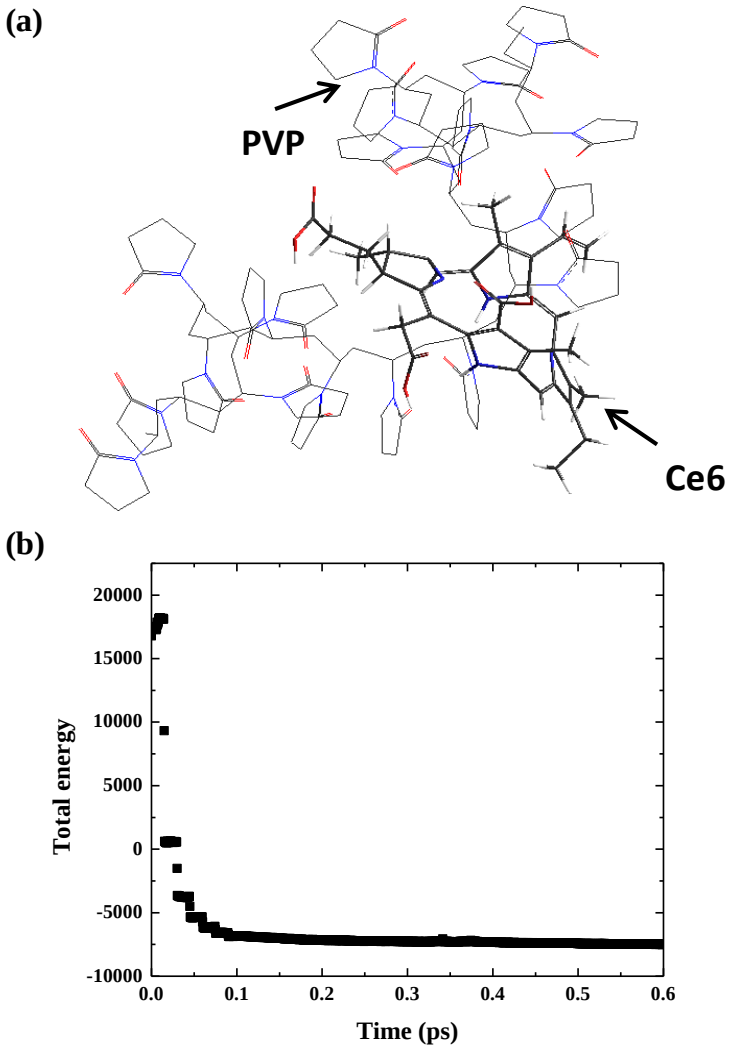

Figure 18: Molecular dynamics simulation of Ce6-PVP system: (a) conformation of Ce6-PVP complex and (b) energy vs. time profile of the simulation period.

to be widened, which could be attributed to the increased mobility of the pyrrolic N-ring in the presence of the polar solvent. This facilitated the passage of PVP through the widened porphyrin macrocycle of Ce6. In the presence of the polar solvent, PVP also showed increased mobility of the pyrrolidone moieties, resulting in entanglement of the Ce6 molecule with the PVP structure. Particularly, the pyrrolidone moieties were found to be closely associated with a mean approximate distance of 6 Å from the Ce6 molecule, suggesting the possibility of hydrophobic interaction. It was possible for the PVP molecule to pass through more than one Ce6 molecule, as long as the PVP molecule involved was linear. As a consequence, the PVP molecule would present a number of PVP-binding sites for Ce6. Hence, for PVP K25 molecule with more than 100 monomer units, it could be extrapolated that more than one Ce6 molecule would be entangled with the PVP polymer. The free energy (ΔG) obtained at the end of the simulation run was found to be negative (-7403 kJ/mol) as similar to that obtained from thermodynamics study (Table 6), indicating that the conformation of Ce6 and PVP determined by the MD simulation study was nearly accurate. The Ce6-PVP complex was thermodynamically stable, as indicated by an asymptote in the energy vs. time plot (Figure 18b), thus confirming the formation of stable Ce6-PVP complex through hydrophobic interaction.

4.A.2.7. Summary

The studies in this section showed that PVP facilitated the conversion of Ce6 aggregates into monomeric form by forming Ce6-PVP molecular complexes. The PVP with lowest molecular weight (K17) exhibited the highest disaggregation efficiency as shown by the PARAFAC analysis and binding constants. Thermodynamic parameters calculated from temperature-dependent binding studies suggested that complex formation mainly

occurred by hydrophobic interaction between PVP and Ce6. A molecular dynamics simulation from theoretical perspective was also in good agreement with the experimental findings. Furthermore, the spectral changes of Ce6 brought about by different grades of PVP have been adequately explained on the basis of absorption and fluorescence spectroscopic principles. Therefore, the various photophysical characteristics pertaining to disaggregation of Ce6 could effectively be used as a tool in subsequent studies to demonstrate the disaggregation potential of other pharmaceutical adjuvants.

4.A.3. Utilization of sucrose esters for disaggregation of Ce6 aggregates

4.A.3.1. Overview

In this section, the effect of sucrose ester-based surfactants on Ce6 aggregates was elucidated using spectroscopic and coarse grain simulation techniques. Surfactants have previously been used in the disaggregation of porphyrin and other photosensitizers. Recently, Dutta et al. demonstrated the usefulness of charged surfactants like SDS and CTAB, which formed electrostatic complexes with chlorin p6, a structural analog of Ce6 [152]. Considering the toxicities arising from charged surfactants in the *in vivo* system, the utilization of non-ionic and biocompatible surfactants is highly recommended for disaggregation of Ce6. Sucrose esters are examples of novel non-ionic and biocompatible surfactants. Till date, these surfactants have not been explored for the disaggregation of Ce6 or any other fluorescence dyes. Hence, studies were carried out to investigate the disaggregation efficacy of three sucrose ester surfactants having lauryl (C12), myristyl (C14) and palmityl (C16) groups respectively as alkyl chains. The relative disaggregation efficacy of each of the surfactants was determined employing EEM spectroscopic methods. The Ce6-sucrose ester interaction was macroscopically simulated using dissipative particle dynamics (DPD) as a visualization tool. In addition, the response parameters of DPD model were correlated with the experimental findings to elucidate the disaggregation phenomenon.

4.A.3.2. Absorption and fluorescence spectra of Ce6 in the presence of sucrose esters

In order to investigate the disaggregation potential of the different sucrose ester, absorption and fluorescence spectra of Ce6 were obtained with varying sucrose ester concentrations. All the spectroscopic measurements were conducted at pH 5.0 to

emphasize its relevance to tumour physiological environment. The concentration of sucrose esters were varied from below CMC to above CMC and the concentrations of sucrose esters were designated in terms of their corresponding CMCs in the present study. It was rationalized that disruption of photosensitizer aggregates was accentuated near the CMC of the surfactants, whereby the monomers were incorporated into the resultant micelles. The CMC values of the different sucrose esters used were obtained from the literature (Table 7). Figure 19 shows the absorption spectra of Ce6 in the presence of sucrose ester monolaurate (SEL) from below CMC to 20-times of its CMC.

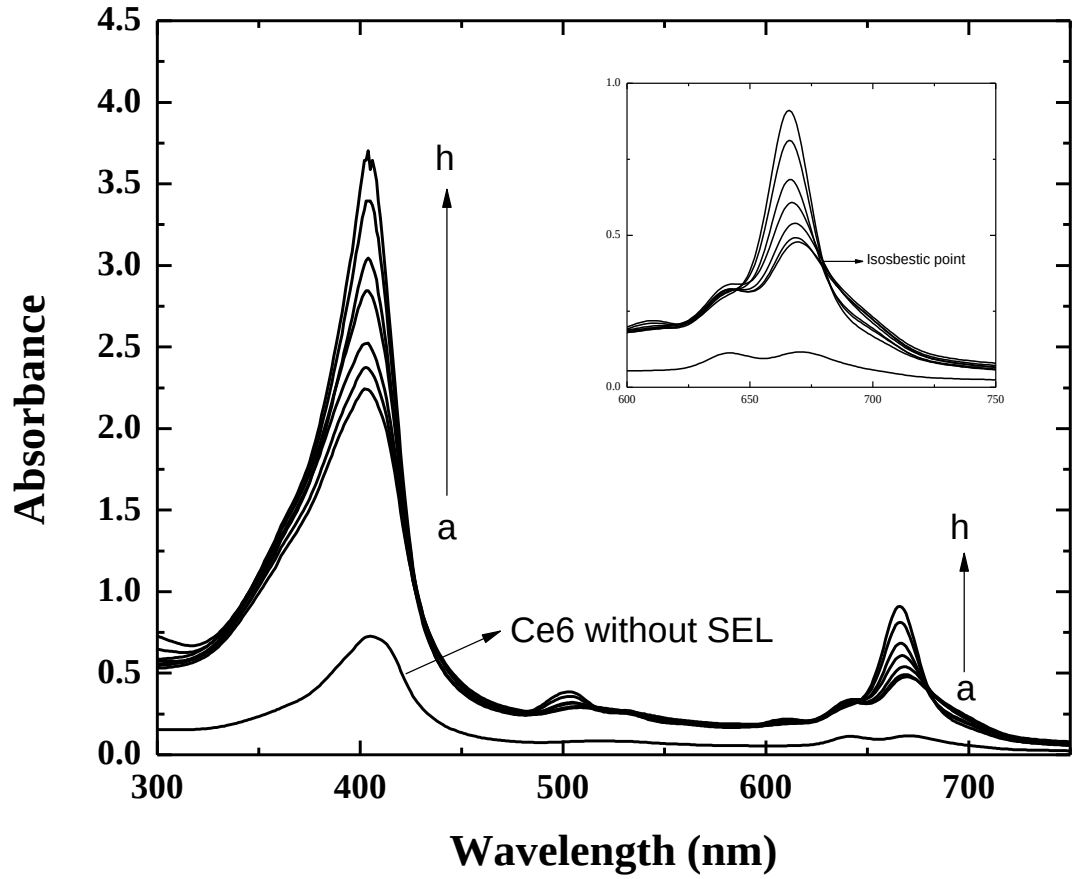

Figure 19: uv-vis spectra of Ce6 for varying concentrations of SEL [a to h = 0.5 x CMC to 20 x CMC] (inset: Q band characteristics).

The absorbance of both Soret and Q bands were found to increase, indicating increased polarity in the Ce6 microenvironment. One possible reason could be association of disrupted aggregates with the surfactant micelles, thereby diminishing hydrophobicity in the microenvironment. As observed in the case of PVP, Q band similarly showed a sharp peak at 673 nm, suggesting disaggregation effect of SEL. Furthermore, isosbestic points were clearly observed on increasing concentrations of SEL, which suggests the existence of aggregate-monomer equilibrium in the system. Similar observations were also made for sucrose ester monomyristate (SEM) and sucrose ester monopalmitate (SEP) (figure not shown).

Figure 20 shows the corresponding fluorescence spectra of all the three sucrose esters at different concentrations. Collectively for all the spectra, a bathochromic shift was observed. The emission maxima shifted from 644 nm to 673 nm, implying the conversion of Ce6 aggregates into monomeric form. The disruption of Ce6 aggregates as evidenced by a new emission peak at 670 nm was first observed at twice the CMC (2 x CMC) concentration of SEL. Further increase in SEL concentration resulted in complete disappearance of the aggregation peak (at 644 nm) and presence of only one sharp peak (at 673 nm), indicating the existence of monomer-rich Ce6 in the system. Unlike PVP, where it caused reduction in the fluorescence intensity of Ce6, the fluorescence intensity of Ce6 increased in presence of sucrose esters. This could be attributed to incorporation of Ce6 into the highly electron rich hydrophobic micellar core. Interestingly, the concentration of sucrose ester needed to induce aggregate to monomer varied significantly with the type of sucrose ester: 2 x CMC for SEL, 5 x CMC for SEM and 40 x CMC for SEP. Table 7 shows the aggregation number of the different sucrose esters.

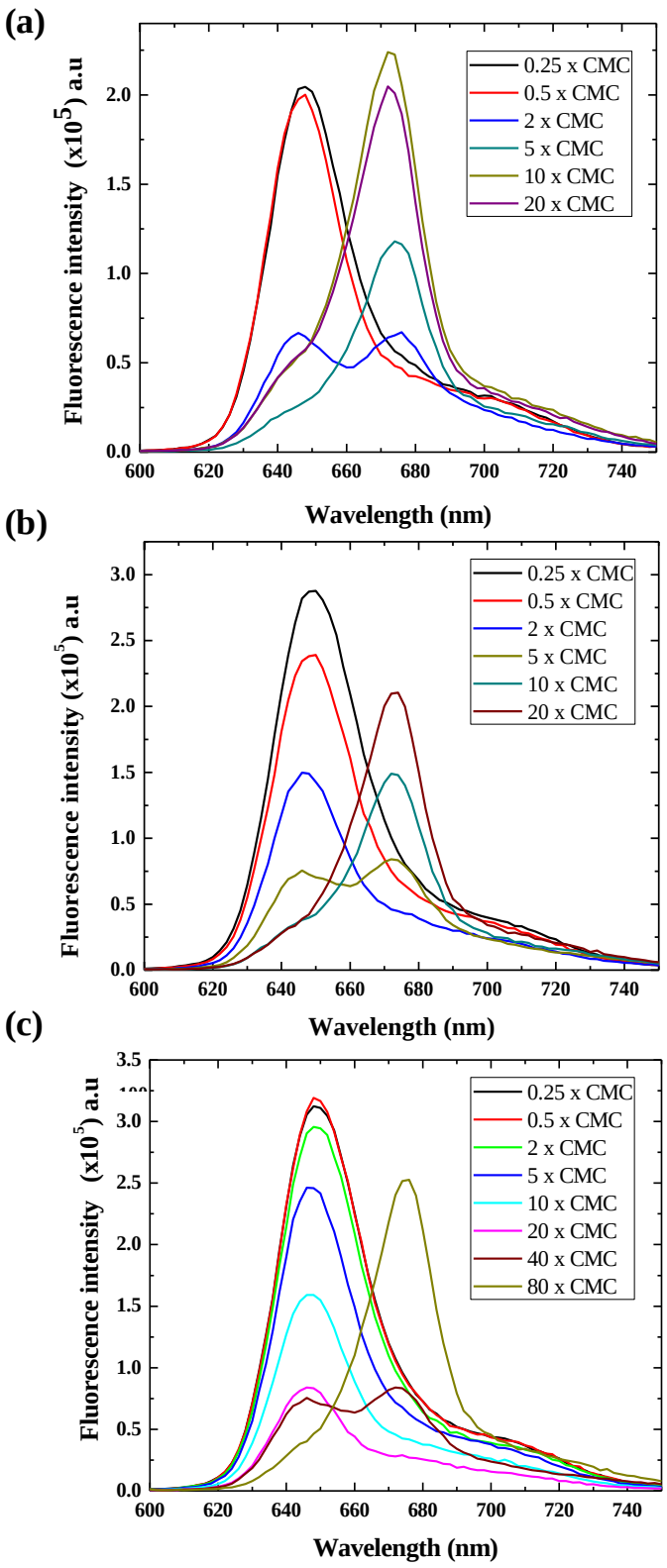

Figure 20: Fluorescence emission spectra of (a) SEL, (b) SEM and (c) SEP [concentrations are represented as a function of CMC].

Aggregation number refers to average number of surfactant molecules required to form a micelle. From Table 7, it was evident that aggregation number did not vary significantly for different sucrose esters [184]. This apparently reflects that a much higher number of micelles were required for complete disaggregation of Ce6 as the alkyl chains of sucrose esters increased and the disaggregation rank order could be SEL > SEM > SEP. However, the CMC of sucrose esters were found to vary largely and followed to decrease steeply as the alkyl chain length increases (Table 7) [184]. The large difference in CMC further reflects that there could be marginal concentration difference for disaggregation

Table 7: Properties and binding constants of sucrose esters comprising different alkyl chains

Sucrose ester	**Molecular weight**	**CMC (mM)**	**Aggregation number**	**K_b x 10^3 (Mol^{-1})**	**C_{cd} (mM)**
SEL	525	0.35	96	3.7 ± 0.2	1.75
SEM	552	0.08	122	5.1 ± 0.1	1.6
SEP	580	0.01	160	8.5 ± 0.6	0.8

K_b = binding constant.
C_{cd} = Concentration of sucrose ester required for complete disaggregation

effect for SEM and SEP compared to SEL. Therefore, it was quite evident that the low concentration of particularly SEM and SEP could not produce sufficient micelles to incorporate all the available Ce6 monomers, suggesting the need for higher concentrations (above CMC) of SEM and SEP for complete disaggregation. Therefore, the true disaggregation rank order could be SEP > SEM > SEL. This was found to be in agreement when concentration for complete disaggregation of Ce6 was quantified for different sucrose esters using PARAFAC analysis, as described in the following section.

4.A.3.3. Effect of different alkyl chains of sucrose ester on steady-state fluorescence anisotropy of Ce6

Steady-state fluorescence anisotropy values in the presence of different sucrose esters were determined. Figure 21 shows the increment in anisotropy value of Ce6 as the concentration of sucrose ester increases. Increase in anisotropy value could be ascribed to

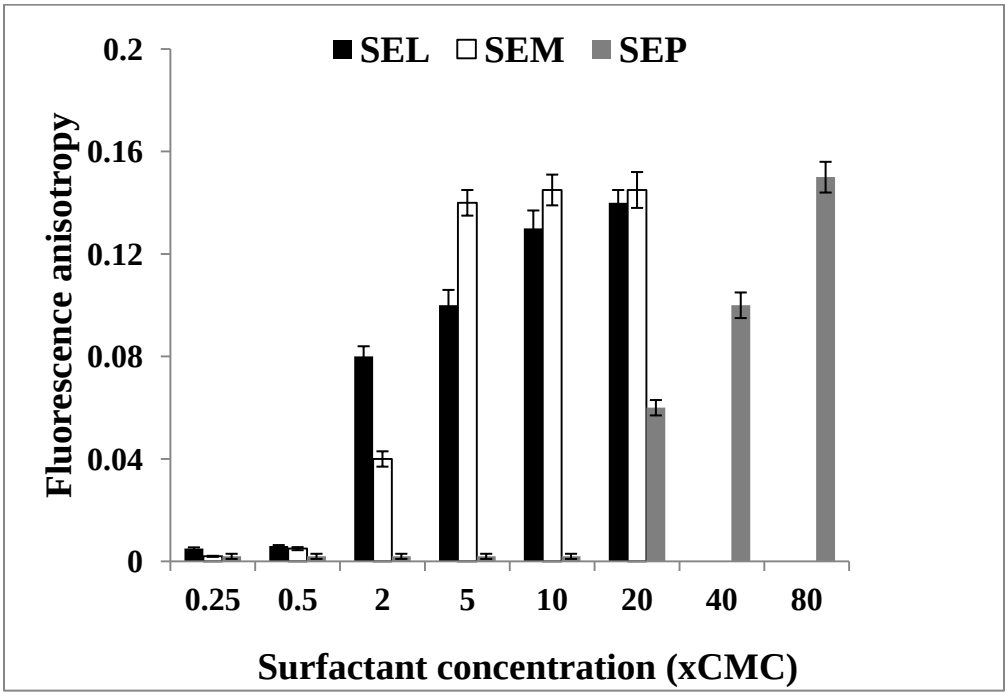

Figure 21: Variation of fluorescence anisotropy of Ce6 with varying alkyl chains of sucrose esters (n = 3).

incorporation of Ce6 monomers in the micellar core, which substantially restricted the rotational movement of Ce6. It was noted that the increase in fluorescence anisotropy for varying sucrose ester concentrations exhibited close correlation at which red shifts were observed in the fluorescence spectra. For all the three sucrose esters the steep increase in fluorescence anisotropy corresponded with the first red shift in the emission spectra. This indicates that the disruption of Ce6 aggregates was followed by the incorporation of the Ce6 monomers inside the hydrophobic micellar core.

4.A.3.4. Quantification of relative disaggregation efficiency of sucrose esters with different alkyl chain using EEM spectroscopy

EEM spectra of Ce6 were collected for each of the sucrose esters and PARAFAC algorithm was applied to determine the number and fraction of underlying species present at various sucrose ester concentrations. The initial addition of sucrose ester resulted in a decrease in fluorescence emission intensity, while a steep rise in fluorescence intensity was observed at sufficiently higher concentration. The lowering of fluorescence intensity was ascribed to further aggregation of Ce6 molecules while the steep rise in fluorescence intensity was ascribed to the incorporation of all the Ce6 molecules into the micellar core of the surfactants [152]. Such deviation of fluorescence intensities led to inaccurate determination of underlying species concentration and subsequently affected the correlation coefficient (r^a) in PARAFAC analysis for each set of data points. Therefore, concentrations of underlying species were only taken into consideration for r^a values greater than 0.95. As observed for different PVP grades, effect of sucrose esters also resulted in dissociation of Ce6 aggregates into intermediate and completely monomerized species. This was deduced from the higher average correlation coefficient of PARAFAC analysis when the number of species, *N*, was considered as 3 (r^a = 0.97) instead of 2 (r^a = 0.91. The three underlying species were pure Ce6 aggregates, intermediate Ce6 which was partially bound with sucrose ester and pure Ce6 monomers. Figure 22 shows the fractions of the three different Ce6 species in different concentrations of the sucrose esters. These fractions collectively made up 100 % of the Ce6 concentration, i.e., 50 µM.

The apparent concentration (C_{cd}) of the sucrose ester at which complete disaggregation occurred was calculated from the PARAFAC analysis and presented in Table 7. The C_{cd}

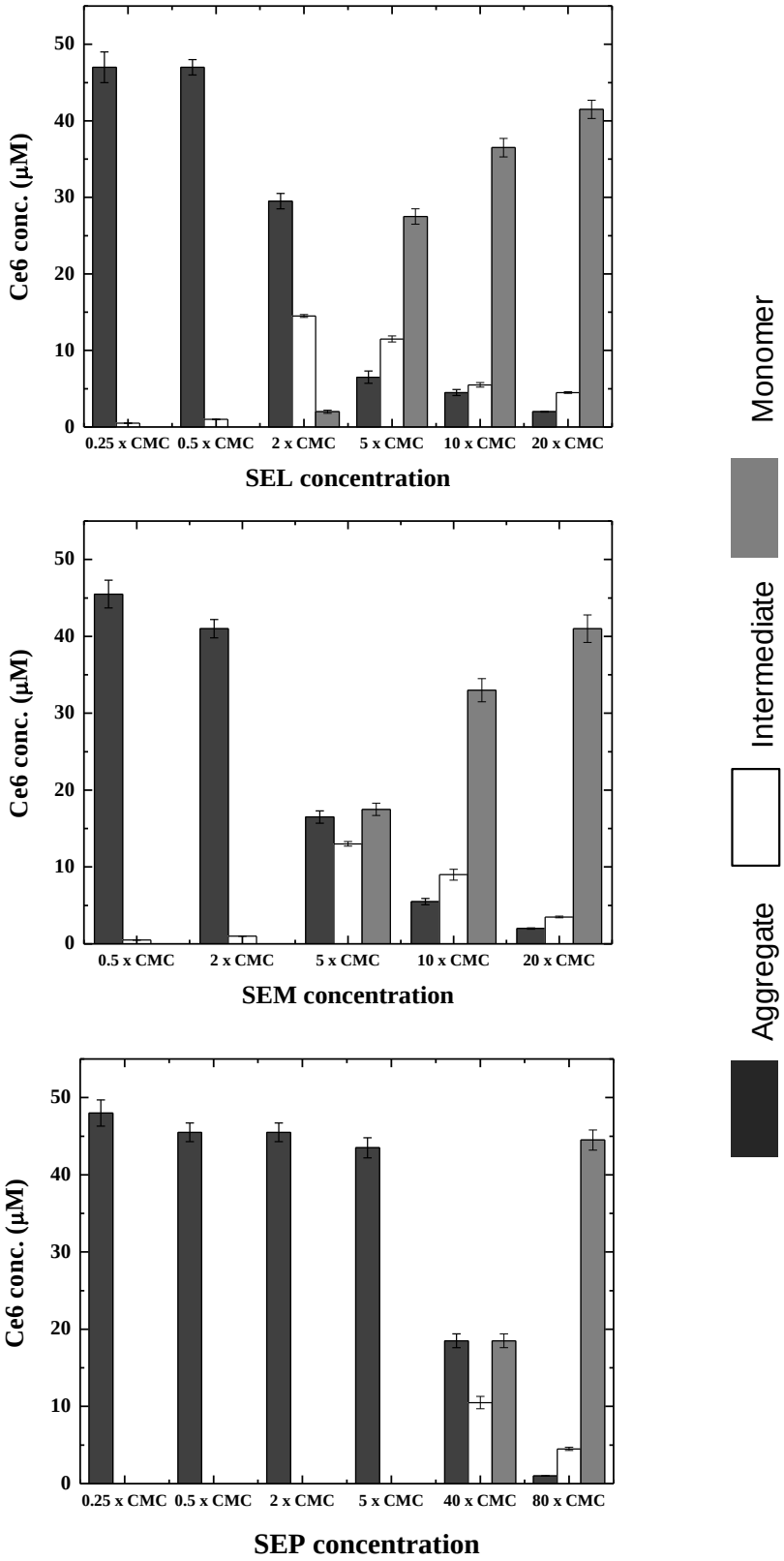

Figure 22: Fraction of different species of Ce6 present with increasing concentrations of (a) SEL, (b) SEM and (c) SEP (n = 3).

value of the sucrose esters decreased in the following order: SEL > SEM > SEP. This implies that a higher concentration of sucrose ester with shorter alkyl chain was required for complete disaggregation of Ce6. The disaggregation effect of sucrose esters could be rationalized based on micellization, which was thought to be the main driving force for disruption of Ce6 aggregates. As mentioned earlier, the CMC of sucrose esters strikingly decreased as their alkyl chain length increased. Thus, the requirement of apparently large number of micelles for SEP (80 x CMC) for complete disaggregation could be attributed to the need for complete incorporation of all the Ce6 monomers. As the CMC of SEP was much lower than SEL and SEM, it could be deduced that insufficient amount of micelles were produced at the CMC of SEP, which subsequently resulted in attainment of concentration (80 x CMC), much higher than its CMC for complete disaggregation. This also translates to the fact that the C_{cd} of SEP (80 x CMC) does not necessarily reveal the presence of large number of micelles compared to SEM and SEL indicating poor disaggregation ability of Ce6. Hence, the true rank order of disaggregation efficiency was SEP > SEM > SEL. This finding also corroborates the importance of alkyl chain length orientation at the interphase. Alkyl chain length increased from SEL to SEP resulting in reduced flexibility and better packing of surfactant molecules at the interphase, thus probably increasing the ability to retain Ce6 into the micellar core.

4.A.3.5. Binding constant of Ce6-sucrose ester complex

The binding efficiency between Ce6 and the sucrose ester with different alkyl chain length was calculated using Eq. (11). The binding constant values (K_b) are presented in Table 7. It was noted that SEP had a higher K_b value than its less lipophilic counterparts. The K_b values for the Ce6-sucrose ester were relatively lower than those reported for

Cp6-surfactant ionic interactions [152]. This could be ascribed to the presence of weak non-covalent interactions between Ce6 and sucrose esters, in comparison with the strong electrostatic interaction between Cp6 and ionic surfactants (SDS, CTAB). The K_b values for Ce6-sucrose ester decreased in the following order: SEP > SEM > SEL, indicating that sucrose ester with larger alkyl chain had higher association capability with the photosensitizer molecules, which will enhance its disaggregation efficiency.

4.A.3.6. Determination of binding mode between Ce6 and sucrose esters

The mode of interaction between Ce6 and sucrose esters was investigated using FT-IR spectroscopy and thermodynamics study. FTIR spectra of Ce6 and sucrose ester monolaurate (SEL) showed characteristic stretching and bending vibrations in the range of 400 to 4000 cm^{-1} (Figure 23). The FT-IR spectrum of freeze-dried Ce6-SEL mixture was mostly similar to that of SEL spectrum without any noticeable shift, possibly indicating that Ce6 was incorporated into the micellar core and remained in encapsulated form. This suggests that the possible binding mode was established through non-covalent interaction. This was further verified by temperature-dependent binding studies conducted at 288 K, 297 K, and 310 K respectively. The mode of binding, such as electrostatic, covalent or hydrophobic, could be assessed from the changes in enthalpy and entropy of the system as mentioned in section 4.A.2.5. The binding constant values obtained at different temperatures using Eq. (11) were fitted into Van't Hoff's Eq. (12) and the variations of enthalpy (ΔH) and entropy (ΔS) in the system were estimated. The values of ΔG, ΔH and ΔS for Ce6-sucrose ester system at three different temperatures are shown in Table 8. The interaction between Ce6 and sucrose esters was spontaneous as indicated by negative ΔG values. The positive values for ΔH and ΔS suggest that the

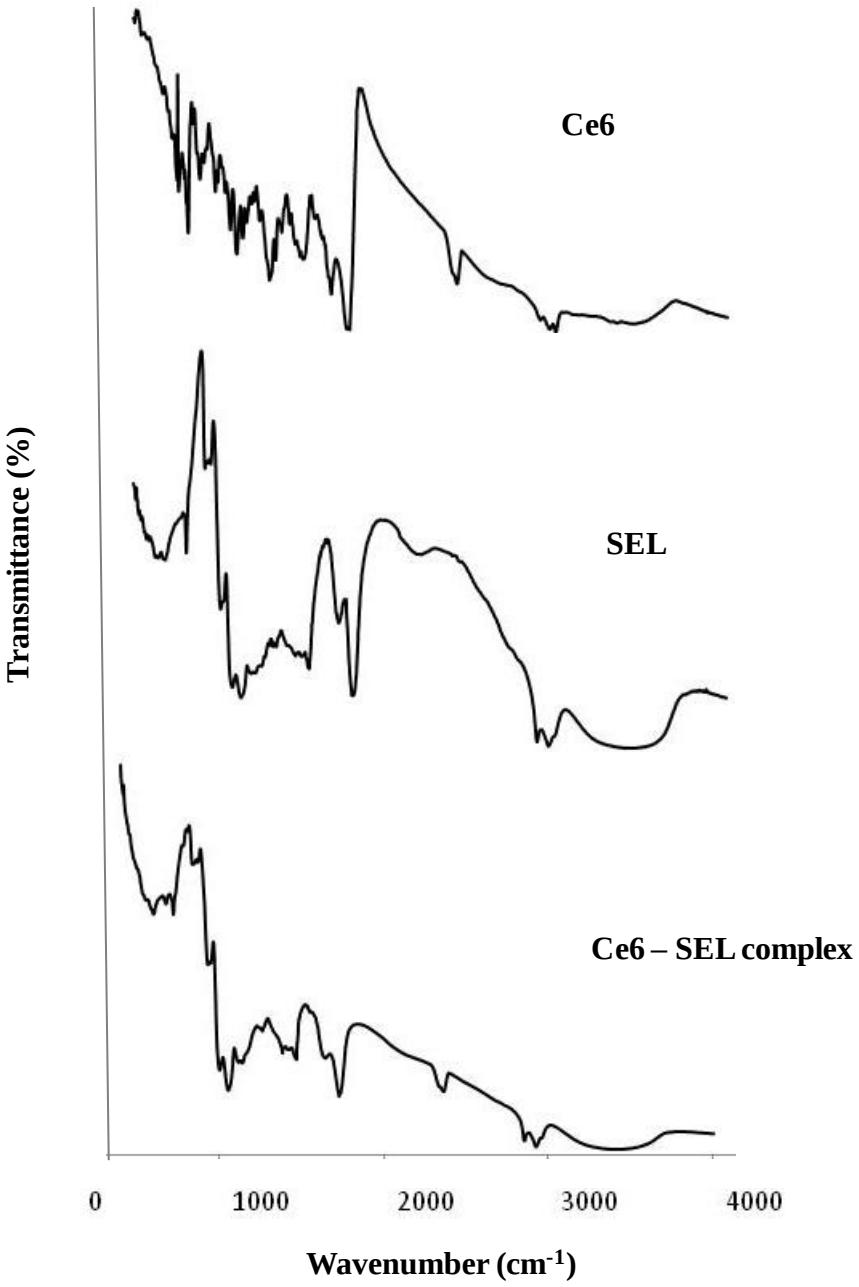

Figure 23: FTIR spectra of pure Ce6, sucrose monolaurate and their freeze dried mixture.

binding was largely favoured by non-covalent hydrophobic interaction. Similar trends (negative values) were observed for ΔH and ΔS values in case of SEM and SEP, corroborating the evidence of hydrophobic interaction between Ce6 and sucrose esters.

Hence, the findings suggest that the Ce6 monomers were predominantly present in the hydrophobic micellar core of the sucrose esters.

Table 8: Thermodynamic parameters for binding of Ce6 with sucrose esters of different alkyl chains

Sucrose esters	ΔG, 288 K ($kJ\ mol^{-1}$)	ΔG, 297 K ($kJ\ mol^{-1}$)	ΔG, 310 K ($kJ\ mol^{-1}$)	ΔH ($kJ\ mol^{-1}$)	ΔS ($kJ\ mol^{-1}T^{-1}$)
SEL	-2120	-2422	-3025	486.2	36.1
SEM	-2143	-2626	-3311	498.4	37.5
SEP	-2866	-3638	-4024	537.1	42.2

4.A.3.7. Simulation of disaggregation effect of sucrose esters on Ce6 aggregates using DPD model

The disaggregation action of sucrose esters on Ce6 aggregates was further investigated by dissipative particle dynamics (DPD), a coarse grain simulation model [185]. In this study, the disaggregation potential of the different sucrose esters was evaluated on the basis of varying hydrophobic chain lengths using the DPD model. The model assumes that surfactant molecules near its critical micelle concentration disperses the Ce6 aggregates and eventually incorporate Ce6 monomers into the micellar core. All the components of each sucrose ester-Ce6 system, such as S1, L1, M1, P1, W1 and C1 were designated by beads (Figure 24). As mentioned in the methodology section, the distinct hydrophobic and hydrophilic groups of the sucrose ester were each designated by a bead, resulting in each surfactant molecule represented by 2 beads. The degree of interaction between

different beads was determined by deriving their FH parameter. These were calculated using COMPASS force field and shown in Table 9. FH parameter, also known as DPD

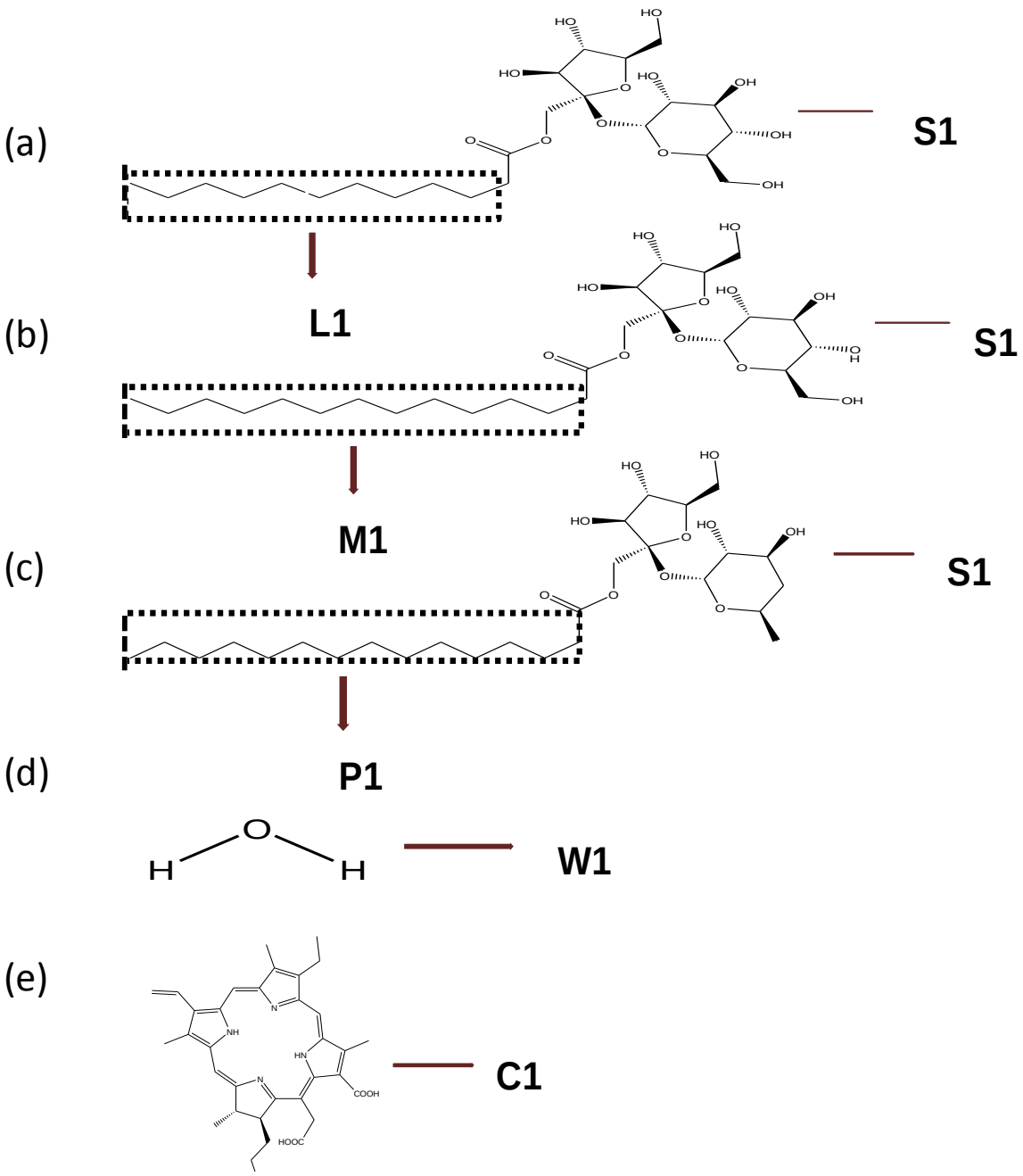

Figure 24: Notation of different components for DPD simulation: (a) SEL [L1 – lauric acid, S1 – sucrose], (b) SEM [M1 – myristic acid], (c) SEP [P1 – palmitic acid], (d) water and (e) Ce6.

input parameters (χ_{ij}) indicates the relative affinity between two dissimilar beads. The value of FH parameter is high when two beads, *i* and *j* are incompatible while $a_{ij} \leq 0$ suggests excellent compatibility between two beads.

Table 9: DPD input parameters of different beads designating sucrose ester, Ce6 and water

	S1	**L1**	**M1**	**P1**	**C1**	**W1**
S1	0	-	-	-	-	-
L1	24.88	0	-	-	-	-
M1	33.17	-	0	-	-	-
P1	57.97	-	-	0	-	-
C1	73.28	47.38	108.9	140.9	0	-
W1	14.3	26.59	38.65	74.92	246.9	0

Figure 25 shows the snapshots of each of the sucrose ester-Ce6 system with increasing sucrose ester concentration at the end of 20,000 simulation steps. The water molecules were discarded from the simulation box to provide a better understanding of the underlying interaction between Ce6 and the sucrose esters. As can be seen from Figure 25, the Ce6 monomers were incorporated into the micelles as the surfacatant concentration increased. At the highest surfacatant concentration corresponding to complete disaggregation (C_{cd}), no free Ce6 aggregates (denoted by blue) were observed indicating that all the molecules were incorporated into the micellar core. As can be seen from the snapshots, a relative reduction in number of surfactant molecules (red and green

beads) were observed as the alkyl chain length of sucrose esters increased. This clearly suggests that significantly lesser amount of micelles were produced as the alkyl chain length of sucrose esters increased due to their low CMC values, as described earlier. The produced micelles therefore could not accommodate all the Ce6 present in the system,

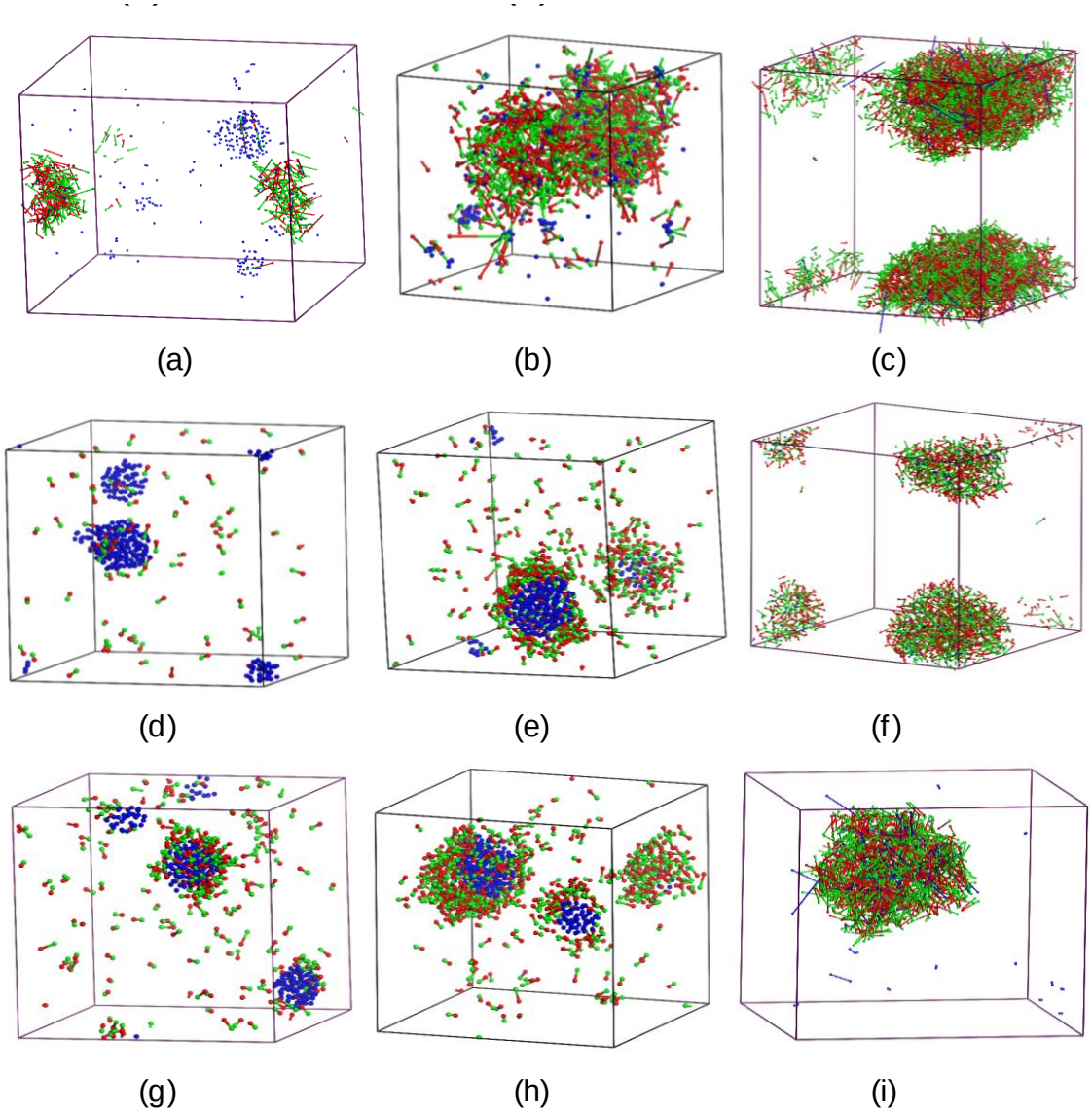

Figure 25: Snapshots of DPD simulation for various systems, (a) to (c) SEL and (d) to (f) SEM at 0.5, 2, 20 x CMC respectively, (g) to (i) SEP at 20, 40, 80 x CMC. [surfactant head and tail: green and red, Ce6: blue].

which aptly explains the requirement of relatively higher concentrations of SEP (80 x CMC) compared to SEM (5 x CMC) and SEL (2 x CMC) for complete disaggregation. At this concentration of SEP, the availability of micelles significantly increased resulting in complete disaggregation and the proposed disaggregation rank order was valid.

Figure 26 shows the diffusion coefficient of Ce6 in the presence of different sucrose esters at their maximum concentration employed. Diffusion coefficient is an important DPD response parameter, which could be utilized to illustrate the effect of various surfactants on Ce6 aggregates. The effect of diffusion coefficient on Ce6 disaggregation could be explained on the basis of Stokes-Einstein equation as given below [186]:

$$D = \frac{k_B T}{6\pi\delta r_c} \qquad \textbf{\textit{Equation}}\ (31)$$

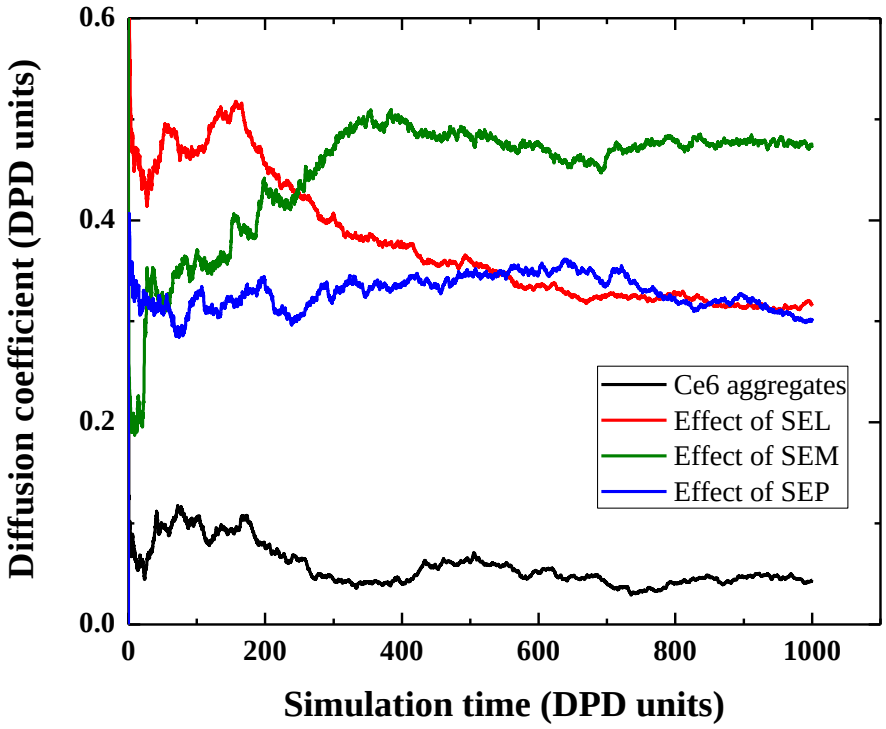

Figure 26: Variation of diffusion coefficients of Ce6 for different sucrose esters at their corresponding C_{cd}.

where D is the diffusion coefficient at temperature T, r_c is the radius of diffusing molecule, δ is the viscosity of the medium and k_B is the Boltzmann constant. Assuming a non-significant increase in viscosity of the aqueous phase on increasing sucrose ester concentration in the millimolar range, diffusion coefficient is inversely related to the radius of the diffusing molecule. Figure 26 shows the lowest diffusion coefficient was that obtained for Ce6 aggregates alone. Addition of sucrose ester to Ce6 resulted in 3-5 times increase in the diffusion coefficient at the end of the simulation run, indicating disaggregation of Ce6 aggregates to form entities with smaller hydrodynamic radius.

Another important DPD response parameter is the root mean square (RMS) end-to-end distance ($<h^2>^{1/2}$) of the sucrose ester molecule at various stages of the simulation period. As the disaggregation of Ce6 aggregates was preferentially occurred at micellar concentration range, it could be speculated that molecular orientation of surfactants at and above critical micelle concentration might have affected the ordering of the alkyl chains at the interphase as well as the disaggregation efficiency of the surfactants. RMS end-to-end distance is a concept, which describes the degree of curliness of a polymer chain [185]. For the same polymer chain, the RMS end-to-end distance will be reduced if the chain curves instead of being straight. For surfactant model, $<h^2>^{1/2}$ denotes the total linear length of the surfactant molecule, which mostly comprises the length of the hydrocarbon chain. Figure 27 shows the variation of end-to-end distance of the sucrose esters at different concentrations. The end-to-end distance for SEL at concentrations below CMC was fairly constant. It increased markedly at CMC and tended to level off at higher concentrations. The same trend was observed for SEM and SEP. The greater end-to-end distance of the sucrose ester molecule at and above CMC suggests a tightly packed

and orderly arrangement of the molecules to form the micelles. In such a situation, there would be reduced conformational mobility of the alkyl chains [187]. As can be seen from Figure 27, a significant increase in $\langle h^2 \rangle^{1/2}$ was noticed at CMC and concentrations equivalent to (10-20) x CMC (for all the sucrose esters), above which no further increase in $\langle h^2 \rangle^{1/2}$ was observed. Therefore, the ordering of surfactant molecules at the interphase was mostly completed in that concentration range. Thus, it could be rationalized that such

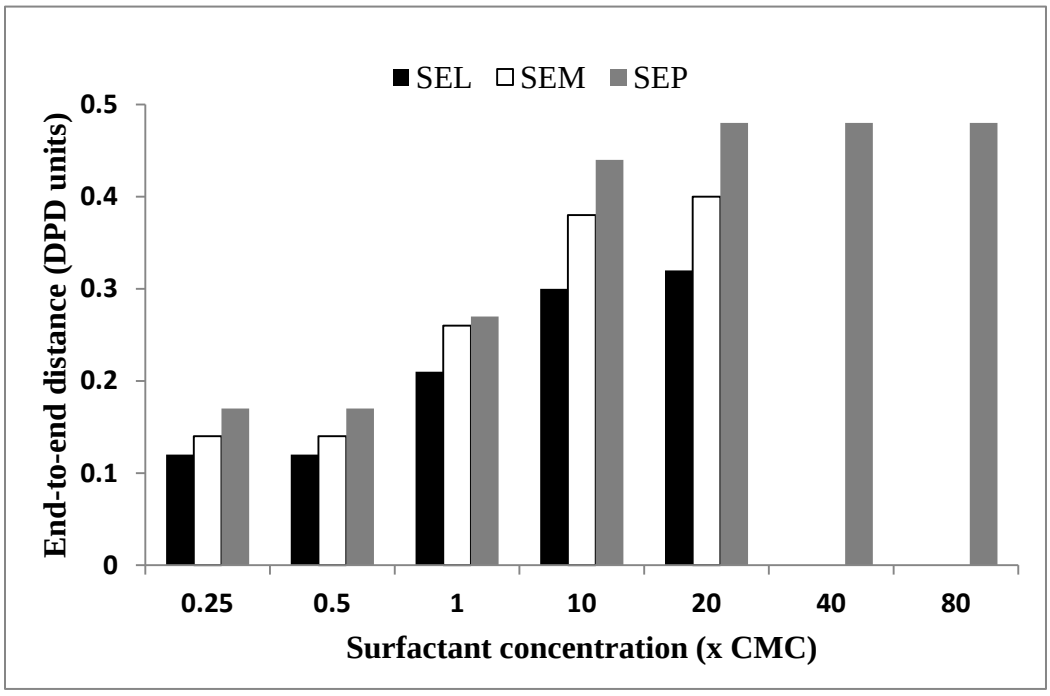

Figure 27: Variation of end-to-end distance of different sucrose esters with their increasing concentrations.

orientation facilitated the disaggregation efficiency by increasing the ability to retain Ce6 at the core due to increased micellar volume. This was supported by the findings of Kawaguchi et al. (1991) on structural studies of a homologous series of sucrose ester micelles [188]. The study revealed that the volume of the micellar core was higher in case of SEP due to increase in alkyl chain length. In addition, it was reported that due to

difference in alkyl chain packing orientations, SEP micelles had prolate (ellipsoidal) shape where SEL and SEM micelles had oblate (spherical) shape. Considering the fact that being a larger molecule (7.2 Å), the retention of Ce6 monomers in the SEP micelles could have been more favoured than its counterparts.

4.A.3.8. Summary

The studies in this section demonstrated the disaggregation behaviour of sucrose esters of different alkyl chain length on Ce6 aggregates. Ce6-surfactant interaction was visualized at the molecular level using DPD coarse grain simulation, findings of which were in good agreement with the experimental observation. Disaggregation efficiencies of sucrose esters were illustrated with the use of PARAFAC algorithm employing EEM spectroscopic methods. The results showed that disaggregation ability was significantly increased on increasing alkyl chain length of sucrose esters, based on the consideration that lesser amount of SEP was required than SEM and SEL as their CMC value steeply decreased. Sucrose esters with longer alkyl chains might have better capacity to retain Ce6 at the core due to enhanced conformational rigidity and less leakage. The rank order of relative disaggregation efficiency was SEP > SEM > SEL. Overall, the study established the useful application of a novel multivariate technique to quantify the extent of disaggregation by sucrose esters of varying alkyl chains, while the DPD model served as a visualization tool to illustrate the mode of Ce6-sucrose ester interaction.

4.A.4. Photodynamic efficacy of various Ce6-disaggregating agent formulations

4.A.4.1. Overview

The influences of different factors, such as pH and Ce6 concentration, and pharmaceutical adjuvants, such as PVP and sucrose esters, on Ce6 aggregation have been investigated. The present section focuses on the photodynamic efficacy of various Ce6-disaggregating agent formulations in terms of *in vitro* singlet oxygen generation, intracellular uptake and anti-proliferative activity. Different liquid formulations comprising Ce6 with disaggregating agents were prepared for investigation using human oral squamous carcinoma (OSC) cells as tumour xenograft model.

4.A.4.2. *In vitro* singlet oxygen generation

The photodynamic efficacy of different Ce6-disaggregating agent formulations was first investigated in terms of *in vitro* singlet oxygen generation. As the optimal PDT effect is largely dependent on the singlet oxygen production which kills the tumour cell, this study was highly significant. The extent of singlet oxygen production was measured by the concomitant decrease in RNO absorbance, where the labile nitroso group (of RNO) is converted to nitro group in presence of oxygen. Thus, upon irradiation by laser, singlet oxygen species were generated by Ce6, which immediately converted the oxygen-sensitive p-nitrosoaniline (RNO) to more stable p-nitroaniline. This would reduce the absorbance of RNO. Therefore, the latter could be used to indicate the singlet oxygen generation by Ce6. Based on the findings of earlier disaggregation studies, PVP K17 and sucrose monopalmitate (SEP) were selected for use. All the formulations were prepared at pH 5 to simulate the *in vivo* tumour physiological environment. The

Ce6:disaggregating agent ratios employed in the formulations were similar to those used in the earlier disaggregation studies. Figure 28 shows the reduction of RNO absorbance by the action of singlet oxygen species generated by Ce6 in the presence of different

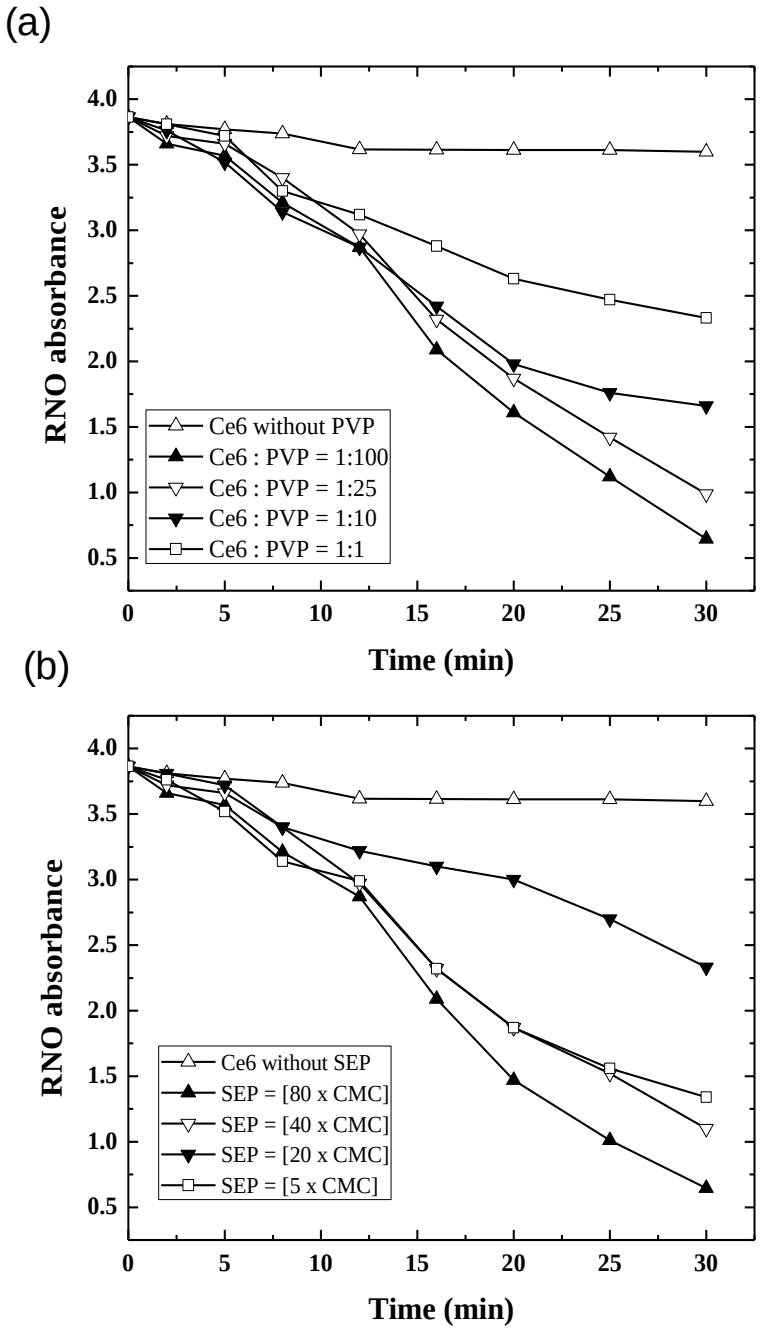

Figure 28: Singlet oxygen generation efficiency of Ce6 in the presence of different concentrations of (a) PVP K17 and (b) SEP.

concentrations of PVP K17 and sucrose esters, using pure Ce6 as control. As the concentration of PVP K17 and SEP increased, the monomeric Ce6 fraction increased, which significantly enhanced the singlet oxygen generation efficiency leading to oxidation of the nitroso group of RNO.

4.A.4.3. Intracellular uptake of Ce6 from various formulations

Solutions with varying ratios of disaggregating agent to Ce6 were prepared to assess the cellular uptake of Ce6 by OSC cells. The formulations were designated by codes and their corresponding components are shown in Table 10. Figure 29 shows the trend of Ce6

Table 10: Composition of various Ce6-disaggregating agent formulations

Disaggregating agent (C_1)	**Codes**	**Amount of Ce6 (C_2)**	**Ce6: disaggregating agent (C_2: C_1) (w/w)**
SEP [a]	SEP 1	50 μM	50 μM : [20 x CMC]
	SEP 2	50 μM	50 μM : [40 x CMC]
	SEP 3	50 μM	50 μM : [80 x CMC]
PVP [b]	PVP 1	50 μM	1:10
	PVP 2	50 μM	1:100
	PVP 3	50 μM	1:1000

[a] *Molecular weight = 580*
[b] *Molecular weight = 10000*

uptake from different formulations over a period of 24 hr. The control consisted of Ce6 without any disaggregating agent. As can be seen, from Fig. 29, cellular uptake of both Ce6 formulations consisting of PVP or SEP increased gradually from 4 hr to 24 hr as that

of the control. However, the cellular uptake by the PVP or SEP formulations were higher at specific concentrations of the adjuvants employed. The highest cellular uptake (6.4 µg)

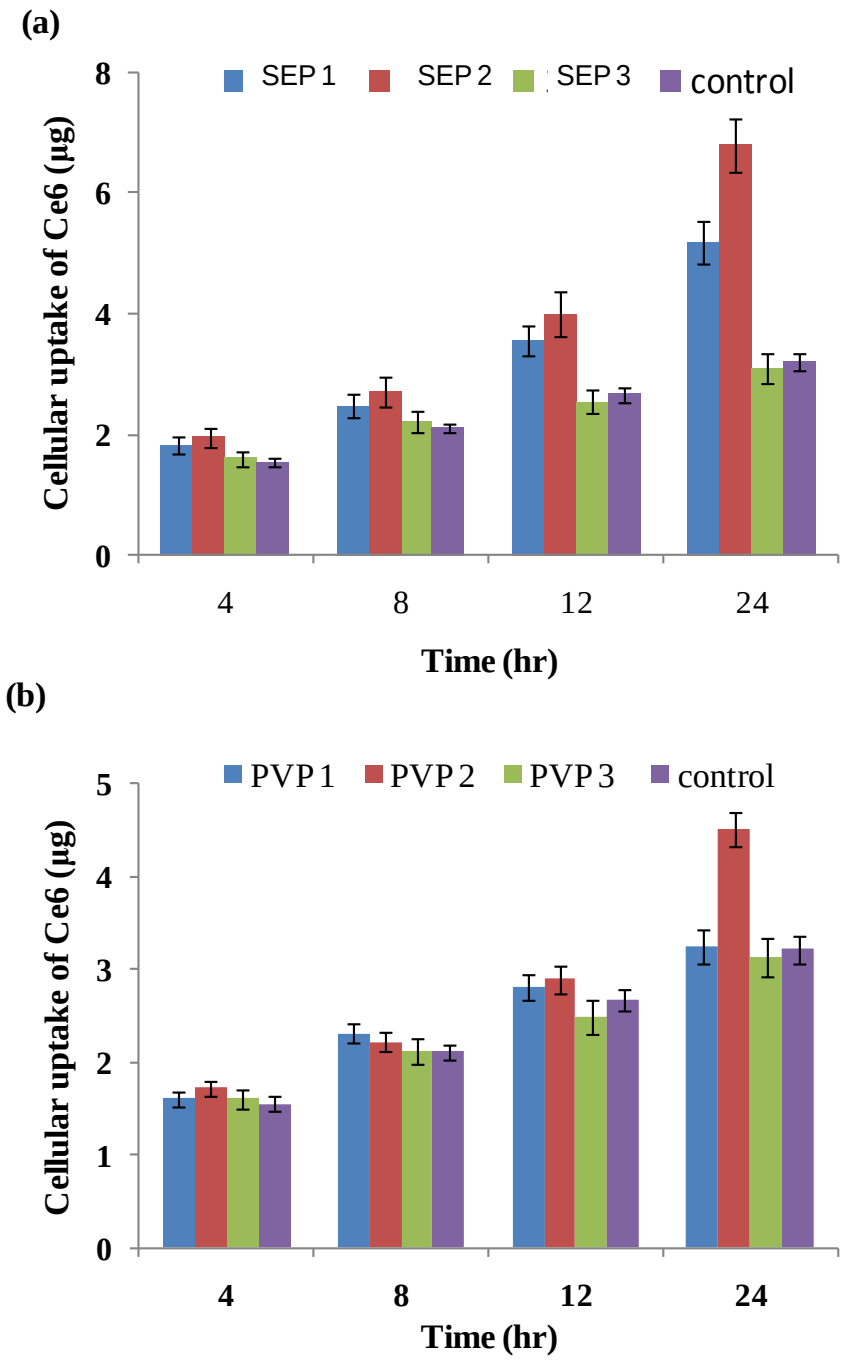

Figure 29: Uptake of Ce6 by OSC cells from formulations consisting of (a) Ce6-SEP and (b) Ce6-PVP K17 (n = 6).

was demonstrated by SEP at a concentration of [40 x CMC]. The uptake of Ce6 was almost double that of the control (3.32 μg). This could be attributed to the disaggregation of Ce6 and entrapment of Ce6 in the micelles. Studies showed that the lectin present in the cell surface aids in internalization of sugar-based derivatives, while the highly lipophilic plamityl chains could easily permeate through the cell membrane resulting in enhanced uptake capasity [189]. However, the uptake of Ce6 was slightly reduced at higher SEP concentration [80 x CMC], which could be due to high concentration of SEP affecting the cell membrane and the uptake of Ce6.

Formulations with different PVP concentrations also showed gradual increase in cellular uptake, which was comparable to that of the control. However, significantly higher uptake (4.88 μg) was demonstrated by the formulation consisting Ce6:PVP ratio of 1:100. PVP has been reported to possess mucoadhesive property which may aid in drug attachment to cells thereby promoting drug uptake [190]. However, insignificant difference (p-value) in Ce6 uptake was observed between the control and the PVP 2 formulation. Further increase in PVP concentration at a Ce6:PVP ratio of 1:1000 (PVP 3 formulation), where all the aggregates virtually exist as PVP-bound monomerized species, the uptake value fall to 3.3 μg, similar to that of pure aggregates. This could be attributed to increasing hydrophilicity of the Ce6-PVP complex which slowed down the extent of uptake. Additionally, high PVP concentration would have increased the viscosity of the PVP 3 formulation and might have a negative impact on cellular uptake [191]. The substantial cellular uptake by aggregates (control) is not surprising as it could be ascribed to high lipophilicity of parent Ce6 molecule in the acidic pH environment of the OSC cells. Considering the fact that aggregates are joined together by weak

hydrophobic force, a substantial Ce6 uptake would have been possible in the form of monomers, which might had dissociated from the aggregates at the lipophilic boundary of the cell membrane. Considering SEP 2 and PVP 2 formulations, lesser amount of adjuvants was required for SEP 2 as can be seen from Table 10. Thus SEP was more useful than PVP in promoting Ce6 uptake.

4.A.4.4. Anti-proliferative activity of Ce6-disaggregating agent formulations

Various formulations consisting of different concentrations of Ce6 (1-25 μg/mL) at constant PVP K17:Ce6 (100:1) or constant SEP concentration (40 x CMC) were prepared. The anti-proliferative activity of the formulations was evaluated by MTT assay. The latter is a simple *in vitro* method for determining cell viability by photometric measurements. The yellow tetrazolium MTT (3-(4,5-dimethylthiazolyl-2)-2,5-diphenyltetrazolium bromide) would be reduced by metabolically active cells, in part by the action of dehydrogenase enzymes, to form purple-coloured crystals known as formazan. The Formazan crystals would dissolve in the solvent, DMSO, used in the method and the absorbance of the resultant was determined. A higher absorbance of the formazan solution indicates greater cell viability or lower anti-proliferative activity of the test formulations [192]. The anti-proliferative activity of different Ce6 formulations was calculated as described by Eq. (27). The IC_{50} values of the control, Ce6-PVP K17 and Ce6-SEP formulations were calculated using Graph Pad Prism (version 5; CA, USA) for the purpose of comparing their anti-proliferative activity.

For all the formulations, Ce6 had little effect on the cell viability when the cells were kept in the dark, implying that the inactivated Ce6 was non-toxic in the dark condition.

After irradiation, cell viability in the different formulations decreased to varying extent. The anti-proliferative activities of different test formulations are shown in Figure 30. The

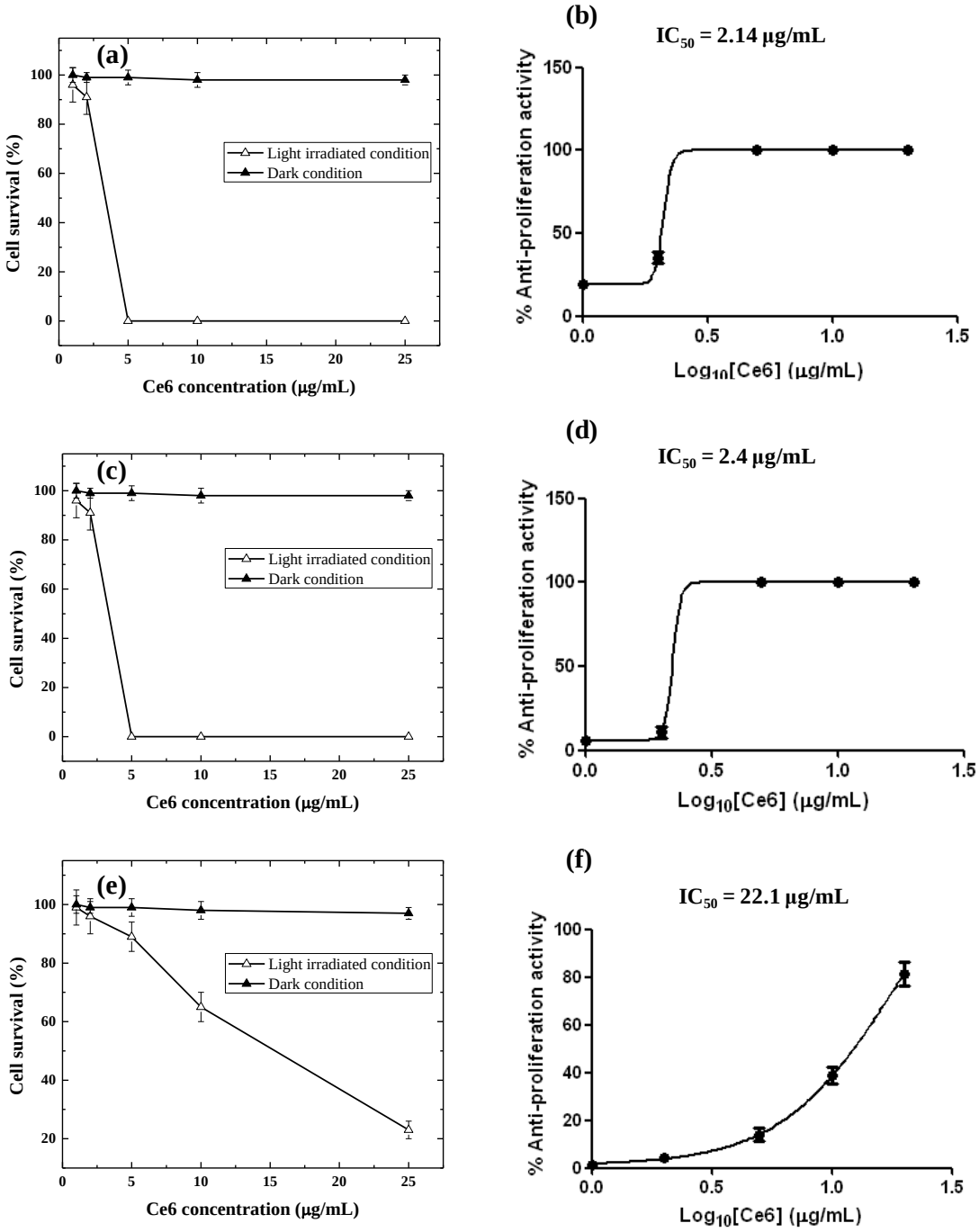

Figure 30: Percent cell survival and corresponding anti-proliferative activity of Ce6-SEP2 formulation (a - b), Ce6-PVP2 formulation (c - d) and control (e - f) (n = 6).

IC_{50} values were found to decrease in the following order: SEP (2.14 μg/mL) < PVP (2.4 μg/mL) << aggregates (22.1 μg/mL). Formulations containing SEP and PVP K17 clearly showed potent anti-proliferative activity as indicated by their IC_{50} values, which were approximately 10 times less than that of the control. Collectively, the results confirmed the disaggregation action of PVP K17 and SEP, enabling the production of monomer-rich Ce6 which is largely responsible for the PDT activity of Ce6. The high IC_{50} value (22.1 μg/mL) of the control suggests that the Ce6 in the control was mostly aggregated with little anti-proliferative activity. Thus, aggregation of Ce6 reduced the generation of singlet oxygen species, which explains the higher concentrations of Ce6 needed to destroy the OSC cells. Hence, anti-proliferative activity was mostly associated with efficiency of singlet oxygen generation but not solely dependent on the extent of cellular uptake.

4.A.4.5. Summary

The studies in this section investigated in vitro photodynamic efficacy of Ce6 formulations with disaggregating agents such as PVP K17 and SEP. High singlet oxygen generation was detected in the formulations, along with enhanced cytotoxic potentials. Although the intracellular uptake of these formulations differed significantly and found to be substantially high than the pure aggregates in certain cases. The suitable properties of SEP and PVP facilitated higher uptake efficiency than the aggregates. The results also suggested that it is not necessarily the intracellular uptake but the extent of singlet oxygen generation, which was the rate-limiting step for PDT-induced cell death. Therefore, it could be postulated that a fair balance between lipophilicity and monomer-rich Ce6 species is highly required to produce the optimum photodynamic efficacy. The excellent

in vitro photodynamic efficacy of Ce6-PVP and Ce6-SEP formulation further warrants their suitable application as drug carrier for delivery of Ce6. The studies also reflected the importance of singlet oxygen generation for cytotoxic activity, however additional studies are required to elaborate the type of photochemical transformation (Type 1 or Type 2) encountered to elicit anti-proliferative action on OSC cells.

4.B.1. Dissolution enhancement of Ce6 by formulating into sucrose ester-based nanosuspension

4.B.1.1. Overview

The useful properties of sucrose esters have been illustrated in the earlier section, which could be successfully utilized in preparing a delivery system for Ce6. High disaggregation along with high intracellular uptake of Ce6 brought about by the sucrose esters rendered them an ideal choice as drug carrier for Ce6. Therefore, it was postulated that an optimal sucrose ester-based formulation could substantially enhance the *in vitro* dissolution of Ce6 along with substantial accumulation of Ce6 in OSC cells. In addition, Ce6 would be expected to exist mostly as monomeric species, thus providing high photodynamic activity. With this hypothesis, the production of Ce6-sucrose ester nanosuspension was investigated using a central composite design, where different formulation factors were varied to optimize the particle size, zeta potential, encapsulation efficiency (EE) and *in vitro* drug release of the nanosuspensions. The PDT activity of the optimized formulations in OSC cells was further investigated in terms of singlet oxygen generation and cytotoxic potential.

4.B.1.2. Preparation of Ce6-sucrose ester nanosuspension

Sucrose ester is a group of non-ionic surfactants synthesized by esterification of sucrose with fatty acid. Sucrose esters were found to be useful in the formulation of microemulsion and transdermal-based dosage forms. In addition, these glyco-conjugated compounds were found to aid cellular uptake owing to their cell-compatible sucrose moiety, while the alkyl chains of different lipophilicity also facilitated efficient cellular uptake [158-160, 189]. In the earlier studies, sucrose esters were found to be capable of

disrupting the Ce6 aggregates, followed by entrapment of the Ce6 monomers in the micellar core. Li et al. (2011) proposed that a combination of sucrose esters was more effective than a single sucrose ester in the preparation of nanosuspension, as the combination offers a fair balance between hydrophilicity and lipophilicity facilitating desirable drug release characteristics [193]. In the present study, a modified hot-melt emulsification process was employed to prepare a sucrose ester-based nanosuspension where the Ce6 was encapsulated in sucrose ester matrix. Upon contact with the dissolution medium, the sucrose esters would gradually dissolve. As sucrose esters are basically modified surfactants, their dissolution at concentrations above CMC would produce micelles, in which Ce6 would remain as monomeric species. Therefore, the modified nanosuspension approach employed would fulfill two important objectives, namely enhancing the dissolution and preventing the aggregation of Ce6. Sucrose monolaurate (SEL) was fairly water-soluble, while sucrose ester monopalmitate (SEP) had partial aqueous solubility at room temperature. Thus, although the presence of excess SEL potentiates faster dissolution of the sucrose ester matrix, it could instantaneously be solubilized during the formulation preparation and result in partitioning of the drug to the aqueous phase. Therefore, using SEL-rich sucrose ester matrix, the encapsulation efficiency of the formulation would be generally low. Therefore, in order to achieve balance between encapsulation efficiency and *in vitro* dissolution, a combination of SEL and SEP was used in the formulation. The influence of varying ratios of SEP to SEL with a fixed total weight (200 mg) was investigated. In the design model, a higher proportion of SEP with respect to SEL was used to increase the encapsulation efficiency of Ce6. A mixture of dichloromethane (DCM) and acetone (AC) were used as organic phase in the

preparation of hot-melt emulsion. Ce6 was readily soluble in DCM. Being immiscible with water, DCM would be dispersed as droplets in the aqueous phase. Several studies have suggested that a mixture of miscible and immiscible solvents often increase the emulsification efficiency by controlling the diffusivity of the solvent [194]. Acetone (AC) is an example of a volatile miscible solvent. When the drug is dissolved in a volatile miscible solvent dispersed in an aqueous medium, the solvent would aid in diffusion of the drug into the aqueous medium, where the drug would precipitate as nanoparticles. It was therefore postulated that a combination of miscible and immiscible solvents could be employed to prepare a nanosuspension with desired characteristics. This is because of the fact that solvent evaporation of the immiscible solvent (DCM) is a controlled procedure, which could generate uniform small-sized particles, while the diffusion of miscible solvent (AC) is generally rapid and could precipitate particles of larger size fractions [195]. Therefore, the proportion of DCM to AC was varied with a fixed total volume of 5 mL in the present study. The maximum drug loading and encapsulation efficiency were also investigated by varying the concentration of Ce6 used. Thus, factors such as SEP to SEL ratio (X_1), amount of Ce6 (X_2) DCM to AC ratio (X_3) and were designated as independent variables in the central composite design (CCD) model employed. These factors were varied over 5 levels. The CCD model was chosen over other statistical models, such as box behnken design, because it allows more number of levels to precisely investigate the effects of the above-mentioned factors on formulation characteristics. Figure 31 depicts the schematic diagram for the preparation of SEP/SEL-Ce6 NS. An O/W emulsion was initially formed by addition of DCM/AC mixture containing SEP/SEL and Ce6 to the aqueous phase preheated at 60˚C. This primary

emulsion was then immediately poured into a large volume of ice-cold water to facilitate the precipitation of SEP/SEL to stabilize the nanosized droplets produced. The AC in the nanosized droplets would diffuse rapidly into the aqueous phase, while DCM would gradually evaporate. The diffusion/evaporation of AC/DCM would further cause the precipitation of SEP/SEL and Ce6, as well as the formation of pores on the surface of the sucrose ester matrix. The latter effect could additionally aid to enhance the dissolution potential of SEP/SEL-Ce6 NS.

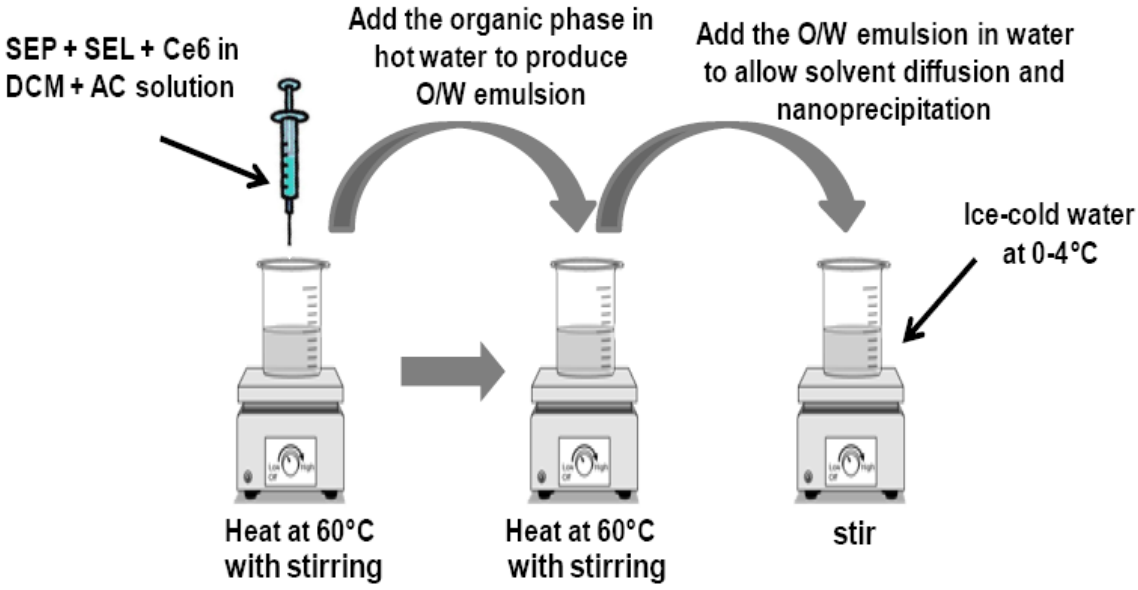

Figure 31: Schematic diagram of modified hot-melt emulsification method for the preparation of SEP/SEL-Ce6 nanosuspension.

4.B.1.3. Evaluation of central composite design results

4.B.1.3.1. Particle size (Y_1)

The average experimental results from the joint effects of the three independent variables on the particle size of SEP/SEL-Ce6 NS are shown in Table 11. The mean particle size (Y_1) of the NS formulations varied from 76 nm to 304 nm indicating that the particle size was affected by the different levels of independent variables. The smallest mean particle

Table 11: Observed responses in central composite design for SEP/SEL-Ce6 NS

Batch	Independent variables			Dependent variables			
1	X_1	X_2 (mg)	X_3	Y_1 (nm) ± SD	Y_2 (mV) ± SD	Y_3 (%) ± SD	Y_4 (%) ± SD
1	7.20	12.09	3.24	187.4 ± 8	-21.3 ± 2.8	86 ± 6.4	132 ± 6.4
2	1.91	12.09	3.24	107.2 ± 4	-16.5 ± 2.2	50 ± 3.1	134 ± 5.5
3	7.20	32.91	3.24	199.4 ± 6	-20.1 ± 1.7	69 ± 4.4	106 ± 3.2
4	0.11	22.50	2.13	76 ± 4	-11.6 ± 1.1	36 ± 3.2	94 ± 5.4
5	1.91	12.09	1.01	118.2 ± 6	-14.6 ± 1.6	43 ± 3.6	138 ± 2.9
6	1.91	32.91	3.24	95.5 ± 4	-12 ± 1.4	45 ± 4.2	121± 6.8
7	1.91	32.91	1.01	107.4 ± 8	-13.2 ± 2	37 ± 5.7	111 ± 12.4
8	4.55	22.50	2.13	232.4 ± 6	-18.1 ± 2.1	68 ± 4,1	138 ± 11
9	4.55	22.50	4.00	184.7 ± 9	-18.7 ± 2.1	77 ± 3.1	143 ± 9.7
10	4.55	40.00	2.13	237.5 ± 11	-17.7 ± 2.3	56± 4.9	125 ± 12.1
11	7.20	12.09	1.01	282.3 ± 14	-19.1 ± 2	66 ± 5.1	120 ± 9.8
12	9.00	22.50	2.13	266.7 ± 12	-22 ± 2.3	62 ± 3.4	173 ± 6.2
13	7.20	32.91	1.01	304.3 ± 17	-20.4 ± 2.2	56 ± 3	111 ± 8.3
14	4.55	22.50	2.13	224.2 ± 11	-19.2 ± 1.6	69 ± 4.3	146 ± 11.4
15	4.55	22.50	0.25	262.7 ± 13	-18.7 ± 1.3	59 ± 6.3	141 ± 12.3
16	4.55	22.50	2.13	231 ± 14	-18.2 ± 1.8	72 ± 6	152 ± 7.2
17	4.55	5.00	2.13	240 ± 11	-18.1 ± 1.1	81 ± 5.2	130 ± 6.1

X_1 = SEP:SEL ratio, X_2 = amount of Ce6, X_3 = DCM:AC ratio, Y_1 = mean particle size, Y_2 = Zeta potential, Y_3 = encapsulation efficiency, Y_4 = time required for 90 % dissolution (t_{90})

size was obtained particularly at lower level of SEP:SEL ratio (X_1) and higher level of DCM:AC ratio. An equation that can adequately describe the influence of the selected variables on the mean particle size was obtained after conducting a multiple regression analysis on the results along with the statistical validation of the model as shown in Table 12. From the coefficient values and probabilities of significance, SEP:SEL ratio (X_1) and DCM:AC ratio (X_3) were found to have significant effect on the particle size. In addition, there were also significant interaction effects indicating strong influence of the process variables on the particle size of NS. The Ce6 concentration did not have any substantial effect on particle size as observed from the insignificant p-value (> 0.05).

F-test was performed to determine the significance of the regression model. The low probability value ($p < 0.05$) for mean particle size indicates that the model was statistically significant. The goodness of fit of the model was checked by adjusted determination coefficient (R^2). This was found to be high (~ 90%) indicating a high level of significance for the model. The p-value of lack of fit was found insignificant suggesting there is a large probability (12.1%) of lack of fit due to error. The above analysis shows the adequacy of the regression model for particle size.

From the values of the coefficients, it could be inferred that increasing ratio of SEP:SEL (X_1) had a positive effect on the particle size. In contrast, the ratio of DCM:AC (X_3) had a negative effect on the particle size. Overall, the extent of influence by the independent variables on the particle size was ranked as follows: SEP:SEL ratio > DCM:AC ratio > Ce6 concentration. The response surface plots representing the variation of particle size as a function of the independent variables are presented in Figure 32. As can be seen, increase in SEP:SEL ratio (X_1) in the formulation increased the particle size, while a

Table 12: Summary of results of regression analysis for responses Y_1, Y_2, Y_3 and Y_4 of SEP/SEL-Ce6 NS formulations

Response	Model	R^2	Adjusted R^2	SD	F value	p-value (Lack of fit)	p-value (model)
Size (Y_1)	Quadratic	0.945	0.906	5.19	13.58	0.1213	0.0012
Zeta potential (Y_2)	Quadratic	0.976	0.947	0.71	32.75	0.44	<0.0001
EE (Y_3)	Quadratic	0.943	0.911	5.35	13.02	0.31	0.0014
% drug release (Y_4)	Quadratic	0.906	0.953	11.83	0.50	0.19	0.033

Regression equation of the fitted model [a]

$$Y_1 = 231.24 + 63.36X_1 + 0.44X_2 - 25.88X_3 + 7.12X_1X_2 - 22.03X_1X_3 - 1.38X_2X_3 - 28.22X_1^2 - 4.36X_2^2 - 9.84X_3^2$$

$$Y_2 = -18.54 - 8.08X_1 + 1.5X_2 - 0.19X_3 - 1.75X_1X_2 + 0.74X_1^2 + 0.35X_2^2$$

$$Y_3 = 69.98 + 10.67X_1 - 5.86X_2 + 5.73X_3 - 2X_1X_2 + 2.25X_1X_3 - 8.39X_1^2 - 1.49X_2^2 - 1.67X_3^2$$

$$Y_4 = 155.26 + 7.07X_1 - 4.11X_2 + 0.76X_3 - 0.88X_1X_2 + 0.87X_1X_3 - 7.37X_1^2 - 9.84X_2^2 - 4.71X_3^2$$

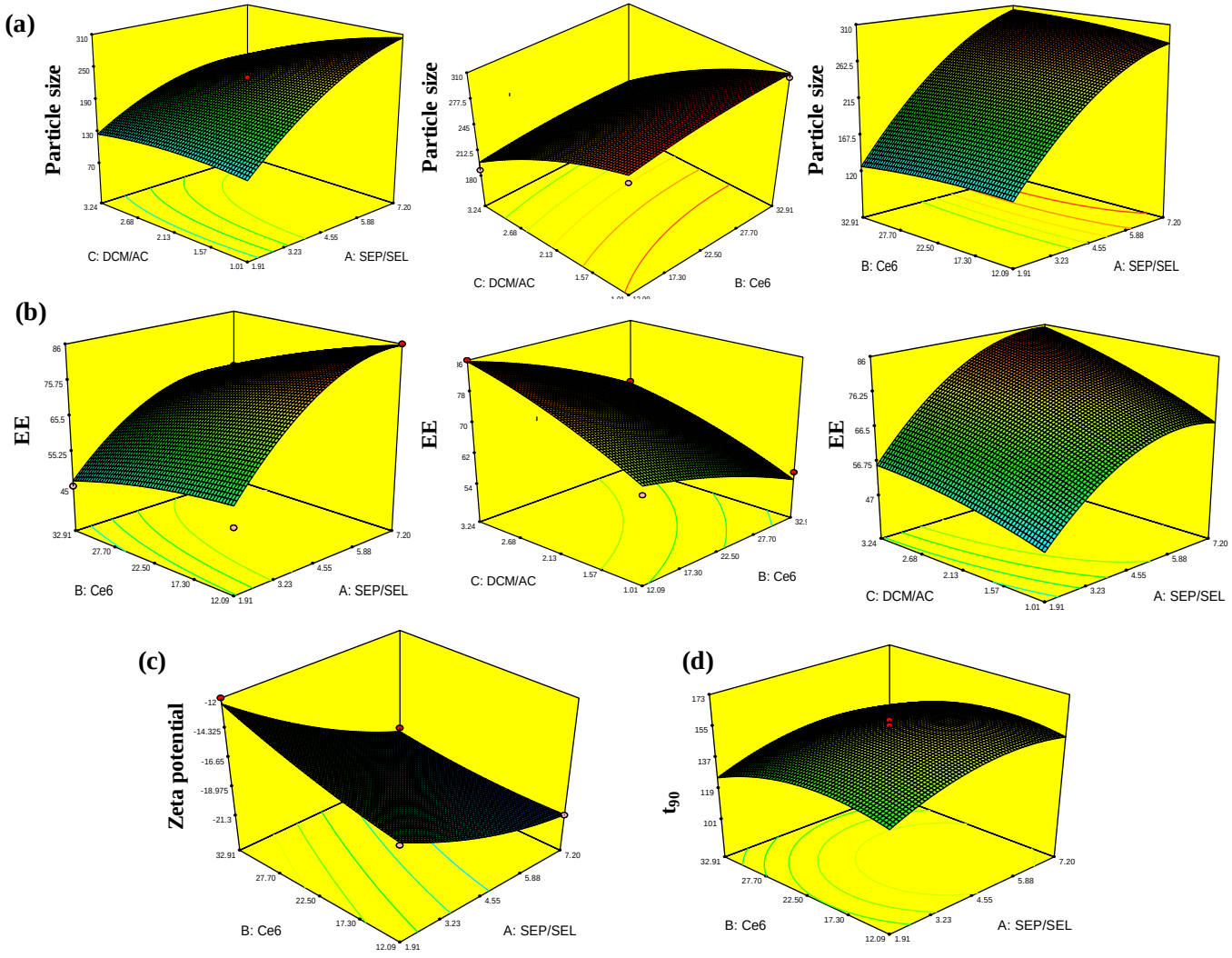

Figure 32: Response surface plots of (a) particle size, (b) encapsulation efficiency, (c) zeta potential and (d) *in vitro* drug release.

higher DCM:AC ratio (X_3) in the formulation decreased the particle size. The trends were in agreement with the findings of the regression analysis. The scientific basis of the underlying responses from this statistical model could be accounted by the higher aqueous solubility of SEL in comparison with SEP. This is because SEL would produce micelles more readily than SEP when in contact with water. Thus, the large number of micelles produced by using a higher fraction of SEL as matrix material would shift the Z-average diameter to the lower side. The existence of the micelles and the nanoparticles was indicated by the high polydispersity index (PDI of 0.95) of the nanosuspension prepared at SEP:SEL ratio (X_1) of 0.11. When SEP content increased, the possibility of micelle formation was lowered and the average particle size increased with corresponding PDI < 0.5.

When DCM:AC ratio (X_3) was increased, the mean particle size of the nanosuspension shifted to the lower side. The presence of a larger fraction of DCM would slow down the solvent diffusion process, with precipitation taking place more gradually through evaporation of DCM. The latter led to the production of comparatively smaller sized particles. On the other hand, with higher AC content, solvent diffusion process would be faster, resulting in more rapid precipitation of the stabilized nano-droplets and a higher propensity for larger particle size.

4.B.1.3.2. Zeta potential (Y_2)

The regression model for zeta potential (ZP) was also constructed. It was found to be statistically significant in terms of p-value, lack of fit, adjusted R^2 and regression coefficients (Table 12 and Figure 32). Zeta potential was found to be negatively affected by SEP:SEL ratio (X_1), while DCM:AC ratio (X_3) and amount of Ce6 (X_2) had little

effect. The response surface plot shows an increase in ZP from -22 mV to -11.6 mV with decrease in SEP:SEL ratio (X_1) from 9 to 0.11.The same trend was observed for nanoparticle size, suggesting that the fraction of micelle content increased with an increase in the SEL content resulting in highly polydispersed species namely micelles and nanoparticles. This was reflected in the high polydispersity index (PDI of 0.95) of the formulation using SEP:SEL ratio (X_1) of 0.11. Increase in SEP content resulted in production of lesser fraction of micellar species and more uniform-sized nano-precipitated particles (PDI < 0.5). This resulted in higher ZP value indicating better stability of the NS formulation.

4.B.1.3.3. Encapsulation efficiency (Y_3)

The p-value, lack of fit and adjusted R^2 values for EE were found to be significant, indicating that the effects of the dependent variables conformed to a quadratic model (Table 11). Encapsulation efficiency was found to be positively affected by SEP:SEL ratio (X_1) and amount of Ce6 (X_2) while DCM:AC ratio (X_3) exerted a negative effect. All the independent variables as well as their interaction parameters were found to have significant effect on EE, indicating that EE was highly affected by the formulation factors. The response surface plots show the individual as well as the combined effects of the factors on EE. The latter was found to vary markedly 36 % to 86 % (Figure 32). As can be seen from the response surface plots, increase in SEP:SEL and DCM:AC ratios increased the EE, while increase in Ce6 concentration had the opposite effect. Increasing Ce6 concentration in a constant amount of sucrose ester matrix negatively affected encapsulation efficiency as lesser amount of Ce6 become available for completely embedded in the matrix, while the rest is partitioned to the outer aqueous phase. Thus,

increase in Ce6 aptly accounts for the decrease in EE. Increase in SEP:SEL ratio (X_1) on the other hand, lowered the possibility of instantaneous dissolution due to the presence of the lesser amount of SEL. This prevents immediate partitioning of Ce6 present in the fraction of a soluble matrix material. This was reflected when EE relatively decreased when SEP:SEL ratio (X_1) was decreased, i.e. fraction of SEL was increased. The variation of solvent mixture was also found to have substantial impact on EE as the latter was found highest when the highest DCM:AC ratio (X_3) employed. As explained earlier, AC would diffuse more readily than DCM into the aqueous phase. When AC fraction was higher, the Ce6 dissolved in the solvent mixture of the O/W emulsion therefore had higher propensity to diffuse into the external aqueous phase. In contrast, when DCM fraction was higher, a major fraction of Ce6 remained in immiscible DCM phase and would not result in significant loss of Ce6 to the aqueous phase. Thus, a higher proportion of DCM in the solvent mixture increased the EE for Ce6.

4.B.1.3.4. Time required for 90 % dissolution (Y_4)

Time required for 90 % dissolution (t_{90}) of Ce6 from the different formulations was fitted into the regression equation. High adjusted R^2 and lack of fit with p-value less than 0.05 were obtained, indicating statistical significance of the quadratic model. From the different values of regression coefficient, it was inferred that SEP:SEL ratio (X_1) and amount of Ce6 (X_2) had significant impact on the *in vitro* dissolution of Ce6. The t_{90} of different NS formulations were varied from minimum 94 min to maximum 173 min when X_1 was lowest and highest, respectively (Table 11 and Figure 32). A lower SEP:SEL ratio employed would result in nanoparticles with a higher fraction of SEL in the matrix. As SEL was more soluble in water, it would enhance the dissolution of the matrix containing

the Ce6. Decrease in drug dissolution with increase in SEP fraction could be attributed to the increased hydrophobicity of the matrix and therefore, further time was required for complete dissolution/disintegration of the matrix. It was also observed that increase in Ce6 content had slightly positive impact on the *in vitro* release. This could be explained on the basis of Ce6 encapsulation in the sucrose ester matrix. A higher amount of Ce6 in constant amount of sucrose esters will probably result in inefficient encapsulation. Precisely, the possibility of Ce6 to remain embedded in the matrix was lesser and therefore, Ce6 could be remained adsorbed or loosely bound to surface of the ester matrix, which upon dissolution showed instantaneous dissolution in the nanoprecipitate form.

4.B.1.3.5. Optimization of SEP/SEL-Ce6 nanosuspension

In this study, the influence of 3 independent variables, such as SEP:SEL ratio (X_1), amount of Ce6 (X_2) and ratio of DCM:AC (X_3), on the properties of SEP/SEL-Ce6 NS was investigated. It was unlikely that optimizing one response (i.e. one property) would lead to the best outcome for the others. For this reason, "optimization" was defined as the most preferred experimental conditions that fulfilled the overall desirable properties of the formulation, where the different responses were mostly satisfactory. Optimization can be performed by mathematical or graphical approaches using Design Expert® software. The numerical optimization method involved a desirability function, d_i, that varied over the range of $0 \leq d_i \leq 1$ [196]. This function indicates that at what extent the experimental and predicted values are close to each other.

The desirable particle size was set to approximately 200 nm as particles of similar size had provided the effective EPR effect as well as the ability for uptake by the Payer's

patches [197]. Particle size smaller than 200 nm was not chosen because it necessitates the need for higher SEL content, which had a negative impact on encapsulation efficiency. The ZP of the optimized formulation was set to lower minimum to ensure higher stability. The EE and t_{90} were set to higher maximum to ensure effective encapsulation and faster dissolution of Ce6. The desirability function for each of the responses was then combined to obtain the overall desirability function (d_i), which was calculated using the following equation:

$$d_i = (d_1 \times d_2 \times d_3 \times d_4)^{1/4} \qquad \textbf{\textit{Equation}}\ (\mathbf{32})$$

The overall desirability for the optimized formulation is shown by the optimized values of the independent variables in Table 13. Formulations were subsequently prepared according to the optimized values of independent variables and the values of dependent variables were experimentally determined and shown in Table 13. As can be seen, the responses of the dependent variables (i.e. experimental values) were found to be very close that with the predicted values (i.e. desired values) indicating the applicability of this statistical design for the optimization of the formulation. The experimental response values were in good agreement that with the predicted values, as shown by small percentage prediction errors (Table 13). The characteristic features of the optimized formulation are shown in Figure 33. The optimized NS showed unimodal particle size distribution with average diameter of 188 nm, along with high stability (ZP = − 20.8 mV) (Figure 33 a,b). Compared to pure Ce6 control, the formulation showed a 10-fold increase in drug dissolution, facilitating approximately 85 % drug release in 2.5 hr (Figure 33c). The dissolution rate of pure Ce6 was very low, which translated to the fact

that fast dissolution from NS probably occurred as micelle-bound form. The aggregation characteristics of the dissolved Ce6 were further analyzed in terms of shifts in fluorescence emission spectrum. Figure 33(d) shows the normalized emission maxima of Ce6 at 679 nm. It was found to match that of micelle-bound Ce6 monomers (Fig. 20 obtained in disaggregation study). The latter exhibited an emission maximum at 673 nm. Such results further reinforced the assessment that dissolution of NS took place in micelle-rich condition and Ce6 existed as monomers in the micelles.

Table 13: Comparative values of predicted and experimental responses for the optimized SEP/SEL-Ce6 nanosuspension

Optimized formulation	Response variable	Constraints	Experimental value	Predicted value	d_i	% prediction error
X_1 = 7.06 X_2 = 15.22 X_3 = 3.24	Y_1 (nm)	Minimize	188	203	0.829	7.38
	Y_2 (mV)	Minimize	-20.8	-21.2		1.88
	Y_3 (%)	Maximize	82.4	85		3.05
	Y_4 (%)	Maximize	171	152.3		-12.8

4.B.1.4. Characterization of SEP/SEL-Ce6 NS

4.B.1.4.1. FTIR analysis

The effect of sucrose esters on enhanced dissolution of Ce6 was further investigated using IR spectroscopy in the light of solid-state interactions. Figure 34 shows the FTIR spectra of Ce6 with the following characteristic peaks: 1710 cm^{-1} (C=O vibration), 2962 cm^{-1} (C–H vibration) with weak stretching at 3303 cm^{-1} (mild N–H vibration) and 3440 cm^{-1} (mild O–H vibrations) [198]. SEP:SEL (7:1) also showed characteristic C–H, O-H and C=O vibrations at the corresponding absorption bands of 2952 cm^{-1},

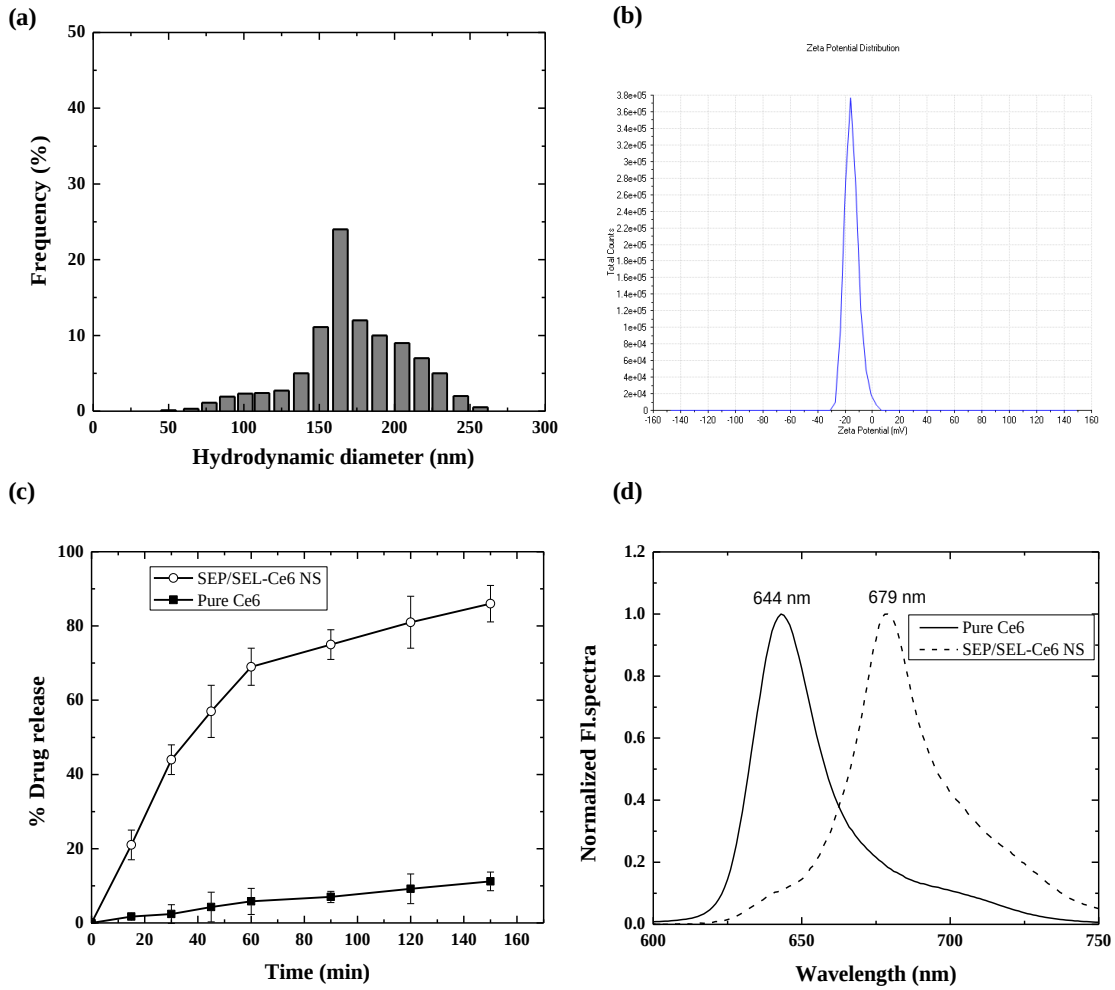

Figure 33: (a) Particle size distribution, (b) zeta potential, (c) *in vitro* drug release (n = 6) and (d) fluorescence emission characteristics of the optimized SEP/SEL-Ce6 nanosuspension.

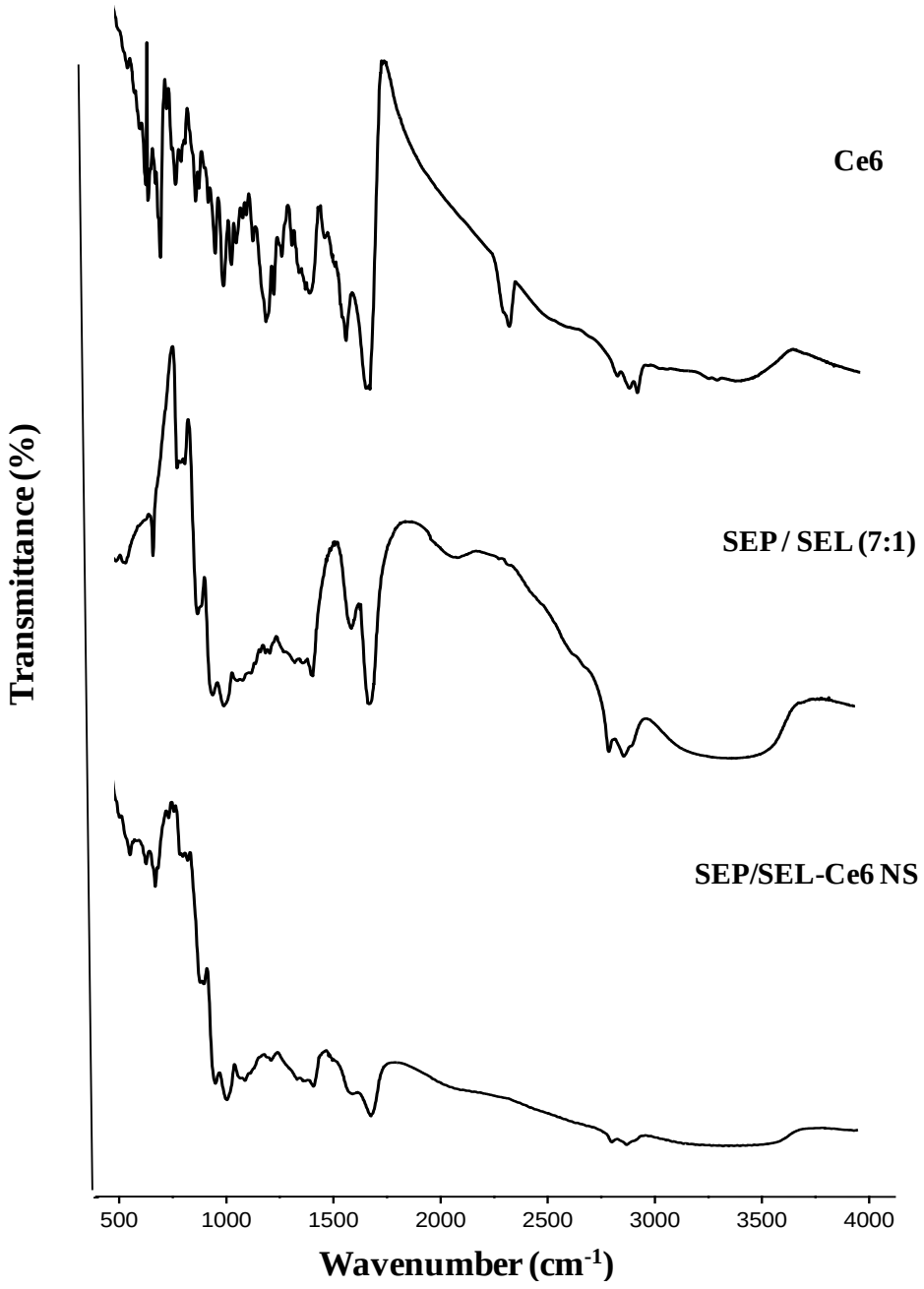

Figure 34: FTIR spectra of Ce6, sucrose esters and optimized SEP/SEL-Ce6 formulation.

3422 cm^{-1} and 1710 cm^{-1}. The FTIR spectrum of the freeze-dried nanosuspension was relatively similar to that of SEP/SEL, albeit of lower intensity (transmittance). This strongly suggested that Ce6 was efficiently incorporated in the sucrose ester matrix, resulting in effective encapsulation of Ce6, particularly for the SEP-rich formulation.

4.B.1.4.2. DSC analysis

The DSC thermograms of pure Ce6, SEP:SEL (7:1) and freeze-dried nanosuspension are shown in Figure 35. The Ce6 thermogram did not show any melting endotherm, however

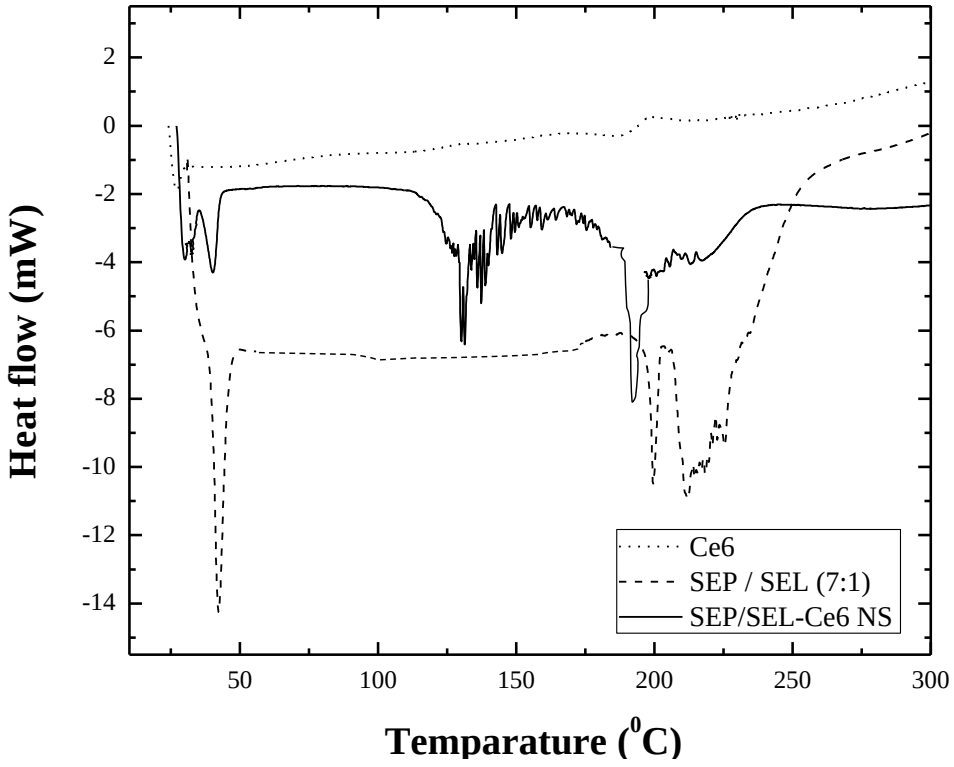

Figure 35: DSC thermograms of Ce6, sucrose esters and optimized SEP/SEL-Ce6 formulation.

above 250˚C, the thermogram followed an upward curve indicating degradation of Ce6 at high temperature (~300˚C). The mixture of sucrose esters showed two characteristic endotherms, one at 46˚C and the other at 200˚C, indicating complete melting of fatty acid chains and sucrose respectively. Interestingly, SEP/SEL-Ce6 NS showed an additional endotherm at 135˚C apart from the endotherms of the sucrose esters, which could be assigned to the melting of incorporated Ce6 in the SEP/SEL matrix. Such finding possibly suggests the presence of amorphous form of Ce6 in the sucrose ester matrix.

4.B.1.4.3. PXRD analysis

The X-ray diffractograms of pure Ce6, Ce6-sucrose ester physical mixtures and SEP/SEL-Ce6 nanosuspension are shown in Figure 36. Ce6 on its own and in the presence of the sucrose esters showed diffraction patterns characteristics of compounds in crystalline form. Complete disappearance of the diffraction patterns was observed for SEP/SEL-Ce6 nanosuspension, which strongly indicates that Ce6 was probably present in amorphous form in the sucrose ester matrix [199-201].

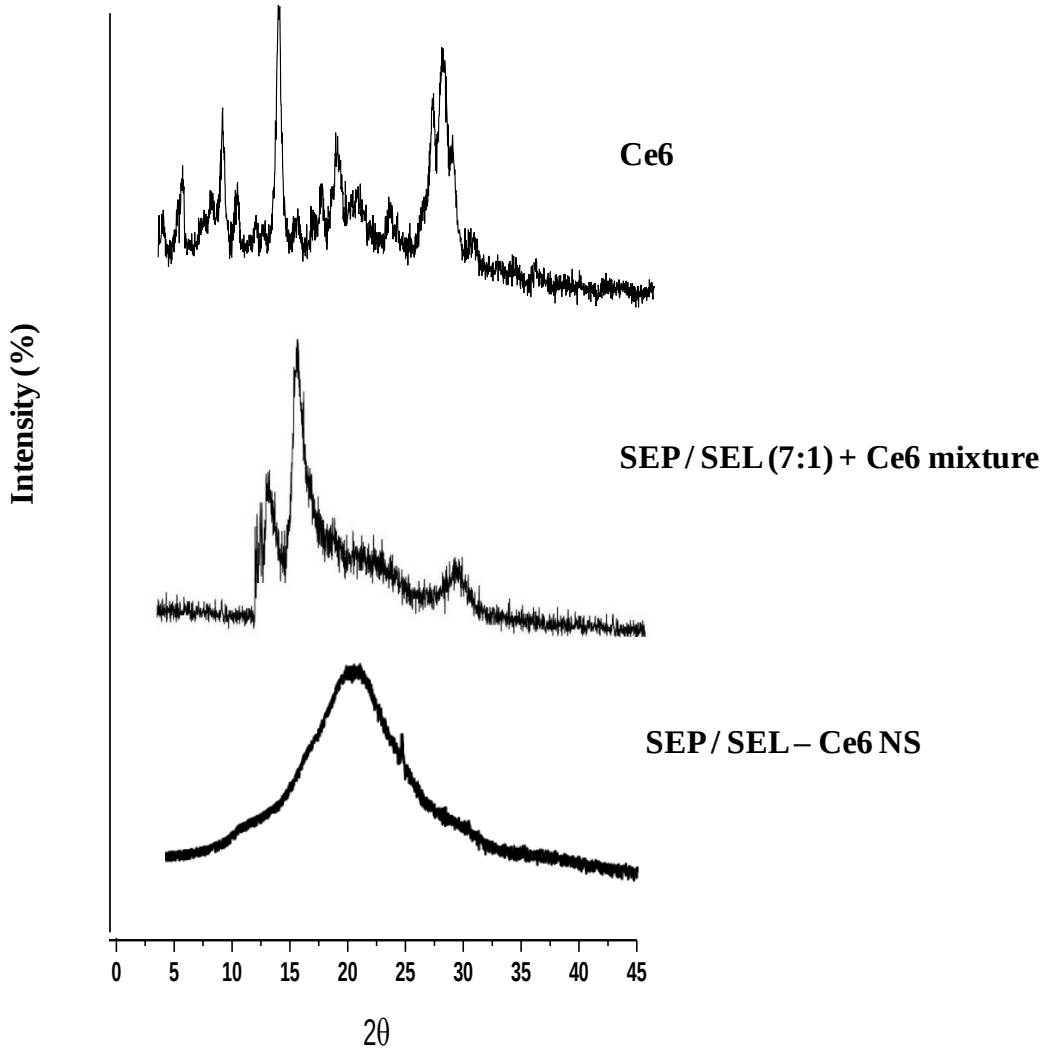

Figure 36: X-ray diffractograms of pure Ce6, physical mixtures of sucrose esters and Ce6 and optimized SEP/SEL-Ce6 NS formulation.

4.B.1.4.4. Morphology of SEP/SEL-Ce6 nanoprecipitates

Morphology of SEP/SEL-Ce6 in the optimized formulation was determined by taking TEM pictures of the freshly prepared nanosuspension. Figure 37 shows Ce6 particles in the nanosize range, with mean diameter of 100−150 nm.

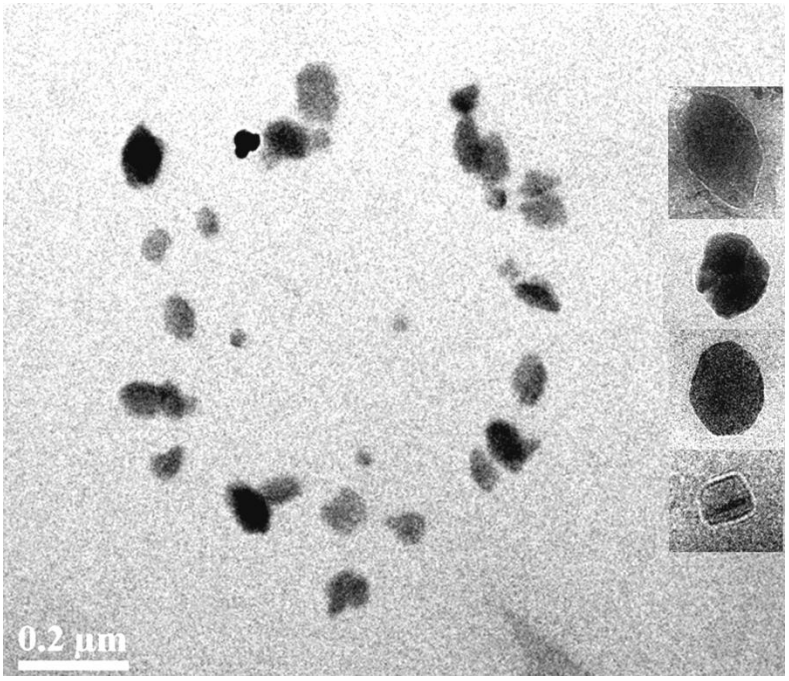

Figure 37: TEM images of optimized SEP/SEL-Ce6 nanosuspension (inset: close view of nanoparticles)

4.B.1.5. PDT efficacy of SEP/SEL-Ce6 NS

4.B.1.5.1. In vitro singlet oxygen generation

The SEP/SEL-Ce6 NS was placed in the dissolution medium and aliquot samples were collected at different time intervals for assay of singlet oxygen generation. The extent of *in vitro* singlet oxygen generation, which is inversely proportional with the absorbance of RNO, is shown in Figure 38. As can be seen, singlet generation was increased by 2-4 folds in comparison with the control (pure Ce6). The proportionate increase in singlet oxygen generation than the control suggested that the photophysical properties of Ce6

were not changed after being incorporated in the sucrose ester matrix as NS form [202]. The increase in singlet oxygen generation with time could be attributed to the increased

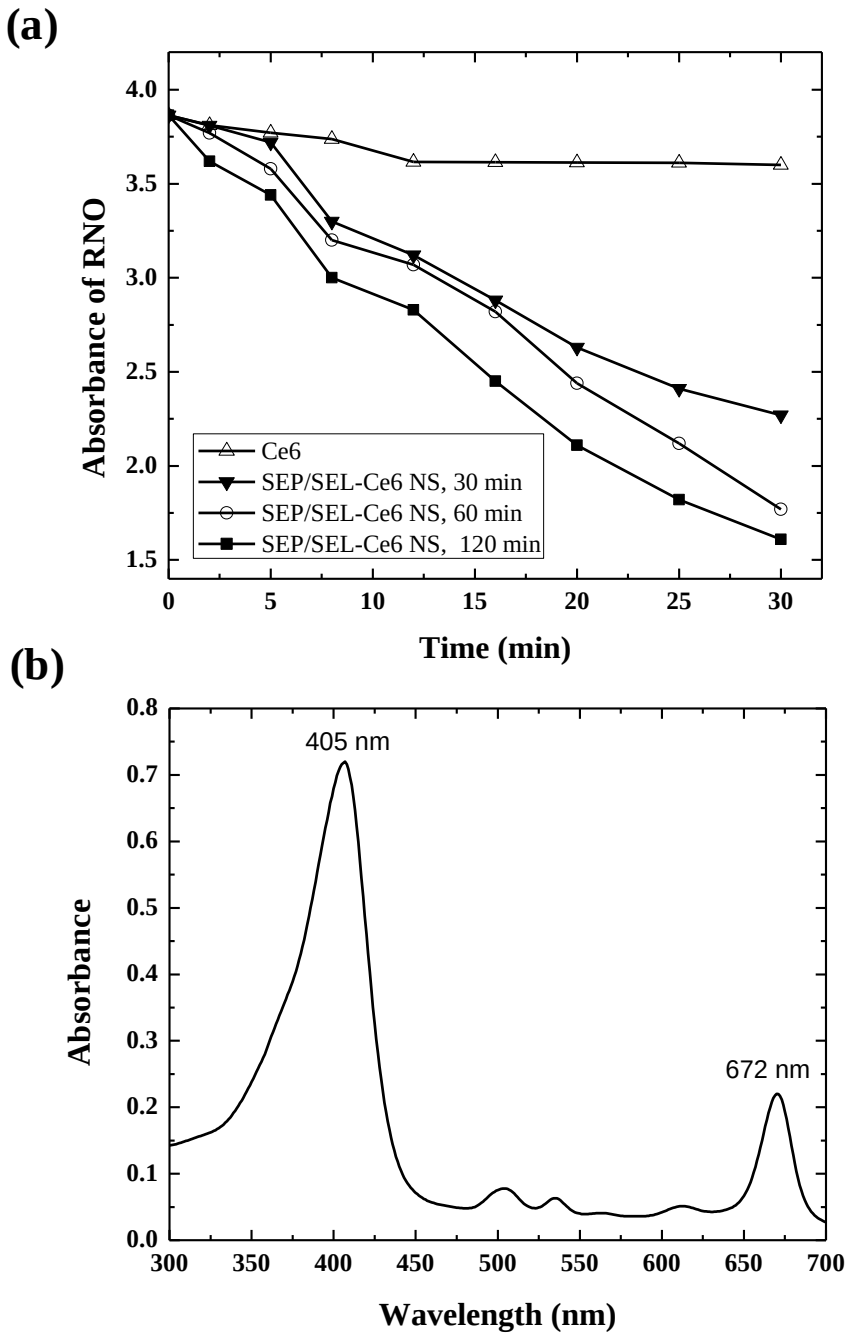

Figure 38: (a) Singlet oxygen generation at different time intervals and (b) typical uv-vis spectrum of optimized SEP/SEL-Ce6 NS, collected from the dissolution medium.

availability of Ce6 through gradual degradation of the sucrose ester matrix. In order to substantiate the basis of improved singlet oxygen generation efficiency, the absorption spectra of the corresponding SEP/SEL-Ce6 NS samples were obtained. A typical absorption spectrum of the nanosuspension sample collected from the dissolution medium is shown in Figure 38(b). As can be seen, both Soret and Q bands were sharp, indicating the presence of monomeric Ce6 in the solution. This is because the dissolution of the sucrose ester matrix resulted in soluble micelle in which Ce6 was largely present as monomers. Therefore, it was evident that monomer-rich Ce6 enhanced singlet oxygen generation *in vitro*.

4.B.1.5.2. Cellular uptake and intracellular distribution

The uptake and intracellular localization of Ce6 from SEP/SEL-Ce6 NS in OSC cells was investigated by confocal laser scanning microscopy in dark conditions. As can be seen from Figure 39(a) more than 65 % of the Ce6 content SEP/SEL-Ce6 NS was taken up by the cells within 4 hr. The results showed a rapid intracellular passage across the cell membrane for SEP/SEL-Ce6 NS, which was almost twice faster than that for the Ce6 solution (control).The significant increase in cellular uptake compared to the control could be ascribed to the lipophilicity of SEP, which facilitated the passage of Ce6 across the lipophilic cell membrane. Furthermore, from the dissolution study, it was shown that Ce6 was present not as the free form but as micelle-bound form. Therefore, it could be argued that the Ce6 containing NS droplets had facilitated rapid intracellular accumulation through cell-mediated endocytosis pathways. The intracellular distribution of Ce6 from SEP/SEL-Ce6 NS was imaged by fluorescence microscopic technique using DAPI as the nucleus staining dye. The chlorin ring structure of Ce6 would generate a

strong fluorescence signal, thus enabling confirmation of the uptake and intracellular localization of the photosensitizer by deep red fluorescence emission. Figure 39 (b,c) shows the intracellular accumulation of Ce6 from NS after 1 and 4 hr respectively. The OSC cells were pretreated with DAPI, which was located in the nucleus and produced

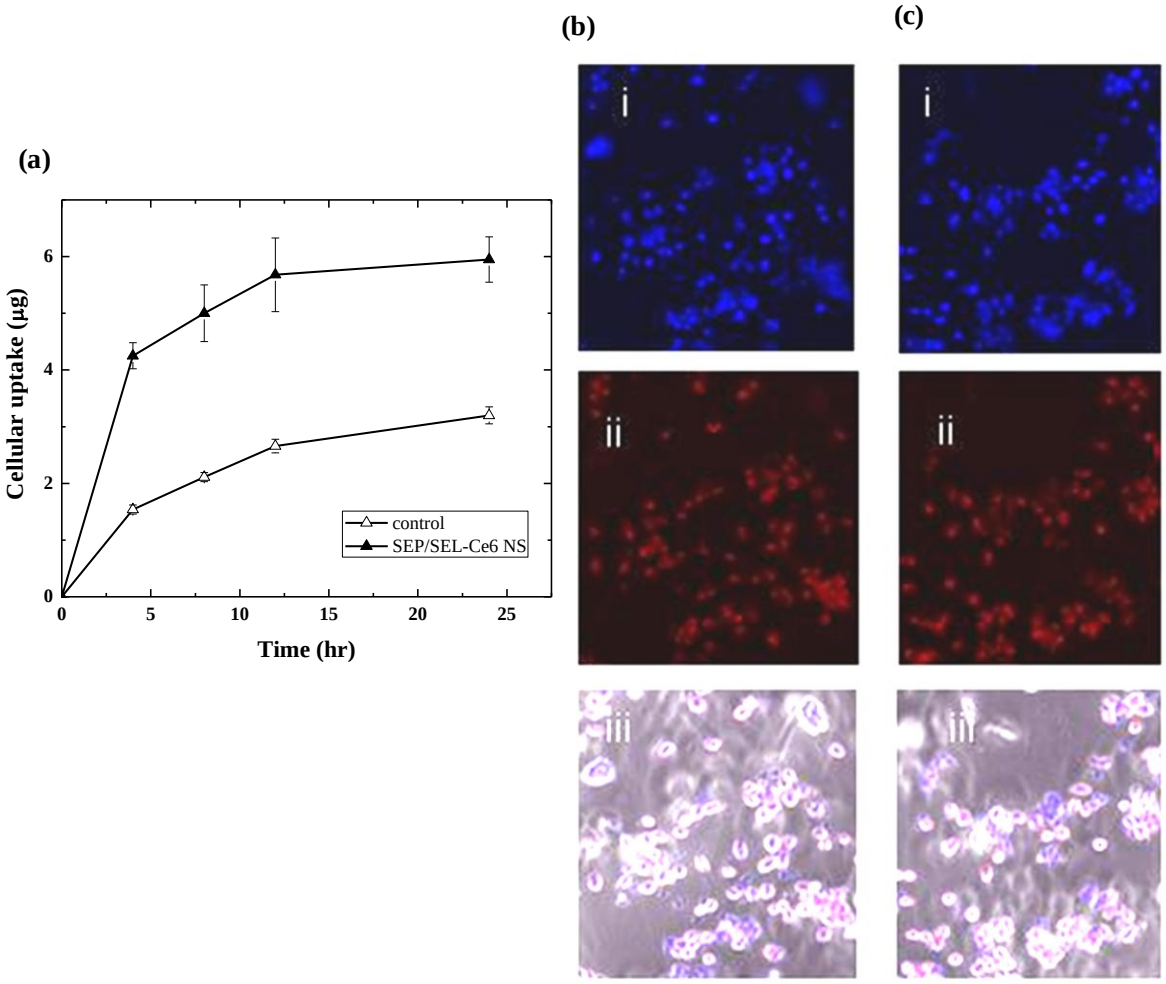

Figure 39: (a) cellular uptake of optimized SEP/SEL-Ce6 NS (n = 6) and confocal laser scanning microscopy images of OSC cells incubated with SEP/SEL-Ce6 NS for (b) 1 hr and (c) 4 hr [i= DAPI filter; ii = Cy5.5 filter and iii = phase contrast mode].

blue fluorescence. After incubation with SEP/SEL-Ce6 NS, the cells exhibited a strong red colour in the cytoplasm, indicating efficient cellular uptake of Ce6. When both DAPI

and Ce6 filters (phase contrast mode) were active, the cells were found to retain mostly the blue fluorescence of the nucleus while the rest showed by red colour, indicating Ce6 was not localized in the nucleus. Thus, Ce6 was preferentially accumulated in the cytoplasm and exhibited cytotoxic effects on lysosomes. Interestingly, no nuclear fragmentation, a marker of cell-apoptosis, was observed after DAPI staining, confirming the absence of cell toxicity in the absence of light exposure [203-204].

4.B.1.5.3. Cytotoxic effect on OSC cell-line

The *in vitro* cytotoxicity of Ce6 to OSC cells was evaluated by determining the cell survival after 4 hr of incubation under either dark or laser-irradiated conditions. The cell viability was determined for different concentrations of Ce6 in either free or NS form by MTT assay. In the absence of irradiation, no cytotoxicity was observed for both pure Ce6 (control) and SEP/SEL-Ce6 NS (Figure 40a). This indicates that Ce6 exhibited toxicity only when it was subjected to laser irradiation, i.e. it exhibited selective phototoxicity. The cell survival continued to decrease to different extents and leveled off at higher concentration of Ce6 for the NS formulation and control. Interestingly, the decrease was steep in the case of NS than compared to the control at equivalent Ce6 concentrations. The efficacy of the SEP/SEL-Ce6 NS was determined by its cytotoxic potential in terms of IC_{50} value and compared with that of the control. As can be seen from Figure 40(b), Ce6 in NS exhibited potent cytotoxic effect, which was found to be approximately 15 times greater than that of the control. The much greater effectiveness of SEP/SEL-Ce6 NS could be due to several possible reasons. The most likely reason is that Ce6 in NS was preferentially present as monomers, which facilitated singlet oxygen generation and accounted for the high cell death. In contrast, pure Ce6 existed mostly in the aggregated

form, which markedly reduced the singlet oxygen generation and therefore exhibited comparable cytotoxicity at a much higher concentration. Additionally, it could be argued that the uptake of Ce6 was higher when delivered by the NS vehicle than free Ce6 solution form, particularly when mediated by endocytosis pathway. The above findings are in agreement with other studies that showed different nanoparticle-based

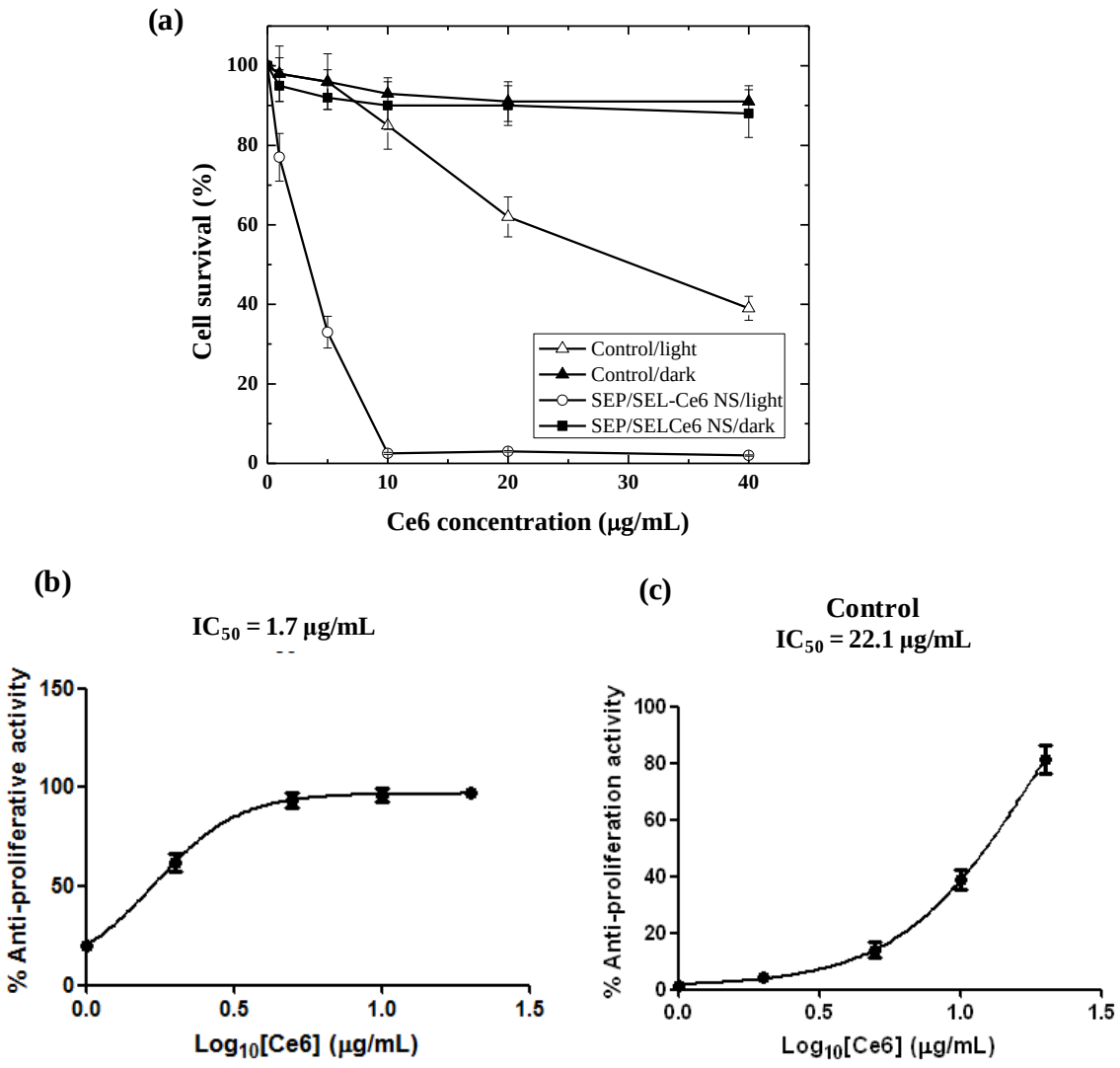

Figure 40: (a) Phototoxicity and (b) inhibitory concentration (50%) of (a) optimized SEP/SEL-Ce6 NS and (c) control (n = 6).

photosensitizer formulations were more effective than equivalent free photosensitizer in solution [205]. Another possible reason could be that Ce6 in nanoparticulate form led to its localization in more sensitive sub-cellular sites, indicating a possible explanation of the increased effectiveness of SEP/SEL-Ce6 NS formulation [206].

It is noteworthy that the IC_{50} of the SEP/SEL-Ce6 NS was 19 % lower than that of the Ce6-SEP(2) solution ($p = 0.02$). In addition, the SEP/SEL-Ce6 NS (Fig. 39a) showed higher intracellular uptake within first 4 hours of incubation compared to Ce6-SEP(2) solution (Fig. 29a), clearly indicating the usefulness of the nanoparticulate carriers. The enhanced uptake of Ce6 from the nanosuspension by the OSC cells could be ascribed to the greater amount of sucrose ester in the nanosuspension compared to the solution. Being surfactants, the sucrose esters probably increase the fluidity of the intracellular junctions, therby aiding permeation of components into the cells. Additionally, due to EPR effect of the nanoparticulate dosage forms, SEP/SEL-Ce6 NS would be more effectively accumulated in the carcinoma cells than the solution form, when administered into the subjects. This would result in significantly higher PDT efficacy of SEP/SEL-Ce6 NS when used *in vivo*.

As PDT is an effective treatment modality for superficial carcinoma, a topical application of the optimized SEP/SEL-Ce6 NS would be more suitable for oral carcinoma condition. The SEP/SEL-Ce6 NS could be freeze-dried and the resultant fine powder could be incorporated into an actuated device. These powdered formulations would be then dispensed from the device on to the affected oral mucosa. The flowability of the freeze-dried formulation could be further enhanced by adding inert agents such as sucrose or trehalose.

The study clearly showed the usefulness of sucrose esters as matrix material for nanosuspension formulation. The combination of the different sucrose ester grades resulted in improved formulation characteristics. Improved encapsulation efficiency was facilitated by SEP, while SEL augmented the drug dissolution. Overall, this work establishes the suitability of sucrose esters as drug carriers in PDT, which has not been reported in the literature.

4.B.1.6. Summary

A modified hot-melt emulsification-solvent diffusion method was employed in the preparation of Ce6-sucrose ester nanosuspension. The Ce6 in the nanosuspension was encapsulated as monomers within nanoparticulate sucrose ester matrix. The properties of the nanosuspension were affected by the hydrophobicity of the sucrose esters, diffusivity of the solvent mixtures and Ce6 loading in accordance with a quadratic regression model. The optimized nanosuspension exhibited high encapsulation efficiency, high stability and rapid release of Ce6. In the optimized formulation, more than 80 % of Ce6 was loaded in the sucrose ester matrix and approximately 85 % Ce6 was available in the dissolution medium within 2.5 hr. The enhanced dissolution was ascribed to amorphous form of Ce6, supported by DSC and XRD studies. The optimized nanosuspension reduced the proliferation of OSC cells to a much greater extent than free Ce6, as indicated by a 15-fold decrease in IC_{50} value than the control. In addition, efficient cellular uptake was also demonstrated with selective accumulation in the cytoplasm. A concomitant high singlet oxygen was observed, implying Ce6 was predominantly present as monomers in the nanoparticulate sucrose ester carrier.

4.B.2. Improved mucoadhesivity of alginate nanoparticles containing Ce6-PVP complex

4.B.2.1. Overview

In this section, the efficacy of nanoparticulate alginate carrier for mucosal delivery of Ce6 was investigated. Sodium alginate is a mucoadhesive biopolymer, which facilitates drug release from its hydrophilic matrix in the mucosal pH condition. To increase the PDT efficacy and permeation of Ce6 to the oral mucosal carcinoma cells, PVP was incorporated into the Ce6 formulation. It was hypothesized that the encapsulation of monomer-rich PVP-bound Ce6 would enhance photodynamic activity by largely increasing the singlet oxygen generation. In this study Ce6 formulations were prepared by a modified solvent diffusion-polymer gelation method with a view to achieve high encapsulation efficiency, high mucoadhesive property and rapid *in vitro* drug dissolution. This was achieved by using various concentrations of Ce6 and PVP in three levels by employing design of experiments. The photodynamic efficacy of the optimized formulation was evaluated using OSC cells as tumor xenograft model.

4.B.2.2. Preparation of alginate nanoparticles containing Ce6-PVP complex

Sodium alginate (Alg) is a biopolymer of interest in nanoparticulate drug delivery owing to its good biocompatibility, biodegradability, mucoadhesion, gelation and film forming properties [207-211]. Alg exists as alginic acid below pH 4.0 where it is insoluble. Disintegration of the alg matrix occurs in phosphate buffer at near neutral to alkaline pH conditions, enabling rapid drug release from the matrix. Alg-based nanoparticulate systems were produced for the delivery of various hydrophilic drugs by ionotropic gelation of very low concentrations of Alg polymer [212-215]. Studies on the

encapsulation of hydrophobic drugs using Alg nanoparticles are limited due to insolubility of the drug in the aqueous medium. In this study, a modified solvent diffusion-polymer gelation method was developed to encapsulate the hydrophobic photosensitizer, Ce6. The effectiveness of this nano-formulation was further improved by incorporating PVP with Ce6 within the Alg matrix. It was postulated that the presence of PVP would allow Ce6 to remain in monomeric form, thus enhancing singlet oxygen generation, while the increased hydrophilicity of the Ce6-PVP complex would aid in rapid drug dissolution. Increase in mucoadhesion was also expected due to the presence of PVP. In the present context, it was anticipated that the degradation of the alginate matrix in the mucosal pH conditions would release the Ce6-PVP complex and therefore, high PDT activity of Ce6 could be obtained.

In this study, a 1:1 mixture of ethanol and acetone was used to solubilize Ce6 and PVP. In order to speed up the solvent evaporation of the solvent mixture (boiling point ~ 68°C), both the solvent mixture and aqueous alginate solution were preheated to 70°C. The solvent mixture was then dispersed in the aqueous solution, where the alginate polymer was attracted to the surface of the dispersed droplets. The use of ultrasonication/homogenization was critical for producing nanosized droplets. The solvent mixture would be lost from the droplets by diffusion or evaporation into the aqueous medium, resulting in precipitation of PVP-Ce6, surrounded by Alg adhered to the surface of the droplet. Upon addition of calcium chloride, the Alg would be cross-linked to form an insoluble matrix with entrapped Ce6-PVP complex.

4.B.2.3. Evaluation of 3^2 factorial design results

As mentioned earlier, design of experiment (DoE) has been widely used in the pharmaceutical field to study the effects of formulation variables on the response parameters [213-214]. In this study, a 3^2 full factorial design was used where the concentrations of Ce6 (x_1) and PVP (x_2) were varied over 3 levels to determine its effects on particle size (y_1), percent encapsulation efficiency (y_2), percent mucoadhesivity (y_3) and *in vitro* drug release (y_4). The various targeted response parameters were statistically analyzed by applying one-way ANOVA (analysis of variance), at 5 % significance level and the significance of the model was estimated using the statistical package, Design-Expert®. The results are shown in Table 14 while the response surface plots for each of the dependent variables are shown in Figure 41.

4.B.2.3.1. Particle size (y_1)

As can be seen from Table 14, the mean particle size of the different formulations varied from 312 nm to 544 nm. Table 15 shows the quadratic model of the effects of Ce6 (x_1) and PVP (x_2) concentrations on particle size. The model was found to be statistically significant in terms of its p-value, lack of fit and adjusted R^2, indicating that particle size was significantly affected by the concentrations of Ce6 (x_1) and PVP (x_2). The regression coefficients presented in Table 15 suggest that particle size was mostly affected by PVP concentration, while Ce6 concentration had limited effect on it. The variation of particle size could be explained by reviewing the process of Ce6-PVP encapsulation in alginate matrix. As PVP concentration increased, the viscosity of the organic solvent phase also gradually increased. Considering the shear force exerted by sonicator and the magnetic stirrer to be almost constant, the constant shear force that was available for dispersing the

organic solvent phase became less effective as viscosity increased with gradual increment in the PVP concentration. Consequently, larger droplets were produced, resulting in the formation of larger particles.

Table 14: Observed responses of the various Ce6-PVP-Alg NP formulations prepared according to the 3^2 factorial design

Batch	Independent variables		Dependent variables			
	x_1 (mg)	x_2 (mg)	y_1 (nm) ± SD	y_2 (%) ± SD	y_3 (%) ± SD	y_4 (%) ± SD
1	12.50	10.00	323.3 ± 14	75.4 ± 6.6	11.17 ± 1.2	81.23 ± 6.6
2	20.00	55.00	389.2 ± 23	59.43 ± 4.3	15.06 ± 0.8	92.12 ± 5.1
3	12.50	100.00	522.2 ± 21	54.92 ± 5.9	41.08 ± 1.8	99.67 ± 5
4	12.50	55.00	348.4 ± 16	60.32 ± 5.1	36.2 ± 2.1	90.08 ± 5.8
5	5.00	10.00	312.3 ± 11	84.22 ± 7.2	16.41 ± 2.2	80.66 ± 7.2
6	20.00	10.00	330.2 ± 8	68.31 ± 5.8	8.23 ± 1.1	78.34 ± 5.3
7	12.50	55.00	366.4 ± 12	61.6 ± 4.8	31.06 ± 2.6	90.59 ± 4.9
8	5.00	100.00	544.2 ± 14	60.16 ± 5.6	47.11 ± 3.4	95.04 ± 4.6
9	5.00	55.00	390.2 ± 11	72.22 ± 4.8	34.23 ± 2.8	93.02 ± 6.8
10	12.50	55.00	378.1 ± 14	59.49 ± 5.1	34.59 ± 3.2	89.7 ± 7
11	20.00	100.00	531.7 ± 18	47.08 ± 3.8	34.87 ± 3	96.54 ± 4.2
12	12.50	55.00	388.3 ± 11	57.32 ± 4.5	35.66 ± 3.8	87.23 ± 6.2

x_1 = amount of Ce6
x_2 = amount of PVP
y_1 = mean particle size
y_2 = encapsulation efficiency
y_3 = mucoadhesivity (%)
y_4 = in vitro release (%)

4.B.2.3.2. Encapsulation efficiency (y_2)

The effects of the independent variables on encapsulation efficiency (EE) of the different Ce6-PVP-Alg NP formulations were also investigated. From Table 14 and Figure 41, EE was found to vary from 47 % to 84 % for different levels of Ce6 and PVP.

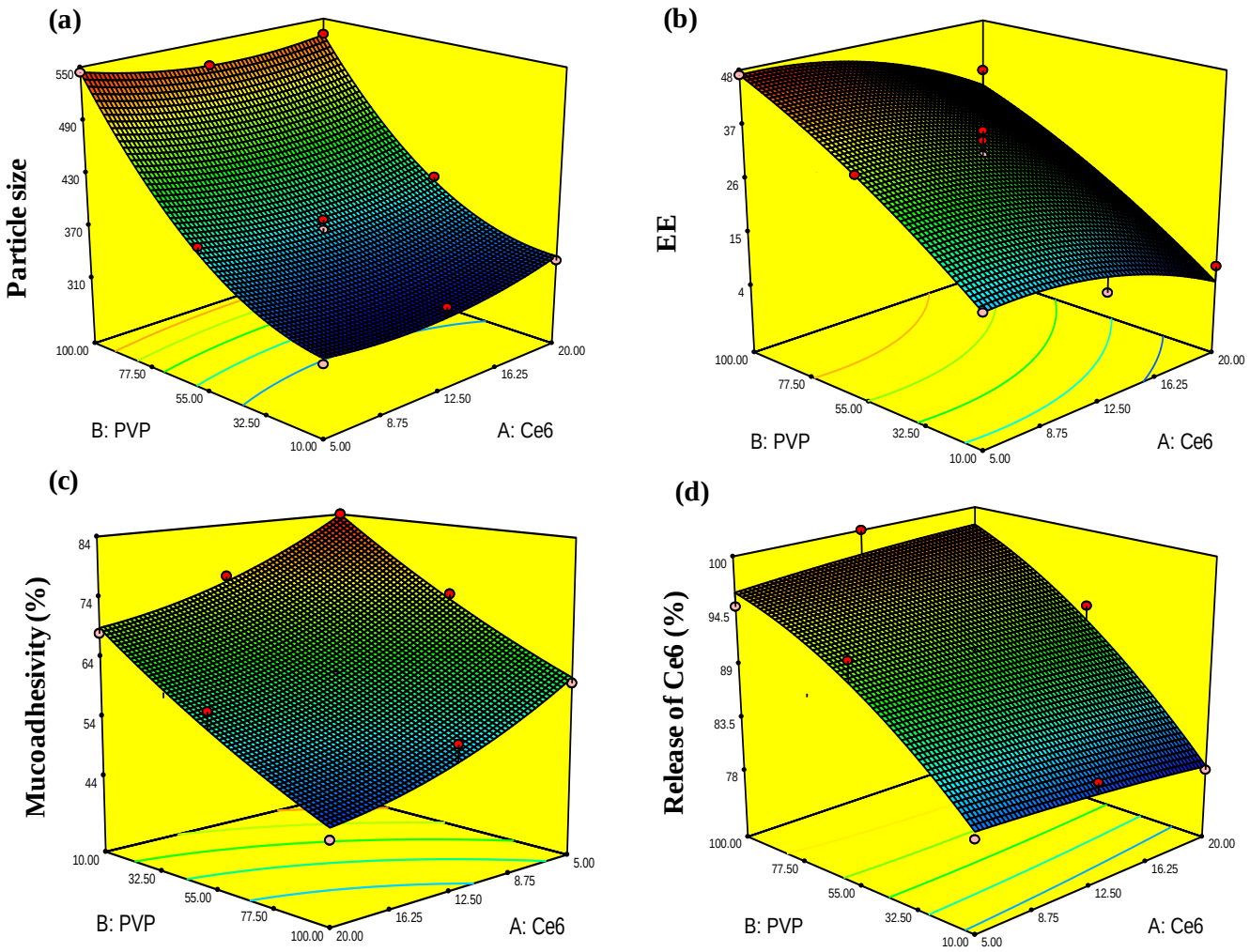

Figure 41: Response surface plots of (a) mean particle size, (b) encapsulation efficiency, (c) % of mucoadhesion and (d) *in vitro* drug release.

The regression model for encapsulation efficiency (EE) was constructed and found to be statistically significant in terms of p-value, lack of fit, adjusted R^2 and regression coefficients. As can be seen from the values of regression coefficients in Table 15, both Ce6 and PVP were found to have significant effect on EE. Increase in Ce6 concentration (x_1) was observed to decrease EE. In the polymer gelation-solvent diffusion method, the Ce6-PVP complex was dissolved in ethanol and acetone, and lost from the dispersed phase via diffusion/evaporation of the organic solvents into the aqueous medium containing Alg. Keeping Alg concentration constant, increase in Ce6 concentration would increase the drug to polymer ratio. The alginate matrix formed would therefore be less effective in retaining Ce6 when the concentration of Ce6 was increased. This aptly explains why the EE was highest when the Ce6 concentration was at the lowest. It was also found that EE tended to decrease with increased PVP concentration (x_2). Increase in PVP concentration would increase the viscosity of the solvent phase, which consequently reduced the rate of solvent diffusion into the aqueous phase. This might had led to poor precipitation of the Ce6-PVP mixture in Alg-bound aqueous phase, leading to leakage of the drug with less effective encapsulation. It was evident from the results that optimum encapsulation could be achieved through a balance of amounts of Ce6 and PVP used.

4.B.2.3.3. In vitro mucoadhesivity (y_3)

The mucoadhesivity of Ce6-PVP-Alg NP was determined by an *in vitro* mucin-based assay. The mucoadhesivity was found to vary from 8 % to 47 % (Table 14 and Figure 41). As can be seen from the values of regression coefficients in Table 15, the effect of x_1 on the mucoadhesivity was little, while x_2 had positive impact on it. A quadratic model was found to be statistically significant for this response variable as indicated by the

Table 15: Summary of results of regression analysis for responses y_1, y_2, y_3 and y_4 of alginate nanoparticles containing Ce6-PVP complex

Response	Model	R^2	Adjusted R^2	SD	F value	p-value (Lack of fit)	p-value (model)
Size (y_1)	Quadratic	0.979	0.979	6.52	95.68	0.72	<0.0001
EE (y_2)	Quadratic	0.874	0.948	2.48	37.59	0.09	0.0006
% mucoadhesivity (y_3)	Quadratic	0.936	0.873	4.72	14.79	0.16	0.0051
% drug release (y_4)	Quadratic	0.906	0.953	2.18	20.44	0.14	0.0024

Regression equations of the fitted models

$$y_1 = 367.9 + 1.67x_1 + 105.3x_2 + 15.63x_1^2 + 48.63x_2^2$$

$$y_2 = 61.26 - 7.5x_1 - 11.5x_2 + 2.34x_1^2 + 1.34x_2^2$$

$$y_3 = 31.53 - 1.17x_1 + 15.1x_2 - 3.82x_1^2 - 2.32x_2^2$$

$$y_4 = 90.89 - 0.17x_1 + 18.83x_2 + 1.06x_1x_2 - 2.24x_2^2$$

p-values, lack of fit and adjusted R^2 values. As the PVP concentration increased, the possibility of complex formation between Ce6 and PVP also increased. The mucoadhesivity was attributed to the mucoadhesive Alg and PVP. As the degradation of polymeric Alg chains occurred with time, the Ce6-bound PVP played a greater role in facilitating mucoadhesion. The mucoadhesivity of Ce6-PVP-Alg NP was compared with that of other formulations [215, 216]. It was noted that Ce6-PVP-Alg NP possessed substantially lower mucoadhesivity on a weight-by-weight basis when compared to nanoparticles prepared by ionotropic complexation between chitosan (CS) and Alg polymers. The high mucoadhesivity of Alg-CS matrix could be ascribed to direct electrostatic interaction between cationic CS and negatively-charged sialic present in mucin. In the case of Ce6-PVP-Alg NP, electrostatic interaction was not present and the only effective interaction was contributed by weak van der Waals force, which accounted for the low mucoadhesivity. Notably, presence of PVP increased mucoadhesivity and therefore, incorporation of PVP in the Alg matrix could be advantageous in the preparation of mucoadhesive formulation.

4.B.2.3.4. In vitro drug release (y_4)

The effects of the independent variables on amount of Ce6 released in 5 hr were investigated. The lowest drug release was observed when concentration of PVP (x_2) was in lower level, while higher level of x_2 resulted in 100 % release within the stipulated time. The p-value, lack of fit and adjusted R^2 values for *in vitro* drug release were found to be significant and the data fitted a quadratic model. As can be seen from the regression coefficient values in Table 15, PVP concentration had pronounced positive effect on the *in vitro* drug release profile, while Ce6 had little effect. An increase in PVP concentration

increased the possibility of Ce6-PVP complex formation and ensured the presence of a higher fraction of PVP-bound monomeric Ce6. The latter was more hydrophilic than pure Ce6. During *in vitro* dissolution, once the degradation of alginate polymeric shell began, the highly hydrophilic Ce6-PVP complex rapidly dissolved in the dissolution medium. When the PVP concentration was on the lower side, all the Ce6 molecules present could not form complex with the available PVP molecules and therefore, a fraction of Ce6 would remain unbound to PVP. Thus, it could be inferred that during *in vitro* dissolution, a longer time would be required for complete dissolution of the unbound Ce6 fraction, which consequently prolonged the overall drug release from Ce6-PVP-Alg NPs.

4. B.2.3.5. Optimization of Ce6-PVP-Alg nanoparticles

The optimal amounts of Ce6 (x_1) and PVP (x_2) were determined by employing the numerical optimization technique on the measured dependent variables, namely mean particle size (y_1), encapsulation efficiency (y_2), percent mucoadhesivity (y_3) and in *vitro* drug release (y_4). It was evident from the previous discussion on the effects of the independent variables on the formulation parameters that a low PVP content in the formulation would have a negative effect on mucoadhesivity and in vitro drug dissolution with mean particle size on the lower range. For this reason, no constraint over particle size was set but the EE, percent mucoadhesivity and drug release were set to maximum. The nanoparticle formulation was prepared using the optimal amounts of Ce6 and PVP derived based on the constraints set. The afore-mentioned properties of the formulation were then evaluated. The desirability coefficient and the predicted values of these properties (i.e. dependent variables) are shown in Table 16. As can be seen, all the predicted values were found to be close to the experimental values. The relatively low

percentage prediction errors suggested high effectiveness of the regression model employed for each of the dependent variables. As shown in Figure 42, the optimized Ce6-PVP-Alg NP formulation showed a normal size distribution, with mean particle size of 466 nm. The EE and percent mucoadhesivity achieved were acceptable. In addition, more than 80 % drug release in pH condition of oral mucosal fluid was achieved in 5 hr. The drug release rate was higher for the first hr, followed by a more gradual release for the remaining of the time span. The overall curve fitting (Table 17) showed that the drug release followed the zero order model in the first hour. Korsemeyer-Peppas model best described the drug release in the later phase, with an *n* value of 0.44, suggesting that the drug transport was mainly mediated by Fickian diffusion. The more rapid initial release could be attributed to extremely small nanoparticles, which had large specific surface area, as well as, to the Ce6 found on the particle surface. In the later phase, drug release was mainly governed by the sequential processes of polymer hydration, solvent penetration, drug dissolution and matrix erosion/disintegration [217].

Table 16: Comparative values of predicted and experimental responses for optimized Ce6-PVP-Alg NP formulation

Optimized formulation	Response variable	Constraints	Experimental value	Predicted value	d_i	Percentage prediction error
x_1 = 11 mg x_2 = 78 mg	y_1 (nm)	in range	466.2	499.8	0.742	6.61
	y_2 (%)	maximize	73.66	72.98		-0.93
	y_3 (%)	maximize	37.82	44.51		15.03
	y_4 (%)	maximize	87.25	95.55		8.68

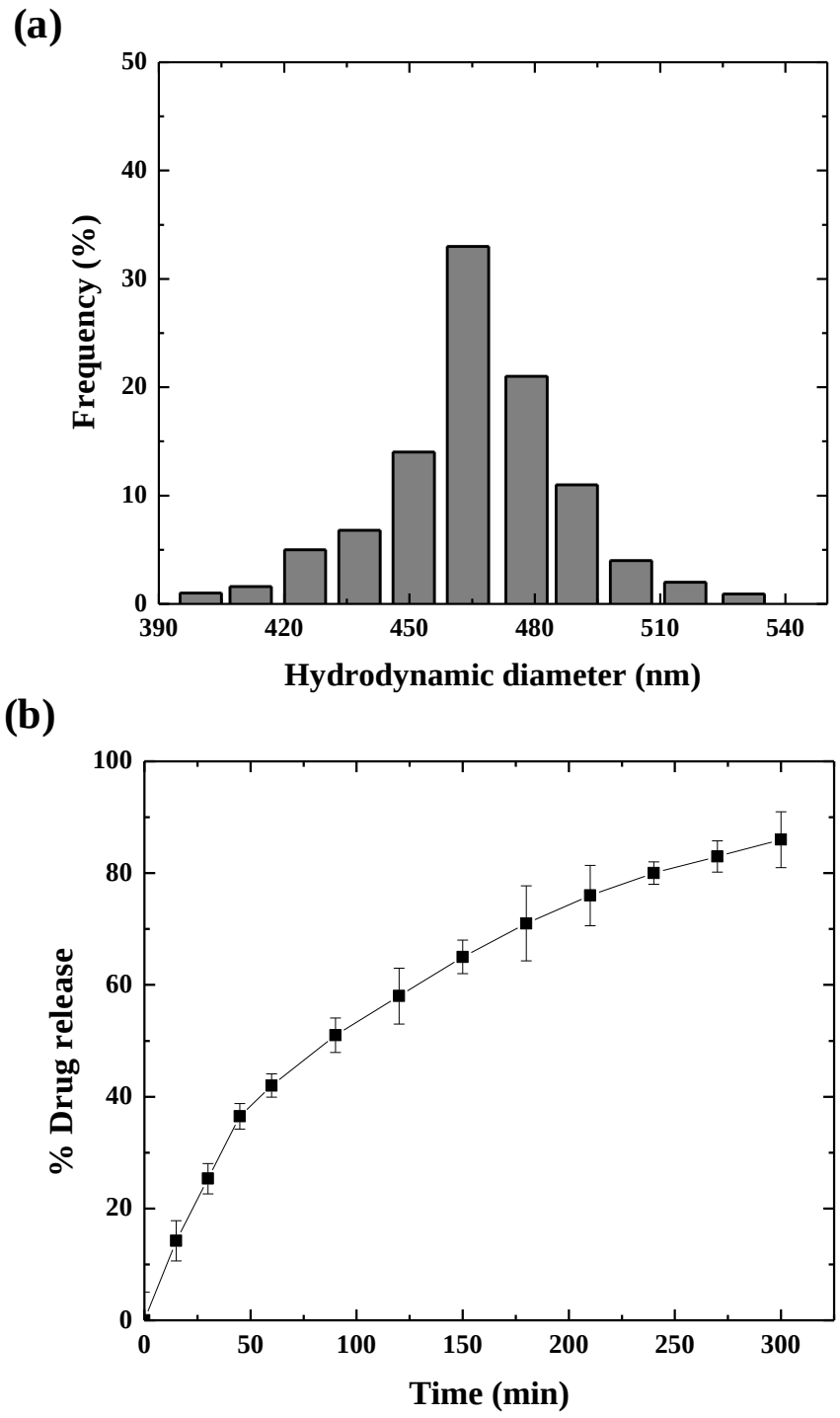

Figure 42: (a) particle size distribution and (b) *in vitro* drug release of optimized Ce6-PVP-Alg NP (n = 6).

Table 17: Dissolution model fitting for *in vitro* release data of optimized Ce6-PVP-Alg NP formulation

Model	Equation	r^a (0- 1 hr)	r^a (1-5 hr)
Zero order	$m_0 - m = K_1 t$	0.994	0.971
First order	$\ln m = K_2 t$	0.975	0.981
Higuchian	$m_0 - m = K_3 t^{1/2}$	0.982	0.984
Korsemeyer-Peppas	$\log(m_0 - m) = \log K_4 + q \log t$	0.984	0.998
Hixon-Crowell	$m_0^{1/3} - m^{1/3} = K_5 t$	0.972	0.974

m_0 = amount of drug release at time, 0
m = amount of drug release at time, t
K_i = dissolution constant (i = 1 to 5)
q = Korsemeyer-Peppas coefficient
r^a = correlation coefficient

4.B.2.4. Characterization of Ce6-PVP-Alg nanoparticles

4.B.2.4.1. FTIR analysis

FT-IR spectra confirmed the Ca^{2+} induced cross-linking of sodium alginate as matrix material for Ce6-PVP complex (Figure 43). In the case of Alg, broad bands were observed at 3423 cm^{-1}, which is ascribed to O−H stretching vibrations [218]. The peak at 1400 cm^{-1} corresponded to symmetric COO− stretching of free carboxylic acid ends [219]. The peaks in the region 1300-1000 cm^{-1} corresponded to C−O stretchings arising from the oxygen linkages between the mannuronic and guluronic acid blocks [218]. In case of Ce6, characteristics peaks at 3440 cm^{-1}, 2962 cm^{-1}, 3303 $cm^{-1}$and 1710 cm^{-1} were observed due to for O-H, C-H, N-H and C=O stretching respectively. PVP also showed the characteristic C-H, N-H and C=O stretching in the afore-mentioned regions. For the Ce6-PVP-Alg NP formulation, the peak at 1400 cm^{-1} was absent indicating a strong

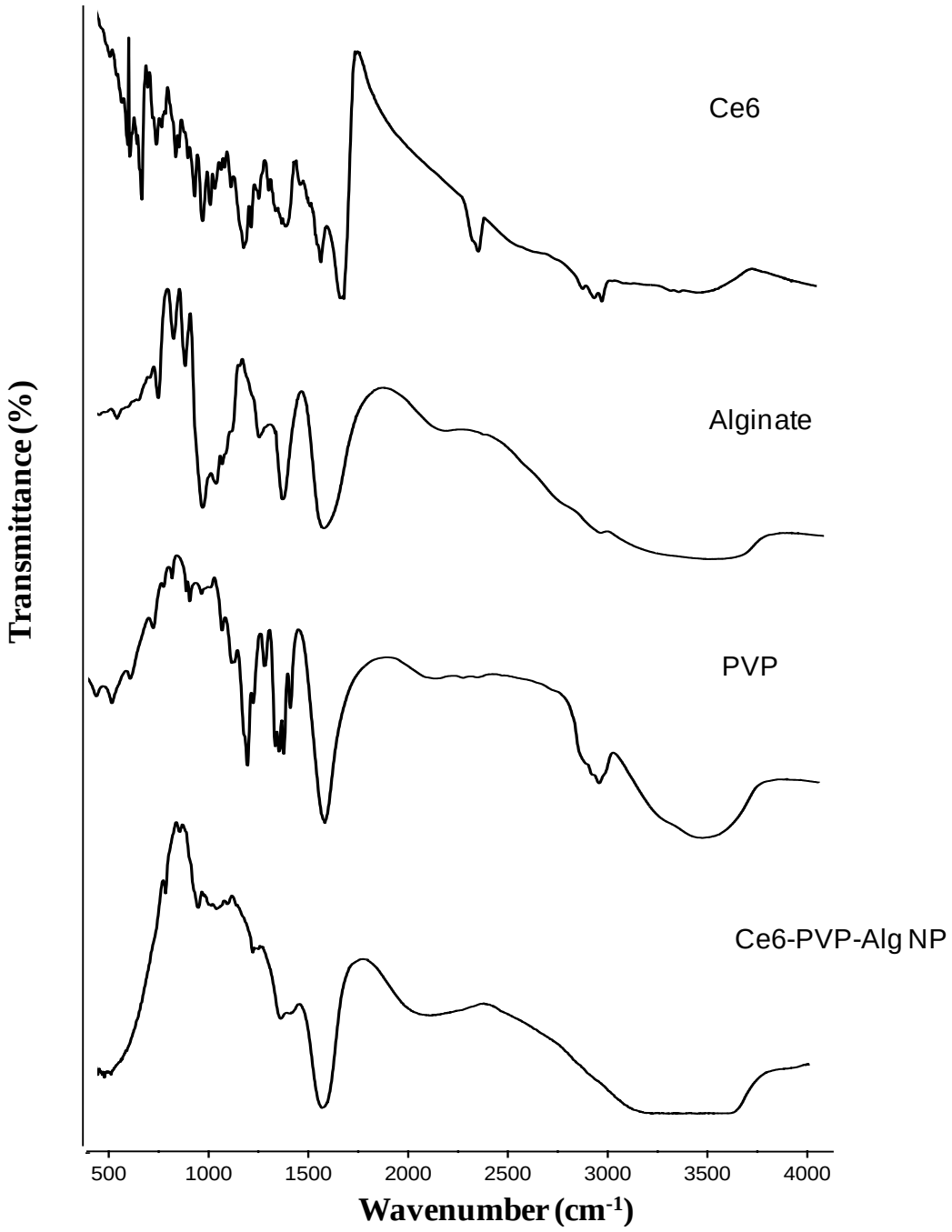

Figure 43: FTIR spectra of Ce6, alginate, PVP and the optimized Ce6-PVP-Alg NP formulation.

complexation of alginate with divalent calcium ions [219]. In addition, no prominent characteristic peaks of Ce6 and PVP were observed in the spectrum for Ce6-PVP-Alg NP, suggesting efficient complexation of Ce6-PVP in the Alg matrix by the divalent calcium ions.

4.B.2.4.2. DSC analysis

The DSC thermograms of sodium alginate, PVP, Ce6, Ca-Alg NP and the optimized Ce6-PVP-Alg NP formulations are shown in Figure 44. As can be seen, the crystalline Ce6 did not show any melting endotherm and showed slightly upward degradation curve at around 300°C. PVP and Alg exhibited melting endotherms in the range of 80-100°C. The thermogram of the optimized Ce6-PVP-Alg NP formulation showed a characteristic shift in melting point at around 125°C without any observable degradation pattern of Ce6. To affirm that the peak at around 125°C is the melting endotherm of calcium alginate, DSC endotherm of blank Ca-Alg NP was also recorded. It showed an endothermic peak at

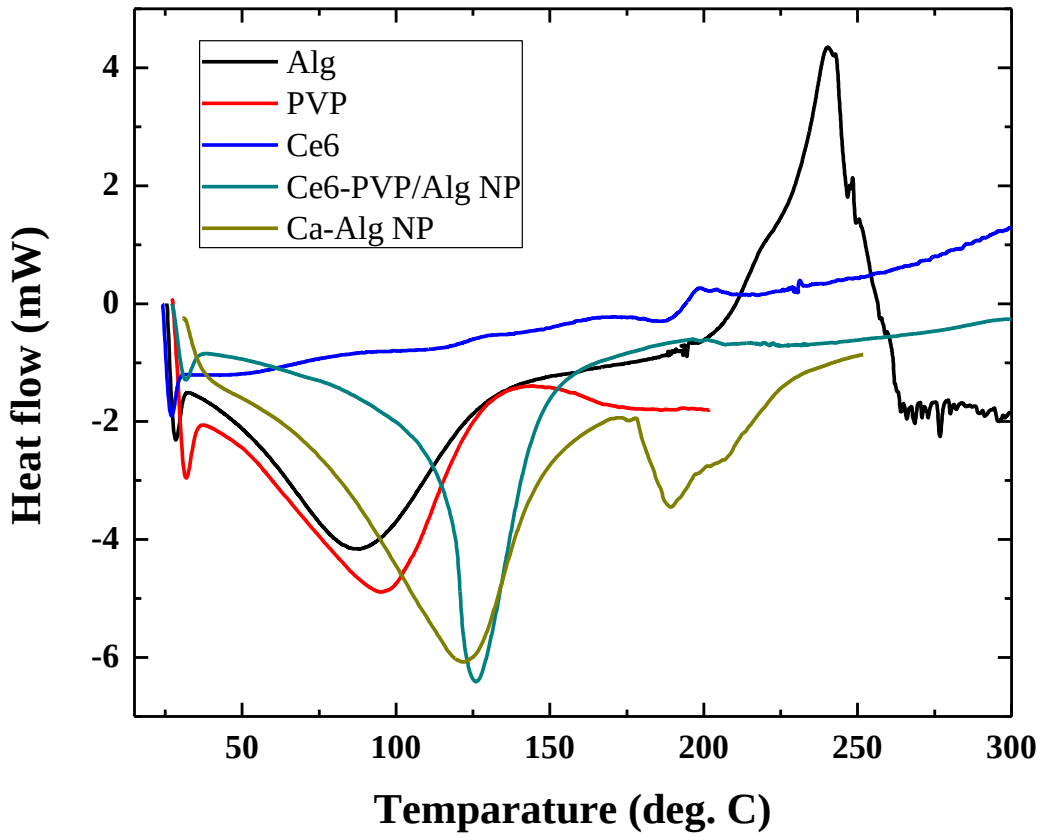

Figure 44: DSC thermograms of Ce6, alginate, PVP and the optimized Ce6-PVP-Alg NP formulation.

similar temperature, indicating that the melting point had shifted to a higher temperature for the cross-linked alginate polymer. Collectively, the findings suggested that Ce6-PVP was molecularly dispersed in the Ca-Alg matrix.

4.B.2.4.3. PXRD analysis

The X-ray diffractograms of Ce6 and the optimized Ce6-PVP-Alg NP formulation are shown in Figure 45. As can be seen, Ce6 showed several intense peaks, indicating its crystalline nature. However, these peaks were absent in the diffractogram of the NP

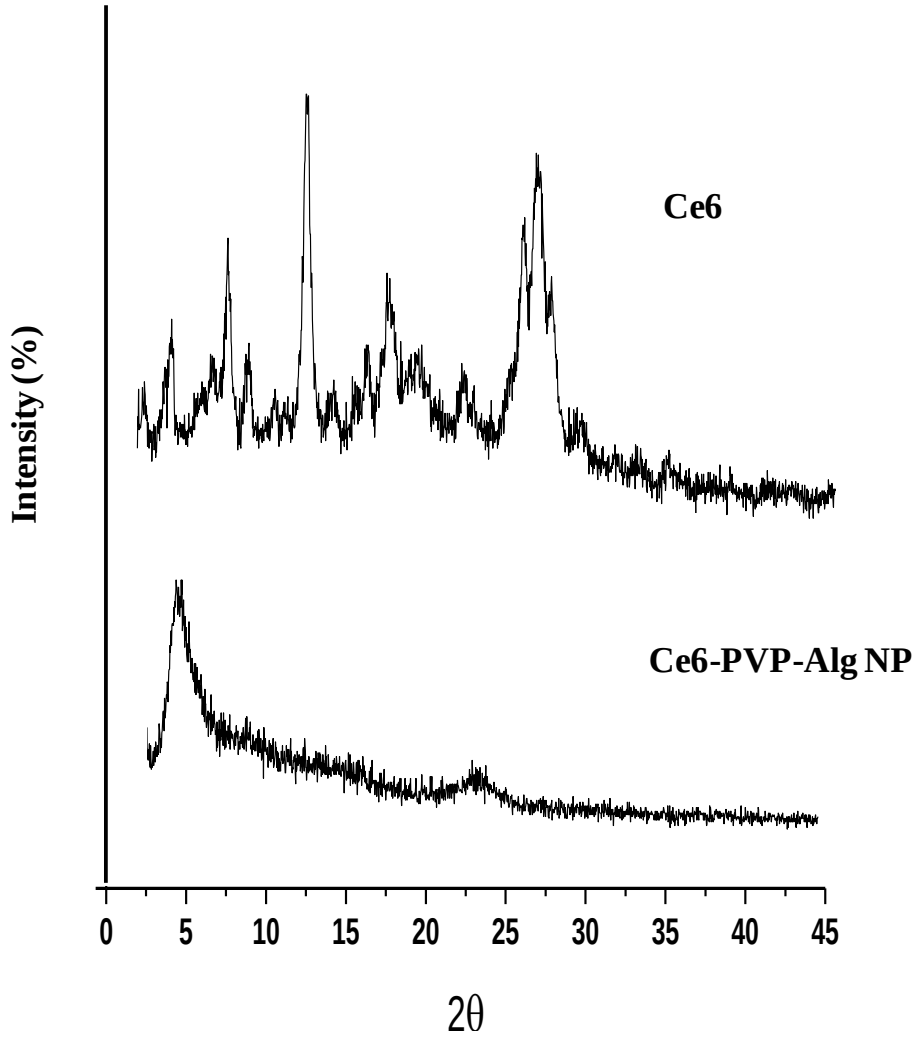

Figure 45: XRD patterns of pure Ce6 and the optimized Ce6-PVP-Alg NP formulation.

formulation, further confirming that Ce6 was effectively entrapped in the Ca-Alg matrix, possibly in molecularly dispersed form.

4.B.2.4.4. Morphology of Ce6-PVP-Alg NP

The TEM photomicrographs showed that the nanoparticles appeared to be spherically distinct particles (Figure 46). Under TEM, the nanoparticles appeared considerably smaller (200-250 nm) than the average particle size (~ 466 nm) detected by DLS measurements. Such discrepancy between the two results could be explained on the basis that dehydration of the hydrogel Ce6-PVP-Alg NP during sample preparation for TEM imaging, which led to the apparent decrease of hydrodynamic radius than that obtained from DLS measurements under hydrated conditions.

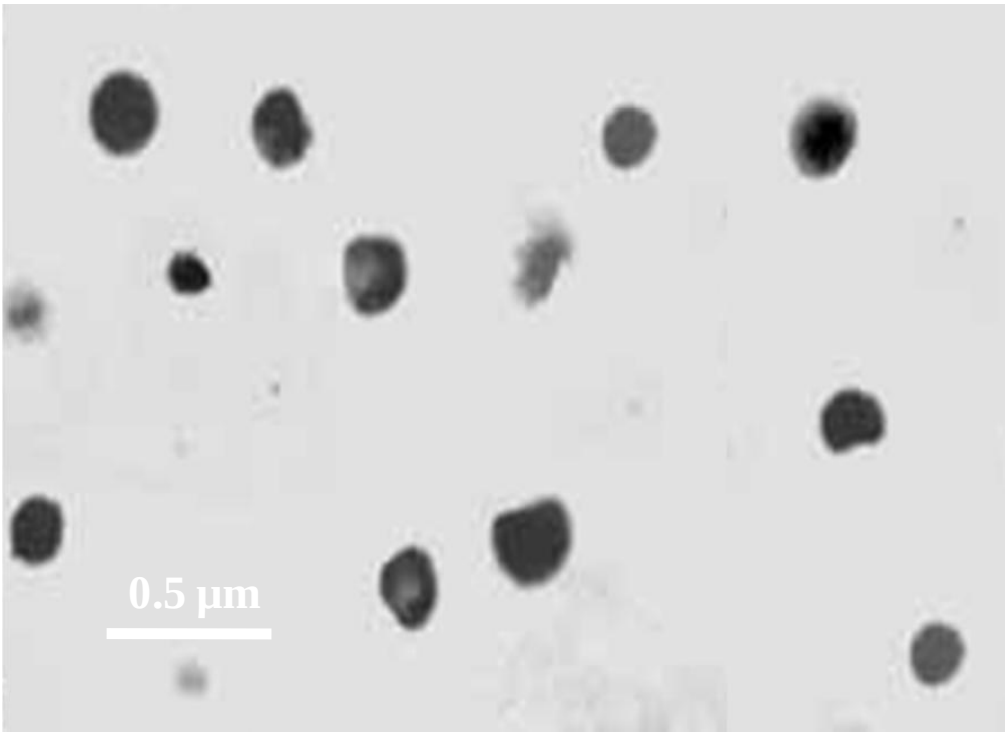

Figure 46: TEM images of the optimized Ce6-PVP-Alg NP formulation.

4.B.2.5. PDT efficacy of Ce6-PVP loaded alginate nanoparticles

4.B.2.5.1. in vitro singlet oxygen generation

Singlet oxygen generation efficiency was determined in accordance with the procedure employed for SEP/SEL-Ce6 NS (section 4.B.1.5.1). The extent of *in vitro* singlet oxygen generation by the optimized Ce6-PVP-Alg NP is shown in Figure 47(a). As can be seen,

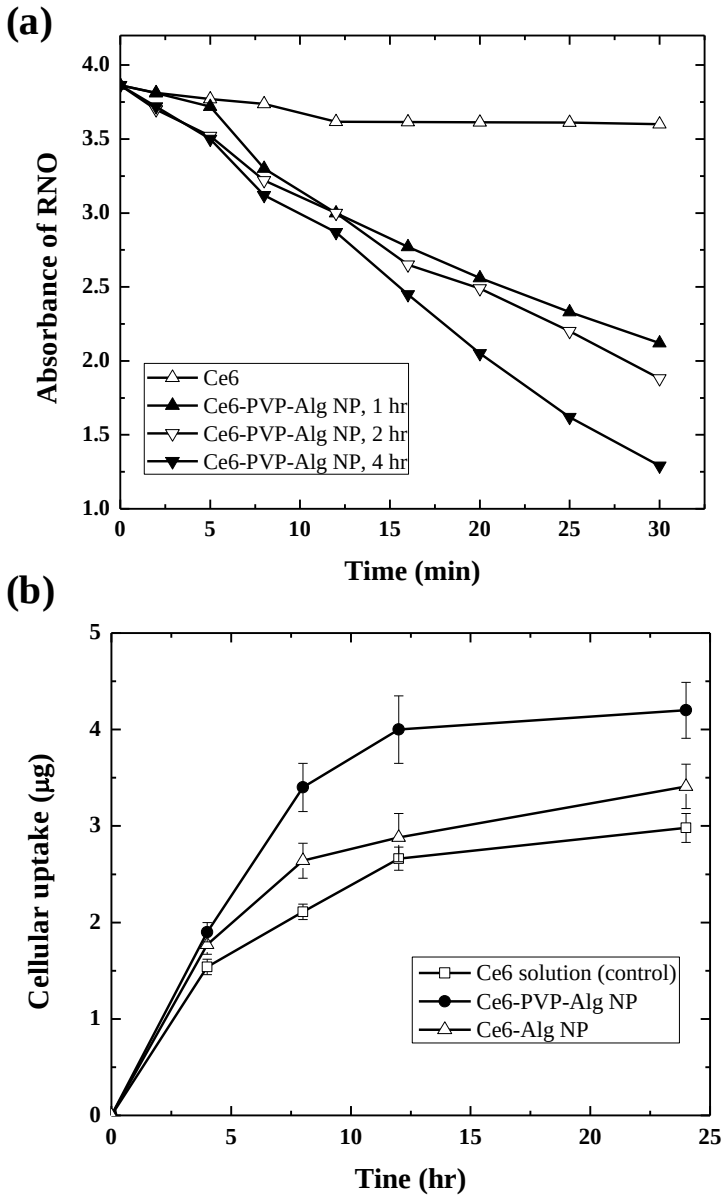

Figure 47: (a) Singlet oxygen generation and (b) cellular uptake of the optimized Ce6-PVP-Alg NP formulation (n = 6).

singlet generation efficiency was found to increase with time that was evidenced by 2-4 folds higher than compared to the control. The proportionate increase in singlet oxygen generation suggested that Ce6 did not undergo any photophysical changes after being incorporated in the Alg matrix in NS form. Such increase in singlet oxygen generation with time could be attributed to increased availability of Ce6 through gradual degradation of the calcium alginate complex. The better singlet oxygen generation capacity of Ce6-PVP-Alg NP than the control could be ascribed to Ce6 monomers, which remained bound to PVP. Therefore, it could be argued that the efficiency of alginate nanoparticles containing Ce6 was notably increased by the introduction of PVP in the system.

4.B.2.5.2. Cellular uptake and intracellular distribution

The uptake and intracellular localization of optimized Ce6-PVP-Alg NP formulation in OSC cells was confirmed by confocal laser scanning microscopy under dark conditions. The extent of intracellular uptake over 24 hr is shown in Figure 47(b). As can be seen, a comparable intracellular accumulation of both formulation and the control was observed in the first 4 hr. Interestingly, 80 % of the uptake was completed within 8 hr of incubation, suggesting that the uptake could be proportionately correlated with the *in vitro* drug dissolution. Finally, the uptake efficiency was found to increase 1.6 times over the control by the end of 12 hr. The cellular uptake of Ce6 was further compared between the optimized Ce6-PVP-Alg NP formulation and a corresponding NP formulation without PVP. The cellular uptake of Ce6 from the latter was found to be lower over the period of 24 hr. This observation indicates the significant role of PVP besides alginate. As the OSC cellular environment has pH of around 5, degradation of Alg matrix could not be ruled out as this would result in the liberation of Ce6-PVP

complex. This further suggests the synergistic effect of both PVP and alginate for improved mucosal permeability of the Ce6. The intracellular distribution of the optimized Ce6-PVP-Alg NP was imaged by fluorescence microscopic technique using DAPI as nucleus staining dye. Figure 48 shows the intracellular accumulation of Ce6 from the optimized Ce6-PVP-Alg NP formulation after 4 and 8 hr respectively. The OSC cells

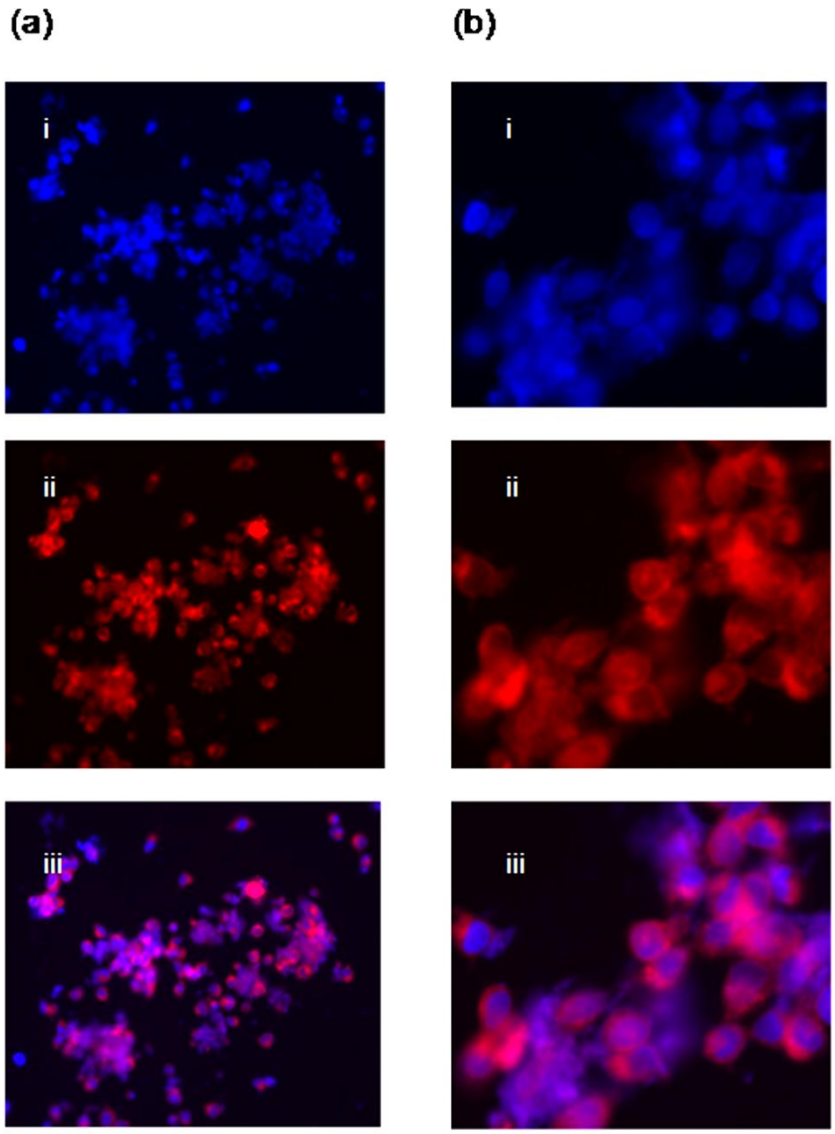

Figure 48: Confocal laser scanning microscopy images of OSC cells incubated with Ce6-PVP-Alg NP optimized formulation for (a) 4 hrs (b) 8 hrs [i = DAPI filter; ii = Cy5.5 filter and iii = phase contrast mode].

exhibited a strong red colour in the cytoplasm, indicating accumulation of Ce6 into the cells. The phase contrast mode showed a blue fluorescence at the centre of the cells, indicating the nucleus was unaffected by Ce6 and retained the stain of DAPI. Such finding corroborated the fact that Ce6-PVP-Alg NPs were preferentially accumulated in the cellular organelles like lysosomes, thus exerting their cytotoxic potential [203-204].

4.B.2.5.3. Cytotoxic effect on OSC cell-line

The *in vitro* cytotoxicity of Ce6-PVP-Alg NP formulation to OSC cells was evaluated by determining the cell survival after 8 hr of incubation under either dark or laser-irradiated conditions, as discussed in section 4.B.1.5.3. As observed in case of SEP/SEL-Ce6 NS, no cytotoxicity was observed for both pure Ce6 (control) and SEP/SEL-Ce6 NS (Figure 49 a) in dark conditions, indicating selective phototoxicity of the chlorin photosensitizer. As can be seen, the cell viability gradually decreased with increase in Ce6 concentration in both free and NP-bound form suggesting phototoxic effect on OSC cell-lines. Although Ce6 in NP-bound form exhibited enhanced cytotoxicity compared to the control as observed by steep decrease in cell viability at equivalent concentrations of Ce6. This was supported by approximately 10-times lower IC_{50} value of the Ce6-PVP-Alg NP formulation than that of the control. This clearly suggested the better effectiveness of Ce6-PVP complex in the nanoparticulate form compared to the solution form of free Ce6. The potent cytotoxicity could be attributed to the presence of PVP-bound Ce6 monomers facilitating the enhanced singlet oxygen generation. These monomeric species became gradually available through degradation of the alginate matrix and exerted their cytotoxic activity. In case of free Ce6 solution, albeit of substantial cellular uptake, Ce6 was mostly present as aggregated from and therefore, the singlet generation was interrupted and a

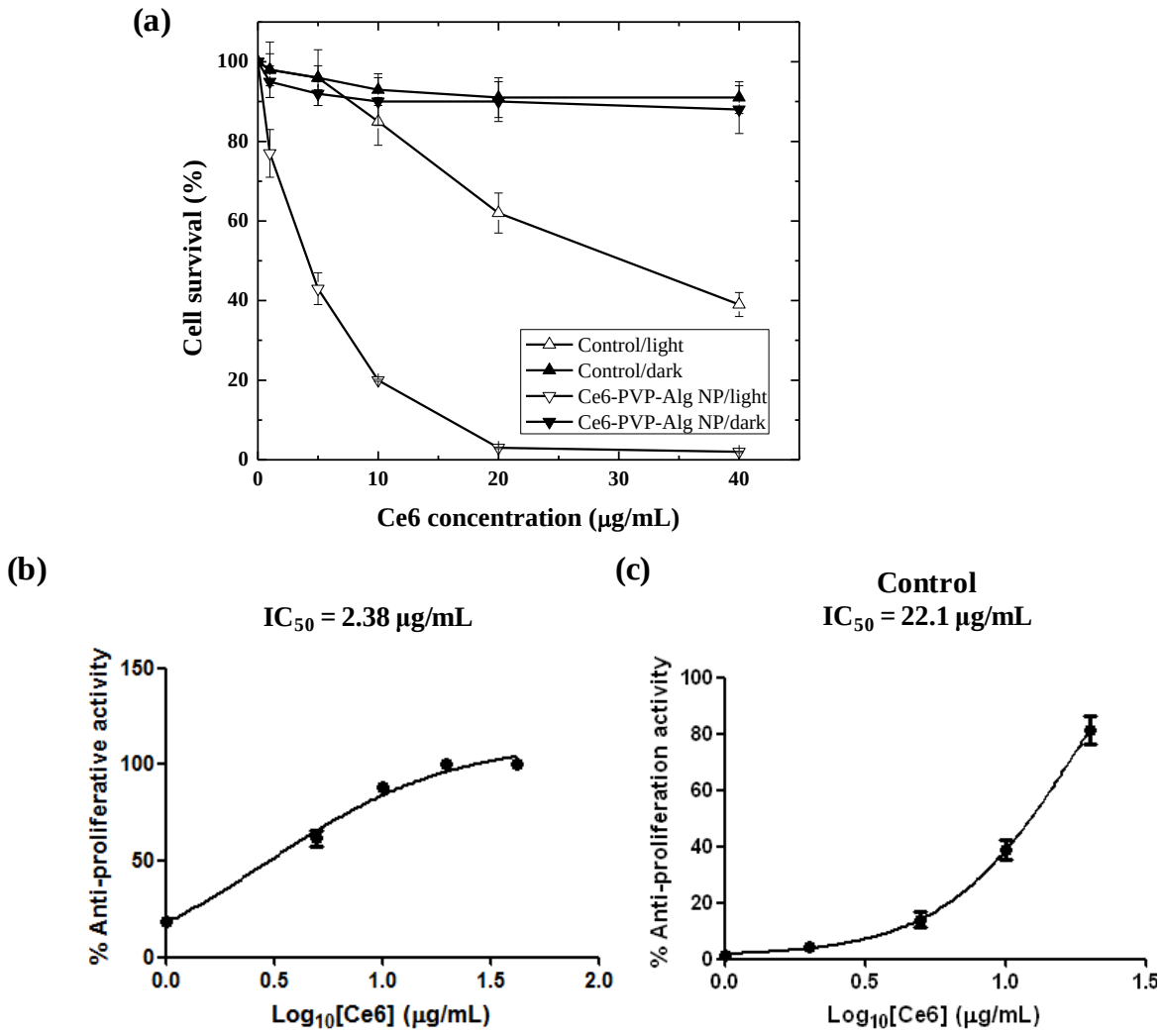

Figure 49: (a) Phototoxicity and (b) inhibitory concentration (50%) of the optimized Ce6-PVP-Alg NP formulation and (c) control (n = 6).

much higher concentration of Ce6 was required to elicit the similar cytotoxic action as that of Ce6-PVP-Alg NPs. Another plausible explanation could be the localization of the photosensitizer was more efficient, when delivered in the nanoparticulates form than in the free form [220-221].

The optimized hydrogel nanoparticulate formulation would be suitable for topical application to the carcinoma in buccal mucosa. The nanoparticulate formulation could be

centrifuged and the concentrated pellet applied to the affected buccal mucosa. The mucoadhesive property of the drug carriers (PVP and alginate) would facilitate improved mucosal absorption at the affected site.

The efficacy of Ce6 in superficial cancers such as carcinoma of the buccal mucosa has not yet been established. This study clearly demonstrated the improved mucosal absoption of the nanoparticulate form of Ce6 with PVP and alginate as drug carriers. These formulations were found to be mucoadhesive. Their mucoadhesivity can probably be further improved by the incorporation of other additives, such as chitosan, poly-lysine or poly-ethylenemine. However, these additives may prolong drug release and therefore not suitable for PDT modality.

4.B.2.6. Summary

In this section, the potential of alginate polymer as a hydrophilic nanoparticulate matrix for mucosal delivery was investigated. The effectiveness of the formulation was further studied by incorporating PVP in the system. PVP was found to form a complex with Ce6. The complex was encapsulated by the alginate matrix cross-linked by calcium. PVP rendered Ce6 in disaggregated state (monomer form) and also enhanced percent mucoadhesivity and drug dissolution, thus aptly increasing the PDT efficacy of the formulation. The formulations were optimized by statistical screening design with the concentrations of Ce6 and PVP as independent variables. Results showed that the independent variables had greatly influenced the formulation characteristics, which revealed statistical significance when fitted in quadratic regression models. The optimized formulation showed a manifold increase in photodynamic potential compared

to the free Ce6 solution and hence, establishing the rationale of oral mucosal delivery of Ce6-PVP complex encapsulated in alginate nanoparticles.

PART 5: CONCLUSION

5. CONCLUSION

Ce6 is a photosensitizer currently used in photodynamic therapy (PDT) to treat cancer. The usefulness of Ce6 is limited by its hydrophobicity and tendency to aggregate. The objectives of this study were to elucidate the factors affecting aggregate formation of Ce6 and explore the use of non-toxic pharmaceutical excipients as disaggregating agents. The suitability of the selected disaggregating agents as drug carriers for Ce6 was also investigated.

Chlorin e6 existed predominantly as aggregates in acidic to near neutral pH conditions as exhibited by broadened absorption spectra, reduced fluorescence intensity and lower quantum yield in the afore-mentioned pH conditions. Under such comditions, the carboxylic acid moieties of Ce6 were unionized and formed H-bonding resulting in aggregation of Ce6 molecules. In alkaline pH conditions, ionization of the carboxylic acid moieties took place, which simultaneously increased Ce6 solubility with reduced aggregate formation propensity resulting in the predominance of Ce6 monomers. Multivariate chemometric approach, PARAFAC algorithm was employed to quantify the extent of aggregate and monomer fraction for varying pH and Ce6 concentrations. It revealed that aggregation was mostly a pH-dependent phenomenon and was not affected by varying Ce6 concentration.

Polyvinylpyrrolidone (PVP) and sucrose ester (SE) were able to reduce the aggregation of Ce6. The disaggregation efficiency varied with the grades of PVP and SE employed. Both the disaggregating agents favoured a hydrophobic binding affinity with Ce6 as reflected from the thermodynamic study and FT-IR spectroscopy. Ce6 monomers formed complex by entangling with PVP macromolecules, while micellization of the Ce6

monomers in the hydrophobic core of SE prompted the disaggregation. The PARAFAC analysis showed that PVP K17 and sucrose monopalmitate (SEP) exhibited highest disaggregation potential on the basis of minimum amount of PVP/SE required for complete disaggregation among the different grades of disaggregating agents employed. It was found that, PVP of lower molecular weight had higher number of molecules per constant PVP weight and therefore had a better probability of complex formation with Ce6, while very low CMC value of SEP facilitated the use of minimal quantity for the study. Henceforth, these were later used as drug carrier for Ce6. Compared to pure (crude) Ce6, the complex composed of Ce6 and disaggregating agents exhibited higher singlet oxygen generation, cellular uptake and anti-proliferative activity against oral mucosal carcinoma cells. This aptly suggested that the monomer rich form of Ce6 predominated in the mixture by the action of PVP/SE, which had better photodynamic efficacy than the aggregate-rich (crude) Ce6.

In the next stage, dissolution enhancement of Ce6 was successfully achieved by formulating into nanosuspension using sucrose ester as matrix by a modified hot-melt emulsification technique. Monomeric Ce6-PVP complex was also encapsulated in alginate nanoparticles, thus providing enhanced mucoadhesivity for improved photodynamic efficacy against oral mucosal carcinoma cells. Sucrose ester facilitated enhanced dissolution of Ce6 by micellization and subsequently retained Ce6 in disaggregated form, thus facilitating improved PDT activity. In addition, the process modification resulted in amorphous form of Ce6 in the resultant nanosuspension. The optimized formulation showed an acceptable size and zeta potential value with 80 % Ce6 encapsulated in SE matrix, which exhibited approximately 85 % release within 2.5 hr.

Alginate nanoparticles consisting of PVP-Ce6 complex exhibited high affinity for mucin and cellular uptake than corresponding nanoparticles without PVP. This was attributed to synergistic effect of alginate and PVP, which facilitated increased mucin absorption and cellular uptake. Both the optimized Ce6-SE nanosuspension and alginate nanoparticles consisting Ce6-PVP complex showed enhanced PDT efficacy. This clearly showed the suitability of PVP or SE as drug carriers as well as disaggregating agent for Ce6.

In summary, this study showed a deep understanding of chlorin e6 photophysics in different pH conditions and in the presence of disaggregating agents, namely PVP and SE. This study is the first of its kind to quantify aggregate-to-monomer conversion by application of novel chemometric approach. Based on the findings, formulation of Ce6 with enhanced PDT activity could be achieved using PVP or SE as drug carriers. These formulations were found to be highly effective against oral mucosal carcinoma cells when used at low concentrations.

PART 6: LIST OF REFERENCES

6. LIST OF REFERENCES

1. Wilson BC (2002) Photodynamic therapy for cancer: principles. Can J Gastroenterol 16:393-396.
2. Dolmans DE, Fukumura D, Jain RK (2003) Photodynamic therapy for cancer. Nat Rev Cancer 3:380-387.
3. Guedes RC, Eriksson LA (2007) Photophysics, photochemistry, and reactivity: molecular aspects of perylenequinone reactions. Photochem Photobiol Sci 6:1089-1096.
4. Huang Z (2005) A review of progress in clinical photodynamic therapy. Technol Cancer Res Treat 4:283-293.
5. Moan J, Peng Q (2003) An outline of the hundred-year history of PDT. Anticancer Res 23:3591-3600.
6. Olivo M, Chin W (2008) Perylenequinones in Photodynamic Therapy: Cellular versus Vascular Response. J Environ Pathol Toxicol Oncol 25:223-238.
7. Pervaiz S, Olivo M (2006) Art and science of photodynamic therapy. Clin Exp Pharmacol Physiol 33:551-556.
8. Sibata CH, Colussi VC, Oleinick NL, Kinsella TJ (2001) Photodynamic therapy in oncology. Expert Opin Pharmacother 2:917-927.
9. Olivo M, Soo KC (2001) Photodynamic Therapy Comes of Age. SGH Proceedings 9:197-201.
10. Oleinick NL, Evans HH (1998) The photobiology of photodynamic therapy: cellular targets and mechanisms. Radiation Res. 150:S146-S156.
11. Dogherty TJ, Lawrence G, Kaufmann JH, Byle D, Weishaupt KR, Goldfarb A (1979) Photoradiation in the treatment of recurrent breast carcinoma. J Natl cancer Inst 62:231.
12. Potter WR, Mang TS, Dougherty TJ (1987) The theory of photodynamic therapy dosimetry: consequences of photo-destruction of sensitizer. Photochem Photobiol 46:97-101.

13. Dogherty TJ, Mang TS (1987) Characterization of intra-tumoral porphyrin following injection of hematoporphyrin derivative or its purified component.Photochem. Photobiol. 46:67.
14. Muschter R (2003) Photodynamic therapy: a new approach to prostate cancer. Curr Urol Rep. 4:221-8.
15. Bellienier DA, Ho YH, Pandey RK, Missert JR, Dogherty TJ (1989) Distribution and elimination of Photofrin II in mice.Photochem. Photobiol. 50:221.
16. Mironov A, Nizhnik A, Nochel A. (1990) Hematoporphyrin derivatives: an oligomeric composition study.Photochem. Photobiol. 4:297.
17. Pandey RK, Goswami LN, Chen Y, Gryshuk A, Missert JR, Oseroff A, Dougherty TJ (2010) Bifunctional agents for imaging and therapy. Methods Mol Biol. 635:223-59.
18. Kessel D, Thompson P, Musselman B, Chang CK, Photochem. Photobiol. 1987. Chemistry of hematoporphyrin-derived photosensitizers. Photochem Photobiol.46:563.
19. Juzeniene A, Peng Q, Moan J (2007) Milestones in the development of photodynamic therapy and fluorescence diagnosis. Photochem Photobiol Sci 6:1234- 1245.
20. Hayata Y, Kato H. Konaka C, Ono J, Takizawa N (1982) Hacmatoporphyrin derivative and laser photoirradiation in the treatment of lung cancer. Chest 81:269-277.
21. Maunoury V, Mordon S, Bulois P, Mirabel X, Hecquet B, Mariette C (2005) Photodynamic therapy for early oesophageal cancer. Dig Liver Dis. 37:491-495.
22. Byme CJ, Marshallsay LV, A.D. Ward AD (1990) The composition of Photofrin IT. J. Photochenl. Photohiol. B 6:13-27.
23. Potter WR, Henderson BW, Bellnier DA, Pandey RK, Vaughan LA, Weishaupt KR, Dougherty TJ. Parabolic quantitative structure-activity relationships and photodynamic therapy: application of a three-compartment model with clearance to the in vivo quantitative structure-activity relationships of a congeneric series of pyropheophorbide derivatives used as photosensitizers for photodynamic therapy. Photochem. Photobiol. 70:781-788.

24. Doiron DR, Svaasand LO, Profio AE (1983) Light dosimetry in tissue: application to photoradiation therapy. Adv Exp Med Biol. 160:63-76.
25. Profio AE, Doiron DR (1981). Dosimetry considerations in phototherapy. Med. Phys. 8:190-196.
26. Rasmussen-Taxdal DS, Ward GE, Figge FH (1955) Fluorescence of human lymphatic and cancer tissues following high doses of hematoporphyrin, Cancer 8:78-81.
27. Figge FH, Weiland GS, Manganiello LO (1948). Cancer detection and therapy: affinity of neoplastic, embryonic and traumatized tissues for porphyrin and metallo-porphyrins. Proc. Soc. Exp. Biol. Med. 68:634-641.
28. Roder B, Wabnitz H (1987) Time-resolved fluorescence spectroscopy of hematoporphyrin, mesoporphyrin, pheophorbide and chlorin e6 in ethanol and aqueous solution. J. Photochem. Photobiol. B 1:103-113.
29. M. Del Governatore M, Hamblin MR , Piccinin EEi, Ugolini, Hasan GT (2000). Targeted photodestruction of human colon cnacer cells using charged 17,1A chlorin e6 immunoconjugates. Br. J. Cancer 82:56-64.
30. Sharman WM, Allen CM, van Lier JE (1999) Photodynamic therapeutics: basic principles and clinical applications. Drug Discov Today. 4:507-517.
31. Pass HI (1993) Photodynamic therapy in oncology: mechanisms and clinical use. J. Natl. Cancer Inst. 85:443-456.
32. Kessel D (1989) In vitro photosensitization with a benzoporphyrin derivative. Photochem. Photobiol. 49:579-582.
33. Kostenich G, Orenstein A, Roitman L, Malik Z, Ehrenberg B (1997). In vivo photodynamic therapy with the new near-IR absorbing water soluble photosensitizer lutetium texaphyrin and a high intensity pulsed light delivery system. J. Photochem. Photobiol. B 39:36-42.
34. Webber J, Herman M, Kessel D, Fromm D (1999) Current concepts in gastrointestinal photodynamic therapy. Ann Surg. 230(1):12-23.
35. Ochsner M (1997) Photodynamic therapy: the clinical perspective. Review on applications for control of diverse tumorous and non-tumorous diseases. Arzneimittelforschung. 47:1185-94.

36. Robertson CA, Evans DH, Abrahamse H (2009) Photodynamic therapy (PDT): a short review on cellular mechanisms and cancer research applications for PDT. J Photochem Photobiol B. 96:1-8.
37. Grune T, Klotz LO, Gieche J, Rudeck M, Sies H (2001) Protein oxidation and proteolysis by the nonradical oxidants singlet oxygen or peroxynitrite. Free Radic Biol Med 30:1243-53.
38. Midden WR, Dahl TA (1992) Biological inactivation by singlet oxygen: distinguishing O2(1 delta g) and O2(1 sigma g+). Biochim Biophys Acta 1117:216-22.
39. Geiger PG, Korytowski W, Lin F, Girotti AW (1997) Lipid peroxidation in photodynamically stressed mammalian cells: use of cholesterol hydroperoxides as mechanistic reporters. Free Radic Biol Med. 23:57-68.
40. Bachowski GJ, Pintar TJ, Girotti AW (1991) Photosensitized lipid peroxidation and enzyme inactivation by membranebound merocyanine 540: reaction mechanisms in the absence and presence of ascorbate. Photochem Photobiol 53:481-91.
41. Sono M, Roach MP, Coulter ED, Dawson JH (1996) Heme-containing oxygenases. Chem Rev 96:2841–2887.
42. Detty MR, Gibson SL, Wagner SJ (2004) Current clinical and preclinical photosensitizers for use in photodynamic therapy. J Med Chem. 47:3897-3915.
43. Kennedy JC, Pottier RH, Pross DC (1990) Photodynamic therapy with endogenous protoporphyrin IX. Basic principles and present clinical-experience. J Photochem Photobiol B 6:143-148.
44. Eisfeld A, Briggs JS (2005) The J- and H-bands of organic dye aggregates. Chem. Phys. 324:376-384.
45. Maiti NC, Mazumdar S, Periasamy N (1998) J- and H-aggregates of porphyrin-surfactant complexes: time-resolved fluorescence and other spectroscopic studies. J. Phys. Chem. B 102:1528-1538.
46. Siddiqui S, Spano FC. (1999) H- and J-aggregates of conjugated polymers and oligomers: A theoretical investigation. Chem. Phys. Lett. Volume 308:99–105.

47. Eichwurzel I, Stiel H and Roder B (2000) Photophysical studies of the pheophorbide a dimer. J. Photochem Photobiol B 54:194-200.
48. Cunderlikova B, Gangeskar L, Moan J (1999) Acid-base properties of chlorin e6: relation to cellula uptake. J. Photochem Photobiol B 53:81-90.
49. Margalit R, Rotenberg M (1984) Porphyrin dimerization in aqueous solutions. Biochem J. 219:445-450.
50. Shiah J, Koiok C, Spikes JD, Eek JK (1998) Influence of pH on aggregation and photoproperties of of N-(2-hydroxypropyl) methacrylamide copolymer-meso-chlorin e6 conjugates. Drug Deliv. 5:119-26.
51. McRae EG (1957) Theory of Solvent Effects on Molecular Electronic Spectra. Frequency Shifts J. Phys. Chem. 61:562-572.
52. Gómez ML, Previtali CM, Montejano HA (2003) Photophysical properties of safranine O in protic solvents. Spectrochim Acta A Mol Biomol Spectrosc. 60:2433-9.
53. Mannekutla JR, Mulimani BG, Inamdar SR (2007) Solvent effect on absorption and fluorescence spectra of coumarin laser dyes: evaluation of ground and excited state dipole moments. Spectrochim Acta A Mol Biomol Spectrosc. 69:419-26.
54. Biswas S, Ahn HY, Bondar MV, Belfield KD (2012) Two-photon absorption enhancement of polymer-templated porphyrin-based J-aggregates. Langmuir. 28:1515-22.
55. Gonçalves PJ, Franzen PL, Correa DS, Almeida LM, Takara M, Ito AS, Zílio SC, Borissevitch IE (2011) Effects of environment on the photophysical characteristics of mesotetrakis methylpyridiniumyl porphyrin (TMPyP). Spectrochim Acta A Mol Biomol Spectrosc. 79:1532-9.
56. Wehry L, Effects of molecular environment on fluorescence and phosphorescence, in: Guilbault G.G. (Ed.), Practical Fluorescence, 2nd ed., Dekker, New York, USA, 1990.
57. Klotz IM (1973) Physiochemical aspects of drug-protein interactions: a general perspective. Ann N Y Acad Sci. 226:18-35.

58. Labouebe MZ, Mattiuzzo M, Lange N, Gurny R, Delie F (2009) Quenching-induced deactivation of photosensitizer by nanoencapsulation to improve phototherapy of cancer. J Drug Target. 17:619-26.

59. Campo MA, Gabriel D, Kucera P, Gunny R, Lange N (2007) Polymeric photosensitizer prodrugs for photodynamic therapy. Photochem Photobiol 83:958-965.

60. Clo E, Snyder JW, Ogilby PR, Gothelf KV (2007) Control and selectivity of photo-sensitized singlet oxygen production: challenges in complex biological systems. Chembiochem, 8:475-481.

61. Svaasand LO (1989) Optical dosimetry for direct and interstitial photoradiation therapy of malignant tumours. Prog Clin Biol Res 170:91-114.

62. Wilson BC, Jeeves WP, Lowe DM (1985) In vivo and post mortem measurements of the attenuation spectra of light in mammalian tissues. Photochem Photobiol 42:153-62.

63. Firey PA, Rodgers MA (1987) Photo-properties of a silicon naphthalocyanine: a potential photosensitizer for photodynamic therapy. Photochem Photobiol 45:535-8.

64. van Leengoed HL, Schuitmaker JJ, van der Veen N, Dubbelman TM, Star WM (1993) Fluorescence and photodynamic effects of bacteriochlorin a observed in vivo in ‘sandwich’ observation chambers. Br J Cancer 67:898-903.

65. Brancaleon L, Moseley H (2002) Laser and non-laser light sources for photodynamic therapy. Lasers Med Sci 17:173-186.

66. Vulcan TG, Zhu TC, Rodriguez CE, His A, Fracker DL, Baas P, Murrer LH, Star WM, Glatstein E, Yodh AG, Hahn SM (2000) Comparison between isotropic and non-isotropic dosimetry systems during intraperitoneal photodynamic therapy. Laser Surg Med 26:292-301.

67. Hayden O, Payne CK (2005) Nanophotonic light sources for fluorescence spectroscopy and cellular imaging. Angew Chem 44:1395-8.

68. Kendall CA, Morton CA (2003) Photodynamic therapy for the treatment of skin diseases. Technol Cancer Res Treat 2: 283-288.

69. Pandey RK (2000) Recent advances in photodynamic therapy. J Porphyr Phthalocyan. 4:368-73.
70. Brown SB, Brown EA, Walker I (2004) The present and future role of photodynamic therapy in cancer treatment. Lancet Oncol 5:497-508.
71. Teicher BA (2000) Molecular targets and cancer therapeutics: discovery, development and clinical validation, Drug Resist. Updat. 3:67-73.
72. Courvreur P, Grislain L, Lenaerts V, Brasseur F, Guiot P, Biornacki A (1986) Biodegradable polymeric nanoparticles as drug carrier for antitumour agents, in: P Guiot, P. Corvreur (Eds.), Polymeric Nanoparticles and Microspheres, Boca Raton, CRC Press: 27-93.
73. Moan J, Peng Q, Sorensen R, Iani V, Neslan JM (1998) The biophysical foundations of photodynamic therapy. Endoscopy 30:387-91.
74. Meetoo D (2009) Nanotechnology: the revolution of the big future with tiny medicine. Br J Nurs 18:1201-6.
75. Zhang L, Gu FX, Chan JM, Wang AZ, Langer RS, Farokhzad OC (2008) Nanoparticles in medicine: therapeutic applications and developments. Clin Pharmacol Ther 83:761-9.
76. Jain KK (2008) Recent advances in nanooncology. Technol. Cancer Res. Treat. 7:1-14
77. Torchilin VP. (2007) Targeted pharmaceutical nanocarriers for cancer therapy and imaging. AAPS J 9:E128-47.
78. Kozlowska D, Foran P, MacMahon P, Shelly MJ, Eustace S, O'Kennedy R (2009) Molecular and magnetic resonance imaging: the value of immunoliposomes. Adv Drug Deliv Rev 61:1402-11.
79. Konan-Kouakou YN, Boch R, Gurny R, Allemann E (2005) In vitro and in vivo activities of verteporfin-loaded nanoparticles. J Control Release 103:83-91.
80. Lee SJ, Koo H, Lee DE, Min S, Lee S, Chen X, Choi Y, Leary JF, Park K, Jeong SY, Kwon IC, Kim K, Choi K (2011) Tumor-homing photosensitizer-conjugated glycol chitosan nanoparticles for synchronous photodynamic imaging and therapy based on cellular on/off system. Biomaterials 32:4021-4029.

81. van Nostrum CF (2004) Polymeric micelles to deliver photosensitizers for photodynamic therapy. Adv Drug Deliv Rev. 56:9-16.
82. Rijcken CJ, Hofman JW, van Zeeland F, Hennink WE, van Nostrum CF (2007) Photosensitiser-loaded biodegradable polymeric micelles: Preparation, characterisation and in vitro PDT efficacy. J Control Release 124:144-153.
83. Derycke AS, de Witte PA (2004) Liposomes for photodynamic therapy. Adv Drug Deliv Rev. 56:17-30.
84. Shum P, Kim JM, Thompson DH (2001) Phototriggering of liposomal drug delivery systems. Adv Drug Deliv Rev. 53:273-84.
85. Lilge L, Wilson BC (1998) Photodynamic therapy of intracranial tissues: a preclinical comparative study of four different photosensitizers. J Clin Laser Med Surg. 16:81-91.
86. Tekade RK, Kumar PV, Jain NK (2009) Dendrimers in oncology: An expanding horizon. Chem Rev 109:49-87.
87. Kojima C, Toi Y, Harada A, Kono K (2007) Preparation of poly(ethylene glycol)-attached dendrimers encapsulating photosensitizers for application to photodynamic therapy. Bioconjug Chem. 18:663-670.
88. Rebeiz N, Arkins S, Rebeiz CA, Simon J, Zachary JF, Kelley KW (1996) Induction of tumor necrosis by delta-aminolevulinic acid and 1,10-phenanthroline photodynamic therapy. Cancer Res. 56:339-44.
89. Bakalova R, Ohba H, Zhelev Z, Nagase T, Jose R, Ishikawa M, Baba Y (2004) Quantum dot anti-CD conjugates: Are they potential photosensitizers or potentiators of classical photosensitizing agents in photodynamic therapy of cancer? Nano Lett 4:1567-1573.
90. Cinteza LO, Ohulchanskyy TY, Sahoo Y, Bergey EJ, Pandey RK, Prasad PN (2006) Diacyllipid micellebased nanocarrier for magnetically guided delivery of drugs in photodynamic therapy. Mol Pharm. 3:415-423.
91. Brigger I, Dubernet C, Couvreur P (2002) Nanoparticles in cancer therapy and diagnosis. Adv. Drug Deliv. Rev 54:631-651.

92. Soppimath KS, Aminabhavi TM, Kulkarni AR, Rudzinski WE (2001) Biodegradable polymeric nanoparticles as drug delivery devices. J Control Release 70:1-20.
93. Konan YN, Cerny R, Favet J, Berton M, Gurny R, Allemann E (2003) Preparation and characterization of sterile sub-200nm meso-tetra(4 hydroxylphenyl) porphyrinloaded nanoparticles for photodynamic therapy. Eur J Pharm Biopharm 55:115-124.
94. Bourdon O, Mosqueira V, Legrand P, Blais J (2000) A comparative study of the cellular uptake, localization and phototoxicity of meta-tetra(hydroxyphenyl) chlorin encapsulated in surface-modified submicronic oil/watercarriers in HT29 tumour cells. J Photochem Photobiol B 55:164-171.
95. Tang W, Xu H, Park EJ, Philbert MA, Kopelman R (2008) Encapsulation of methylene blue in polyacrylamide nanoparticle platforms protects its photodynamic effectiveness. Biochem Biophys Res Commun. 369:579-583.
96. Lee SJ, Park K, Oh YK, Kwon SH, Her S, Kim IS, Choi K, Lee SJ, Kim H, Lee SG, Kim K, Kwon IC (2009) Tumour specificity and therapeutic efficacy of photosensitizer-encapsulated glycol chitosan-based nanoparticles in tumour-bearing mice. Biomaterials 30:2929-2939.
97. Bae BC, Na K (2010) Self-quenching polysaccharide-based nanogels of pullulan/folate-photosensitizer conjugates for photodynamic therapy. Biomaterials 31:6325-35.
98. Hamblin R, Miller JL, Rizvi I, Ortel B, Maytin EV, Hasan T (2001) Pegylation of a chlorin e(6)-polymer conjugate increases tumour targeting of photosensitizer. Cancer Res 61:7155-7162.
99. Regehly M, Greish K, Rancan F, Maeda H, Bohm F, Roder B (2007) Water-soluble polymer conjugates of ZnPP for photodynamic tumour therapy. Bioconjug Chem 18:494-499.
100. Lukyanov AN, Torchilin VP (2004) Micelles from lipid derivatives of water-soluble polymers as delivery systems for poorly soluble drugs. Adv. Drug Deliv. Rev 56:1273-1289.

101. Roby A, Erdogan S, Torchilin VP (2006) Solubilization of poorly soluble PDT agent, meso-tetraphenylporphin, in plain or immunotargeted PEG-PE micelles results in dramatically improved cancer cell killing in vitro. Eur J Pharm Biopharm 62:235-240.

102. Rijcken CJ, Hofman JW, van Zeeland F, Hennink WE, van Nostrum CF (2007) Photosensitiser-loaded biodegradable polymeric micelles: Preparation, characterization and in vitro PDT efficacy. J Control Release 124:144-153.

103. Li B, Moriyama EH, Li F, Jarvi MT, Allen C, Wilson BC (2007) Diblock copolymer micelles deliver hydrophobic protoporphyrin IX for photodynamic therapy. Photochem Photobiol. 83:1505-1512.

104. Nishiyama N, Nakagishi Y, Morimoto Y, Lai PS, Miyazaki K, Urano K, Horie S, Kumagai M, Fukushima S, Cheng Y, Jang WD, Kikuchi M, Kataoka K (2009) Enhanced photodynamic cancer treatment by supramolecular nanocarriers charged with dendrimer phthalocyanine. J Controlled Release 133:245-251.

105. Reinke MH, Canakis C, Husain D, Michaud N, Flotte TJ, Gragoudas ES, Miller JW (1999) Verteporfin photodynamic therapy retreatment of normal retina and choroid in the cynomolgus monkey. Ophthalmology 106:1915-1923.

106. Husain D, Kramer M, Kenny AG, Michaud N, Flotte TJ, Gragoudas ES, Miller JW (1999) Effects of photodynamic therapy using verteporfin on experimental choroidal neovascularization and normal retina and choroid up to 7 weeks after treatment. Invest Ophthalmol Vis Sci. 40:2322–2331.

107. Jiang F, Lilge L, Grenier J, Li Y, Wilson MD, Chopp M (1998) Photodynamic therapy of U87 human glioma in nude rat using liposome-delivered photofrin. Lasers Surg Med 22:74–80.

108. Allen TM, Hansen CB, Lopes de Menezes DE (1995) Pharmacokinetics of long-circulating liposomes. Adv. Drug Deliv. Rev 16:267-284.

109. Fang YP, Wu PC, Tsai YH, Huang YB (2008) Physicochemical and safety evaluation of 5-aminolevulinic acid in novel liposomes as carrier for skin delivery. J Liposome Res 18:31-45.

110. Sadzuka Y, Iwasaki F, Sugiyama I, Horiuchi K, Hirano T, Ozawa H, Kanayama N, Sonobe T (2007) Study on liposomalization of zinc-coproporphyrin I as a novel drug in photodynamic therapy. Int J Pharm 338:209-306.
111. Michalet X, Pinaud FF, Bentolila LA, Tsay JM, Doose S, Li JJ, Sundaresan G, Wu AM, Gambhir SS, Weiss S (2005) Quantum dots for live cells, in vivo imaging, and diagnostics. Science 307:538-544.
112. Yaghini E, Seifalian AM, MacRobert AJ (2009) Qantum dots and their potential biomedical applications in photosensitization for photodynamic therapy. Nanomedicine 4:353-63.
113. Dubertret B, Skourides P, Norris DJ, Noireaux V, Brivanlou AH, and Libchaber A (2002) In vivo imaging of quantum dots encapsulated in phospholipid micelles. Science 298:1759-1762.
114. Chan WC, Nie S (1998) Quantum dot bioconjugates for ultrasensitive nonisotopic detection. Science 281:2016-2018.
115. Samia AC, Chen X, Burda C (2003) Semiconductor quantum dots for photodynamic therapy. J Am Chem Soc 125:15736-15737.
116. Tsay JM, Trzoss M, Shi L, Kong X, Selke M, Jung ME, Weiss S (2007) Singlet oxygen production by peptide-coated quantum dotphotosensitizer conjugates. J Am Chem Soc 129:6865-6871.
117. Kojima C, Toi Y, Harada A, Kono K (2007) Preparation of poly(ethylene glycol)-attached dendrimers encapsulating photosensitizers for application to photodynamic therapy. Bioconjug Chem. 18:663-670.
118. Ideta R, Tasaka F, Jang WD, Nishiyama N, Zhang GD, Harada A, Yanagi Y, Tamaki Y, Aida T, Kataoka K (2005) Nanotechnologybased photodynamic therapy for neovascular disease using a supramolecular nanocarrier loaded with a dendritic photosensitizer. Nano Lett 5:2426-2431.
119. Rosi NL, Giljohann DA, Thaxton CS, Lytton-Jean AK, Han MS, Mirkin CA (2006) Oligonucleotide-modified gold nanoparticles for intracellular gene regulation. Science 312:1027-1030.

120. Giljohann DA, Seferos DS, Prigodich AE, Patel PC, Mirkin CA (2009) Gene regulation with polyvalent siRNA nanoparticle conjugates. J Am Chem Soc 131:2072-2073.

121. Hone DC, Walker PI, Richard EG, Fitzgerald S, Beeby A, Chambrier I, Cook MJ, Russell DA (2002) Generation of cytotoxic singlet oxygen via phthalocyanine stabilized gold nanoparticles: A potential delivery vehicle for photodynamic therapy. Langmuir 18:2985-2987.

122. Oo MK, Yang X, Du H, Wang H (2008) 5-aminolevulinic acid-conjugated gold nanoparticles for photodynamic therapy of cancer. Nanomedicine 3:777-786.

123. Tu HL, Lin YS, Lin HY, Hung Y, Lo LW, Chen Y, Mou CY (2009) In vitro studies of functionalized mesoporous silica nanoparticles for photodynamic therapy. Adv. Mater. 21:172-177.

124. Roy I, Ohulchanskyy TY, Pudavar HE, Bergey EJ, Oseroff AR, Morgan J, Dougherty TJ, Prasad PN (2003) Ceramic-based nanoparticles entrapping water-insoluble photosensitizing anticancer drugs: A novel drug-carrier system for photodynamic therapy. J Am Chem Soc 125:7860-7865.

125. Kim S, Ohulchanskyy TY, Pudavar HE, Pandey RK, Prasad PN (2007) Organically modified silica nanoparticles co-encapsulating photosensitizing drug and aggregation-enhanced two-photon absorbing fluorescent dye aggregates for two-photon photodynamic therapy. J Am Chem Soc 129: 2669-2675.

126. Jain TK, Richey J, Strand M, Leslie-Pelecky DL, Flask CA, Labhasetwar V (2008) Magnetic nanoparticles with dual functional properties: Drug delivery and magnetic resonance imaging. Biomaterials 29: 4012-4021.

127. Gao J, Gu H, Xu B (2009) Multifunctional magnetic nanoparticles: Design, synthesis, and biomedical applications. Acc. Chem. Res 42:1097-1107.

128. Jain TK, Morales MA, Sahoo SK, Leslie-Pelecky DL, Labhasetwar V (2005) Iron oxide nanoparticles for sustained delivery of anticancer agents. Mol Pharm. 2: 194-205.

129. Gu H, Xu K, Yang Z, Chang CK, Xu B (2005) Synthesis and cellular uptake of porphyrin decorated iron oxide nanoparticles – a potential candidate for bimodal anticancer therapy. Chem Commun 34:4270–4272.

130. Gust D, Moore TA, Moore AL (2000) Photochemistry of supramolecular systems containing C60. J Photochem Photobiol B 58:63–71.
131. Andrievsky GV, Bruskov VI, Tykhomyrov AA, Gudkov SV (2009) Peculiarities of the antioxidant and radioprotective effects of hydrated C60 fullerene nanostuctures in vitro and in vivo. Free Radic Biol Med. 47:786-93.
132. Kennedy JC, Pottier RH (1992) Endogenous protoporphyrin IX, a clinically useful photosensitizer for photodynamic therapy. J Photochem Photobiol B 14:275-92.
133. Hogan A, Behan U, Kilmartin DJ (2005) Outcomes after combination photodynamic therapy and immunosupression for inflammatory subfoveal choroidal neovascularisation. Br J Ophthalmol 89:1109-11.
134. Kubler AC, de Carpentier J, Hopper C, Leonard AG, Putnam G (2001) Treatment of squamous cell carcinoma of the lip using Foscan mediated photodynamic therapy. Int J Oral Maxillofac Surg 30:504-9.
135. Isakau HA, Parkhats MV, Knyukshto VN, Dzhagarov BM, Petrov EP, Petrov PT (2008) Toward understanding the high PDT efficacy of chlorine e6–polyvinylpyrrolidone formulations: Photophysical and molecular aspects of photosensitizer–polymer interaction in vitro. J Photochem Photobiol B 92:165-74.
136. Mang TS, Allison R, Hewson G, Snider W, Moskowitz R (1998) A phase II/III clinical study of tin ethyl etiopurpurin (Purlytin)- induced photodynamic therapy for the treatment of recurrent cutaneous metastatic breast cancer. Cancer J Sci Am 4:378-84.
137. Dolmans DE, Fukumura D, Jain RK (2003) Photodynamic therapy for cancer. Nat Rev Cancer 3:380-7.
138. Pinthus JH, Bogaards A, Weersink R, Wilson BC, Trachtenberg J (2006) Photodynamic therapy for urological malignancies: past to current approaches. J Urol 175:1201-7.
139. D'Hallewin MA, Kochetkov D, Viry-Babel Y, Leroux A, Werkmeister E, Dumas D, Gräfe S, Zorin V, Guillemin F, Bezdetnaya L (2008) Photodynamic therapy with intratumoral administration of lipid-based mTHPC in a model of breast cancer recurrence. Lasers Surg Med 40:543-9.

140. Bellnier DA, Greco WR, Loewen GM, Nava H, Oseroff AR, Pandey RK, Tsuchida T, Dougherty TJ (2003) Population pharmacokinetics of the photodynamic therapy agent 2-[1-hexyloxyethyl]-2- devinyl pyropheophorbide-a in cancer patients. Cancer Res 63:1806-13.

141. Colasanti A, Kisslinger A, Kusch D, Liuzzi R, Mastrocinque M, Montforts FP, Quarto M, Riccio P, Roberti G, Villani F (1997) In vitro photo-activation of newly synthesized chlorin derivatives with red-light-emitting diodes. J Photochem Photobiol B 38:54-60.

142. Bachor R, Shea CR, Gillies R, Hasan T (1991) Photosensitized destruction of human bladder carcinoma cells treated with chlorin e6-conjugated microspheres. Proc Natl Acad Sci USA. 88:1580-1584.

143. Chin WW, Heng PW, Lim PL, Lau WK, Olivo M (2008) Improved formulation of photosensitizer chlorin e6 polyvinylpyrrolidone for fluorescence diagnostic imaging and photodynamic therapy of human cancer. Eur J Pharm Biopharm 69:1083-93.

144. Chin WW, Lau WK, Bhuvaneswari R, Heng PW, Olivo M (2007) Chlorin e6 polyvinylpyrrolidone as a fluorescent marker for fluorescence diagnosis of human bladder cancer implanted on the chick chorioallantoic membrane model. Cancer Lett. 245:127-133.

145. Chin WW, Lau WK, Bhuvaneswari R, Heng PW, Olivo M (2010) Effect of polyvinylpyrrolidone on the interaction of chlorin e6 with plasma proteins and its subcellular localization. Eur. J. Pharm. Biopharm. 76 :245-252.

146. Xiao H, Zhua B, Wang D, Pang Y, He L, Ma X, Wang R, Jin C, Chen Y, Zhu X (2012). Photodynamic effects of chlorin e6 attached to single wall carbon nanotubes through noncovalent interactions. Carbon 50: 1681-1689.

147. Lee DJ, Park GY, Oh KT, Oh NM, Kwag DS, Youn YS, Oh YT, Park JW, Lee ES (2012) Multifunctional poly (lactide-co-glycolide) nanoparticles for luminescence/magnetic resonance imaging and photodynamic therapy. Int. J Pharm. 434:257-63.

148. Park W, Park SJ, Na K (2011) The controlled photoactivity of nanoparticles derived from ionic interactions between a water soluble polymeric photosensitizer and polysaccharide quencher. Biomaterials. 32:8261-8270.
149. Schmitt F, Lagopoulos L, Käuper P, Rossi N, Busso N, Barge J, Wagnières G, Laue C, Wandrey C, Juillerat-Jeanneret L (2010) Chitosan-based nanogels for selective delivery of photosensitizers to macrophages and improved retention in and therapy of articular joints. J Control Release. 144:242-50.
150. Taima H, Okubo A, Yoshioka N, Inoue H (2005) Synthesis of cationic water-soluble esters of chlorin e6.Tetrahedron Lett 46:4161-4164.
151. Di Stasio B, Frochot C, Dumas D, Even P, Zwier J, Müller A, Didelon J, Guillemin F, Viriot ML, Barberi-Heyob M (2005) The 2-aminoglucosamide motif improves cellular uptake and photodynamic activity of tetraphenylporphyrin. Eur J Med Chem. 40:1111-22
152. Datta A, Dube A, Jain B, Tiwari A, Gupta PK (2007). The Effect of pH and Surfactant on the Aggregation Behaviour of Chlorin p6: A Fluorescence Spectroscopic Study. Photochem. Photobiol. 75: 488-494.
153. Yuan SL, Cai ZT, Xu GY, Jiang YS (2002) Mesoscopic simulation study on phase diagram of the system oil/water/aerosol OT, Chem. Phys. Lett. 365: 347-353.
154. Guo X, Zhang L, Yu Q, Zhou J (2007) Effect of composition on the formation of poly(DL-lactide) microspheres for drug delivery systems: Mesoscale simulations. Chem. Eng. J. 131: 195-201.
155. Shillcock JC. (2012) Spontaneous vesicle self-assembly: a mesoscopic view of membrane dynamics. Langmuir 28:541-7.
156. Groot RD (2000) Mesoscopic simulation of polymer-surfactant aggregation. Langmuir 16: 7493-7502.
157. Groot RD (2003) Electrostatic interactions in dissipative particle dynamics – simulation of polyelectrolytes and anionic surafactants, J. Chem. Phys. 118:11265-77.

158. Li W, Das S, Ng KY, Heng PW (2011). Formulation, biological and pharmacokinetic studies of sucrose ester-stabilized nanosuspensions of oleanolic Acid. Pharm Res. 28:2020-33.
159. Okamoto H, Sakai T, Danjo K (2005) Effect of sucrose fatty acid esters on transdermal permeation of lidocaine and ketoprofen. Biol Pharm Bull. 28:1689-94.
160. Cázares-Delgadillo J, Naik A, Kalia YN, Quintanar-Guerrero D, Ganem-Quintanar A (2005) Skin permeation enhancement by sucrose esters: a pH-dependent phenomenon. Int J Pharm 297:204-12.
161. Giri TK, Thakur D, Alexander A, Ajazuddin, Badwaik H, Tripathi DK (2012) Alginate based Hydrogel as a Potential Biopolymeric Carrier for Drug Delivery and Cell Delivery Systems: Present Status and Applications. Curr Drug Deliv 9:539-55.
162. Coviello T, Matricardi P, Alhaique F (2006) Drug delivery strategies using polysaccharidic gels. Expert Opin Drug Deliv 3:395-404.
163. Augst AD, Kong HJ, Mooney DJ (2006) Alginate hydrogels as biomaterials. Macromol Biosci 6:623-33.
164. Patil SB, Sawant KK (2009) Development, optimization and in vitro evaluation of alginate mucoadhesive microspheres of carvedilol for nasal delivery. J Microencapsul 26:432-43.
165. Lakowicz JR, Principles of Fluorescence Spectroscopy, Springer, Publishers, New York, 2006.
166. Ulrich KH (1981) Molecular aspects of ligand binding to serum albumin. Pharmacol Rev 33: 17–53.
167. Maruthamuthu M, Subramanian E (1992) Polymer-ligand interaction studies. Part I. Binding of some drugs to poly(N-vinyl-2-pyrrolidone). J. Chem. Sci. 104:417-424.
168. Ross DP, Sabramanian S (1981) Thermodyanmics of protein association reactions-forced contributing to stability. Biochemistry 20:3096-3102.
169. Urbán-Morlán Z, Ganem-Rondero A, Melgoza-Contreras LM, Escobar-Chávez JJ, Nava-Arzaluz MG, Quintanar-Guerrero D (2010) Preparation and

characterization of solid lipid nanoparticles containing cyclosporine by the emulsification-diffusion method. Int J Nanomedicine 7:611-20.

170. Lee DW, Shirley SA, Lockey RF, Mohapatra SS (2006). Thiolated chitosan nanoparticles enhance anti-inflammatory effects of intranasally delivered theophylline. Respir Res. 7: 112.

171. Kraljić I, El Mohsni S (2008) A new method for the detection of singlet oxygen in aqueous solutions. Photochem. Photobiol. 28:577-581.

172. Vermathen M, Marzorati M, Vermathen P, Bigler P (2010) pH-dependent distribution of chlorin e6 derivatives across phospholipid bilayers probed by NMR spectroscopy. Langmuir 26:11085-11094.

173. Parkhats MV, Galievsky VA, Stashevsky AS, Trukhacheva TV, Dzhagarov BM (2009) Dynamics and efficiency of the photosensitized singlet oxygen formation by chlorin e6: The effects of the solution pH and polyvinylpyrrolidone. Opt Spectrosc 107:974-980.

174. Datta A, Dube A, Jain B, Tiwari A, Gupta PK (2002) The effect of pH and surfactant on the aggregation behaviour of chlorin p6: a fluorescence spectroscopic study. Photochem Photobiol. 75:488-94.

175. Levi MAB, Scarminio IS, Poppi RJ, Trevisan MG (2004) Three-way chemometric method study and UV-Vis absorbance for the study of simultaneous degradation of anthocyanins in flowers of the Hibiscus rosa-sinensys species. Talanta 62:299–305.

176. JiJi RD, Andersson GG, Booksh KS (2000) Application of PARAFAC for calibration with excitation-emission matrix fluorescence spectra of three classes of environmental pollutants. J. Chemom. 14: 171–185.

177. Smith GJ, Ghiggino KP (1993) The photophysics of haematoporphyrin dimers or aggregates in aqueous solution. I The photophysics of haematoporphyrin dimers or aggregates in aqueous solution. J. Photochem. Photobiol. B 19:49-54.

178. Weishaupt KR, Gomer CJ, Dougherty TJ (1976) Identification of singlet oxygen as the cytotoxic agent in photoinactivation of a murine tumor. Cancer Res. 36:2326-2329.

179. Ahuja N, Katare OP, Singh B (2007) Studies on dissolution enhancement and mathematical modeling of drug release of a poorly water-soluble drug using water-soluble carriers. Eur J Pharm Biopharm 65:26-38.

180. Mote US, Bhattar SL, Patil SR, Kolekar GB (2010) Interaction between felodipine and bovine serum albumin: fluorescence quenching study. Luminescence 5:1-8.

181. Leckband D (2000) Measuring Forces that Control Protein Interactions. Ann. Rev. Biophys. Biomol. Structure 29:1-26.

182. am Ende MT, Peppa NA (1999) FTIR spectroscopic investigation and modeling of solute/polymer interactions in the hydrated state. J Biomater Sci 10:1289-302.

183. Selvam S, Andrews ME, Mishra AK (2009) A photophysical study on the role of bile salt hydrophobicity in solubilizing amphotericin B aggregates. J Pharm Sci 98:4153-4160.

184. Vlahov IR, Vlahova PI, Linhardt RJ (1997) Regioselective Synthesis of Sucrose Monoesters as Surfactants. J. Carbohydr. Chem. 16: 1-10.

185. Lu ZY, Wang YL (2013) An introduction to dissipative particle dynamics. Methods Mol Biol. 924:617-33.

186. Luschtinetz F, Dosche C (2009) Determination of micelle diffusion coefficients with fluorescence correlation spectroscopy (FCS). J Colloid Interface Sci. 338: 312-315.

187. Dong FL, Li Y, Zhang P (2004) Mesoscopic simulation study on the orientation of surfactants adsorbed at the liquid/liquid interface. Chem. Phys. Lett. 399: 215–219.

188. Kawaguchi T, Hamanaka T, Kito Y, Machida H (1991) Structural studies of a homologous series of alkyl sucrose ester micelle by x-ray scattering. J. Phys. Chem. 95: 3837-3846.

189. Zhang M, Zhang Z, Blessington D, Li H, Busch TM, Madrak V, Miles J, Chance B, Glickson JD, Zheng G (2003) Pyropheophorbide 2-deoxyglucosamide: a new photosensitizer targeting glucose transporters. Bioconjug Chem. 14:709-14.

190. Gavini E, Rassu G, Sanna V, Cossu M, Giunchedi P (2005) Mucoadhesive microspheres for nasal administration of an antiemetic drug, metoclopramide: in-vitro/ex-vivo studies. J Pharm Pharmacol. 57:287-94.

191. ten Tije AJ, Verweij J, Loos WJ, Sparreboom A (2003) Pharmacological effects of formulation vehicles: implications for cancer chemotherapy. Clin Pharmacokinet. 42:665-85.

192. Sobottka SB, Berger MR 1992. Assessment of antineoplastic agents by MTT assay: partial underestimation of antiproliferative properties. Cancer Chemother Pharmacol. 30:385-93.

193. Li W, Das S, Ng KY, Heng PW (2011) Formulation, biological and pharmacokinetic studies of sucrose ester-stabilized nanosuspensions of oleanolic Acid. Pharm Res. 28:2020-33.

194. Murakami H, Kobayashi M, Takeuchi H, Kawashima Y (1999) Preparation of poly(DL-lactide-co-glycolide) nanoparticles by modified spontaneous emulsification solvent diffusion method. Int J Pharm. 187:143-52.

195. McCarron PA, Donnelly RF, Marouf W (2005) Celecoxib-loaded poly(D,L-lactide-co-glycolide) nanoparticles prepared using a novel and controllable combination of diffusion and emulsification steps as part of the salting-out procedure. J Microencapsul. 23:480-98.

196. Zhou YZ, Alany RG, Chuang V, Wen J (2012) Optimization of PLGA nanoparticles formulation containing L-DOPA by applying the central composite design. Drug Dev Ind Pharm. 39:321-330.

197. Shakweh M, Ponchel G, Fattal E (2004) Particle uptake by Peyer's patches: a pathway for drug and vaccine delivery. Expert Opin Drug Deliv. 1:141-63.

198. Gladkova OL, Parkhats MV, Gorbachova AN, Terekhov SN (2010) FTIR spectra and normal-mode analysis of chlorin e(6) and its degradation-induced impurities. Spectrochim Acta A Mol Biomol Spectrosc. 76:388-94.

199. Das S, Ng WK, Kanaujia P, Kim S, Tan RB (2011) Formulation design, preparation and physicochemical characterizations of solid lipid nanoparticles containing a hydrophobic drug: effects of process variables. Colloids Surf B Biointerfaces. 88:483-9.

200. Ranpise NS, Kulkarni NS, Mair PD, Ranade AN (2010) Improvement of water solubility and in vitro dissolution rate of aceclofenac by complexation with beta-cyclodextrin and hydroxypropyl-beta-cyclodextrin. Pharm Dev Technol. 15:64-70.

201. Gupta MK, Vanwert A, Bogner RH (2003) Formation of physically stable amorphous drugs by milling with Neusilin. J Pharm Sci. 92:536-51.

202. Lee SJ, Koo H, Jeong H, Huh MS, Choi Y, Jeong SY, Byun Y, Choi K, Kim K, Kwon IC (2011) Comparative study of photosensitizer loaded and conjugated glycol chitosan nanoparticles for cancer therapy. J Control Release 152:21-9.

203. Chen K, Wacker M, Hackbarth S, Ludwig C, Langer K, Röder B (2010) Photophysical evaluation of mTHPC-loaded HSA nanoparticles as novel PDT delivery systems. J Photochem Photobiol B. 101:340-7.

204. Preuss A, Chen K, Hackbarth S, Wacker M, Langer K, Röder B (2011) Photosensitizer loaded HSA nanoparticles II: in vitro investigations. Int J Pharm. 404:308-16.

205. Roy I, Ohulchanskyy TY, Pudavar HE, Bergey EJ, Oseroff AR, Morgan J, Dougherty TJ, Prasad PN (2003) Ceramic-based nanoparticles entrapping water-insoluble photosensitizing anticancer drugs: a novel drug-carrier system for photodynamic therapy. J Am Chem Soc. 125:7860-5.

206. Kim WJ, Kang MS, Kim HK, Kim Y, Chang T, Ohulchanskyy T, Prasad PN, Lee KS (2009) Water-soluble porphyrin-polyethylene glycol conjugates with enhanced cellular uptake for photodynamic therapy. J Nanosci Nanotechnol. 9:7130-5.

207. Swain S, Behera A, Beg S, Patra CN, Dinda SC, Sruti J, Rao ME (2012) Modified Alginate Beads for Mucoadhesive Drug Delivery System: An Updated Review of Patents. Recent Pat Drug Deliv Formul. 6:259-277

208. Patil SB, Sawant KK (2008) Mucoadhesive microspheres: a promising tool in drug delivery. Curr Drug Deliv. 5:312-8.

209. Edsman K, Hägerström H (2005) Pharmaceutical applications of mucoadhesion for the non-oral routes. J Pharm Pharmacol. 57:3-22.

210. Sarmento B, Ribeiro A, Veiga F, Sampaio P, Neufeld R, Ferreira D (2007) Alginate/chitosan nanoparticles are effective for oral insulin delivery. Pharm Res. 12:2198-206.

211. Douglas KL, Tabrizian M (2005) Effect of experimental parameters on the formation of alginate-chitosan nanoparticles and evaluation of their potential application as DNA carrier. J Biomater Sci 16:43-56.

212. Ahmad Z, Pandey R, Sharma S, Khuller GK (2006) Alginate nanoparticles as antituberculosis drug carriers: formulation development, pharmacokinetics and therapeutic potential. Indian J Chest Dis Allied Sci. 48:171-6.

213. Chu JS, Amidon GL, Weiner ND, Goldberg AH (1991) Mixture experimental design in the development of a mucoadhesive gel formulation. Pharm. Res. 8:1401–1407.

214. Garcia-Gonzalez N, Kellaway IW, Blanco-Fuente H, Anguiano-Igea S, Delgado-Charro FJ, Blanco-Mendez J (1993) Design and evaluation of buccoadhesive metoclopramide hydrogels composed of poly (acrylic acid) crosslinked with sucrose. Int. J. Pharm. 100: 65–70.

215. de Campos AM, Diebold Y, Carvalho EL, Sánchez A, Alonso MJ (2004) Chitosan nanoparticles as new ocular drug delivery systems: in vitro stability, in vivo fate, and cellular toxicity. Pharm Res. 21:803-10.

216. Meng J, Sturgis TF, Youan BB (2011) Engineering tenofovir loaded chitosan nanoparticles to maximize microbicide mucoadhesion. Eur J Pharm Sci. 18:57-67.

217. Motwani SK, Chopra S, Talegaonkar S, Kohli K, Ahmad FJ, Khar RK (2008) Chitosan-sodium alginate nanoparticles as submicroscopic reservoirs for ocular delivery: formulation, optimisation and in vitro characterisation. Eur J Pharm Biopharm. 68:513-25.

218. Sarmento B, Ferreira D, Veiga F, Ribeiro A (2006) Characterization of insulin-loaded alginate nanoparticles produced by ionotropic pre-gelation through DSC and FTIR studies. Carbohyd Polym. 66:1–7.

219. Mladenovska K, Cruaud O, Richomme P, Belamie E, Raicki RS, Venier-Julienne MC, Popovski E, Benoit JP, Goracinova K 2007. 5-ASA loaded chitosan-Ca-

alginate microparticles: Preparation and physicochemical characterization. Int J Pharm. 10:59-69.

220. Khdair A, Gerard B, Handa H, Mao G, Shekhar MP, Panyam J (2008) Surfactant-polymer nanoparticles enhance the effectiveness of anticancer photodynamic therapy. Mol Pharm. 5:795-807.

221. Boyle RW, Dolphin D (1996) Structure and biodistribution relationships of photodynamic sensitizers. Photochem Photobiol. 64:469-85.

LIST OF PUBLICATIONS

Journal publication

- Optimization in solvent selection for chlorin e6 in photodynamic therapy. Shubhajit Paul, Paul Wan Sia Heng, Lai Wah Chan. Journal of Fluorescence. 2013 23(2):283-91.
- Elucidation of monomerization effect of PVP on chlorin e6 aggregates by spectroscopic, thermodynamic and molecular simulation studies. Shubhajit Paul, Sushithra Selvam, Paul Wan Sia Heng, Lai Wah Chan (accepted in Journal of Fluorescence).
- Elucidating surfactant-chlorin e6 aggregate interaction using coarse-grain modeling and fluorescence spectroscopic technique (to be communicated)
- Monomerization of chlorin e6 aggregates by bovine serum albumin: a spectroscopic and molecular docking study (to be communicated)
- Formulation optimization and in vitro characterization of surfactant-lipid nanoparticles of chlorin e6 for enhanced photodynamic activity (manuscript under preparation)

Oral presentation

- Shubhajit Paul, Christine Cahyadi, Chan Lai Wah and Paul Heng Wan Sia, Nanoparticl formulations for the delivery of poorly water soluble drugs – oral presentation in International Pharmatech Conference on Drug Delivery 2010, (KL) Malaysia.

Poster presentations

- Shubhajit Paul, Chan Lai Wah and Paul Heng Wan Sia, Formulation optimization and in vitro characterization of surfactant-lipid nanoparticles of chlorin e6 for enhanced photodynamic activity. Poster presented in 26th AAPS Annual meeting and exposition 2012, Chicago, United States.

- Shubhajit Paul, Chan Lai Wah and Paul Heng Wan Sia, Elucidating surfactant-chlorin e6 aggregates interaction using coarse grain modeling and fluorescence spectroscopic technique. Poster presented in 26th AAPS Annual meeting and exposition 2012, Chicago, United States.

- Shubhajit Paul, Chan Lai Wah and Paul Heng Wan Sia, Optimization of solvent selection for photodynamic therapy. Poster presented in 25th AAPS Annual meeting and exposition 2011, Washington DC, United States.

- Shubhajit Paul, Chan Lai Wah and Paul Heng Wan Sia, Use of excitation-emission matrix fluorescence spectroscopy for characterization of aggregation-disaggregation phenomena of chlorin e6 as a function of pH and disaggregating agents. Poster presented in 25th AAPS Annual meeting and exposition 2011, Washington DC, United States.

- Shubhajit Paul, Susithra Selvam, Chan Lai Wah and Paul Heng Wan Sia, A photophysical study on the disaggregation of Chlorin e6 by PVP using fluorescence spectroscopy. Poster presented in 5th Asian Association for Schools of Pharmacy 2011, (Bandung) Indonesia.

- Shubhajit Paul, Chan Lai Wah and Paul Heng Wan Sia, Nanoparticle formulations for the delivery of poorly water soluble drugs, poster presented in 6th ANSC Symposium on Drug Delivery, Singapore 2010.